Development of cortical bone biomarkers for the prediction of femur strength

vorgelegt von
M. Sc.
Gianluca Iori
ORCID: 0000-0001-8611-3281

von der Fakultät III - Prozesswissenschaften
der Technischen Universität Berlin
zur Erlangung des akademischen Grades

Doktor der Ingenieurwissenschaften
–Dr.-Ing. –

genehmigte Dissertation

Promotionsausschuss:

Vorsitzender: Prof. Dr. Aleksander Gurlo
Gutachter: Prof. Dr. rer. nat. Kay Raum
Gutachterin: Prof. Dr.-Ing Claudia Fleck
Gutachter: Prof. Dr. Richard Weinkamer

Tag der wissenschaftlichen Aussprache: 09. September 2019

Berlin 2019

Abstract

Osteoporosis is a skeletal disease caused by the imbalance between bone resorption and formation. In osteoporosis, the risk of fracture increases due to the structural deterioration of the bone. Hip fractures are associated with increased mortality and morbidity and lead to a decline in the quality of life. Due to these reasons, hip fractures represent a principal component of the total social burden produced by osteoporosis.

Even though the incidence of hip and other fragility fractures is rising due to the aging of our population, osteoporosis remains to date undertreated and underdiagnosed. The standard assessment of osteoporosis involves the evaluation of epidemiological risk factors and a measurement of the bone mass. This strategy however, can capture only a moderate portion of the fracture risk.

The structure of cortical bone is an important determinant of fracture resistance. At the same time, the signs of pathological resorption and osteoporosis might be visible in the architecture of cortical bone. Common modalities, however, do not achieve enough resolution for imaging the cortical microstructure. New technologies have recently provided means for the assessment of the bone architecture at peripheral skeletal sites. This allowed the association of specific changes of the cortical microstructure in distal bones with a higher fracture risk. Nevertheless, the number of structural parameters investigated in cortical bone has remained limited, and their association with hip strength is unclear.

This work investigates *ex vivo* the link between the cortical bone architecture of the human tibia and the strength of the proximal femur. The aim is to establish parameters (biomarkers) describing the cortical structure that can point towards an increased risk of fracture of the hip.

In the first chapter of the thesis, the pathogenesis of osteoporosis and basic knowledge on bone strength, together with available methods for the characterization of fracture risk are introduced. The experimental and computational techniques utilized for this work are described in chapter 2.

Chapters 3 and 4 focus on the development of cortical bone biomarkers of impaired femur strength. Here, the architecture of cortical bone in the tibia is assessed, with emphasis on the system of cavities that pervade cortical tissue. Measurements of cortical geometry and porosity and of the density and size distribution of the pores are conducted on scanning acoustic microscopy images of the tibia shaft. This establishes that a thinner cortical bone in the tibia and the higher prevalence of large pores within it are both associated with reduced femur strength. At the same time, cortical thickness and larger pores in the tibia reflect a focal thinning of cortical bone and a reduction of trabecular density in the femoral neck. Together, the results of chapters 3 and 4 indicate that the thickness and the prevalence of large pores in the cortical bone of the tibia can identify an impairment of femur strength.

Following, a method for the accurate assessment of porosity from micrometer-level cavities in cortical bone is developed. This uses data from high-resolution peripheral quantitative computed tomography (HR-pQCT), which can be collected at the tibia *in vivo*. In chapter 5, the method is validated for the measurement of cortical bone porosity. Finally, its application is extended to estimate the prevalence of large pores in cortical bone (chapter 6).

In conclusion, this thesis identifies the thickness and the prevalence of large pores of the cortical bone of the tibia as biomarkers of impaired femur strength. The assessment of these two biomarkers *in vivo* should be validated for the prediction of hip fracture risk.

Zusammenfassung

Osteoporose ist eine Skeletterkrankung, die aufgrund eines unausgeglichenem Verhältnisses zwischen Knochenaufbau und −abbau zu einer Degeneration der Knochenstruktur führt und somit das Frakturrisiko erhöht. Eine Oberschenkelhalsfraktur zieht eine hohe Morbidität und Mortalität nach sich und vermindert die Lebensqualität der Betroffenen langfristig. Allein in Deutschland werden die mit Oberschenkelhalsfarakturen assoziierten Behandlungskosten auf ca. 2.5 Milliarden Euro pro Jahr geschätzt.

Die Diagnose von Osteoporose erfolgt in der Regel über eine Messung der Knochenmasse und Bewertung epidemiologischer Risikofaktoren. Diese Vorgehensweise führt jedoch dazu, dass ein Großteil des Frakturrisiko unbewertet bleibt.

Die Architektur des kortikalen Knochens ist maßgeblich für die Knochenfestigkeit verantwortlich. Spuren von verstärkter Knochenresorption und damit frühe Stadien von Osteoporose können in der kortikalen Mikroarchitektur sichtbar werden. Die Bildgebung der Mikroarchitektur von Knochen erfordert eine hohe Auflösung. Gegenwärtig kann diese wegen der hohen Strahlendosis nur an den Extremitäten des Skeletts erreicht werden. Mithilfe innovativer Methoden, wie die hochauflösende periphere quantitative Computertomografie (HR-pQCT), konnten Veränderungen der Mikrostruktur distaler kortikaler Knochen mit einer erhöhten Inzidenz von Frakturen assoziiert werden. Allerdings wurden bisher nur wenige Strukturparameter betrachtet und der Zusammenhang zwischen der Mikroarchitektur und der Festigkeit des proximalen Femurs bleibt weiterhin unklar.

In dieser Dissertation wird ein Zusammenhang zwischen der kortikalen Mikroarchitektur der Tibia und der Festigkeit des proximalen Femurs hergestellt. Dazu wurden in dieser Arbeit verschiedene Parameter (Biomarker) ex vivo untersucht, die die kortikale Mikroarchitektur beschreiben und auf eine erhöhte Brüchigkeit des Oberschenkels hinweisen können.

Das erste Kapitel erklärt die Pathogenese der Osteoporose und beschreibt die Grundlagen der Knochenbiomechanik. Zudem wird die Methodik zur Bestimmung des Frakturrisikos erläutert. Die in dieser Arbeit angewendeten Materialien und Methoden sind in Kapitel 2 zu finden.

In Kapitel 3 und 4 werden die Biomarker entwickelt, die mit einer beeinträchtigten Festigkeit des Oberschenkels in Zusammenhang stehen. Dazu wird die Architektur des kortikalen Knochens und sein Porensystem charakterisiert. Kortikale Geometrie, Knochenporosität und Porengrößenverteilung werden mittels akustischer Rastermikroskopie an humanem Tibiaproben untersucht. Es wird gezeigt, dass die kortikale Dicke und die Prävalenz von großen kortikalen Poren in der Tibia mit der Knochenfestigkeit des proximalen Femurs und mit der kortikalen Mikroarchitektur des Oberschenkelhalses assoziiert sind.

Die letzten beiden Kapiteln dieser Dissertation erweitern die Messung der kortikalen Porosität mittels HR-pQCT. Eine auf der Knochenmineraldichte basierte Methode für die Porositätsmessung wird in Kapitel 5 vorgestellt, die auch Poren mit einem Durchmesser unterhalb der HR-pQCT Bildauflösung einschließt. Im Anschluss wird diese Methode für eine Abschätzung der Prävalenz von Poren mit großem Durchmesser angewandt und getestet (Kapitel 6).

In der vorliegenden Arbeit werden Veränderungen in der kortikalen Mikroarchitektur der Tibia identifiziert, die in Relation zu einer beeinträchtigten Festigkeit des Oberschenkels stehen. Als nächstes sollten in vivo Messungen der kortikale Dicke und Poren mit großem Durchmesser in der Tibia für eine Voraussage des Risikos einem Oberschenkelhalsbruch herangezogen und validiert werden.

Table 1. List of acronyms and abbreviations.

BMC	Bone mineral content
BMD	Bone mineral density
$BMD_{95\%}$	BMD distribution (95%) quantile
BMD_{PEAK}	BMD distribution peak
BMD_{STD}	BMD inhomogeneity (standard deviation)
BMD_{WIDTH}	BMD distribution width
BMU	Bone multicellular unit
BV/TV	Bone volume fraction
Ct.Ar	Cortical bone area
Ct.Po	Cortical bone porosity
Ct.Th	Cortical bone thickness
Ct.Wba	Areal portion of cortical tissue
CT	Computed tomography
CV	Coefficient of variation
DXA	Dual X-ray absorptiometry
ECM	Extracellular matrix
FE	Finite element
FN	Femoral neck
FOV	Field of view
HR-pQCT	High-resolution peripheral quantitative computed tomography
HU	Hounsfield unit
hvFE	Homogenized voxel finite element
OP	Osteoporosis
Po.A	Pore area
Po.D	Pore density
Po.Dm	Pore diameter
$Po.Dm_{10\%}$	Pore diameter distribution (10%) quantile
Po.n	Pore number
QCT	Quantitative computed tomography
$relCt.Po_{60\mu m}$	Relative proportion of porosity (from pores with diameter > 60 μm)
RMSE	Root mean square error
ROI	Region of interest
RVE	Representative volume element
SAM	Scanning acoustic microscopy
SEE	Standard error of the estimate
SOS	Speed of sound
T.Ar	Bone tissue area
Tb.N	Trabecular number
Tb.Sp	Trabecular separation
Tb.Th	Trabecular thickness
TOF	Time of flight
Tt.Ar	Total bone cross-sectional area
VOI	Volume of interest

Contents

Chapter 1: Introduction

1.1 Bone structure and function

Bone is one of the organs constituting the skeletal system of vertebrates. The skeleton is composed of different tissue types, such as mineralized bone tissue, cartilage, bone marrow and blood vessels, which are populated by several distinct linages of cells. The skeleton provides protection and support for other organs. The musculoskeletal system allows complex articulation between body parts preserving, at the same time, mechanical stability of the whole. These are key characteristics for a precise and efficient motion in a gravity environment. In this context, bone sustains and transmits the forces generated by the interaction of the organism with the outer world, and provides the necessary rigidity of the system. In birds and mammals, the marrow contained in the cavity of long bones is the site of hematopoiesis: the production of blood cells. Besides these functions, bone has also evolved to provide a site for calcium storage and homeostasis [1], whose were suddenly required when amphibians left the oceans for a new, calcium poor landscape.

In the next paragraphs, I will concentrate on one single aspect of bone function which is the mechanical one. I will start by describing structural and compositional aspects of the building blocks of the bone material. These are the features that confer to healthy bone its unique mechanical performance. I will then describe with more detail separate aspects of what I have just called "mechanical performance". This is the part where I introduce the most relevant mechanical properties of bone. A short but necessary introduction to bone biology comes afterward. In the last part of this first chapter, I will move to the case in which something (or many things) go wrong. These are the topics of osteoporosis and bone fragility, of their implication for material scientists and of the technology for their monitoring in living humans.

1.1.1 The hierarchical structure of bone

The hierarchical arrangement of bone (Fig. 1) spans several length scales: from the atomic level of its basic constituents (bottom of Fig. 1), to the several centimeters of human long bones (top of Fig. 1).

At the bottom of the hierarchy are **type I collagen fibrils**, **carbonated hydroxyapatite (hAp) crystals** and **water**. These represent the major components of the bone **extracellular matrix (ECM)**. After these three constituents, bone contain different non collagenous proteins (osteocalcin and osteopontin are probably the most famous) and various types of cells. Triple helices of collagen chains are assembled following a precise staggered pattern that allows the nucleation of hAp particles in intrafibrillar gap regions (~40 nm gaps between the tail of a collagen molecule and the head of the next). Enzymes promote the formation of acicular crystals of carbonated hAp in these regions from calcium and phosphate ions that are abundant in the body [2]. Crystals grow and merge into platelets that slowly invade the ~0.24 nm-thick overlap region between collagen molecules, imposing a compressive pre-stress of the matrix [3]. Due to its tendency to form aggregates that span more levels of the hierarchy, the hAp component in bone has sometimes been regarded as a mineral foam pervading the collagen fabric [4]. In healthy bone however, a layer of structural water incorporated on their surface allows hAp platelets to maintain the high aspect ratio that confers flexibility and toughness to the assembly [5]. Together, water, collagen and hAp crystals form the building block of the **mineralized collagen fibril**. More details on the assembly of mineralized collagen fibrils can be found in [6–9].

A large part of the mineralized collagen fibrils is arranged close to parallel in larger filamentous arrays called **collagen fibril bundles**. Bundles, in turn, are layered in sheets of uniformly aligned fibrils with a typical width of 3−7 μm (the **lamella**), while intra-bundle space is filled with disordered, randomly oriented and less dense collagen fibrils [10]. Such tissue sheets represent the building block of **lamellar bone**: the following level of the bone tissue hierarchy. For a comprehensive review on the structure and function of lamellar bone see Weiner et al. [11].

At the next level of organization, lamellar sheets form **trabecular** and **osteonal** (compact) bone, tissue types ranging several hundreds of microns and already visible by the human eye. Trabecular bone (also known as spongy or cancellous bone) fills the extremities of long bones (epiphysis) and the vertebrae. It is a highly porous, lightweight network of struts (the trabeculae) that can vary in shape, depending on site and mechanical function, between rod- and a plate-like geometries. Osteonal tissue builds up the outer compact shell (**cortical bone,** Fig. 2B) of most adult human bones. Here, the basic building block is the **Osteon**: a cylindrical complex made by concentric lamellae that envelop a central cavity (the Haversian canal) of 25 to 200 μm in diameter [12–14]. **Haversian canals** (Fig. 2C) host blood and lymphatic vessels and are connected laterally by cavities called Volkmann's canals. In the diaphysis of long bones, Osteons are mostly oriented longitudinally but spiral around the axis of the diaphysis [15] and present often irregular branching [16]. The outer diameter of osteons varies largely across species and anatomical location [17–19]. In humans, osteons can range between 150 and 300 μm in diameter [20,21] and reach several millimeters of length [21,22]. Adjacent lamellae building the walls of the osteon show a twist in fibril orientation that creates a twisted or oscillating plywood [23,24]. Each osteon finally, is wrapped by a foil of highly mineralized tissue known as the **cement line**. The outer surface of cortical bone is called **periosteum** and is formed by few layers of circumferential lamellae covered with lining cells and by an outer fibrous layer. In long bones, the inner surface separating the cortex from the bone marrow is also formed by a thin layer of connective tissue and bone cells and is called **endosteum**.

The final level in the hierarchy of bone structure is represented by whole bones and their characteristic macroscopic shape. At this level, long bones can be divided based on architecture and function into an **epiphysis** (the bone extremity, hosting bone's growth plate during early life and covered with cartilage at the joint articulation with other bones) and a **diaphysis** (the shaft or core of the bone composed mainly of compact cortical bone and marrow).

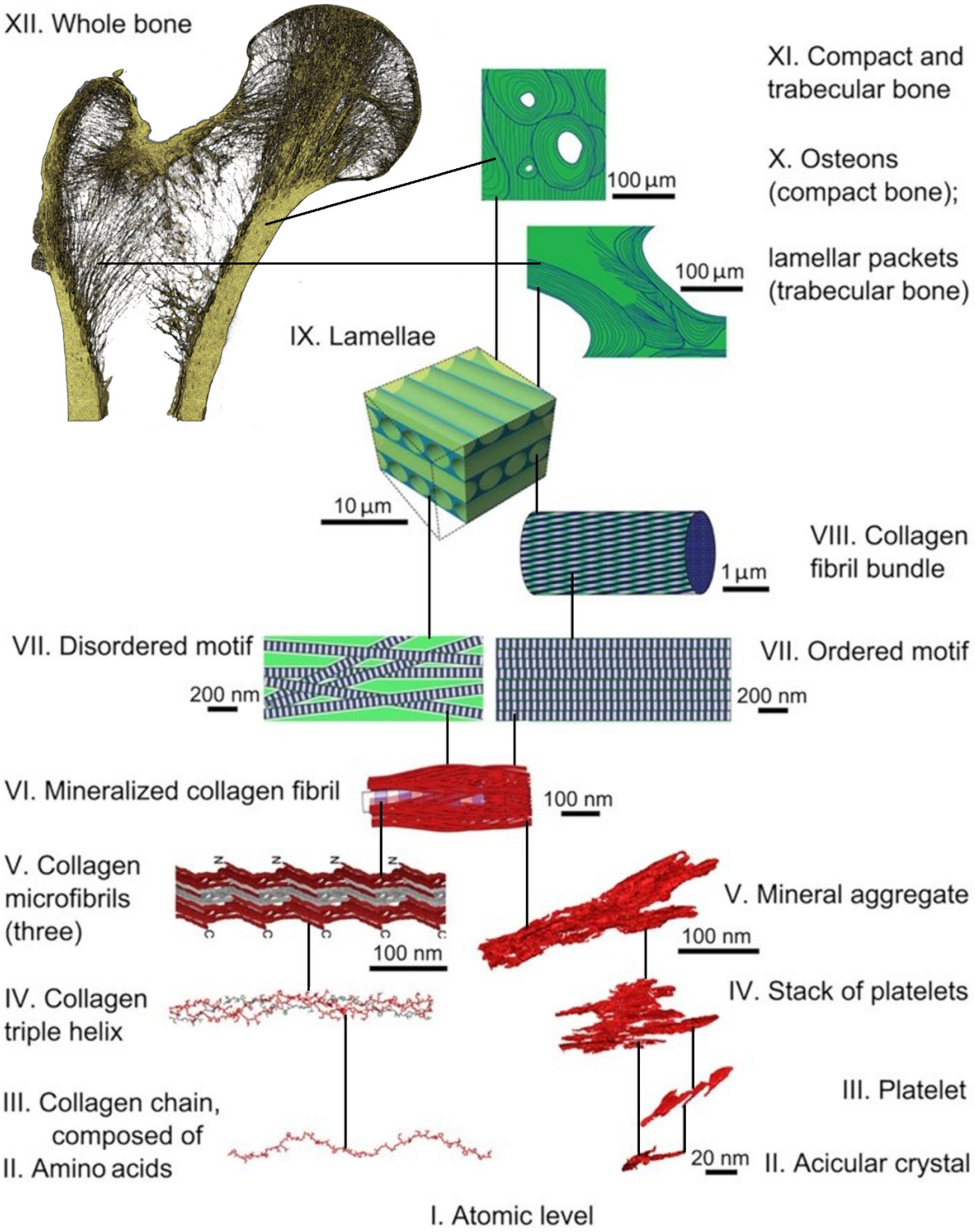

Fig. 1. Hierarchy of the bone structure. Modified from [25] with permission from AAAS.

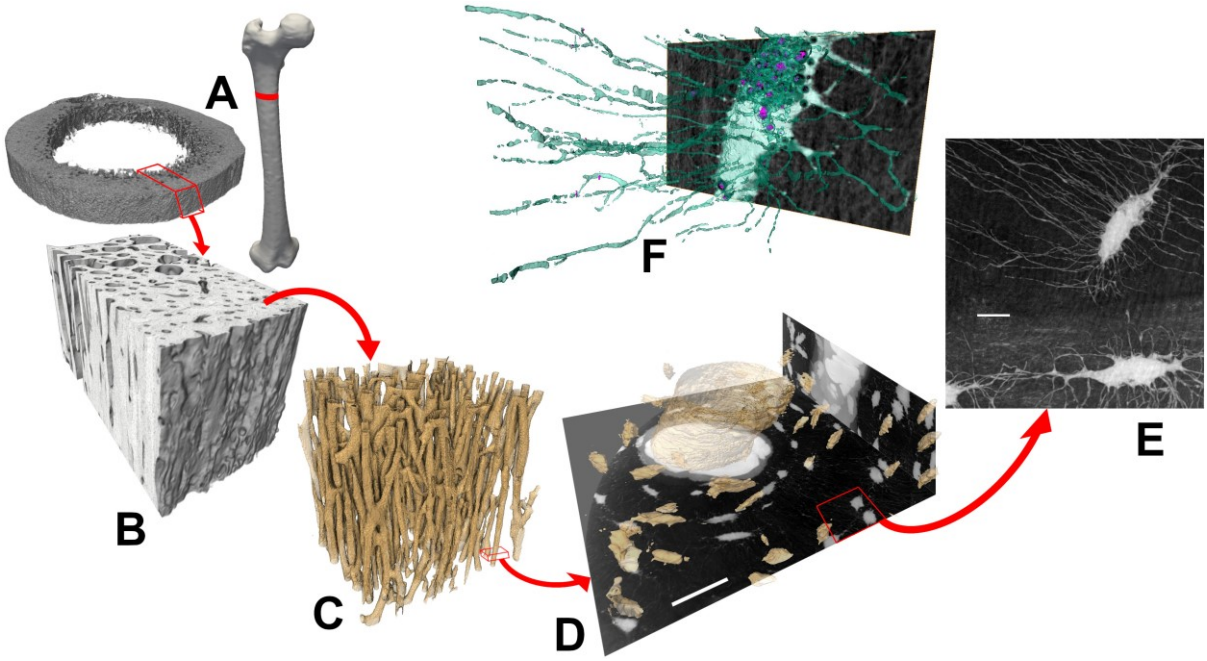

Fig. 2. Hierarchy of bone porosity in human cortical bone. As the organization of the bone material spans several length scales, so does the system of cavities in it. (A) Cross-section of the proximal femur shaft. The diaphysis of long bones is hollow and hosts marrow. (B) Detail of the cortical bone. The transition from cortical to trabecularized endosteal bone leads to a gradient in pore size, with larger pores closer to the marrow cavity. (C) Haversian and Volkmann's canals in cortical bone. Blood (and lymphatic) vessels run into these canals for the transport of nutrients. Haversian canals are aligned preferentially with the axis of the bone and present multiple lateral branches. (D) Detail of Haversian canal with the system of osteocyte lacunae disposed concentrically around the central void. Each lacuna is literally a cave into the mineralized matrix that hosts one osteocyte cell. Osteocytes remain embedded within the bone tissue during matrix deposition, are connected with long dendrites that run through canaliculi and are responsible for mechanosensation (see section 1.1.3). White bar: 20 µm. (E) Detail (projection of minimum intensity) of osteocyte lacunae and of the network of canaliculi. Together, lacunae and canaliculi form the lacuno-canalicular network (LCN). The LCN contributes to only 1% of the total cortical bone porosity [26]. White bar: 5 µm. (F) 3D rendering of an osteocyte lacuna. Images obtained with HR-pQCT (A) and synchrotron microCT (B, C) and phase contrast nanoCT (D-F).

1.1.2 Bone adaptation and regeneration

To the eyes of an external observer, the shape and size of each bone look perfectly optimized to fulfil a peculiar mechanical function [27]. In this sense, the architecture of each bone of the skeleton is a unique product of evolution [28]. Alongside with genetics, functional adaptation to external requirements is constantly influencing the shape and architecture of bones. Besides this, healthy bone is constantly regenerating itself in order to avoid the accumulation of fatigue damage. The mechanisms driving the continuous modification of the bone structure are known as bone modelling and remodelling.

Modelling refers to the adaptation of the bone shape according (and as a response) to a new mechanical demand. In a young organism, bones grow to keep the pace of the general increase in size and mass of the body. Long bones grow in length via endochondral ossification, which occurs specifically at the growth plates (in the epiphyses) and I will not describe here. Once formed, long bones keep growing even after the fusion of the growth plates, which occurs between age 12 and 19 [29]. This is accomplished by adding new tissue on the external surface of the bone (periosteal apposition), while removing, at the same time, tissue from the marrow cavity (endosteal resorption) [30,31]. As a result, certain regions of long bones such as the

femoral neck keep increasing in diameter throughout the entire adulthood [32]. In short, modelling can be seen as the removal of tissue from a certain bone surface and the formation of new tissue somewhere else [33].

Bone adaptation has attracted the interest of scientist since more than one century. Initially, bone adaptation was conceived as a rule by which the body would solve a specific optimization problem: that of achieving maximum bone strength with minimum amount of material [27,34]. This is the example of Julius Wolff's "Gesetz", which was dismantled, in recent years, as ill-posed [35,36]. Modern readings of bone modelling see adaptation as the outcome of a biological regulatory process [37].

Remodelling consists in the resorption of old tissue followed by the formation of new bone on the same site. Remodelling accomplishes the renewal of aged portions of the bone in which damage has accumulated, by replacing these with newly formed osteoid (not yet mineralized bone matrix). Remodelling is activated by mechanical load and is dictated by the ability of particular cells of mesenchymal origin to respond to mechanical strain. In humans, such specialized cells are the osteocytes (see section 1.1.3), although in other species remodelling occurs also in the absence of osteocytes [17]. It was initially thought that a threshold in the level of local strain would exist for the initiation of tissue remodelling [38]. Today, the combination of high resolution imaging and numerical simulations has confirmed mechanical loading as the principal (but not the only) agent driving remodelling, and has proved false the presence of a strain threshold activating tissue resorption and formation [39].

1.1.3 Bone biology

In the fetal skeleton, in regions of new bone apposition (e.g. the growing bones of children) and within repairing fracture gaps, bone initially grows in a primary, non-lamellar form (also called woven bone). After its appearance, woven bone is soon replaced by lamellar bone. Given the focus of this thesis on adult bone, I will not discuss woven tissue here.

Lamellar bone (secondary bone) is formed by breaking down old tissue and forming new osteoid in its place. For the description of bone biology I will concentrate on this process which, as we have seen, is called remodelling. It should be kept in mind, however, that despite the formal distinction between them, bone modelling and remodelling involve identical cellular mechanisms. Furthermore, I will focus on the remodelling of osteonal bone only. From a point of view of the cellular cascade that it involves, the remodelling of trabeculae can be considered analogous to that of osteonal bone.

Remodelling is triggered by local damage or strain of the bone matrix. **Osteocytes** are the cellular sensors responsible for the mechanosensing ability of bone and for signaling a biochemical "alarm" from tissue regions where remodelling should intervene. Osteocytes can monitor broad tissue regions thanks to a network of dendrites that pervades long canaliculi in lamellar bone (Fig. 2E and F). At the same time, the canaliculi connect osteocytes with the vasculature and with the bone surface (e.g. with the walls of Haversian canals, Fig. 2D), where lining cells reside and signals should be delivered. In response to fatigue damage or unloading, Ostecytes undergo apoptosis [40], initiating a not yet fully understood signaling cascade that recruits osteoclast precursors to the area of need. From this point onward, osteonal remodelling (i.e. the construction of a new osteon) takes place inside the so-called **Bone Multicellular Unit** (BMU).

A **BMU** (Fig. 3) is a functional gathering of different cell types where old tissue is resorbed and new osteoid is deposited. If sectioned transversally along its axis, an active BMU appears as a hole or pit with the shape of a cone [41]. The direction of the cutting cone will determine the axis of the newly formed osteon. At the bottom of the pit, where a narrow erosion front

advances, active primary **osteoclasts** are densely packed (orange arrowheads in Fig. 3). Osteoclast are big, multinucleate cells that differentiate from monocyte/macrophage precursors close to the bone surface and are responsible for the resorption of the old mineralized matrix [42]. Osteoclasts shape their cytoskeleton to adhere to the bone matrix, forming a sealed cavity where mineral and collagen are dissolved by an acidic secretion produced by the cell [42]. Right after the initial resorption surface, a wide portion of the BMU is populated by **osteoprogenitors** (the precursors of **osteoblasts**, the bone forming cells) side by side with secondary osteoclasts (yellow arrowheads in Fig. 3). In this reversal and resorption region, tissue removal continues, even though at a slower pace, with the cone being widened further. When the density of osteoprogenitors reaches a certain threshold, these cells differentiate into active osteoblasts that synthesize new osteoid. After this point in time, osteoid formation reduces the diameter of the cutting cone, until the final size of the new Haversian canal is reached.

A large amount (~70%) of the final mineral content is deposited in the newly formed osteoid within weeks from its appearance. The full mineralization of the ECM however, is reached only after several months [16,43]. Mineralization involves complex, poorly understood processes, and is mediated either by noncollagenous proteins that are embedded in the ECM (where collagen provides the template for hAp nucleation), or by the interaction of the matrix with mineral vesicles [44].

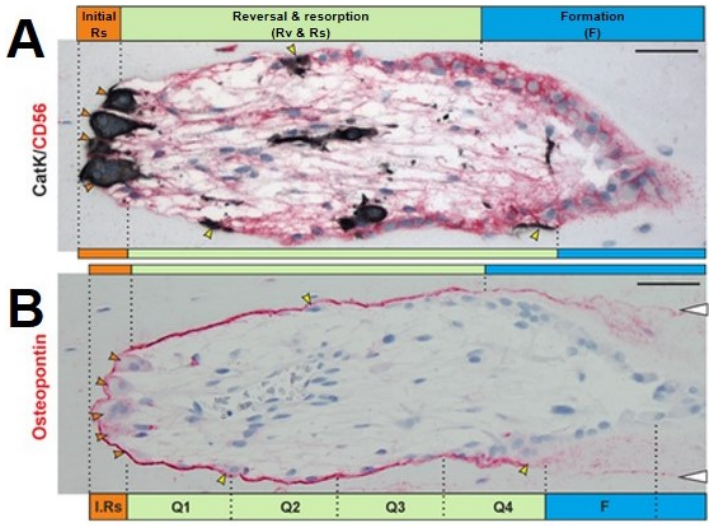

Fig. 3. The Bone Multicellular Unit. (A) Transverse section through a cutting cone immunostained for osteoclastic (black) and osteoblast lineage cell (red) markers. (B) Consecutive section of (A), immunostained for the cement line marker osteopontin (red). Orange arrowheads: primary osteoclasts. Yellow arrowheads: secondary osteoclasts. White arrowhead: cement line. Reprinted from [41] with permission from Wiley.

Once the osteoid is deposited and during the mineralization phase, most osteoblasts undergo apoptosis and die. A limited number of cells, however, survives, trapped within the ECM, and further differentiates into osteocytes. During differentiation, osteocytes develop the long dendritic processes (Fig. 2E and F) that I have already introduced. The **lacuno-canalicular network** (LCN, composed of canaliculi and osteocyte lacunae) serves for the transport of hormones and cell nutrients. Osteocytes have an half-life of 25 years and constitute more than 90% of the cells in the mature human skeleton [16,45].

Table 2. Concepts of bone mechanics that will help us throughout the thesis.

Stiffness	Describes the ability of a component or sample to resist without undergoing deformation when an external load is applied. It is measured as the applied force divided by the resulting deformation of the considered body. Stiffness is not a characteristic of the material but an extensive property, meaning that it depends on the physical dimensions of the problem as well as on the conditions of load. Corresponding material (or intensive) properties are the **elastic or Young's moduli**, describing the linear-elastic relation between stress and strain for a given material.
(Bone) **Strength**	The ultimate force that a bone (or a sample) can withstand under a specific type of loading. Different loading scenarios can lead to different values of strength. **Example 1:** if a sample of bone tissue is loaded in compression and tension, the strength in compression is generally 40% higher than the strength in tension [46]. **Example 2:** when the proximal femur is loaded in the conditions of physiological standing, its strength is more than double than the strength during a fall to the side. Yield strength is the load after which a material loses its linear elastic behavior. After yield, bone can still resist deformation but is irreversibly damaged and cannot return to the original shape. Yield strength is lower than ultimate strength. Also, strength under prolonged cyclic loading (fatigue strength) is lower than ultimate strength.
Fracture (or failure)	Fracture occurs when a certain load exceeds the strength of a sample or bone. This means that fracture is not determined uniquely by the capacity of a given bone to resist high loads (its strength) but also by the type and magnitude of the applied load. **Example 1:** during a car accident, the energy transferred to the body (and therefore to the bones) by the sudden deceleration induces forces that can be order of magnitudes larger than those acting on the skeleton during everyday activities. In addition, such forces act along unusual trajectories, for which the skeleton is not optimized. Under such circumstances, fracture must be expected. **Example 2:** a bone fracture following a low energy trauma such as a fall to the ground from a standing position generally hints to a condition of bone fragility. Contrary to Example 1, this fracture might be caused by a reduction of the bone strength below the desirable level. Such fractures are referred to as **fragility fractures**.
Toughness	Toughness refers, in general, to the ability of a material or sample to dissipate energy before fracturing. The term, however, can have two meanings. **Material toughness** is a material (or intensive) property and is independent of the type of load. It is the quantity of energy required to propagate a crack in the material. **Fracture toughness**, instead, is the extensive quantity defining the work to fracture of a certain sample/bone subject to a specific load.

1.1.4 Bone mechanics

Bone is a self-repairing, lightweight composite with an outstanding combination of **elastic modulus**, **strength** and **toughness** (fracture resistance) [47]. Such characteristics (for which you can find a definition in Table 2), are often mutually exclusive in the field of material science [48].

While humans design artifacts from scratch and employ a large variety of materials for their production, biology evolves its structures in a more conservative way. The formation of new features proceeds via small, random variations of preexisting solutions and utilizes elements that are readily available in the environment. Nature fabricates bone with a limited selection of components, at ambient temperature and with minimum energy expense. The key for the outstanding mechanical performance of bone, is the masterful combination and arrangement of its components in the hierarchical structure described in section 1.1.1 [36,49].

From nano- to mesoscale mechanics

Atomistic representations of the collagen-hydroxyapatite mineral nano-composite in bone are able to explain the high stiffness reached by the material as well as the dependence of its elastic modulus with the degree of **tissue mineralization** [50]. Uncoiling of tropocollagen proteins and sliding at the interfaces between collagen and mineral crystals can be predicted by such models and represent a mechanism by which bone dissipates energy while deforming [50–52].

The increase of both elastic modulus and strength for growing values of tissue mineralization, however, is explained by the staggered organization of mineral platelets within collagen fibrils [9,53]. The high aspect ratio and the extreme vicinity of parallel platelets leads to the transfer of tension through the mineral phase accompanied by diffuse shearing of the collagen matrix [53]. This deformation mechanism in bone allows to overcome the limit imposed by the ultimate tensile stress of collagen and was confirmed by experimental results [54].

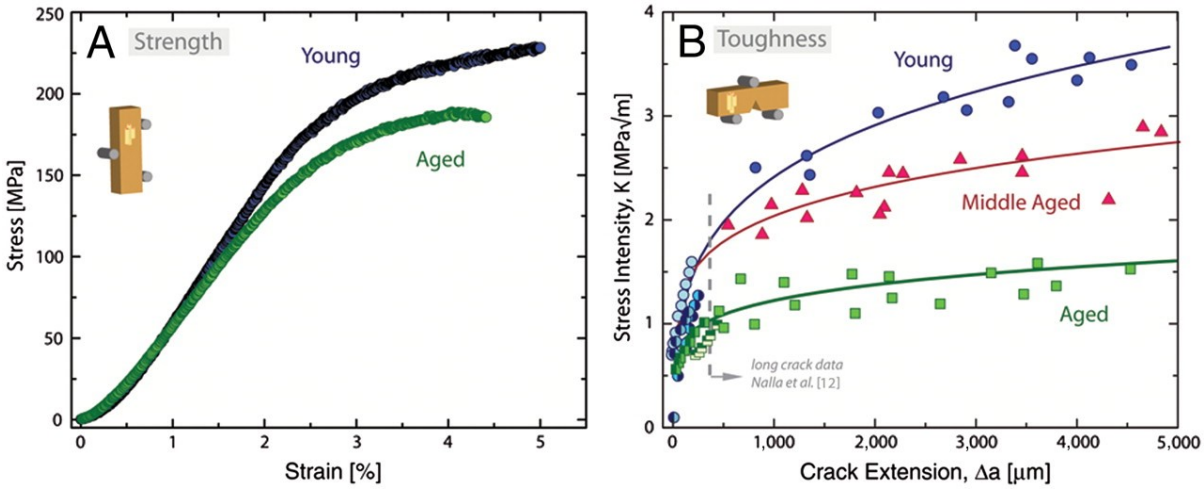

Fig. 4. Strength (A) and fracture-toughness (B) of human cortical bone as a function of age. Reprinted from [55] as allowed by PNAS.

The result is a **quasi-brittle** material with a linear-elastic behavior followed by a **long post-yield life** (Fig. 4) [55]. At the mesoscale (few hundreds of microns up to several millimeters) the elastic modulus and the yield strength of cortical and trabecular tissue are higher in compression than in tension, conferring to the material bone its characteristic mechanical **asymmetry** [46]. At such length scale, bone is often viewed as a 2-phase composite, in which

a mineralized collagen matrix (phase A) is pervaded by marrow or blood filled inclusions (phase B) [56]. From this point of view, the relative proportion between the two phases (or the volume fraction of bone) is the main determinant of tissue elasticity, strength and toughness, as extensively reported from as early as 1969 [57–61].

The ability of the collagen matrix to dissipate energy while undergoing deformation as well as the presence of water inclusions confer to bone tissue a **viscoelastic** behavior [62]. This is manifested as damping during cyclic loading, as stress relaxation in the elastic regime [63] and as a general dependence of the stress-strain curve on the strain rate. For samples of bulk cortical bone material, higher strain rates lead to an increase of the measured stiffness [64]. Tensile strength and work to fracture, on the contrary, decrease when the strain rate is increased [64].

The role of tissue orientation

From the nanometer level of collagen fibrils up to the organization of osteons and trabeculae, the alignment of the bone structure is finely controlled (Fig. 1). The arrangement and orientation of the tissue determines the final **anisotropy** of its mechanical response. In cancellous bone, orientation, shape and connectivity of single trabeculae determine elastic and yield tensors that can vary from close to isotropic (such as in the vertebrae) to highly anisotropic, with a principal component aligned with the principal load direction (see, for an example, the trabecular bone in the femur neck at the top of Fig. 1) [60]. Similarly, compact bone displays elastic and failure properties that are close (but not perfectly) transverse orthotropic [65,66], with an axis of symmetry aligned with the axes of the osteons and with the principal direction of load.

Toughening mechanisms in bone

Bone's unique ability to resist fracture is accomplished with a variety of mechanisms that act at different levels of the hierarchy. Some of these are introduced below. For a complete review of the origin of toughness in bone (and mineralized tissue in general) you can refer to [67,68].

When a crack propagates through bone tissue, a large region of material away and ahead of the crack tip is affected, showing microcracks and diffuse matrix damage [67]. At the nanometer level of collagen molecules, energy is dissipated in this area by sliding of the fibrils and formation of dilatational bands [69,70]. The latter (observed using confocal and atomic force microscopy) constitute a separation between mineral aggregates, with stretching of their osteocalcin and osteopontin connections [69]. Behind the crack tip, intact collagen fibrils form bridges between the crack edges, holding them together. At a micrometer level, microcracks and uncracked ligaments of tissue ahead of the crack tip reduce the stress concentration [71]. At the level of lamellar tissue, mechanisms for crack deflection come into play. The plywood nature of lamellar bone deviates a crack propagating through an osteon. This happens because fracture can travel easily only along the direction of collagen fibrils: when pulled, a single fibril of collagen type I can withstand stresses up to 0.60 GPa and 100% strain without breaking [72]. Finally, when the crack reaches the edge of an osteon, its propagation is again hindered by a solid membrane of highly mineralized tissue represented by the cement line [73]. As a result, a large amount of energy (and a very long path) are required for a crack to find its way out of an osteon.

Organ mechanics as the final result

A description of single properties of the bone material cannot provide an explanation for the mechanical behavior of whole bones. This should be considered, instead, the result of the interaction between structural and mechanical features at single levels of the hierarchy. In the femur, the amount, type, and orientation of bone tissue guarantee maximum strength and rigidity of the organ during gait. In the extraordinary event of a fall, however, impact forces act on the bone along unusual directions. In this case, the femur has lower stiffness and strength,

but can absorb a higher amount of energy thanks to its longevity after yield [74]. In this sense, the final player of bone mechanics is adaptation, which modifies the structure according to external demands.

1.2 Osteoporosis

Osteoporosis (OP) literally means "porous bone". OP is a non-communicable systemic skeletal disorder that affects the structure of bone and reduces its resistance to fracture. In 1994, the World Health Organization (WHO) has agreed on an operational standard for the assessment of osteoporosis based on the **bone mineral density** (BMD) measured with dual-energy X-ray absorptiometry (DXA) [75]. According to the report from 1994, OP is defined as the condition in which BMD at the lumbar spine or proximal femur falls 2.5 SD or more below the average BMD of a young and healthy reference population.

In the next sections I will briefly describe the mechanisms that are recognized causes of OP. I will then discuss hip fractures due to their central role in this thesis. Finally, the technology for the assessment of osteoporosis and fracture risk is presented.

1.2.1 Pathophysiology

The remodelling mechanism described in sections 1.1.2 and 1.1.3 allows constant renewal of skeletal tissues without loss of bone mass. In fact, until 30-40 years of age in both women and men, the total mass of the skeleton is generally increased or conserved. It is in this period of life that peak bone mass is achieved. After this point and due to **aging**, the balance between bone resorption and formation turns toward a net loss of the total bone mass. This happens to all of us, and it is why reaching a peak bone mass during youth is crucial for retarding the onset of osteoporosis [76].

Aging affects bone formation by impairing osteoblast maturation [77] and function [78]. At the same time, the differentiation, activation and survival of osteoclasts increase with age [79], supposedly favoring bone resorption. The molecules receptor activator of nuclear factor-kB (RANK) and its ligand (RANKL) and osteoprotegrin (OPG) have a central role for osteoclast activity. Osteocytes and osteoprogenitors express RANKL that binds to RANK on the surface of osteoclasts, promoting their activity and differentiation [80]. This might be the reason why osteoprogenitors are often observed in close vicinity to an active osteoclast on active resorption surfaces (Fig. 3). Osteoprotegerin (OPG), which binds to RANKL, is secreted and used by mature osteoblasts to inhibit osteoclast activation.

Estrogen regulates the expression of both RANKL and OPG. For these reasons, the estrogen deficiency associated with **menopause** causes rapid bone loss and deterioration of the bone microarchitecture [81], putting women after menopause at a greater risk of fracture.

The mechanical factor

As described in section 1.1.3, bone remodelling is directly regulated by local strain levels [39] and therefore by mechanical loading. As a consequence, periods of **disuse** following immobilization and prolonged bed rest, spinal cord injury or spaceflight, lead to a significant loss of bone structure and mass [82].

The fact that muscle strength and bone mass decline jointly during both aging and disuse [83], together with the observation that the largest strain levels on the periosteum are caused by muscle activity [84], support the centrality of the mechanical factor for bone loss [37]. Despite inspiring novel strategies for combating osteoporosis [85], this view might overlook the importance, after menopause, of the endocrine mechanisms described in the previous paragraph.

Aging and disuse are associated with a similar drift towards adipogenesis (and therefore reduced osteoblastic differentiation) in bone marrow [86,87], reduced osteoid formation and an increase in serum markers of bone resorption [88]. Discerning the effects of the two is complicated by the altered response of bone remodeling to disuse with age [89] and by the difficulty in performing such research on humans. To date, spaceflight provides the most valuable model of human bone disuse: exposure to 6 months of microgravity during missions on the International Space Station leads to an average 3% bone loss at the lumbar spine [90] and in the trabecular bone of the tibia [91], which is higher than the rate of bone loss in postmenopausal osteoporosis [82,92].

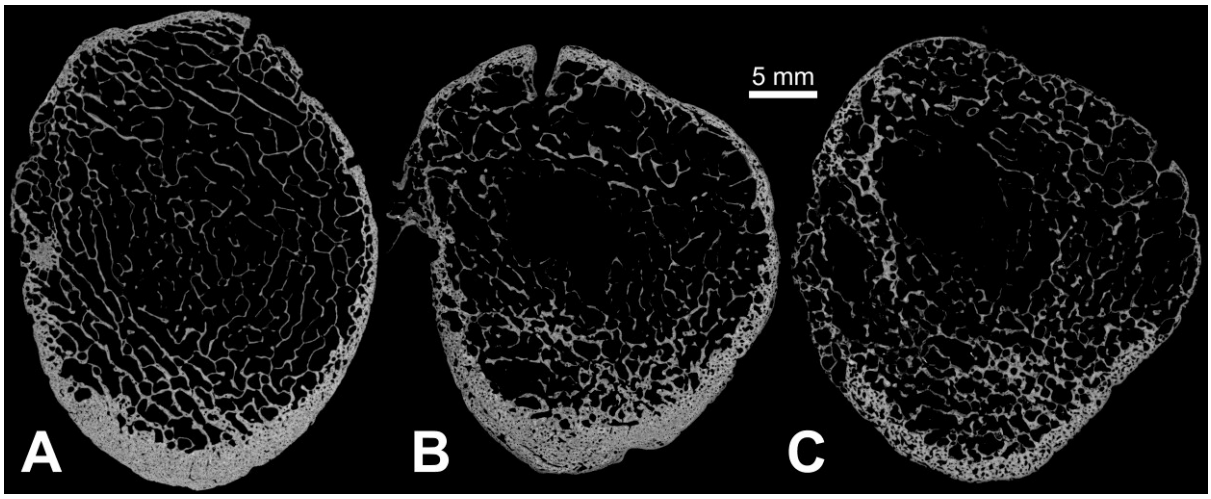

Fig. 5. Effect of osteoporosis on the bone structure of the human femoral neck. Sections imaged *ex vivo* with 100-MHz, 12-µm pixel size scanning acoustic microscopy. (A) 85 years old woman with low bone mass (osteopenia); $aBMD_{neck}$: 616 mgHA/cm³; femur strength: 3.0 kN. (B) 69 years old woman with low bone mass; $aBMD_{neck}$: 599 mgHA/cm³; femur strength: 2.5 kN. (C) 92 years old woman with osteoporosis; $aBMD_{neck}$: 448 mgHA/cm³; femur strength: 1.7 kN. Reference $aBMD_{neck}$ and femur strength values obtained *ex vivo* with DXA and mechanical tests, respectively.

Effects on the bone structure

Osteoporosis has been associated with normal, increased as well as with decreased bone turnover [93]. It is still unclear to which extent OP is caused by an increase in osteoclast activation, by impaired bone formation from osteoblasts or, as recently suggested, by the uncoupling between the two processes [94]. Osteoporosis, however, is generally linked to a negative BMU balance, in which resorption prevails over formation and the total amount of bone is reduced. Osteoporotic trabecular bone becomes thinner, tends to become rod-like and loses connectivity [95]. At the same time, cortical bone becomes thinner and more porous due to the progressive increase in size of the pores and accumulation of BMUs [96,97].

Resorption proceeds from the endosteal surface, which has made authors postulate a mediator role of bone marrow in bone turnover [98]. Giant pores appear close to the endosteum as clusters of remodelling BMUs [99], leading to the gradual **trabecularization** of the endosteum. Apposition on the periosteal side increases the cross sectional area of long bones with growth but does not generally keep the pace of endosteal resorption [100]. As a result, osteoporosis leads to a phenotype of bone fragility which is characterized by the combination of thinner cortices pervaded by larger pores and by a thinner, less dense and more sparsely connected trabecular microarchitecture (Fig. 5) [101].

1.2.2 Hip fracture

This section contains few facts on the incidence and burden of fragility (and particularly hip) fractures in Europe. The most important risk factors for fracture are also introduced. For a complete review of these topics see references [102–104].

Epidemiology

- In 2010, 3.5 million fragility fractures were sustained in the EU only (for a definition of fragility fracture see Table 2). Of these, approximately two thirds occurred in women and 610,000 were hip fractures [103]. In the same year, the number of individuals who reported a hip fracture during their lifetime was 3.3 million.
- Due to the increasing age of our population, the annual number of fragility fractures is expected to rise to 4.5 million (+28% compared to 2010) by 2025 [103].
- At the age of 50, Swedish women have a 22.9% probability to sustain a hip fracture during their life [105], which is similar to the lifetime probability of wrist (20.8%) and spine (15.1%) fractures. At age 80, however, the lifetime probability of a hip fracture is double than that of a fracture at other sites [105].

Consequences

- Hip fractures are associated with an increase in **mortality**. Most deaths occur in the 3-6 months after the fracture [106]. Among the elderly, the mortality rate in the year after a hip fracture reaches 36% [107]. In 2010, half (50% for women and 47% for men) of the total number of deaths associated to fragility fractures (43,000) in the EU were caused by hip fractures [103].
- The **cost** of osteoporosis on European healthcare systems in 2010 was estimated to be €37 billion. Since hospitalization and treatment of incident fractures represent the largest portion (66%) of this cost, and since hip fractures almost always require hospitalization and surgery, hip fractures contribute to a large portion (54%) of the total burden of osteoporosis [103].
- Hip fractures are painful and almost always lead to long immobilization. Despite advances in rehabilitation, the functional decline caused by a hip fracture is rarely recovered. Due to these reasons, hip fractures represent a cause of **morbidity** and drastic **decline in the quality of life** [104].

1.2.3 Risk factors for fracture

In addition and independently to a low BMD, several risk factors have been identified for the development of osteoporotic fractures. These include **age**, **sex**, **body mass index**, **history of fracture** (both previous fragility fracture as well as parental history of hip fracture), cigarette **smoking** and **alcohol intake** above 3 units per day. **Glucocorticoid** treatment [108] and concomitant diseases such as **chronic kidney disease** [109] and **diabetes** [110] do also increase the probability of fracture. Finally, fracture risk varies between **ethnicity** [111] and **country** around the world [102].

It is uncertain whether **fall history** represent a risk factor for osteoporotic fractures. On one hand, hip fractures are nearly always caused by a fall to the ground, even if a small amount of spontaneous fractures exists [112,113]. This would support interventions strategies based on a type of physical exercise that targets balance improvement and thus reduces the overall risk of falls. On the other hand, only 1% of all falls lead to a fracture of the hip [114]. Due to this and to the additional fact that the age factor partially incorporates the subject predisposition to

recurrent falls, current tools for the prediction of the individual fracture risk do not generally take falls into account [115].

1.2.4 Management of osteoporosis

Osteoporosis is undertreated. A review from 2013 suggested that, in the EU, there is a 57% gap between the number of women at high risk of fracture and those receiving osteoporosis treatment [103]. Of all patients sustaining a hip fracture, about 35% receives a new osteoporosis diagnosis and only 21% of them is initiated on anti-resorptive treatment [116]. This despite the "*almost universal agreement that individuals with documented hip or vertebral fracture have established osteoporosis*" [117]. In general, the last decade has seen an alarming decline in the uptake of osteoporosis medications [118]. This is in part due to the high media coverage of the side effects of the use of bisphosphonates such as osteonecrosis of the jaw [119] and atypical femur fractures [120].

1.2.4.1 The DXA T-score

The WHO defines osteoporosis as a BMD of 2.5 SD or more below the average value of the young (30 years of age), healthy population [75]. The measurement is performed with DXA, which uses X-ray photons at two different energies to obtain a projection image in the coronal plane of (typically) the proximal femur or lumbar spine. Attenuation coefficients are corrected for the amount of soft tissue surrounding the bone thanks to the absorption information provided by photons of two different energy levels. After this, the pixels are converted to bone mineral content (BMC) values. Integrating over a specific area (e.g. femoral neck), a measurement of the subject areal BMD is obtained [121]. Large population studies provided reference aBMD distributions for different skeletal sites and different age, sex and ethnic groups [122]. The difference between the subject aBMD and that of a young, normal adult in units of SDs is called **T-score**. According to the WHO guidelines, a T-score < -2.5 equals osteoporosis, T-score between -2.5 and -1.0 equals osteopenia and a T-score > -1.0 is considered normal. The term **osteopenia** does not describe a disease but is used for epidemiological description [104].

1.2.4.2 Assessment of fracture risk

The rationale for a threshold T-score of -2.5 for the diagnosis of OP is that this level includes 95% of all individuals who will sustain a fragility fracture [75]. OP diagnosis and assessment of fracture risk, however, are not the same thing. Due to the fact that its operational definition is based on BMD, a DXA measurement remains the bottom line in osteoporosis diagnosis. The use of BMD alone, however, presents several limitations. As an example of these, fracture risk increases largely with age and independently of BMD, meaning that a T-score < -2.5 entails a much lower risk of fragility fracture for the elderly than for a younger population [123]. As seen in section 1.2.3, several concomitant factors have been recognized, contributing to the subject's risk of fracture independently of BMD.

FRAX

FRAX® is an algorithm for the calculation of the fracture risk which was introduced by the university of Sheffield in 2008. It incorporates most important risk factors (see section 1.2.3) plus, when available, the femoral neck T-score from DXA, to return 10-year probability of hip and major osteoporotic fractures (the latter including hip, spine, forearm or shoulder). If FRAX is probably the most used algorithm (more than 80 countries have included FRAX in their guidelines for the management of OP [124]), other tools for the prediction of fracture risk exist. Examples are the Garvan and the QFracture® calculators. The German Osteology Society

(DVO) has proposed an algorithm for the assessment of fracture risk specific for Germany in 2014 [125].

Markers of bone turnover

There is a modest but significant association between fracture risk and the concentration of biochemical indices of bone turnover in the blood serum. Within the variety of suggested markers, the International Osteoporosis Foundation (IOF) has recommended the utilization of one marker of bone resorption (serum C-terminal telopeptide of type I collagen, s-CTX) and one marker of bone formation (serum procollagen type I N propeptide, s-PINP) in clinical studies and in association with fracture risk [126]. Despite recent evidence and efforts, bone turnover markers can only provide an indirect measure of fracture risk and require further standardization [104].

1.2.4.3 Common guidelines

Fig. 6A shows a common guideline for the management of osteoporosis based on a measurement of the individual fracture risk. The procedure starts with an assessment of the subject fracture risk based on clinical risk factors (CRFs). The algorithm recommends to the physician whether to start or not treatment. Note that a measurement of the subject BMD with DXA is only prescribed when the subject's fracture probability falls within a lower and an upper risk thresholds [104] (Fig. 6B). Based on the approach of Fig. 6, treatment is recommended without further BMD information for individuals at high risk. At the same time, DXA is not recommended to those individuals at low risk. The rationale for the latter, low risk threshold for the prescription of DXA has to do, primarily, with limited availability of the device. With unrestricted and fully non-invasive access to BMD, a lower threshold would become unnecessary [104], and bone density (or strength) screening could be performed regardless of risk. Central DXA scanners cost between 80,000 and 160,000 € and it is estimated that only few European countries would have enough scanners installed to service the osteoporosis screening of the population [104].

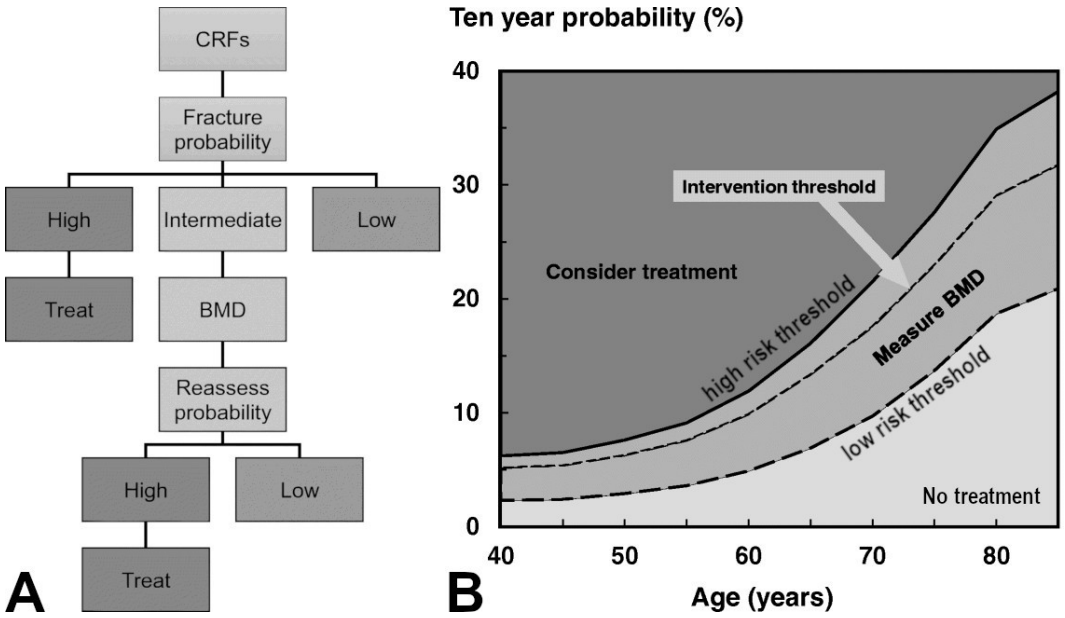

Fig. 6. (A) Management algorithm for the assessment of fracture risk and prescription of osteoporosis treatment. (B) Guideline for the assessment of BMD and treatment decision based on 10-year fracture probability and age. Modified from [127] with permission from Springer Science and Business Media.

1.3 Measuring bone strength

Insufficient DXA availability is one of the limitations of an approach for OP diagnosis that relies on the assessment of the bone mineral density. At the same time, it is estimated that an OP diagnosis based on BMD and with cutoff at T-score = –2.5 can address only half of the total burden caused by fragility fractures [128,129]. A DXA scan can identify fairly well old individuals at high risk but misses 80% of the fractures occurring in women between age 50 and 59 [128]. At the same time, we said that age alone predicts a large proportion of the risk in the elderly, even without BMD information [123]. This means that BMD fails at identifying subjects at high risk of fragility fracture in the portion of the population where this is more needed.

Fragility fractures are the outcome of moderate loads (generally a trauma from a fall) on bones with insufficient strength (Table 2). Therefore, methods that can directly assess bone strength in living subjects could provide better fracture risk predictions than DXA measurements. A variety of techniques has been proposed for this purpose, which can be used as alternatives or in addition to a BMD measurement. In the following paragraphs, I will describe the use of high resolution imaging, finite element modelling and quantitative ultrasound examinations of bone strength.

1.3.1 Finite element models for the prediction of bone strength

A **finite element (FE) model** is a numerical approximation of a problem of the physical world. The problem considered here is the mechanical response of a rigid body (a bone) subject to a set of external loads. If the problem is linear elastic, the physical law describing the relation between stresses and strains in the bulk material is Hooke's law for linear elasticity. For a complex shape such as bone, the forces acting on the surface of the body give rise to internal strain and stress fields that are heterogeneous and highly non-linear. Therefore, the solution of the problem depends on the physical laws governing the phenomenon at stake as well as on the geometry of its domain. What the FE does, is to decouple the geometric aspect from the solution of the equations of linear elasticity.

Principles

A theoretical description of the FE method (FEM) is beyond the scope of this thesis and can be found in [130]. In essence, the idea of FEM is to divide (discretize) the whole rigid body into multiple parts with small (but yet finite) size. These are the finite elements of the model. Within each element, the constitutive relations (generalized Hooke's law) are the equations connecting stresses and strains by means of the constitutive matrix of the material. The relation between internal stresses and the forces acting on the surface of the element is given by the conservation principle and gives the set of equilibrium equations. Finally, the relation between strain and displacements is provided by the set of partial differential equations known as kinematic equations. If the elements of the model are small enough, the FEM assumes displacement (the variable of interest) to vary in a way that can be described by a polynomial function of the displacements at the element nodes. This allows to reduce the problem to a system of ordinary differential equations (ODEs), relating external forces and displacements of each node of the element with its elastic properties. A larger system is assembled for the whole body putting together all the elements within the domain: this will have one equation for each node of the model. An approximate solution of the system (i.e. displacements and forces on each node of the model; stresses and deformations of each element) can be found with an iterative solver.

From quantitative computed tomography to finite element models of femur strength

First applications of the finite element method for problems of civil and aeronautical engineering appeared between the 1950s and 1960s. In orthopedics, FE made its first appearance in 1972 [131], but it was only in 1991 that the first calculation of femur strength using a subject specific FE model was published [132]. The basic steps for the development of a subject-specific FE model of femur strength from computed tomography (CT) data are described in Table 3 and illustrated in Fig. 7.

Subject-specific FE models can provide accurate predictions of the femur strength [133–136], as well as of the local strains and stresses in the bone [134,137,138]. The advantage for fracture prediction in comparison with DXA, however, remains small [139,140]. The technique is particularly interesting for the opportunistic screening in subjects undergoing pelvic or abdominal CT for reasons other than osteoporosis. Its main limitation remains the fact that it requires a CT scan of the central body, which is associated with a high dose of ionizing radiation (< 3.0 mSv for protocols dedicated to the hip; up to 10 mSv for abdominal QCT).

Table 3. CT2FE: workflow for the development of finite element models of femur strength.

1. CT acquisition	An abdominal or pelvic quantitative CT provides the input data for the procedure. In the volume of Fig. 7A, each voxel contains an X-ray attenuation coefficient in Hounsfield Units (HU). A phantom of materials of known densities is scanned together with the subject, allowing for the calibration of HUs to BMD values. Alternatively, it is possible to perform the calibration from the HU of other tissues of the body [141] or using a rule built-in the device.
2. FE discretization (meshing)	The outer geometry of the femur is segmented from the images. A mesh (generally tetrahedral) is generated from the 3D of the bone. Alternatively, the voxels of the image are directly converted to hexahedral elements (Fig. 7B).
3. Mapping of material properties	Material properties are assigned to each finite element based on the local density (Fig. 7C). Elastic and yield constants are derived from local density since the latter is the main determinant of the mechanical properties of bone tissue at the length scales from few hundreds of microns up to several millimeters (see section 1.1.1). The mapping is usually performed using available empirical laws [60,142].
4. Boundary conditions	External forces (or displacements) are applied to simulate the conditions of physiological tasks or extraordinary events such as a fall on the greater trochanter.
5. Numerical solution and post processing	The system of linear equations is solved using an iterative method. Material yield can be implemented with Newton's method for non-linearity. This divides the analysis in multiple (time or displacement) steps; at each iteration, the material properties of all element that reached the yield point are updated and the gerenal solution is recalculated. Typical model outputs are nodal displacement and forces as well as element damage and strain and stress tensors at each step.

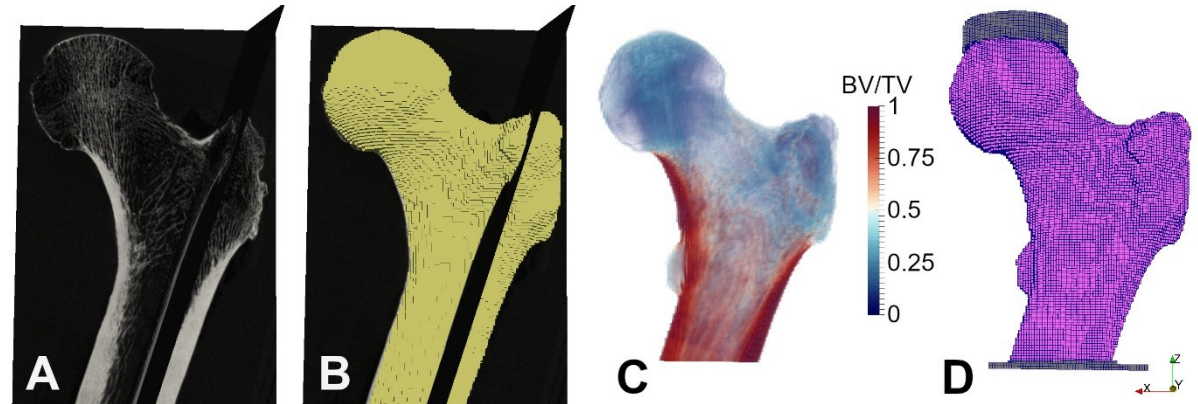

Fig. 7. From CT data to FE models of hip strength. (A) CT image. (B) Meshing. (C) Material mapping based on the local bone volume fraction. (D) Application of boundary conditions.

1.3.2 High resolution peripheral quantitative computed tomography

We have seen how bone loss is the result of structural deterioration of the bone architecture (section 1.2.1). Particularly, osteoporotic resorption leads to a rarefaction of trabeculae and to a thinning and accumulation of cavities in cortical bone. Since OP is caused by factors (e.g. hormonal changes or disuse) that affect the whole organism, it must be possible to observe its progression at different sites of the skeleton, including bones that are more relevant for fracture (e.g. hip and spine) but also the bones of the extremities. Moving the target of X-ray towards the extremity of the body reduces the effective radiation dose and allows an improvement of the image quality. This is the rationale of measurements of the peripheral skeleton with QCT.

Peripheral QCT (pQCT) was introduced shortly after the appearance, in a British hospital in 1971, of the first prototype of a CT scanner [143,144]. The technique reached quickly the current scanner layout: a light and relatively cheap device dedicated to the forearm and, more recently, to the tibia. pQCT is generally equipped with a small-angle fan beam X-ray source [145] which allows enough resolution to measure gross properties of the bone architecture such as the cross sectional area and thickness of single slices. Apart from their (macroscopic) architecture, pQCT can quantify the vBMD of the radius or tibia. The technique was used to describe the age- and sex-related differences in peripheral bone density and geometry [146,147], as well as the relationship between such quantities and the occurrence of fracture [148–150]. During almost four decades the technique reached only moderate distribution: around 1000 of these machines are currently in use, mainly in Europe [145].

In 2004, the Swiss producer Scanco launched high-resolution peripheral quantitative computed tomography (HR-pQCT): a new generation of pQCT developed from the company's expertise in microCT systems. For the work described in the next chapters, a second generation HR-pQCT (XtremeCT-II; Scanco Medical AG, Brüttisellen, Switzerland) was utilized. XtremeCT-II was introduced in 2014, is equipped with a cone-beam X-Ray source and a CCD detector and can scan in 3D the distal radius and tibia of humans with a FOV-length of 14.0 cm and a voxel size of 60.7 µm. Custom protocols allow the imaging of the human knee [151] and the reduction of the voxel size to 30.3 µm (although the latter is not feasible in vivo). Scanning time and radiation dose for the standard (in vivo) acquisition protocol are ~2 min and ~6 µSv, respectively, meaning that with a dose equivalent to that of DXA, a 3D description of trabecular and cortical microarchitecture at unprecedented resolution can be obtained. Apart from providing direct measurements of the bone microarchitecture, HR-pQCT images can become the input of microFE models for the direct assessment of bone strength [152]. Since its

introduction, several measures of the bone microstructure and strength from HR-pQCT have been associated with fracture risk, both retrospectively and prospectively [153]. Fig. 8 summarizes the results of the first (unpublished) systematic review of the association between HR-pQCT measurements and fragility fractures [153]. According to the most recent data, the HR-pQCT parameters that can better predict fracture are the total and trabecular vBMD, cortical thickness and trabecular spacing [153].

Despite the opportunity represented by HR-pQCT, its application has remained limited, until now, to research involving human subjects. The cost of the device (much higher than that of DXA) is not reimbursed by national health agencies and represents the major limitation to the widespread of HR-pQCT and to its use in the clinical routine.

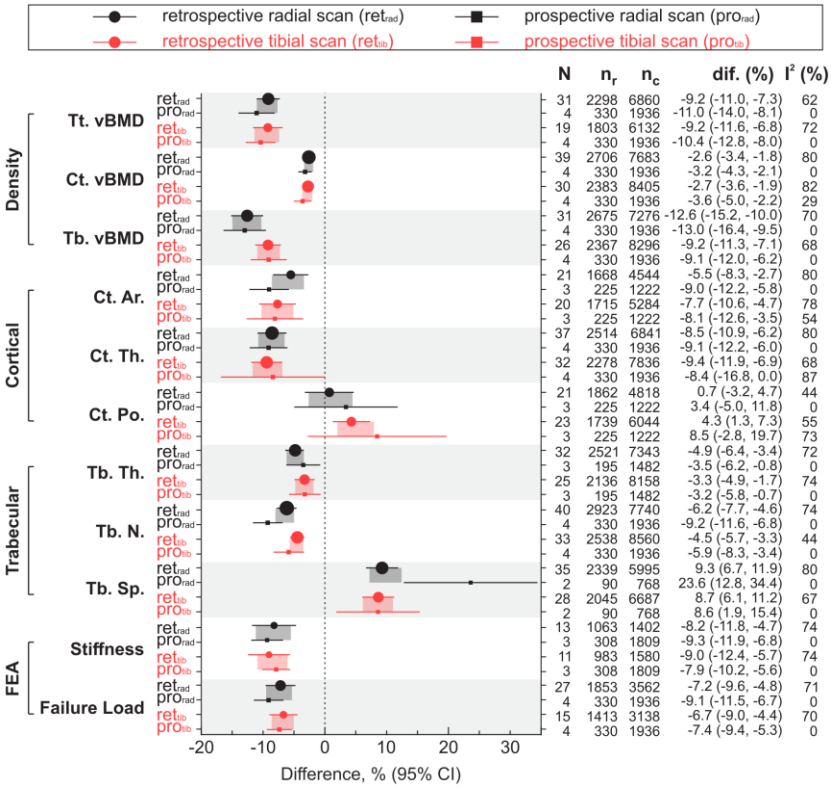

Fig. 8. Fracture-related differences in radial and tibial HR-pQCT parameters from retrospective and prospective studies of fragility fractures (unpublished data).
Results of the first systematic review on the topic suggest that all HR-pQCT parameters describing bone density, microstructure and strength are significantly altered in individuals with fracture history. Smaller and larger differences were observed for cortical and trabecular bone vBMD of the radius, respectively.
Courtesy of Dr. Nicholas Mikolajewicz [153].

1.3.3 Quantitative ultrasound for the assessment of bone strength

Quantitative ultrasound (QUS) refers to the use of ultrasound waves for the measurement of one or more physical property of a sample or tissue (bone in our case). The first application of QUS in the field of osteoporosis diagnosis dates back to 1984, when Langton et al. established that the frequency dependent attenuation of US waves travelling through the calcaneus (heel bone) could discriminate women with osteoporosis [154].

Compared to X-ray photons, ultrasound waves interact with the bone architecture in a more complex manner. X-rays travel relatively undisturbed through the human body, so the field of densitometry (i.e. OP diagnosis) can only rely on a measurement of the absorption of X-ray photons by atoms (principally Ca) of bone. Biomedical ultrasound uses mechanical waves with characteristic wavelengths (few tens of microns up to several millimeters) that are comparable, in size, to the features of the bone architecture. In principle, this means that each interface of the bone structure reflects and refracts any incident US wave. The complex interaction of US with the medium, therefore, contains information on the structure of the latter. Compared with X-rays, QUS is non-invasive and safe since it does not use ionizing radiation. In addition, modern QUS devices are relatively cheap and often portable. During more than 3 decades, a

variety of QUS techniques have emerged, that employ different physical principles for the assessment of various structural and compositional properties of bone (Fig. 9). In the next paragraphs, I will briefly introduce the most relevant QUS approaches for bone strength prediction, with a focus on most recent applications that target cortical bone in particular. A review of QUS for osteoporosis diagnosis can be found in [155,156].

1.3.3.1 The early years: ultrasound trough transmission

Transverse (or trough) transmission refers to the use of two transducers (a transmitter and a receiver) to measure US waves travelling transversally through the skeletal site under examination. Such waves can be analyzed in terms of their **speed of sound (SOS)** or of the integral of their frequency dependent attenuation, also called **broadband ultrasound attenuation (BUA)**. The transverse transmission method proposed by Langton et al. in 1984 for a measurement of BUA at the calcaneus (Fig. 9A) represents the most utilized QUS solution for the management of osteoporosis to date [154]. Similarly to DXA, this approach provides an estimate of the total amount of bone within the propagation path and cannot distinguish between cortical and trabecular bone nor provide measures of architectural features of the two. In recent years, transverse transmission has been applied to other sites such as the forearm (Fig. 9B) and used in combination with Biot theory to model trabecular density and cortical thickness of the radius [157]. The correlation of such measurements with reference quantities from radiographs of living subjects was moderate [158].

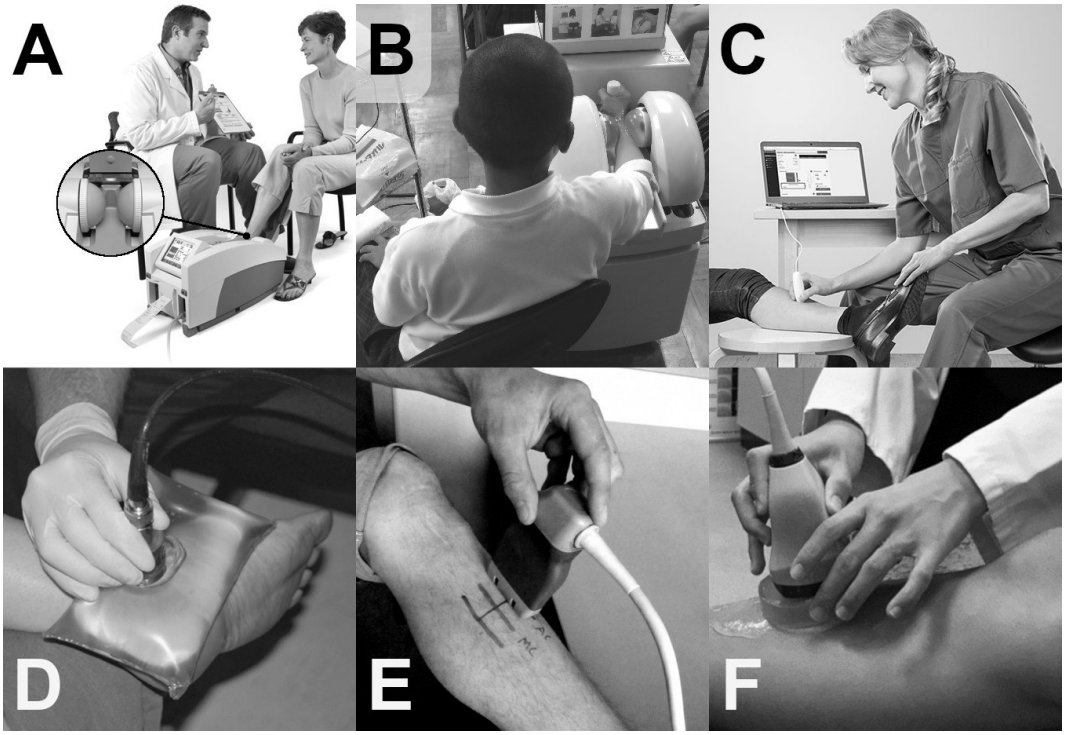

Fig. 9. QUS devices for the measurement of bone. (A) General Electric Lunar (Madison, WI) Achilles®. (B) Child receiving a through transmission QUS measurement at the forearm in a Japanese school with an Oyo (Kyoto, Japan) LD-100® system. (C) Bone Index (Kuopio, Finland) Bindex®. (D) Trabecular backscatter measurement at the calcaneus with a custom system. Reprinted from [159] with permission from ASA. (E) 1-MHz bidirectional axial transmission probe from Azalée (Paris, France). (F) Linear 4D array (BK Medical®, Peabody, MA) used in combination with a medical ultrasound scanner (Ultrasonix SonixTOUCH) for a cortical backscatter measurement in the tibia at Charité – Universitätsmedizin Berlin.

1.3.3.2 Pulse-echo approaches

Fig. 9C and D show two examples of the application of single element US transducers in pulse-echo mode. In this setup, the same transducer is used to emit and record an ultrasound wave after this is reflected back by the bone structure. In particular, the device of Fig. 9C detects waves reflected by the front (periosteal) and back (endosteal) surfaces of the tibia diaphysis, allowing an estimate of the thickness of the cortical bone wall [160]. It is available on the market with a portable and cheap layout and, when combined with subject characteristics, can provide OP diagnosis in a cost effective manner [161,162]. Its main limitation is the fact that it requires an assumption regarding the value of the transversal SOS in cortical bone, which is why its measurements are treated as an index of the true bone thickness. Fig. 9D shows another type of pulse-echo US measurement at the calcaneus. At this site, bone is mainly trabecular, so a frequency analysis of the backscattered waves is performed to obtain information on the average trabecular thickness [163].

1.3.3.3 Ultrasound axial transmission

Axial transmission (AT) refers to ultrasound waves that are transmitted to the diaphysis of a long bone such as the radius or tibia and detected after they have propagated axially in the outer cortical shell of the bone (Fig. 9E). AT is typically used for measurements of cortical bone. The device of Fig. 9E (dedicated for AT measurements) is composed of a series of transducers that are aligned with the tibia axis. If the bone thickness is lower than the ultrasound wavelength λ, the velocity of the fastest wave (or **first arriving signal, vFAS**) corresponds to the longitudinal SOS in bone [164]. SOS depends mainly on the mass density and elasticity of bone (see Eq. (6) in section 2.2.2.1) and was associated with fracture risk independent of BMD and age [165].

After the FAS, a variety of signals travelling at lower speed in the cortical bone are recorded by AT. These are the so called **guided waves (GW)** and correspond to the vibrational modes of the cortical bone. In Fig. 9E, a prototype of bidirectional axial transmission (BDAT) optimized for the separation of distinct GWs in the human tibia measures signals travelling in opposite directions of the diaphysis. These are emitted by the two transducers positioned on each side of the probe and recorded by a central array of US receivers. After the measurement, a response matrix is assembled from the temporal Fourier transforms of the signals recorded by each receiver element. Singular value decomposition (SVD) of the response matrix allows the reconstruction of dispersion curves in the frequency-wave number domain, from which distinct GW modes can be distinguished [166]. If one assumes the slab of cortical bone to behave like a homogeneous free plate, the solution of the guided modes can be obtained analytically from the Rayleigh-Lamb equation. In particular, the energy contained by each vibrational mode will be determined by the thickness and stiffness matrix of the plate, where the latter can be modelled in terms of cortical bone porosity. One can, therefore, solve the ideal problem analytically for a given set of plate porosity and thickness values. Each measurement on a real bone is then compared with the database of analytical solutions (inverse problem), and an estimate of the cortical bone thickness and porosity is obtained [167]. Cortical thickness and porosity from GW analysis have been validated in recent years on bone samples *ex vivo* [167,168] as well as *in vivo* on living humans [169]. Both thickness and porosity form GW analysis have proved ability in discriminating fragility fractures in postmenopausal women [170].

1.3.3.4 Assessment of the structure of cortical bone with clinical ultrasound

During three decades of life, the field of QUS for the management of osteoporosis has evolved from dedicated systems like those of Fig. 9A and B that provide attenuation measurements similar to the aBMD of DXA, towards more portable solutions (Fig. 9C-F) that can target specific features of the bone architecture. This shift corresponded to the development of a deeper understanding of the pathophysiology of osteoporosis and of the changes in the bone structure that this entails. A new paradigm towards bone investigations with ultrasound makes use of conventional US systems that are widely available in clinical settings. Thanks to hardware improvements (e.g. increased sensitivity of the probes) and the development of new approaches for signal processing, clinical ultrasound devices might represent an unexpected opportunity for the non-invasive assessment of bone strength.

Ultrasound imaging of cortical bone

For ultrasound imaging, bone has traditionally represented an obstacle rather than an opportunity. This because when ultrasound waves encounter a strong impedance mismatch such as at the bone-soft tissue interface, a large part of their energy is reflected back. In addition, signal interpretation is complicated by the refraction of waves occurring due to the SOS mismatch between the two media. Finally, the amount of energy that can travel in bone is limited further by the strong ultrasound attenuation of hard tissues. In 2018, Renaud et al. provided a proof of concept for the reconstruction of images of the cortical bone of the radius and tibia in living humans from ultrasound signals acquired with a clinical scanner (Fig. 10A) [171]. The paper describes a method for image reconstruction based on the modelling of the wave refraction within layers of cortical bone tissue with different anisotropic elastic properties and SOS. The cortical thickness measured on ultrasound images by Renaud et al. was in perfect agreement with reference values obtained with HR-pQCT. In the tibia, the technique was applied at the anterior medial portion of the diaphysis and could easily scan the entire length of the bone.

Cortical bone backscatter (CortBS)

The quantitative analysis of the ultrasound backscatter has been applied extensively for the ultrasound characterization of soft tissue. Successful examples of it are the detection of fibrotic and metastatic tissue regions in the liver or in lymph nodes [172,173].

When ultrasound waves encounter an obstacle (sphere or cylinder) along their path, with a diameter smaller than the wavelength, the amplitude of the backscatter (i.e. the energy returning back) increases monotonically with the size of the obstacle. More precisely, this phenomenon occurs when the product $ka < 1$, where a is the radius of the scatterer and $k = 2\pi/\lambda$ is the wave number. Such regime is called Mie scattering. A method that takes advantage of Mie scattering for the analysis of the size of pores in cortical bone has been recently proposed (Fig. 9F and Fig. 10B) [174]. The pores in cortical bone are treated as water filled cylinders (scatterers) included in a solid matrix of mineralized tissue. For a cylinder with a radius of 35 µm (as a typical Haversian canal) and radial SOS in bone of 3240 m/s [171] the condition $ka < 1$ gives a frequency limit of 15 MHz. Clinical ultrasound transducers work with frequencies in the 1-20 MHz range and are therefore perfectly suitable for CortBS. If confirmed for living subjects, CortBS might provide estimates of the size distribution of pores in cortical bone [175].

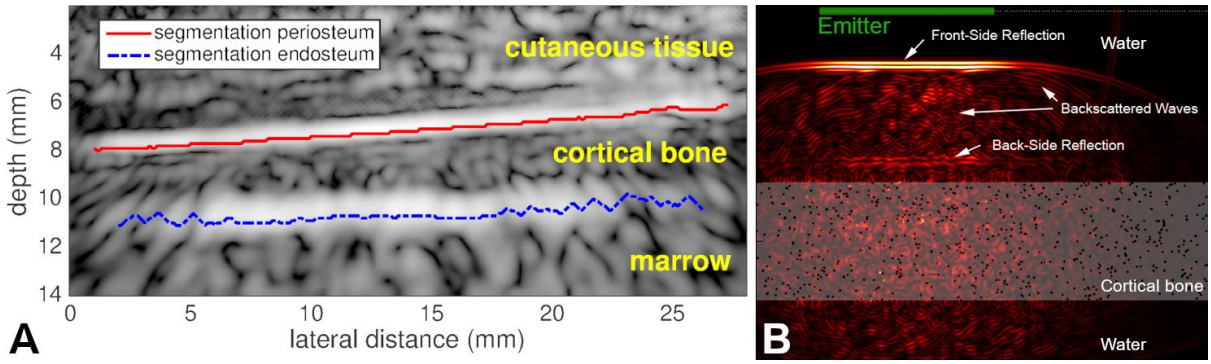

Fig. 10. QUS measurements of cortical bone with clinical ultrasound technology. (A) First *in vivo* images of the cortical shell in the human tibia acquired with a clinical ultrasound scanner [171]. Courtesy of Dr. Guillaume Renaud. (B) Finite difference time domain 2D simulation of ultrasound backscatter from an idealized slab of cortical bone. The spectral content of ultrasound waves backscattered by the porous microstructure conveys information on the size and density of the pores [175].

1.4 State of the art

In section 1.1.4, I introduced the concept of bone strength, and described the relationship between fracture resistance and microstructure in bone taken as a material. This relationship has been the subject of numerous *ex vivo* investigations (see [176–178] for reviews). The paragraphs on osteoporosis (section 1.2) have focused on the limitations of the current strategy for the management of fracture risk which is based on the assessment of the BMD by DXA. Finally, in the last part of the introduction (section 1.3), I presented recent technological advancements that allow the assessment of the bone architecture (and thus of its strength) in subjects and non-invasively. In particular, I described two methods (HR-pQCT and QUS), that can provide measurements of the microstructure of cortical bone *in vivo* at the tibia.

The possibility to retrieve such microstructural information *in vivo* poses the question of which properties of the tibial bone architecture can be used as proxies for the strength of bones of the central skeleton (e.g. hip and spine), that represent a more urgent target for fracture risk prediction. The first attempt to use the structure of the tibia as a surrogate for skeletal health was made in 1999 [179]. In the following years, several works with pQCT demonstrated the association of tibial vBMD or geometric properties (e.g. area, moment of inertia or thickness of the tibia cross-section) with fracture incidence at central sites [148–150].

The introduction of HR-pQCT opened the path to the assessment of a broader range of microstructural parameters of trabecular and cortical bone. Since 2004, a growing number of studies has proven the ability of HR-pQCT to discriminate several types of fractures. The results (yet unpublished) of the first systematic review on HR-pQCT show that individuals with both retrospective and prospective fractures have reduced cortical thickness and a less dense, rarefied trabecular architecture in the distal tibia (Fig. 8).

Despite the promising findings, cortical bone has been traditionally neglected in the study of bone fragility [180,181], and its architecture described only by cortical thickness and porosity. Almost all works that investigated the direct association between the tibia and proximal femur strength, have done it assessing only the tibial vBMD [182–185]. In Kroker et al., the architecture of the distal tibia was indirectly included through microFE-derived predictions of bone strength [185]. A single study investigated the association between the cortical bone microstructure of the tibia and proximal femur strength [186]. The unique structural parameter considered was cortical porosity, and the assessment of proximal femur limited to standing loading conditions [186].

1.5 Aim of the study

In this thesis, femur strength is investigated *ex vivo* in direct association with the structure of cortical bone of the human tibia. Structural "fingerprints" of bone resorption in the tibia are developed based on the understanding of the effects of aging and osteoporosis on the cortical bone architecture. The aim is to identify structural biomarkers of reduced femur strength in an anatomical site that can be assessed non-invasively *in vivo*.

Specific objectives are:

- To determine which parameters of the cortical bone microstructure in the human tibia can most effectively indicate an impairment of femur strength.
- To propose a measurement of such parameters with available HR-pQCT technology.

1.6 Thesis outline

The thesis is divided in the following chapters:

Chapter 1 (Introduction)	The background and scope of the research are introduced.
Chapter 2 (Methods)	Presents the materials and methods utilized for the research.
Chapter 3 (STUDY 1)	The microstructure of cortical bone in the tibia is analyzed *ex vivo* in association with a reduction of the stiffness and strength of the proximal femur of the same subjects. Cortical bone thickness and the prevalence of large pores in cortical bone of the tibia are proposed as structural biomarkers of reduced femur strength.
Chapter 4 (STUDY 2)	Extends the findings of Chapter 3 by looking at the association between the microstructure of cortical bone of the tibia and the deterioration of the femoral neck architecture.
Chapter 5 (STUDY 3)	Presents an improved measurement of cortical bone porosity from HR-pQCT images.
Chapter 6	Proposes a method for the measurement of the prevalence of large pores in cortical bone from HR-pQCT images.
Chapter 7 (Conclusions)	Summarizes the findings and offers a general conclusion of the research.

Chapters 3 to 5 are manuscripts published (chapter 3 and 5) or submitted for publishing (chapter 4) to peer-reviewed journals. Details of the publication notification and of my personal contribution to each specific study can be found at the beginning of the corresponding chapter.

Chapter 2: Methods

2.1 Human samples

The research described in this thesis was made possible by twenty donors who agreed to the scientific use of their bodies after death. Information on the age, sex and medical condition of these subjects is collected in Table 4. Samples were collected at the University Medical Center Schleswig-Holstein. Available, were the left and right femora from each subject, together with the left tibiae from 19 of them. All the specimens were frozen at -20 °C right after dissection and kept frozen between the experiments.

Table 4. Details of the 20 human donors investigated.

ID	Sex	Age	Condition / Medication	T-Score	ID	Sex	Age	Condition / Medication	T-Score
#1	m	88	Pancreatic cancer	−3.00	#11	m	70		−1.27
#2	m	82	Amputation (tibiae)	−4.24	#12	w	72	Bladder cancer; Oral cancer	−1.87
#3	w	80	Lung cancer (Pancoast)	−3.63	#13	w	85		−2.32
#4	w	94	(Reported) Osteoporosis	−3.67	#14	w	84		−2.52
#5	w	83		−2.80	#15	w	82		−3.27
#6	m	90		−3.02	#16	w	69	Non-Hodgkins lymphoma	−2.44
#7	w	88		−3.25	#17	m	71		−2.33
#8	m	80		−3.19	#18	w	94		−3.79
#9	w	82		−2.81	#19	w	92	Colorectal cancer	−3.59
#10	w	92		−3.55	#20	m	94		−3.87

For the femora, I developed a protocol for sample preparation (Fig. 11B) that allowed combined HR-pQCT, mechanical testing and scanning acoustic microscopy (SAM) analyses. After measuring the total length of the femur, the proximal end was cut 80 mm below the midpoint of the lesser trochanter and perpendicular to the diaphysis axis. Approx. 30 mm of the diaphysis were embedded in polyurethane (SG 140/PUR 12, ebalta, Arundel, UK), hosting five radiopaque cement markers for orientation of the HR-pQCT images (Fig. 11C-E).

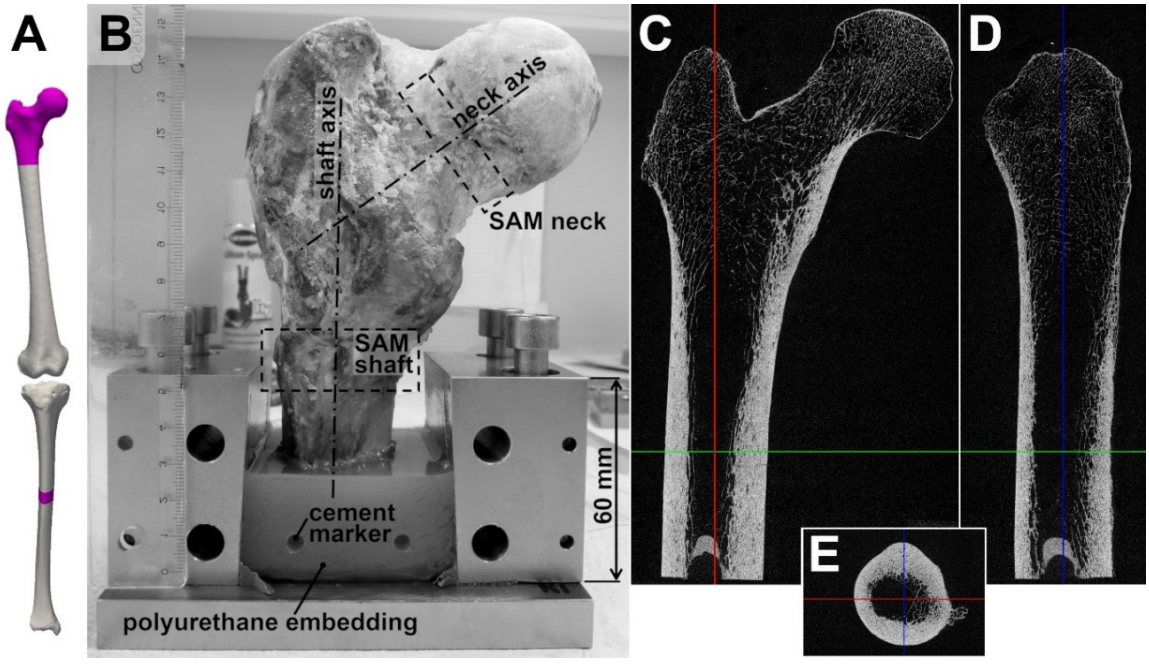

Fig. 11. (A) Overview of the bone regions analyzed from femur and tibia bones. (B) Proximal femur sample during preparation for combined DXA, HR-pQCT, mechanical testing and SAM. (C-E) Cross sections through the 30.3 µm HR-pQCT reconstruction of the femur.

The left tibiae were prepared for measurements with QUS methods (BDAT and CortBS, both applicable *in vivo*) which are not included in this thesis. After BDAT and CortBS, cross sections of the tibiae were extracted at the midhaft (Fig. 11A) for site-matched microCT and SAM. More details about the preparation of tibia samples can be found in chapter 3 and 4.

2.2 Imaging of the bone structure

2.2.1 HR-pQCT

An XtremeCT II scanner was utilized to image the proximal femora of the 20 human donors of Table 4 at 30.3 µm voxel size. Fig. 11C-E show sections through the HR-pQCT reconstruction. The bones were degassed inside a desiccator before scanning to remove air bubbles. A custom plastic chamber was used to hold the femora with the diaphysis axis parallel to the scanner z-axis during acquisition. The chamber was sealed and allowed to maintain the samples in 1% PBS with addition of penicillin (50 U/ml) and streptomycin (50 µg/ml) during the scan. Table 5 collects scanning and reconstruction settings.

Table 5. HR-pQCT image acquisition and reconstruction settings.

X-ray tube energy [kVp]	68	Rotation angle range	180	Image matrix	4608 × 4608
X-ray tube current [µA]	1470	Scan time [h]	~ 8	Voxel size [µm]	30.3
Integration time [ms]	200	FOV length [mm]	146 – 182	File format	.ISQ
Number of projections	3000	Number of stacks	14 – 18	File size [GB]	~200

2.2.1.1 Image processing

The MATLAB software implementing the procedures described in the next sections can be downloaded from: https://github.com/gianthk/simpleCT/.

The first step required to work with a file of ~200 GB is to create a downsampled version of it. The volume at lower resolution is explored to define the limits of specific VOIs for subsequent analyses (e.g. femoral neck or shaft as in Fig. 11B). Downsampled images with factor 10 served also as inputs for the FE analysis of femur strength (see section 2.3.2). Operations on ISQ files are implemented in the MATLAB class ISQdata of the simpleCT toolbox.

BMD calibration

Hounsfield Units were converted to bone mineral density (BMD) using the calibration rule:

$$BMD = HU \times \left(\frac{density_{slope}}{\mu_{scaling}} \right) + density_{offset} \quad (1)$$

The parameters $density_{slope}$, $density_{offset}$ and $\mu_{scaling}$ are built-in the scanner and controlled daily by scanning a calibration phantom of materials with known densities.

Segmentation

Masks of the cortical and trabecular bone compartments were calculated with an algorithm proposed in 2010 by Burghardt et al. [187]. Originally, this was developed for 82 µm voxel size HR-pQCT images of the tibia. The application to datasets with 30.3 µm voxel size (see chapters 4 and 5) required the tuning of the algorithm settings. For the specific case of femoral neck sections, the procedure was modified as described in Fig. 12. Table 6 presents several methods for the segmentation of bone tissue voxels from the background of the image. Different bone tissue thresholds were use for this work, depending on specific performance and recommendations from the literature.

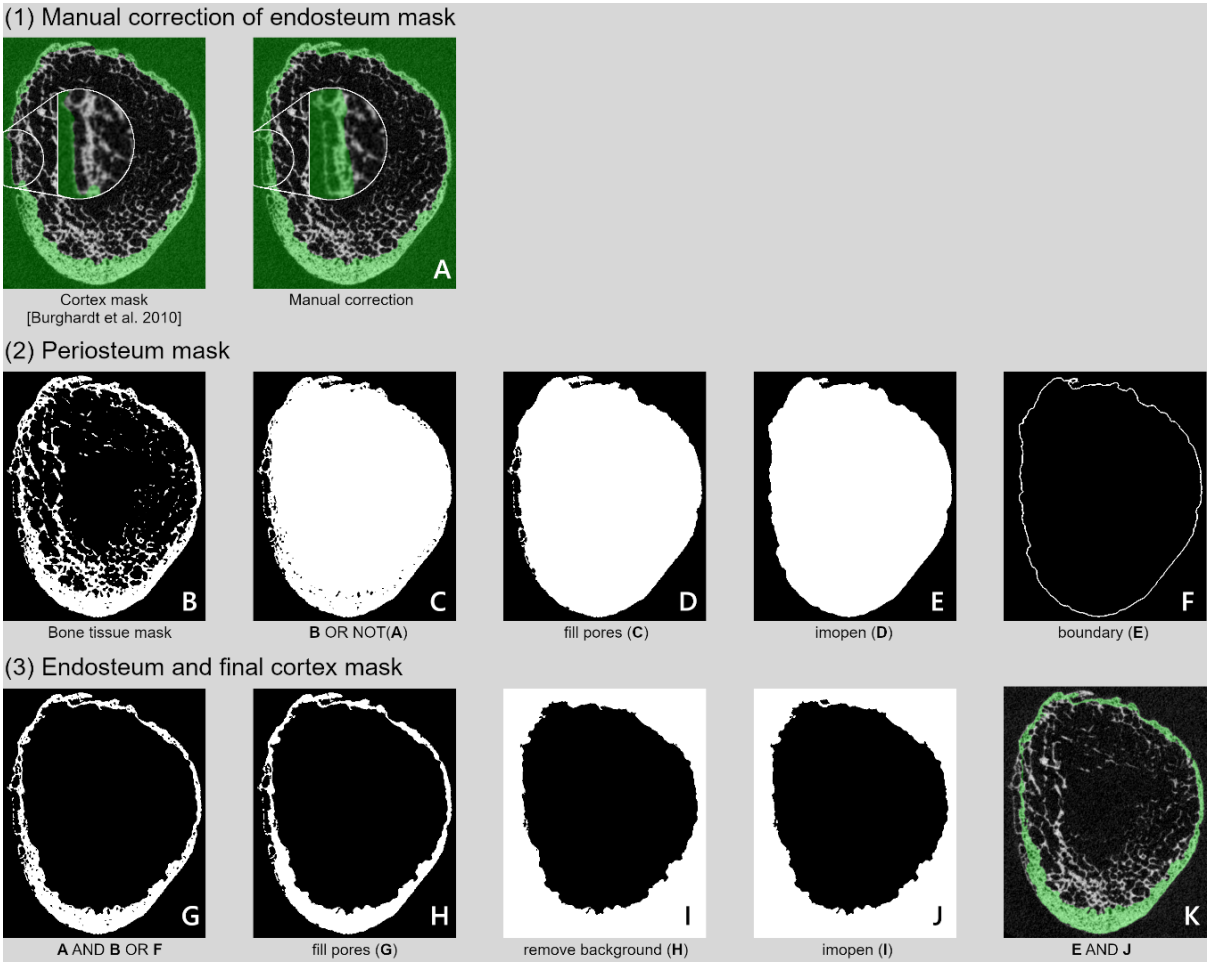

Fig. 12. Semi-automatic segmentation of femoral neck cortical bone from HR-pQCT images.

Table 6. Automatic thresholding methods for CT images.[a]

Name	Description	Type
Otsu	Minimizes the sum of the variances of foreground and background voxels. [188]	Global; adaptive
Isodata	A first guess threshold is obtained as half the maximum of the image dynamic range. Following, a new threshold is calculated as the midpoint between background and foreground voxels sample means. The image is segmented again with the updated value. Isodata repeats the last two steps until the threshold does not change anymore. [189]	Global; adaptive
40% of max vBMD	This is the input for the procedure of Burghardt et al. for the automatic detection of the cortical bone compartment. [187]	Global; adaptive
Wellner	The threshold is varied across the image based on the local mean (or median) in the proximity of each pixel. [190]	Local; adaptive

[a] The function threshbone of simpleCT contains MATLAB implementations of these algorithms.

Histomorphometry

Table 7 contains a list of the histomorphometric parameters for cortical and trabecular bone characterization that are used in the next chapters. For each parameter, a graphical description of its meaning and calculation is provided.

Table 7. List of bone histomorphometric parameters.[b] Nomenclature as per [191].

Acronym	Name	Unit	Description
MoI	Moment of Inertia[a]	[kg m²]	$MoI = \sum_{i=1}^{n} m_i r_i^2$ [a] The moment of inertia is calculated on binary masks. All pixels have unit mass.
I_{xx}, I_{yy}	Second moments of area	[m⁴]	$I_{xx} = \sum_{i=1}^{n} y_i^2 \Delta x \, \Delta y$; $I_{yy} = \sum_{i=1}^{n} x_i^2 \Delta x \, \Delta y$
Tt.Ar	Total Area	[mm²]	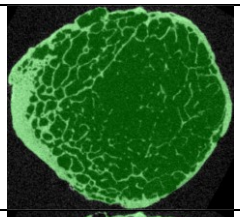
T.Ar	Tissue Area	[mm²]	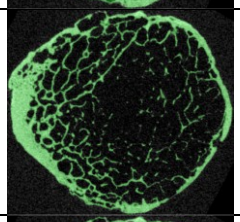
Ct.Ar	Cortical bone area	[mm²]	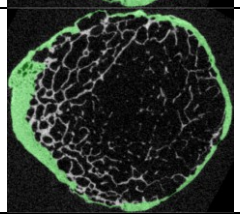
Ct.Wba	Portion of cortical tissue area	[%]	$Ct.Wba = Ct.Ar/Tt.Ar$
Ct.Th	Cortical thickness	[mm]	Most frequent minimum distance between periosteum (blue) and endosteum (red) surfaces 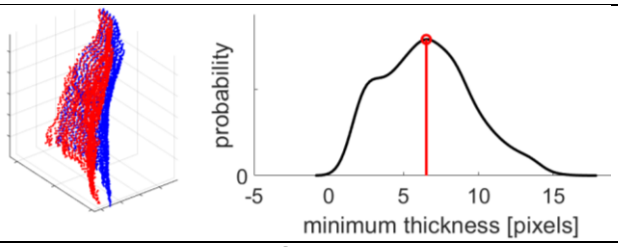
Ct.Po	Cortical porosity	[%]	A) $Ct.Po = 100 \times \left(1 - \frac{Ct.V \wedge T.V}{Ct.V}\right)$ B) Modified from A). Voids laterally connected to the background are first removed. Second, a hysteresis region grow loop (along the z-axis) searches for excluded voxels vertically connected to high fidelity pores and adds them back to the pore mask. [187] C) Derived from vBMD as described in chapter 5. [192]
Tb.Th	Trabecular thickness	[mm]	Average thickness; based on the method from Hildebrand and Rüegsegger. [193]
Tb.Sp	Trabecular separation	[mm]	Same method as Tb.Th but applied to the background of the image.
Tb.N	Trabecular number	[mm^{-1}]	$Tb.N = 1/(Tb.Th + Tb.Sp)$
$Tb.\frac{BV}{TV}$	Trabecular bone volume fraction	[%]	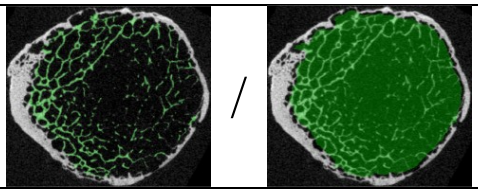

[b] Text in blue contains links to MATLAB implementations of the algorithms on the simpleCT toolbox.

2.2.2 Scanning Acoustic Microscopy

2.2.2.1 Acoustic theory

Wave equation and speed of sound

The equation of motion for a unit volume of solid free from external forces is:

$$\rho \frac{\partial^2 u_i}{\partial t^2} = \frac{\partial \sigma_{ij}}{\partial x_j} \tag{2}$$

Where u_i is the particle displacement along the direction i, ρ is the density of the bulk material and σ the stress acting on it [194].

Let's now consider the example of a shear wave. Under the assumption of linear elasticity we have, from Hooke's law:

$$\sigma_s = \mu \frac{\partial u_i}{\partial x_j} \tag{3}$$

Relating the shear stress σ_s and the deformation $\partial u_i / \partial x_j$ by means of the shear modulus μ.

This allows to rewrite (2) as:

$$\rho \frac{\partial^2 u_i}{\partial t^2} = \mu \frac{\partial^2 u_i}{\partial x_j^2} \tag{4}$$

Which is the equation of a shear wave propagating along j with solution:

$$u_i = U \bar{p}_i e^{-i(\omega t \pm \bar{k}_j x_j)} \tag{5}$$

Where $\bar{k}_j = \frac{2\pi}{\lambda} \bar{n}_j$ the wave vector, $\bar{p}_i$ the unit polarization vector, and $\bar{n}_j$ defines the direction perpendicular to the wave front. Substituting this in (4) and considering that the phase velocity is $v = \omega / k$ we obtain the velocity of a shear wave:

$$v_s = \sqrt{\frac{c_{44}}{\rho}} \tag{6}$$

This relates the longitudinal velocity of a shear wave v_s to ρ and to the component c_{44} of the material's stiffness tensor (which is the shear modulus μ). The velocity of a compressive wave in an analogous way will be:

$$v_{ii} = \sqrt{\frac{c_{ii}}{\rho}} \qquad (i = 1, 2, 3) \tag{7}$$

Acoustic Impedance

The characteristic acoustic impedance of an anisotropic material relates traction (tensile stresses σ_i) with particle displacement velocity v_j:

$$Z_{ij} = -\frac{\sigma_i}{\frac{\partial u_j}{\partial t}} \tag{8}$$

Acoustic impedance is the product of mass density of the medium and the speed of sound for a given wave propagating in it:

$$Z = \rho v \tag{9}$$

Its unit is the $Mrayl = 1 \times 10^6 kg\ m^{-2}\ s^{-1}$.

Finally, if wave propagation and particle displacement directions are the same, it can be demonstrated that the impedance Z_{ii} in the direction i is proportional to the mass density and to the stiffness coefficient c_{ii} of the material:

$$Z_{ii} = \sqrt{c_{ii}\rho} \tag{10}$$

Relationship with reflection coefficient

When a sound wave hits the interface between two materials with different acoustic impedance Z_1 and Z_2, a portion of the incident energy is reflected back. The stress amplitude of the reflected wave with respect to the incident energy is given by the reflection coefficient:

$$R = \frac{Z_2 - Z_1}{Z_2 + Z_1} \tag{11}$$

Ultrasound attenuation

Attenuation of ultrasound waves is caused by the distinct phenomena of scattering and absorption. Scattering occurs when the wave encounters a series of obstacles (the scatterers) with a mismatch of the acoustic impedance (e.g. pores in cortical bone). Scatterers deflect and reflect the wave back and forth, modifying its trajectory, amplitude and frequency. Absorption is the result of processes such as thermal conductance and viscoelasticity that, in general, convert part of the acoustic energy in heat. A common approach to describe acoustic attenuation is that of an exponential decay in amplitude of the acoustic pressure and intensity fields (p and I, respectively) with distance from the ultrasound source (x):

$$p = p_0 \mathrm{e}^{-\alpha x} \qquad I = I_0 \mathrm{e}^{-2\alpha x} \tag{12}$$

In which α is a frequency-dependent attenuation coefficient and $p_0 = p_{z=0}$ and $I_0 = I_{z=0}$.

2.2.2.2 Scanning Acoustic Microscopy principles

A scanning version of the acoustic microscope was first described in 1974 by Lemons and Quate from the Microwave Laboratory of Stanford University [195]. An image of the acoustic properties of a tissue can reveal information which is complementary to that provided by light techniques [196]. This has made Scanning Acoustic Microscopy (SAM) particularly interesting for the imaging of biological structures

In modern setups (Fig. 13A) [194], SAM is composed of a focused (generally spherical) ultrasound transducer mounted on a high-precision motion stage that can navigate the three dimensions of the available scanning field. A pulser/receiver fires the transducer at a fixed time step during motion. In a pulse-echo setup, as the one used for the current work, the same pulser/receiver is also responsible for directing the recorded signals to the AD-card, where these are digitized. A computer program controls each component of the hardware, synchronizing stage position and signal acquisition by means of signals (triggers) that are handled by the AD-card. Table 8 summarizes the technical specifications of the custom-built SAM that was utilized for the current research.

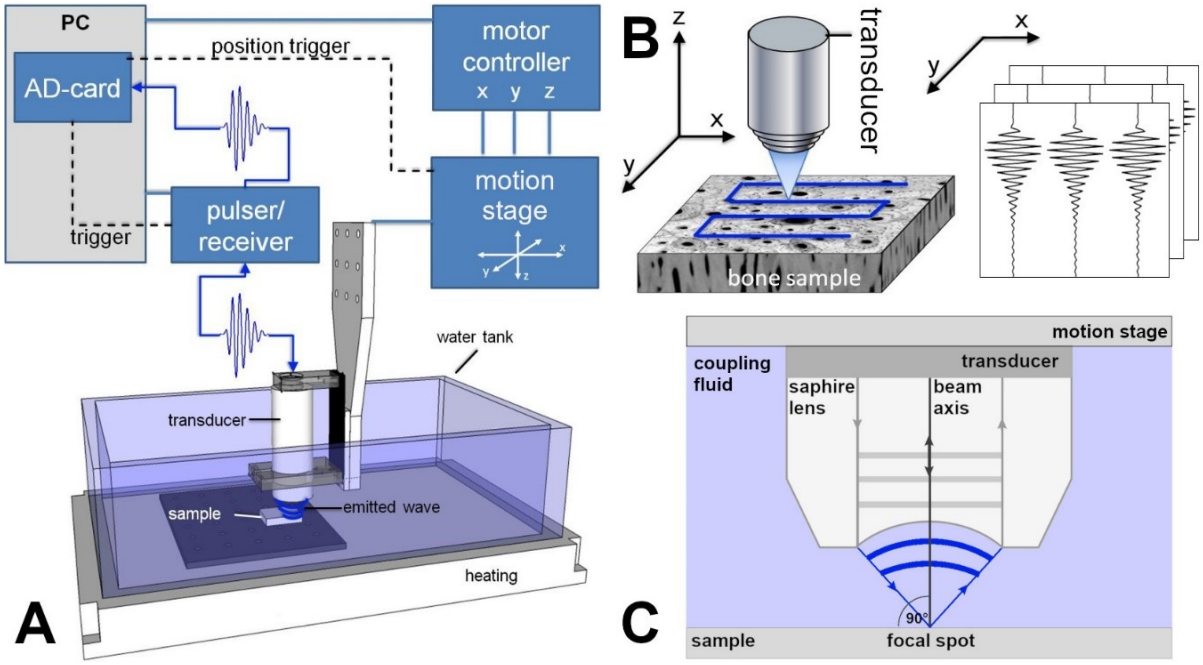

Fig. 13. (A) Scanning-acoustic-microscopy (SAM) setup. (B) Schematics of SAM raster scanning. (C) SAM transducer in confocal configuration: the spherically focused beam hits the sample surface at normal incidence. Adapted from [197,198] with permission from Dr. Rohrbach and Dr. Schrof.

Table 8. SAM specifications.

AD-card			
Model	CompuScope 12400	Sample rate [MS/s]	400
Manufacturer	GaGe, Lockport, IL	Resolution	12-bit
Pulser/receiver			
Model		5900PR	
Manufacturer		Panametrics-NDT, Waltham, MA	
Maximum bandwidth (-3 dB)		1 kHz – 200 MHz	
Transducer			
Model	KSI 100/60°	Nominal frequency [MHz]	100
Manufacturer	KSI, Herborn, Germany	Bandwidth (-6 dB) [MHz]	84.4 – 100.7 [199]
Type	Spherically focused	Depth of focus [µm]	139 [199]
Beam diameter at focus [µm]	19.8 [199]		
Software			
		SAM 200 Ex (C++), Q-BAM, Halle Germany	

2.2.2.3 Sample preparation for SAM

The protocol for the preparation of cross sections from femur and tibia bones for SAM imaging was adapted from previously published works [200]. A brief description of the procedure is provided in Table 9.

Table 9. Quick protocol for sample preparation for SAM.

1. Extract a 21-mm-thick section (see position of femur shaft section in Fig. 11A) performing parallel cuts with a diamond-coated band saw. Thaw and wash (remove bone marrow) the section in 1% PBS.
2. Embed 2 to 4 mm of one extremity in fast curing acrylic resin (VariKleer®, Buehler Ltd., Illinois) together with a 20-mm-high plastic ring form (ø 50 mm, Buehler Ltd.). The ring will provide mechanical support during grinding of the sample.
3. Grind and polish (constant speed: 50 rpm) one surface on a planar grinder (Phoenix 4000, Buehler Ltd.). Grind the surface until perfectly flat. Use decreasing grain sizes (ISO/FEPA grit: P80, P600, P1200, P2500 and P4000, Buehler Ltd.). Wash the sample under running water after each step.
4. Submerge the sample in 1% PBS and vacuum degas inside a desiccator for at least 30 min to remove air bubbles. Final clean of the surface with a soft paintbrush before scanning.

2.2.2.4 SAM signal acquisition and processing

Once ground until perfectly flat and polished (see Table 9), the sample is positioned in a scanning chamber filled with degassed 1% PBS and maintained at a constant temperature of 25°C during the scan. The stage is adjusted to align the sample surface with the x-y plane of the motion stage and the transducer is moved along the z-axis until the confocal configuration is reached (Fig. 13C). Emitted waves will hit the sample surface at normal incidence. When the acquisition starts, the transducer performs a raster scan (C-scan, Fig. 13B) of the selected area of the sample with 12-µm lateral steps along x and y. The signal-processing steps are illustrated in Fig. 14. Each signal is digitized at 400 MHz and band pass filtered with a type II Chebyshev filter with cutoff frequencies of 5 and 200 MHz to remove high-frequency noise. The signal amplitude is obtained as the maximum of the envelope of the Hilbert transform of the signal. After each C-scan, a second scan is conducted on a linear region of interest (ROI) of the bone surface. The line is scanned several times (Bz-scan) changing the height of the transducer within a certain range (i.e. ± 120 µm around the confocal position of Fig. 13C). The Bz-scan is used to calculate a time-of-flight-based calibration curve that relates time of flight (TOF, hence defocus position) and voltage loss [199]. A phantom consisting of two homogeneous materials (i.e. titanium and PMMA) with known acoustic impedance is scanned before and after each measurement of a sample. This procedure allows to calculate the coefficients of a linear relationship for the conversion of voltage to reflection coefficients [199]. Finally, reflection coefficients are converted to acoustic impedance Z with Eq. (11). In the equation, Z_1 and Z_2 correspond to the acoustic impedance of water (known) and bone, respectively. For an explanation of the relationship between acoustic reflection coefficients, acoustic impedance and the elastic properties of the medium under examination see the acoustic theory section 2.2.2.1 above.

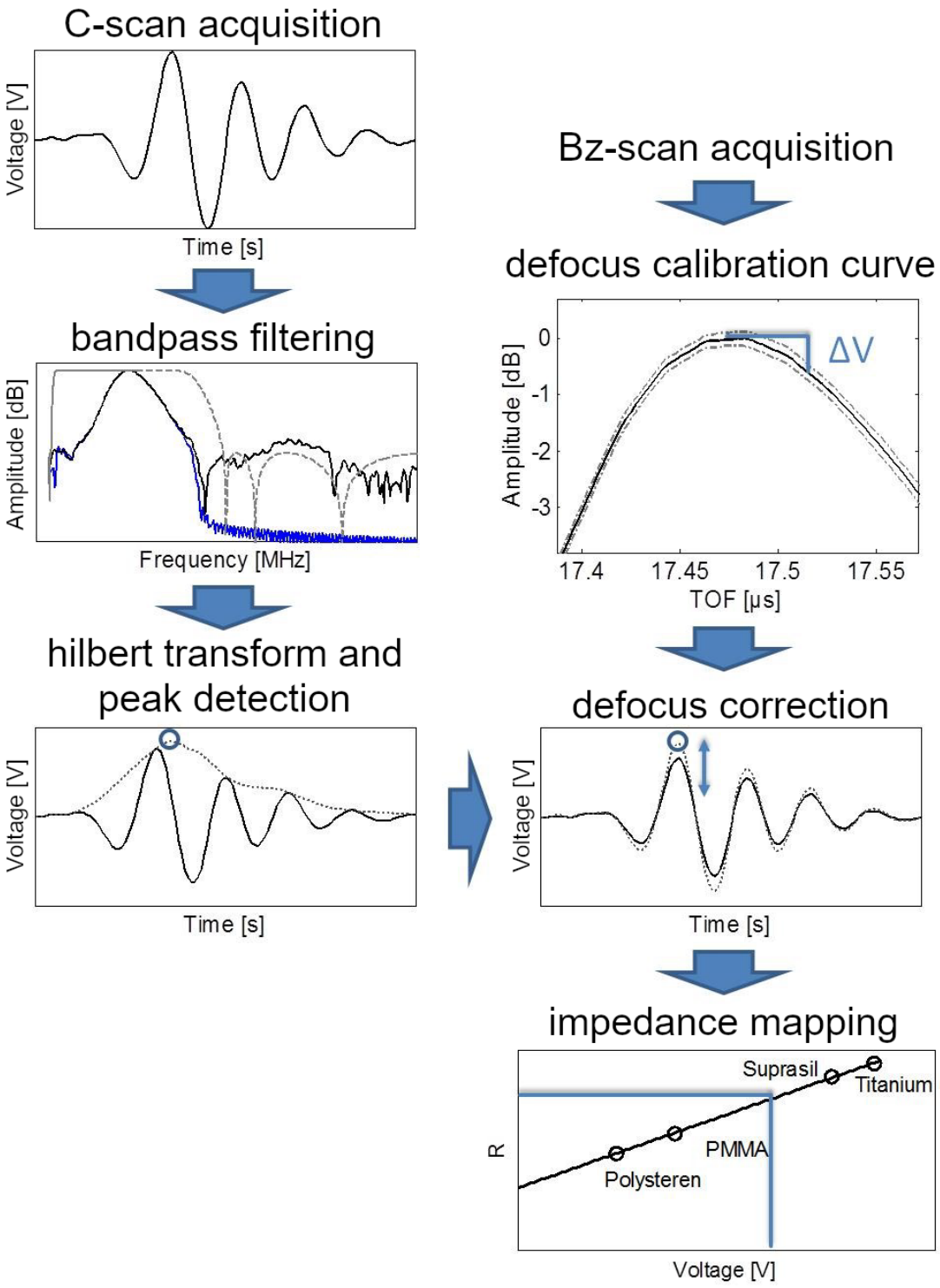

Fig. 14. SAM signal processing. Time signals of the C-scan (left column) are bandpass filtered with cutoff frequencies of 5 and 200 MHz. The pixel intensity is the peak in the envelope of the Hilbert-transformed signal. The defocus calibration curve obtained from the Bz-scan allows to estimate the amplitude loss (ΔV) associated with a deviation of the TOF from the confocal one. In particular, a signal arriving earlier or later than expected will correspond to an out-of-focus position of the transducer (positive or negative, respectively). Thanks to the Bz-scan, it is possible to correct the intensity of each pixel based on the TOF of the corresponding time signal. Voltage values are then converted to reflection coefficients (R) with a linear function. The coefficients for the conversion to R are computed for each experiment performing a scan of a PMMA-titanium phantom before and after each sample measurement. Adapted from [197] with permission from Dr. Rohrbach.

2.2.2.5 SAM image processing

Segmentation

In chapter 5 of the thesis, binary masks of the bone tissue are obtained from SAM images using an adaptive global threshold [201]. The method was developed for acoustic impedance maps of bone samples embedded in PMMA, in which the distribution of the pixel intensity follows a bimodal distribution [201]. Since I did not use PMMA embedding (samples were scanned fresh), the acoustic impedance distribution of the SAM images utilized for this thesis was unimodal. In this case, the segmentation of single, particularly small cortical bone pores was better achieved using a threshold which is locally adapting (for chapters 3 and 4 a Wellner threshold [190] was used; see Table 6). After thresholding, the tissue mask is cleaned by filling all single-pixel holes and removing small particles enclosed in the pores. These are selected automatically based on their area or on the portion of their surface connected to the bone tissue (simpelCT\removeparticles.m).

Histomorphometry

A large part of the analysis of bone histomorphometry from SAM images corresponds to what I have already described in Table 7 for CT images. Volumetric quantities are replaced by their areal equivalents (e.g. Ct.Ar and T.Ar instead of Ct.V and T.V, respectively). In addition, SAM allows to measure the diameter, area and degree of circularity of each pore in cortical bone. The analyses that I will present in chapters 3 and 4 make extensive use of measurements of the pore-size distribution obtained from SAM.

2.2.2.6 SAM measurements for this research

The locations of SAM measurements utilized in the next chapters are summarized in Fig. 15. From the 20 pairs of legs of the donors of Table 4, SAM scans were performed at the proximal shaft of the left and right femora (chapter 5) and at the midhaft of the left tibiae (chapters 3 and 4).

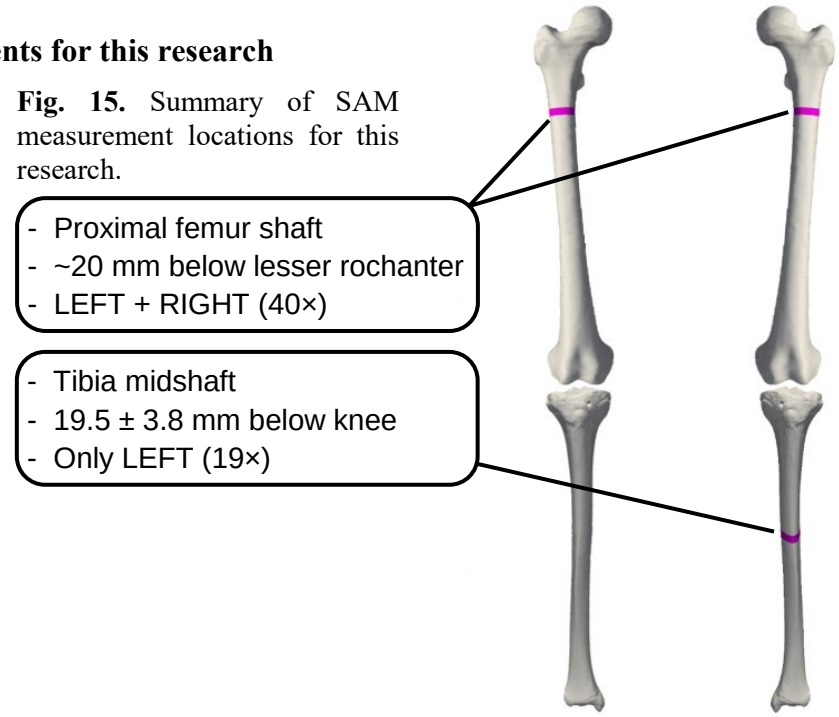

Fig. 15. Summary of SAM measurement locations for this research.

2.3 Measuring proximal femur strength

2.3.1 Mechanical tests

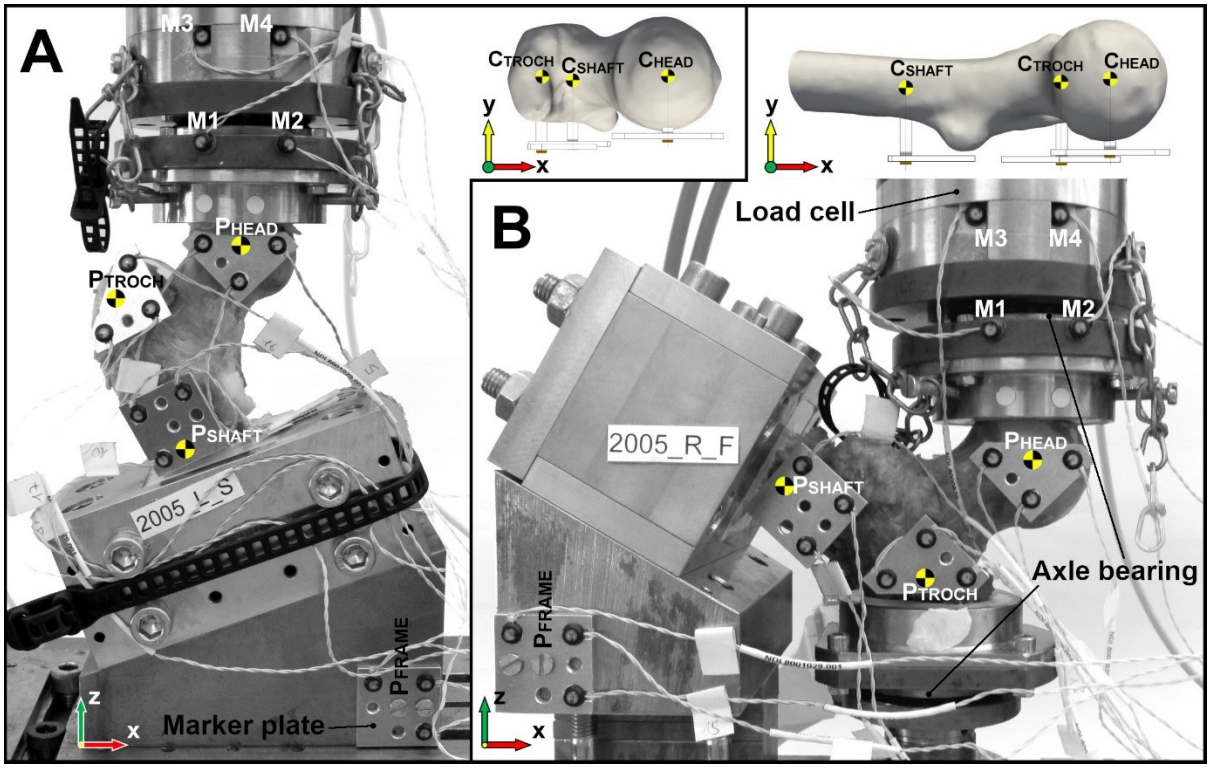

Fig. 16. Setup of mechanical test of proximal femur failure. STANCE: 20° inclination in the frontal plane, load direction in the plane defined by the femoral neck and shaft axes. Sideways FALL: 0° internal rotation, 30° adduction angle. 7 infrared markers are attached to the setup. 3 sets of 3 markers each are mounted on aluminum plates and attached to the bone surface at P_{HEAD}, P_{SHAFT} and P_{TROCH}. A set of 3 markers on a further plate is attached to the machine frame (P_{FRAME}).

The left and right femora of 10 donors were arbitrarily selected from the 19 donors of Table 4 and prepared for mechanical failure tests. For the experiment, I replicated a protocol established by Dall'Ara et al. in 2013 (Fig. 16) [202]. I assigned one leg (randomly selected) to mechanical testing in a configuration representative of the hip loading during a side-backwards fall (FALL, 0° internal rotation, 30° adduction angle). The contralateral femur was tested simulating one-legged stance loading of the hip (STANCE, 20° inclination in the frontal plane, load direction in the plane defined by the femoral neck and shaft axes). Samples were left thawing in 0.9% saline solution for at least 10 hours before the experiment, for a total number of 3 freezing-thawing cycles at the time point of mechanical testing. 30 mm (in addition to the 30 mm already embedded, see Fig. 11B) of the femoral shaft were embedded in polyurethane ensuring load distribution over 60 mm of the diaphysis. Custom designed axle bearings (Fig. 16) allowed two free translations and one rotation in the plane orthogonal to the loading axis through the femoral head and, for FALL tests, through the greater trochanter. At the femoral head and trochanter, loads were introduced over 10 mm (approx.) of the bone using embedding caps that were custom-molded for each sample. Bone-embedding contact surfaces were lubricated with Vaseline to reduce friction.

Setup and sample displacements were measured in 3D using a set of 16 infrared markers (Optotrak Certus, Northern Digital Inc., Canada). 4 markers were attached to the actuator of the press (M1 to M4 in Fig. 16) and the remaining 12 markers, in sets of 3, to the bone surface and

to the experimental setup. Each set of 3 markers was mounted on a custom aluminum plate which was fastened to the bone using orthopedic screws (4 mm, DePuy Synthes, Raynham, MA, USA). By displacing jointly with the attachment region, each plate allowed the calculation of the full 3D displacement vector (3 displacements and 3 angles of rotations) of a known position on the bone cortex (Table 10). In the previous versions of this setup the bone rotations were not available. One additional aluminum plate was attached to the frame of the setup to control its compliance.

Table 10. Positions for the recording of 3D displacements on the bone surface.

P_{HEAD}	Posterior surface: midpoint of the femoral head
P_{SHAFT}	Posterior surface of the femoral shaft (~10 mm below the lesser trochanter)
P_{TROCH}	Posterior surface of the greater trochanter

Before starting the failure test, a preconditioning cycle of 10 compressions until 0.8 mm was applied and the contact with embedding caps re-adjusted. After this, the main load was applied on the femoral head at a fixed displacement rate of 5 mm/min and until failure. The axial force was recorded using a 100 kN load cell (U3 force transducer, HBM, Germany) and the position of each marker using a 3D motion capture system (Optotrak Certus, Northern Digital Inc., Canada) at 100 Hz. A video of the anterior side of the femur (the side free of aluminum plates) was recorded with a laboratory camera (PowerShot SX160 IS, Canon, Japan).

Data processing

Force and displacement readings were synchronized to the start of the test by detecting the first peak in the second derivative of each signal. The full displacement vector of the points P_{HEAD}, P_{SHAFT} and P_{TROCH} was derived from the markers displacement along x, y and z and from the exact geometry of the aluminum plates. Knowing the exact sample size (thickness) at these locations (this information was obtained from the HR-pQCT images), and assuming the deformations of the bone section to be negligible, it is possible to calculate displacements and rotations of the three centroids: C_{HEAD}, C_{SHAFT} and C_{TROCH}) (see inserts on the top of Fig. 16).

The strength of each femur was calculated as the ultimate force recorded during the experiment (Fig. 17). Femur stiffness was defined as the maximum slope recorded during at least 20% of the load-displacement curve before yield [203]. For this, the vertical components of displacement from markers M1 and M2 (see Fig. 16) were averaged [202]. Displacements and rotations of the centroids C_{HEAD}, C_{SHAFT} and C_{TROCH} were used to verify a posteriori the hypothesis of frictionless contact on the femur head. Results of this analysis are presented in appendix A of the thesis.

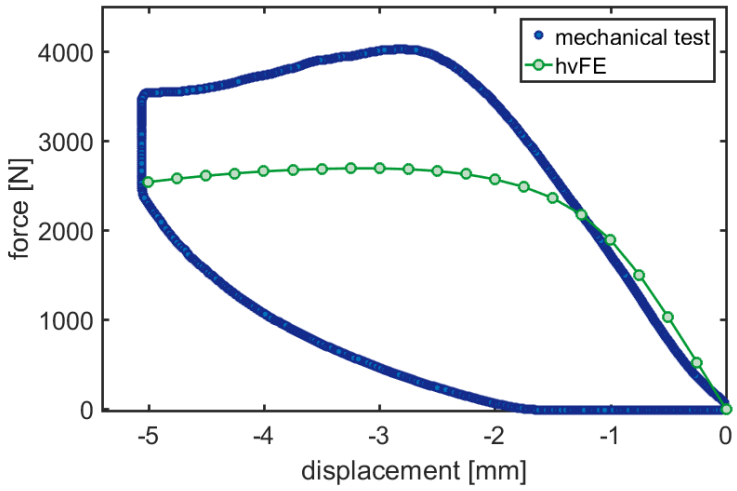

Fig. 17. Force-displacement plots for FALL mechanical test (blue) and homogenized voxel FE simulation (green) of proximal femur failure. Femur strength is considered as the maximum recorded reaction load. Experimental femur stiffness as the maximum slope of at least 20% of the force-displacement curve before yield [203]. Stiffness from hvFE simulations is taken simply as the maximum slope of the curve.

2.3.2 Simulations with the Finite Element

Nonlinear homogenized voxel FE models of femur strength were developed from the HR-pQCT datasets of all samples following the procedure described and validated in vitro in 2013 by Dall'Ara et al. [202] Fig. 18 shows a schematic view of the two simulated loading configurations (STANCE and FALL). Details of the pipeline for FE generation and solution are reported in Table 11.

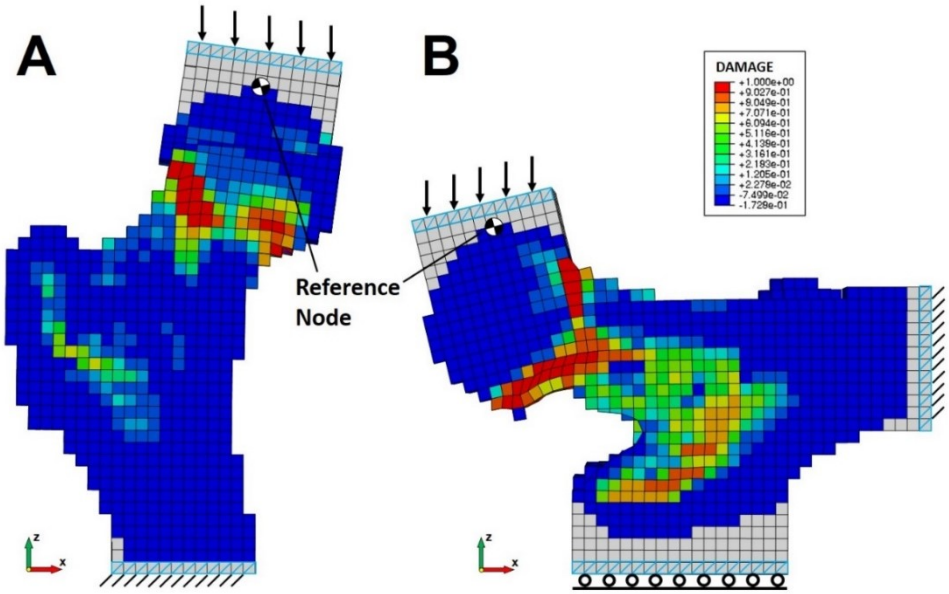

Fig. 18. Nonlinear homogenized voxel FE models for the simulation of proximal femur strength in one-legged standing (STANCE, A) and sideways falling (FALL, B) conditions.

Table 11. Pipeline for the automatic generation of nonlinear homogenized voxel FE models of femur strength. The models were generated with medtool (medtool 4.1, Dr. Pahr Ingenieurs e.U, Pfaffstätten, Austria) and solved in Abaqus (Abaqus 6.12, Simulia, Dassault Systemes, Velizy Villacoublay, France) on a quad-core Intel Xeon® workstation equipped with 32 GB of memory. A set of 80 nonlinear analyses required a total CPU time of ~63 hours.

Step		Description
1.	Coarsening #1	Downsample the HR-pQCT volume with factor 10 to 0.303³ mm³ isotropic voxels
2.	Air bubble Removal	A Detect air and water HU peaks from the histogram of the entire CT volume
		B Set the intensity of all voxels with $HU < \frac{HU_{air}+HU_{H2O}}{2}$ to HU_{H2O}
3.	$HU \rightarrow BMD$	As described in section 2.2.1.1
4.	3D rotate	A Segment cement markers (Fig. 11B) based on BMD and track their coordinates
		B Compute 3D rigid transformation matrices aligning the sample in the position of STANCE and FALL testing from the markers coordinates
		C Apply 3D transformations
5.	Coarsening #2	Downsample with factor 9 → 2.727³ mm³ isotropic voxels

Step		Description
6.	$BMD \rightarrow \frac{BV}{TV}$	BMD is converted to BV/TV with a linear function as in [202]. Slope and offset of the calibration rule are derived from 3D registered HR-pQCT and SAM cross sections of the femur shaft. Briefly: after 3D registering SAM and HR-pQCT images, an isotropic 1 mm grid is overlaid to both. Local BV/TV is calculated from the binarized SAM. Local average BMD for the corresponding grid ROI is obtained from the HR-pQCT image. A linear fit of all data points with 1% < BV/TV < 100% provides the linear calibration rule for conversion of BMD to BV/TV. See chapter 5 and [192] for more details on the method.
7.	Remove background	A Calculate binary mask of the bone tissue (Isodata method in Table 6; [189]) B Clean the mask by morphological filling; remove all unconnected objects C Multiply the mask to the BV/TV volume data to set background voxels to zero
8.	Crop	Reduce image size to the ROI occupied by the sample; remove 60 mm of the diaphysis embedded in polyurethane
9.	Embed	A Embed 3 bone voxels (~8 mm) to simulate polyurethane cap voxels on: - STANCE: head (cranial side) and shaft - FALL: head (medial), greater trochanter (lateral) and shaft B Add 1 voxel-thick steel plate to simulate mechanical testing system
10.	Generate FE voxels	Direct conversion of voxels to linear hexaedron elements; generation of Abaqus input file
11.	Boundary Conditions	A Create reference node on the center of mass of all nodes from the upper surface of the femoral head (most cranial or medial surface, for STANCE and FALL configurations, respectively; Fig. 18) B Apply kinematic coupling between the nodes of the upper surface of the steel plate above the femoral head and the reference node already created C Allow all rotations and translation in the x-y plane of the reference node D Fix all rotations and translations of the nodes on the bottom surface of the steel plate below the femur shaft E (only FALL) Allow rotation and translation in the x-y plane of all nodes on the bottom surface of the steel plate below the greater trochanter cap F Fix maximum (negative) axial displacement of the reference node to 5 mm
12.	Material properties mapping	Elastic and yield properties are directly mapped based on the voxel BV/TV. The constitutive law implements a piecewise Hill yield criterion. This is described in the work of Garcia et al. [204] In our case, the contribution of local fabric information is neglected. Anisotropic material (elastic and yield) constants for the model are taken from the experimental work on trabecular bone samples of Rincón-Kohli and Zysset [60] (Table 12). Material constants for cortical bone are extrapolated from those of Table 12 with a monotonic function of BV/TV as in [202]. Cortical bone is defined as all voxels having BV/TV > 0.5. At BV/TV = 1, the scaling provides elastic modulus, compressive and tensile yield stresses of 24 GPa, 266 MPa and 200 MPa, respectively.
13.	Solve	Abaqus/Standard uses Newton's method to solve quasi-static analyses
14	Postprocess	A Calculate reaction force as the average vertical component of force from all nodes on the upper surface of the steel plate above the femoral head B Femur strength: maximum reaction force during the simulation (Fig. 17) Femur stiffness: maximum slope of the force-displacement curve (Fig. 17)

Table 12. Elastic and yield parameters for the material model. [60]

	Elasticity					**Yield stress**		
Constant	ε_0 [MPa]	ν_0	μ_0 [MPa]	k	l	σ_0 [MPa]	χ_0	τ_0 [MPa]
Tension (+)	6614	0.246	2654	1.33	1.0	54.8	−0,246	44.6
Compression (−)						72.9	0.333	

I conducted a sensitivity study on the FE element voxel size by comparing the results obtained with 2.727^3 mm³ isotropic voxels with 0.909^3 mm³ ones. For the latter case, the scaling factor for step 5 (coarsening #2) in Table 11 was modified from 9 to 3. Results of the sensitivity analysis are presented in the appendix B of the thesis.

References of chapters 1 and 2

1. Bouillon R, Suda T. Vitamin D: calcium and bone homeostasis during evolution. BoneKEy Rep. 2014;3. doi:10.1038/bonekey.2013.214
2. Reznikov N, Steele J a. M, Fratzl P, Stevens MM. A materials science vision of extracellular matrix mineralization. Nat Rev Mater. 2016;1: 16041. doi:10.1038/natrevmats.2016.41
3. Almer JD, Stock SR. Internal strains and stresses measured in cortical bone via high-energy X-ray diffraction. J Struct Biol. 2005;152: 14–27. doi:10.1016/j.jsb.2005.08.003
4. Hellmich Christian, Ulm Franz-Josef. Micromechanical Model for Ultrastructural Stiffness of Mineralized Tissues. J Eng Mech. 2002;128: 898–908. doi:10.1061/(ASCE)0733-9399(2002)128:8(898)
5. Wilson EE, Awonusi A, Morris MD, Kohn DH, Tecklenburg MM, Beck LW. Highly Ordered Interstitial Water Observed in Bone by Nuclear Magnetic Resonance. J Bone Miner Res. 2005;20: 625–634. doi:10.1359/JBMR.041217
6. Weiner S, Traub W. Bone structure: from angstroms to microns. FASEB J. 1992;6: 879–885. doi:10.1096/fasebj.6.3.1740237
7. Landis WJ, Hodgens KJ, Arena J, Song MJ, McEwen BF. Structural relations between collagen and mineral in bone as determined by high voltage electron microscopic tomography. Microsc Res Tech. 1996;33: 192–202. doi:10.1002/(SICI)1097-0029(19960201)33:2<192::AID-JEMT9>3.0.CO;2-V
8. Weiner S, Wagner HD. The material bone: structure-mechanical function relations. Annu Rev Mater Sci. 1998;28: 271–298.
9. Fratzl P, Gupta HS, Paschalis EP, Roschger P. Structure and mechanical quality of the collagen–mineral nano-composite in bone. J Mater Chem. 2004;14: 2115–2123. doi:10.1039/B402005G
10. Reznikov N, Shahar R, Weiner S. Three-dimensional structure of human lamellar bone: The presence of two different materials and new insights into the hierarchical organization. Bone. 2014;59: 93–104. doi:10.1016/j.bone.2013.10.023
11. Weiner S, Traub W, Wagner HD. Lamellar bone: structure–function relations. J Struct Biol. 1999;126: 241–255.
12. Currey JD, Shahar R. Cavities in the compact bone in tetrapods and fish and their effect on mechanical properties. J Struct Biol. 2013;183: 107–122. doi:10.1016/j.jsb.2013.04.012
13. Perilli E, Bala Y, Zebaze R, Reynolds KJ, Seeman E. Regional Heterogeneity in the Configuration of the Intracortical Canals of the Femoral Shaft. Calcif Tissue Int. 2015;97: 327–335. doi:10.1007/s00223-015-0014-5

14. Cooper DML, Matyas JR, Katzenberg MA, Hallgrimsson B. Comparison of Microcomputed Tomographic and Microradiographic Measurements of Cortical Bone Porosity. Calcif Tissue Int. 2004;74: 437–447. doi:10.1007/s00223-003-0071-z
15. Cohen J, Harris WH. The Three-Dimensional Anatomy of Haversian Systems. JBJS. 1958;40: 419.
16. Buckwalter JA, Glimcher MJ, Cooper RR, Recker R. Bone biology. I: Structure, blood supply, cells, matrix, and mineralization. Instr Course Lect. 1996;45: 371–386.
17. Atkins A, Dean MN, Habegger ML, Motta PJ, Ofer L, Repp F, et al. Remodeling in bone without osteocytes: Billfish challenge bone structure–function paradigms. Proc Natl Acad Sci. 2014;111: 16047–16052. doi:10.1073/pnas.1412372111
18. Skedros JG, Keenan KE, Williams TJ, Kiser CJ. Secondary osteon size and collagen/lamellar organization ("osteon morphotypes") are not coupled, but potentially adapt independently for local strain mode or magnitude. J Struct Biol. 2013;181: 95–107. doi:10.1016/j.jsb.2012.10.013
19. Jowsey J. Studies of Haversian systems in man and some animals. J Anat. 1966;100: 857–864.
20. Qiu S, Fyhrie DP, Palnitkar S, Rao DS. Histomorphometric assessment of Haversian canal and osteocyte lacunae in different-sized osteons in human rib. Anat Rec A Discov Mol Cell Evol Biol. 2003;272A: 520–525. doi:10.1002/ar.a.10058
21. Cooper DML, Turinsky AL, Sensen CW, Hallgrímsson B. Quantitative 3D analysis of the canal network in cortical bone by micro-computed tomography. Anat Rec B New Anat. 2003;274: 169–179. doi:10.1002/ar.b.10024
22. Cooper DML, Thomas CDL, Clement JG, Hallgrímsson B. Three-dimensional microcomputed tomography imaging of basic multicellular unit-related resorption spaces in human cortical bone. Anat Rec A Discov Mol Cell Evol Biol. 2006;288A: 806–816. doi:10.1002/ar.a.20344
23. Schrof S, Varga P, Galvis L, Raum K, Masic A. 3D Raman mapping of the collagen fibril orientation in human osteonal lamellae. J Struct Biol. 2014;187: 266–275. doi:10.1016/j.jsb.2014.07.001
24. Varga P, Pacureanu A, Langer M, Suhonen H, Hesse B, Grimal Q, et al. Investigation of the three-dimensional orientation of mineralized collagen fibrils in human lamellar bone using synchrotron X-ray phase nano-tomography. Acta Biomater. 2013;9: 8118–8127. doi:10.1016/j.actbio.2013.05.015
25. Reznikov N, Bilton M, Lari L, Stevens MM, Kröger R. Fractal-like hierarchical organization of bone begins at the nanoscale. Science. 2018;360: eaao2189. doi:10.1126/science.aao2189
26. Cooper DML, Kawalilak CE, Harrison K, Johnston BD, Johnston JD. Cortical Bone Porosity: What Is It, Why Is It Important, and How Can We Detect It? Curr Osteoporos Rep. 2016;14: 187–198. doi:10.1007/s11914-016-0319-y
27. Wolff J. Das Gesetz der Transformation der Knochen. Berlin: A. Hirschwald; 1892.
28. Currey JD. How Well Are Bones Designed to Resist Fracture? J Bone Miner Res. 2003;18: 591–598. doi:10.1359/jbmr.2003.18.4.591
29. Crowder C, Austin D. Age ranges of epiphyseal fusion in the distal tibia and fibula of contemporary males and females. J Forensic Sci. 2005;50: 1001–1007.
30. Currey JD. Bones : structure and mechanics. Princeton, N.J.; Oxford: Princeton University Press; 2006.

31. Bass S, Delmas PD, Pearce G, Hendrich E, Tabensky A, Seeman E. The differing tempo of growth in bone size, mass, and density in girls is region-specific. J Clin Invest. 1999;104: 795–804. doi:10.1172/JCI7060
32. Zebaze RMD, Jones A, Knackstedt M, Maalouf G, Seeman E. Construction of the Femoral Neck During Growth Determines Its Strength in Old Age. J Bone Miner Res. 2007;22: 1055–1061. doi:10.1359/jbmr.070329
33. Allen MR, Burr DB. Chapter 4 - Bone Modeling and Remodeling. In: Burr DB, Allen MR, editors. Basic and Applied Bone Biology. San Diego: Academic Press; 2014. pp. 75–90. doi:10.1016/B978-0-12-416015-6.00004-6
34. Roux W. Der kampf der theile im organismus. W. Engelmann; 1881.
35. Huiskes R. If bone is the answer, then what is the question? J Anat. 2000;197: 145–156.
36. Fratzl P, Weinkamer R. Nature's hierarchical materials. Prog Mater Sci. 2007;52: 1263–1334. doi:10.1016/j.pmatsci.2007.06.001
37. Frost HM. Bone "mass" and the "mechanostat": A proposal. Anat Rec. 1987;219: 1–9. doi:10.1002/ar.1092190104
38. Frost HM. From Wolff's law to the Utah paradigm: Insights about bone physiology and its clinical applications. Anat Rec. 2001;262: 398–419. doi:10.1002/ar.1049
39. Christen P, Ito K, Ellouz R, Boutroy S, Sornay-Rendu E, Chapurlat RD, et al. Bone remodelling in humans is load-driven but not lazy. Nat Commun. 2014;5: 4855. doi:10.1038/ncomms5855
40. Jilka RL, Noble B, Weinstein RS. Osteocyte apoptosis. Bone. 2013;54: 264–271. doi:10.1016/j.bone.2012.11.038
41. Lassen NE, Andersen TL, Pløen GG, Søe K, Hauge EM, Harving S, et al. Coupling of Bone Resorption and Formation in Real Time: New Knowledge Gained From Human Haversian BMUs. J Bone Miner Res. 2017; n/a-n/a. doi:10.1002/jbmr.3091
42. Boyle WJ, Simonet WS, Lacey DL. Osteoclast differentiation and activation. Nature. 2003;423: 337–342. doi:10.1038/nature01658
43. Carlisle ER, Fischgrund JS. CHAPTER 27 - Bone Graft and Fusion Enhancement. In: Errico TJ, Lonner BS, Moulton AW, editors. Surgical Management of Spinal Deformities. Philadelphia: W.B. Saunders; 2009. pp. 433–448. doi:10.1016/B978-141603372-1.50030-5
44. An J, Leeuwenburgh S, Wolke J, Jansen J. 4 - Mineralization processes in hard tissue: Bone. In: Aparicio C, Ginebra M-P, editors. Biomineralization and Biomaterials. Boston: Woodhead Publishing; 2016. pp. 129–146. doi:10.1016/B978-1-78242-338-6.00005-3
45. Buenzli PR, Sims NA. Quantifying the osteocyte network in the human skeleton. Bone. 2015;75: 144–150. doi:10.1016/j.bone.2015.02.016
46. Bayraktar HH, Morgan EF, Niebur GL, Morris GE, Wong EK, Keaveny TM. Comparison of the elastic and yield properties of human femoral trabecular and cortical bone tissue. J Biomech. 2004;37: 27–35. doi:10.1016/S0021-9290(03)00257-4
47. Wegst UGK, Bai H, Saiz E, Tomsia AP, Ritchie RO. Bioinspired structural materials. Nat Mater. 2015;14: 23–36. doi:10.1038/nmat4089
48. Ritchie RO. The conflicts between strength and toughness. Nat Mater. 2011;10: 817–822. doi:10.1038/nmat3115
49. Rho J-Y, Kuhn-Spearing L, Zioupos P. Mechanical properties and the hierarchical structure of bone. Med Eng Phys. 1998;20:92–102. doi:10.1016/S1350-4533(98)00007-1
50. Nair AK, Gautieri A, Chang S-W, Buehler MJ. Molecular mechanics of mineralized collagen fibrils in bone. Nat Commun. 2013;4: 1724. doi:10.1038/ncomms2720

51. Qin Z, Gautieri A, Nair AK, Inbar H, Buehler MJ. Thickness of Hydroxyapatite Nanocrystal Controls Mechanical Properties of the Collagen–Hydroxyapatite Interface. Langmuir. 2012;28: 1982–1992. doi:10.1021/la204052a
52. Buehler MJ. Nature designs tough collagen: Explaining the nanostructure of collagen fibrils. Proc Natl Acad Sci. 2006;103: 12285–12290. doi:10.1073/pnas.0603216103
53. Jäger I, Fratzl P. Mineralized Collagen Fibrils: A Mechanical Model with a Staggered Arrangement of Mineral Particles. Biophys J. 2000;79: 1737–1746. doi:10.1016/S0006-3495(00)76426-5
54. Gupta HS, Seto J, Wagermaier W, Zaslansky P, Boesecke P, Fratzl P. Cooperative deformation of mineral and collagen in bone at the nanoscale. Proc Natl Acad Sci. 2006;103: 17741–17746. doi:10.1073/pnas.0604237103
55. Zimmermann EA, Schaible E, Bale H, Barth HD, Tang SY, Reichert P, et al. Age-related changes in the plasticity and toughness of human cortical bone at multiple length scales. Proc Natl Acad Sci. 2011;108: 14416–14421. doi:10.1073/pnas.1107966108
56. Grimal Q, Raum and K, Gerisch A, Laugier P. Derivation of the mesoscopic elasticity tensor of cortical bone from quantitative impedance images at the micron scale. Comput Methods Biomech Biomed Engin. 2008;11: 147–157. doi:10.1080/10255840701688061
57. Currey JD. Effects of Differences in Mineralization on the Mechanical Properties of Bone. Philos Trans R Soc Lond B Biol Sci. 1984;304: 509–518. doi:10.1098/rstb.1984.0042
58. Currey JD. The mechanical consequences of variation in the mineral content of bone. J Biomech. 1969;2: 1–11. doi:10.1016/0021-9290(69)90036-0
59. Granke M, Grimal Q, Saïed A, Nauleau P, Peyrin F, Laugier P. Change in porosity is the major determinant of the variation of cortical bone elasticity at the millimeter scale in aged women. Bone. 2011;49: 1020–1026. doi:10.1016/j.bone.2011.08.002
60. Rincón-Kohli L, Zysset PK. Multi-axial mechanical properties of human trabecular bone. Biomech Model Mechanobiol. 2008;8: 195–208. doi:10.1007/s10237-008-0128-z
61. Cai Xiran, Brenner Renald, Peralta Laura, Olivier Cécile, Gouttenoire Pierre-Jean, Chappard Christine, et al. Homogenization of cortical bone reveals that the organization and shape of pores marginally affect elasticity. J R Soc Interface. 2019;16: 20180911. doi:10.1098/rsif.2018.0911
62. Xu B, Li H, Zhang Y. Understanding the viscoelastic behavior of collagen matrices through relaxation time distribution spectrum. Biomatter. 2013;3. doi:10.4161/biom.24651
63. Fois M, Lamure A, Fauran MJ, Lacabanne C. Study of human cortical bone and demineralized human cortical bone viscoelasticity. J Appl Polym Sci. 2001;79: 2527–2533. doi:10.1002/1097-4628(20010401)79:14<2527::AID-APP1061>3.0.CO;2-J
64. Hansen U, Zioupos P, Simpson R, Currey JD, Hynd D. The Effect of Strain Rate on the Mechanical Properties of Human Cortical Bone. J Biomech Eng. 2008;130: 011011–011011. doi:10.1115/1.2838032
65. Turner CH, Chandran A, Pidaparti RMV. The anisotropy of osteonal bone and its ultrastructural implications. Bone. 1995;17: 85–89. doi:10.1016/8756-3282(95)00148-7
66. Rudy DJ, Deuerling JM, Espinoza Orías AA, Roeder RK. Anatomic variation in the elastic inhomogeneity and anisotropy of human femoral cortical bone tissue is consistent across multiple donors. J Biomech. 2011;44: 1817–1820. doi:10.1016/j.jbiomech.2011.04.009
67. Launey ME, Buehler MJ, Ritchie RO. On the Mechanistic Origins of Toughness in Bone. Annu Rev Mater Res. 2010;40: 25–53. doi:10.1146/annurev-matsci-070909-104427

68. Gupta HS, Zioupos P. Fracture of bone tissue: The ‘hows’ and the ‘whys.’ Med Eng Phys. 2008;30: 1209–1226. doi:10.1016/j.medengphy.2008.09.007
69. Poundarik AA, Diab T, Sroga GE, Ural A, Boskey AL, Gundberg CM, et al. Dilatational band formation in bone. Proc Natl Acad Sci. 2012;109: 19178–19183. doi:10.1073/pnas.1201513109
70. Barthelat F, Rabiei R. Toughness amplification in natural composites. J Mech Phys Solids. 2011;59: 829–840. doi:10.1016/j.jmps.2011.01.001
71. Nalla RK, Kruzic JJ, Ritchie RO. On the origin of the toughness of mineralized tissue: microcracking or crack bridging? Bone. 2004;34: 790–798. doi:10.1016/j.bone.2004.02.001
72. Shen ZL, Dodge MR, Kahn H, Ballarini R, Eppell SJ. Stress-Strain Experiments on Individual Collagen Fibrils. Biophys J. 2008;95: 3956–3963. doi:10.1529/biophysj.107.124602
73. Launey ME, Chen P-Y, McKittrick J, Ritchie RO. Mechanistic aspects of the fracture toughness of elk antler bone. Acta Biomater. 2010;6: 1505–1514. doi:10.1016/j.actbio.2009.11.026
74. Cristofolini L. In vitro evidence of the structural optimization of the human skeletal bones. J Biomech. 2015;48: 787–796. doi:10.1016/j.jbiomech.2014.12.010
75. Assessment of fracture risk and its application to screening for postmenopausal osteoporosis. Report of a WHO Study Group. World Health Organ Tech Rep Ser. 1994;843: 1–129.
76. Hernandez CJ, Beaupré GS, Carter DR. A theoretical analysis of the relative influences of peak BMD, age-related bone loss and menopause on the development of osteoporosis. Osteoporos Int. 2003;14: 843–847. doi:10.1007/s00198-003-1454-8
77. Roholl PJM, Blauw E, Zurcher C, Dormans J a. MA, Theuns HM. Evidence for a diminished maturation of preosteoblasts into osteoblasts during aging in rats: An ultrastructural analysis. J Bone Miner Res. 1994;9: 355–366. doi:10.1002/jbmr.5650090310
78. Pfeilschifter J, Diel I, Pilz U, Brunotte K, Naumann A, Ziegler R. Mitogenic responsiveness of human bone cells in vitro to hormones and growth factors decreases with age. J Bone Miner Res. 1993;8: 707–717. doi:10.1002/jbmr.5650080609
79. Cao J, Venton L, Sakata T, Halloran BP. Expression of RANKL and OPG Correlates With Age-Related Bone Loss in Male C57BL/6 Mice. J Bone Miner Res. 2003;18: 270–277. doi:10.1359/jbmr.2003.18.2.270
80. Nakashima T, Hayashi M, Fukunaga T, Kurata K, Oh-hora M, Feng JQ, et al. Evidence for osteocyte regulation of bone homeostasis through RANKL expression. Nat Med. 2011;17: 1231–1234. doi:10.1038/nm.2452
81. Seeman E. Age- and Menopause-Related Bone Loss Compromise Cortical and Trabecular Microstructure. J Gerontol Ser A. 2013;68: 1218–1225. doi:10.1093/gerona/glt071
82. Bloomfield SA. Disuse Osteopenia. Curr Osteoporos Rep. 2010;8: 91–97. doi:10.1007/s11914-010-0013-4
83. Burr DB. Muscle Strength, Bone Mass, and Age-Related Bone Loss. J Bone Miner Res. 1997;12: 1547–1551. doi:10.1359/jbmr.1997.12.10.1547
84. Rittweger J, Gunga HC, Felsenberg D, Kirsch KA. Muscle and bone-aging and space. J Gravitational Physiol J Int Soc Gravitational Physiol. 1999;6: P133-6.

85. Pagnotti GM, Styner M, Uzer G, Patel VS, Wright LE, Ness KK, et al. Combating osteoporosis and obesity with exercise: leveraging cell mechanosensitivity. Nat Rev Endocrinol. 2019;15: 339. doi:10.1038/s41574-019-0170-1
86. Duque G, Troen BR. Understanding the Mechanisms of Senile Osteoporosis: New Facts for a Major Geriatric Syndrome. J Am Geriatr Soc. 2008;56: 935–941. doi:10.1111/j.1532-5415.2008.01764.x
87. Wronski TJ, Morey ER. Skeletal abnormalities in rats induced by simulated weightlessness. Metab Bone Dis Relat Res. 1982;4: 69–75. doi:10.1016/0221-8747(82)90011-X
88. McGee-Lawrence ME, Carey HV, Donahue SW. Mammalian hibernation as a model of disuse osteoporosis: the effects of physical inactivity on bone metabolism, structure, and strength. Am J Physiol-Regul Integr Comp Physiol. 2008;295: R1999–R2014. doi:10.1152/ajpregu.90648.2008
89. Perrien DS, Akel NS, Dupont-Versteegden EE, Skinner RA, Siegel ER, Suva LJ, et al. Aging alters the skeletal response to disuse in the rat. Am J Physiol-Regul Integr Comp Physiol. 2007;292: R988–R996. doi:10.1152/ajpregu.00302.2006
90. Bouxsein ML, Burkhart K, Allaire B, Anderson D, Lee DC, Keaveny TM. Effect of long duration spaceflight on vertebral strength and trunk muscle morphology [Internet]. Conference talk presented at: QMSKI; 2019 Feb 25; Lake Louise, Alberta (AB), Canada. Available: https://qmski.org/
91. Gabel L, Hulme PA, Liphardt A-M, Heer M, Sibonga JD, Boyd SK. The effect of long-duration spaceflight on bone microarchitecture and density [Internet]. Conference talk presented at: QMSKI; 2019 Feb 25; Lake Louise, Alberta (AB), Canada. Available: https://qmski.org
92. Eriksen EF, Hodgson SF, Eastell R, Riggs BL, Cedel SL, O'Fallon WM. Cancellous bone remodeling in type i (postmenopausal) osteoporosis: Quantitative assessment of rates of formation, resorption, and bone loss at tissue and cellular levels. J Bone Miner Res. 1990;5: 311–319. doi:10.1002/jbmr.5650050402
93. Chavassieux P, Seeman E, Delmas PD. Insights into Material and Structural Basis of Bone Fragility from Diseases Associated with Fractures: How Determinants of the Biomechanical Properties of Bone Are Compromised by Disease. Endocr Rev. 2007;28: 151–164. doi:10.1210/er.2006-0029
94. Delaisse J-M. The reversal phase of the bone-remodeling cycle: cellular prerequisites for coupling resorption and formation. BoneKEy Rep. 2014;3. doi:10.1038/bonekey.2014.56
95. Eriksen EF. Normal and Pathological Remodeling of Human Trabecular Bone: Three Dimensional Reconstruction of the Remodeling Sequence in Normals and in Metabolic Bone Disease*. Endocr Rev. 1986;7: 379–408.
96. Andreasen CM, Delaisse J-M, Eerden BC van der, Leeuwen JP van, Ding M, Andersen TL. Understanding Age-Induced Cortical Porosity in Women: The Accumulation and Coalescence of Eroded Cavities Upon Existing Intracortical Canals Is the Main Contributor. J Bone Miner Res. 2017;33: 606–620. doi:10.1002/jbmr.3354
97. Thomas CDL, Feik SA, Clement JG. Increase in pore area, and not pore density, is the main determinant in the development of porosity in human cortical bone. J Anat. 209: 219–230. doi:10.1111/j.1469-7580.2006.00589.x
98. Frost HM. On rho, a marrow mediator, and estrogen: Their roles in bone strength and "mass" in human females, osteopenias, and osteoporoses—insights from a new paradigm. J Bone Miner Metab. 1998;16: 113–123. doi:10.1007/s007740050035

99. Jordan GR, Loveridge N, Bell KL, Power J, Rushton N, Reeve J. Spatial clustering of remodeling osteons in the femoral neck cortex: a cause of weakness in hip fracture? Bone. 2000;26: 305–313. doi:10.1016/S8756-3282(99)00272-0
100. Ahlborg HG, Johnell O, Turner CH, Rannevik G, Karlsson MK. Bone Loss and Bone Size after Menopause. N Engl J Med. 2003;349: 327–334. doi:10.1056/NEJMoa022464
101. Seeman E. Pathogenesis of bone fragility in women and men. The Lancet. 2002;359: 1841–1850. doi:10.1016/S0140-6736(02)08706-8
102. Kanis JA, Odén A, McCloskey EV, Johansson H, Wahl DA, Cooper C, et al. A systematic review of hip fracture incidence and probability of fracture worldwide. Osteoporos Int. 2012;23: 2239–2256. doi:10.1007/s00198-012-1964-3
103. Hernlund E, Svedbom A, Ivergård M, Compston J, Cooper C, Stenmark J, et al. Osteoporosis in the European Union: medical management, epidemiology and economic burden. A report prepared in collaboration with the International Osteoporosis Foundation (IOF) and the European Federation of Pharmaceutical Industry Associations (EFPIA). Arch Osteoporos. 2013;8: 136. doi:10.1007/s11657-013-0136-1
104. Kanis JA, Cooper C, Rizzoli R, Reginster J-Y, Foundation (IOF) on behalf of the SAB of the ES for C and EA of O (ESCEO) and the C of SA and NS of the IO. European guidance for the diagnosis and management of osteoporosis in postmenopausal women. Osteoporos Int. 2018; 1–42. doi:10.1007/s00198-018-4704-5
105. Kanis JA, Johnell O, Oden A, Sernbo I, Redlund-Johnell I, Dawson A, et al. Long-Term Risk of Osteoporotic Fracture in Malmö. Osteoporos Int. 2000;11: 669–674. doi:10.1007/s001980070064
106. Kanis JA, Oden A, Johnell O, De Laet C, Jonsson B, Oglesby AK. The components of excess mortality after hip fracture. Bone. 2003;32: 468–473. doi:10.1016/S8756-3282(03)00061-9
107. Brody JE. After a Hip Fracture, Reducing the Risk of a Recurrence. The New York Times. 20 Apr 2019. Available: https://www.nytimes.com/2019/04/15/well/live/after-a-hip-fracture-reducing-the-risk-of-a-recurrence.html. Accessed 23 Apr 2019.
108. Staa TP van, Staa TP van, Staa TP van, Leufkens HGM, Cooper C. The Epidemiology of Corticosteroid-Induced Osteoporosis: a Meta-analysis. Osteoporos Int. 2002;13: 777–787. doi:10.1007/s001980200108
109. Ensrud KE, Lui L-Y, Taylor BC, Ishani A, Shlipak MG, Stone KL, et al. Renal Function and Risk of Hip and Vertebral Fractures in Older Women. Arch Intern Med. 2007;167: 133–139. doi:10.1001/archinte.167.2.133
110. Janghorbani M, Dam V, M R, Willett WC, Hu FB. Systematic Review of Type 1 and Type 2 Diabetes Mellitus and Risk of Fracture. Am J Epidemiol. 2007;166: 495–505. doi:10.1093/aje/kwm106
111. Wright NC, Saag KG, Curtis JR, Smith WK, Kilgore ML, Morrisey MA, et al. Recent trends in hip fracture rates by race/ethnicity among older US adults. J Bone Miner Res. 2012;27: 2325–2332. doi:10.1002/jbmr.1684
112. Youm T, Koval KJ, Kummer FJ, Zuckerman JD. Do all hip fractures result from a fall? Am J Orthop Belle Mead NJ. 1999;28: 190–194.
113. Viceconti M, Taddei F, Cristofolini L, Martelli S, Falcinelli C, Schileo E. Are spontaneous fractures possible? An example of clinical application for personalised, multiscale neuro-musculo-skeletal modelling. J Biomech. 2012;45: 421–426. doi:10.1016/j.jbiomech.2011.11.048
114. Tinetti ME, Speechley M, Ginter SF. Risk Factors for Falls among Elderly Persons Living in the Community. N Engl J Med. 1988;319: 1701–1707. doi:10.1056/NEJM198812293192604

115. Kanis JA, McCloskey EV, Johansson H, Oden A, Ström O, Borgström F. Development and use of FRAX® in osteoporosis. Osteoporos Int. 2010;21: 407–413. doi:10.1007/s00198-010-1253-y
116. Haaland DA, Cohen DR, Kennedy CC, Khalidi NA, Adachi JD, Papaioannou A. Closing the osteoporosis care gap – Increased osteoporosis awareness among geriatrics and rehabilitation teams. BMC Geriatr. 2009;9: 28. doi:10.1186/1471-2318-9-28
117. Bauer DC. Osteoporosis Treatment After Hip Fracture: Bad News and Getting Worse. JAMA Netw Open. 2018;1: e180844–e180844. doi:10.1001/jamanetworkopen.2018.0844
118. Kanis JA, Svedbom A, Harvey N, McCloskey EV. The Osteoporosis Treatment Gap. J Bone Miner Res. 2014;29: 1926–1928. doi:10.1002/jbmr.2301
119. Ruggiero SL, Dodson TB, Assael LA, Landesberg R, Marx RE, Mehrotra B. American Association of Oral and Maxillofacial Surgeons Position Paper on Bisphosphonate-Related Osteonecrosis of the Jaws—2009 Update. J Oral Maxillofac Surg. 2009;67: 2–12. doi:10.1016/j.joms.2009.01.009
120. Girgis CM, Seibel MJ. Atypical femur fractures: a review of the evidence and its implication to clinical practice. Ther Adv Musculoskelet Dis. 2011;3: 301–314. doi:10.1177/1759720X11416270
121. Adams JE. Dual-Energy X-Ray Absorptiometry. In: Grampp S, editor. Radiology of Osteoporosis. Berlin, Heidelberg: Springer Berlin Heidelberg; 2003. pp. 87–100. doi:10.1007/978-3-662-05235-8_6
122. Paggiosi MA, Glueer CC, Roux C, Reid DM, Felsenberg D, Barkmann R, et al. International variation in proximal femur bone mineral density. Osteoporos Int J Establ Result Coop Eur Found Osteoporos Natl Osteoporos Found USA. 2011;22: 721–729. doi:10.1007/s00198-010-1336-9
123. Johansson H, Azizieh F, al Ali N, Alessa T, Harvey NC, McCloskey E, et al. FRAX- vs. T-score-based intervention thresholds for osteoporosis. Osteoporos Int. 2017;28: 3099–3105. doi:10.1007/s00198-017-4160-7
124. Kanis JA, Harvey NC, Cooper C, Johansson H, Odén A, McCloskey EV, et al. A systematic review of intervention thresholds based on FRAX. Arch Osteoporos. 2016;11: 25. doi:10.1007/s11657-016-0278-z
125. Neuerburg C, Mittlmeier L, Schmidmaier R, Kammerlander C, Böcker W, Mutschler W, et al. Investigation and management of osteoporosis in aged trauma patients: a treatment algorithm adapted to the German guidelines for osteoporosis. J Orthop Surg. 2017;12: 86. doi:10.1186/s13018-017-0585-0
126. Vasikaran S, Eastell R, Bruyère O, Foldes AJ, Garnero P, Griesmacher A, et al. Markers of bone turnover for the prediction of fracture risk and monitoring of osteoporosis treatment: a need for international reference standards. Osteoporos Int. 2011;22: 391–420. doi:10.1007/s00198-010-1501-1
127. Kanis JA, McCloskey EV, Johansson H, Cooper C, Rizzoli R, Reginster J-Y, et al. European guidance for the diagnosis and management of osteoporosis in postmenopausal women. Osteoporos Int. 2013;24: 23–57. doi:10.1007/s00198-012-2074-y
128. Sanders KM, Nicholson GC, Watts JJ, Pasco JA, Henry MJ, Kotowicz MA, et al. Half the burden of fragility fractures in the community occur in women without osteoporosis. When is fracture prevention cost-effective? Bone. 2006;38: 694–700. doi:10.1016/j.bone.2005.06.004

129. Schuit SCE, van der Klift M, Weel AEAM, de Laet CEDH, Burger H, Seeman E, et al. Fracture incidence and association with bone mineral density in elderly men and women: the Rotterdam Study. Bone. 2004;34: 195–202. doi:10.1016/j.bone.2003.10.001
130. Ottosen N, Petersson H, Saabye N. Introduction to the finite element method. 1992. Dorchester UK Prentice Hall Eur.
131. Huiskes R, Chao EYS. A survey of finite element analysis in orthopedic biomechanics: The first decade. J Biomech. 1983;16: 385–409. doi:10.1016/0021-9290(83)90072-6
132. Lotz JC, Cheal EJ, Hayes WC. Fracture Prediction for the Proximal Femur Using Finite Element Models: Part I—Linear Analysis. J Biomech Eng. 1991;113: 353–360. doi:10.1115/1.2895412
133. Koivumäki JEM, Thevenot J, Pulkkinen P, Kuhn V, Link TM, Eckstein F, et al. Ct-based finite element models can be used to estimate experimentally measured failure loads in the proximal femur. Bone. 2012;50: 824–829. doi:10.1016/j.bone.2012.01.012
134. Grassi L, Väänänen SP, Ristinmaa M, Jurvelin JS, Isaksson H. How accurately can subject-specific finite element models predict strains and strength of human femora? Investigation using full-field measurements. J Biomech. 2016;49: 802–806. doi:10.1016/j.jbiomech.2016.02.032
135. Bessho M, Ohnishi I, Matsumoto T, Ohashi S, Matsuyama J, Tobita K, et al. Prediction of proximal femur strength using a CT-based nonlinear finite element method: Differences in predicted fracture load and site with changing load and boundary conditions. Bone. 2009;45: 226–231. doi:10.1016/j.bone.2009.04.241
136. Nishiyama KK, Gilchrist S, Guy P, Cripton P, Boyd SK. Proximal femur bone strength estimated by a computationally fast finite element analysis in a sideways fall configuration. J Biomech. 2013;46: 1231–1236. doi:10.1016/j.jbiomech.2013.02.025
137. Schileo E, Taddei F, Malandrino A, Cristofolini L, Viceconti M. Subject-specific finite element models can accurately predict strain levels in long bones. J Biomech. 2007;40: 2982–2989. doi:10.1016/j.jbiomech.2007.02.010
138. Taddei F, Cristofolini L, Martelli S, Gill HS, Viceconti M. Subject-specific finite element models of long bones: An in vitro evaluation of the overall accuracy. J Biomech. 2006;39: 2457–2467. doi:10.1016/j.jbiomech.2005.07.018
139. Orwoll ES, Marshall LM, Nielson CM, Cummings SR, Lapidus J, Cauley JA, et al. Finite Element Analysis of the Proximal Femur and Hip Fracture Risk in Older Men. J Bone Miner Res. 2009;24: 475–483. doi:10.1359/jbmr.081201
140. Kopperdahl DL, Aspelund T, Hoffmann PF, Sigurdsson S, Siggeirsdottir K, Harris TB, et al. Assessment of incident spine and hip fractures in women and men using finite element analysis of CT scans. J Bone Miner Res. 2014;29: 570–580. doi:10.1002/jbmr.2069
141. Lee DC, Hoffmann PF, Kopperdahl DL, Keaveny TM. Phantomless calibration of CT scans for measurement of BMD and bone strength—Inter-operator reanalysis precision. Bone. 2017;103: 325–333. doi:10.1016/j.bone.2017.07.029
142. Taddei F, Schileo E, Helgason B, Cristofolini L, Viceconti M. The material mapping strategy influences the accuracy of CT-based finite element models of bones: an evaluation against experimental measurements. Med Eng Phys. 2007;29: 973–979. doi:10.1016/j.medengphy.2006.10.014
143. Genant HK, Boyd D. Quantitative bone mineral analysis using dual energy computed tomography. Invest Radiol. 1977;12: 545–551.
144. Rüegsegger P, Niederer P, Anliker M. An extension of classical bone mineral measurements. Ann Biomed Eng. 1974;2: 194–205. doi:10.1007/BF02368490

145. Prevrhal S, Engelke K, Genant HK. pQCT: Peripheral Quantitative Computed Tomography. In: Grampp S, editor. Radiology of Osteoporosis. Berlin, Heidelberg: Springer Berlin Heidelberg; 2008. pp. 143–162. doi:10.1007/978-3-540-68604-0_10
146. Lauretani F, Bandinelli S, Griswold ME, Maggio M, Semba R, Guralnik JM, et al. Longitudinal Changes in BMD and Bone Geometry in a Population-Based Study. J Bone Miner Res. 2008;23: 400–408. doi:10.1359/jbmr.071103
147. Riggs BL, Melton LJ, Robb RA, Camp JJ, Atkinson EJ, Peterson JM, et al. Population-Based Study of Age and Sex Differences in Bone Volumetric Density, Size, Geometry, and Structure at Different Skeletal Sites. J Bone Miner Res. 2004;19: 1945–1954. doi:10.1359/jbmr.040916
148. Jamal SA, Gilbert J, Gordon C, Bauer DC. Cortical PQCT Measures Are Associated With Fractures in Dialysis Patients. J Bone Miner Res. 2006;21: 543–548. doi:10.1359/jbmr.060105
149. Mikkola T, Sipilä S, Portegijs E, Kallinen M, Alén M, Kiviranta I, et al. Impaired geometric properties of tibia in older women with hip fracture history. Osteoporos Int. 2007;18: 1083–1090. doi:10.1007/s00198-007-0352-x
150. Sheu Y, Zmuda JM, Boudreau RM, Petit MA, Ensrud KE, Bauer DC, et al. Bone strength measured by peripheral quantitative computed tomography and the risk of nonvertebral fractures: The osteoporotic fractures in men (MrOS) study. J Bone Miner Res. 2011;26: 63–71. doi:10.1002/jbmr.172
151. Kroker A, Zhu Y, Manske SL, Barber R, Mohtadi N, Boyd SK. Quantitative in vivo assessment of bone microarchitecture in the human knee using HR-pQCT. Bone. 2017;97: 43–48. doi:10.1016/j.bone.2016.12.015
152. Boutroy S, Van Rietbergen B, Sornay-Rendu E, Munoz F, Bouxsein ML, Delmas PD. Finite Element Analysis Based on In Vivo HR-pQCT Images of the Distal Radius Is Associated With Wrist Fracture in Postmenopausal Women. J Bone Miner Res. 2007;23: 392–399. doi:10.1359/jbmr.071108
153. Mikolajewicz N, Bishop N, Burghardt AJ, Folkestad L, Hall A, Kozloff K, et al. Relationship of fracture risk to HR-pQCT measures of Bone microarchitecture: systematic review and meta-analysis [Internet]. Conference talk presented at: QMSKI; 2019 Feb 26; QMSKI, Lake Louise, Alberta (AB), Canada. Available: https://qmski.org/
154. Langton CM, Palmer SB, Porter RW. The Measurement of Broadband Ultrasonic Attenuation in Cancellous Bone. Eng Med. 1984;13: 89–91. doi:10.1243/EMED_JOUR_1984_013_022_02
155. Laugier P. Instrumentation for in vivo ultrasonic characterization of bone strength. IEEE Trans Ultrason Ferroelectr Freq Control. 2008;55: 1179–1196. doi:10.1109/TUFFC.2008.782
156. Wear KA, Hoffmeister BK, Laugier P. Quantitative Ultrasound and the Management of Osteoporosis. Acoustics Today. 28 Jun 201814. Available: https://acousticstoday.org/quantitative-ultrasound-management-osteoporosis-keith-wear/. Accessed 18 Apr 2019.
157. Otani T. Quantitative Estimation of Bone Density and Bone Quality Using Acoustic Parameters of Cancellous Bone for Fast and Slow Waves. Jpn J Appl Phys. 2005;44: 4578. doi:10.1143/JJAP.44.4578
158. Bréban S, Padilla F, Fujisawa Y, Mano I, Matsukawa M, Benhamou CL, et al. Trabecular and cortical bone separately assessed at radius with a new ultrasound device, in a young adult population with various physical activities. Bone. 2010;46: 1620–1625. doi:10.1016/j.bone.2010.03.005

159. Wear KA, Armstrong DW. Relationships among calcaneal backscatter, attenuation, sound speed, hip bone mineral density, and age in normal adult women. J Acoust Soc Am. 2001;110: 573–578. doi:10.1121/1.1378343
160. Karjalainen J, Riekkinen O, Töyräs J, Kröger H, Jurvelin J. Ultrasonic assessment of cortical bone thickness in vitro and in vivo. IEEE Trans Ultrason Ferroelectr Freq Control. 2008;55: 2191–2197. doi:10.1109/TUFFC.918
161. Karjalainen JP, Riekkinen O, Töyräs J, Hakulinen M, Kröger H, Rikkonen T, et al. Multi-site bone ultrasound measurements in elderly women with and without previous hip fractures. Osteoporos Int. 2011;23: 1287–1295. doi:10.1007/s00198-011-1682-2
162. Soini E, Riekkinen O, Kröger H, Mankinen P, Hallinen T, Karjalainen JP. Cost-effectiveness of pulse-echo ultrasonometry in osteoporosis management. In: ClinicoEconomics and Outcomes Research [Internet]. 29 May 2018 [cited 19 Sep 2018]. doi:10.2147/CEOR.S163237
163. Wear KA, Laib A. The dependence of ultrasonic backscatter on trabecular thickness in human calcaneus: theoretical and experimental results. IEEE Trans Ultrason Ferroelectr Freq Control. 2003;50: 979–986. doi:10.1109/TUFFC.2003.1226542
164. Bossy E, Talmant M, Laugier P. Effect of bone cortical thickness on velocity measurements using ultrasonic axial transmission: A 2D simulation study. J Acoust Soc Am. 2002;112: 297–307. doi:10.1121/1.1480836
165. Nguyen TV, Center JR, Eisman JA. Bone mineral density-independent association of quantitative ultrasound measurements and fracture risk in women. Osteoporos Int. 2004;15: 942–947. doi:10.1007/s00198-004-1717-z
166. Minonzio J-G, Talmant M, Laugier P. Guided wave phase velocity measurement using multi-emitter and multi-receiver arrays in the axial transmission configuration. J Acoust Soc Am. 2010;127: 2913–2919. doi:10.1121/1.3377085
167. Minonzio J-G, Bochud N, Vallet Q, Bala Y, Ramiandrisoa D, Follet H, et al. Bone cortical thickness and porosity assessment using ultrasound guided waves: An ex vivo validation study. Bone. 2018;116: 111–119. doi:10.1016/j.bone.2018.07.018
168. Schneider J, Iori G, Ramiandrisoa D, Hammami M, Gräsel M, Chappard C, et al. Ex vivo cortical porosity and thickness predictions at the tibia using full spectrum ultrasonic guided wave analysis. Arch Osteoporos. 2018; (submitted).
169. Schneider J, Ramiandrisoa D, Armbrecht G, Ritter Z, Felsenberg D, Raum K, et al. In Vivo Measurements of Cortical Thickness and Porosity at the Proximal Third of the Tibia Using Guided Waves: Comparison with Site-Matched Peripheral Quantitative Computed Tomography and Distal High-Resolution Peripheral Quantitative Computed Tomography. Ultrasound Med Biol. 2019;0. doi:10.1016/j.ultrasmedbio.2019.01.008
170. Minonzio J-G, Bochud N, Vallet Q, Ramiandrisoa D, Etcheto A, Briot K, et al. Ultrasound-based estimates of cortical bone thickness and porosity are associated with non-traumatic fractures in postmenopausal women: A pilot study. J Bone Miner Res. 2019;0. doi:10.1002/jbmr.3733
171. Renaud G, Kruizinga P, Cassereau D, Laugier P. In vivo ultrasound imaging of the bone cortex. Phys Med Biol. 2018;63: 125010. doi:10.1088/1361-6560/aac784
172. Mamou J, Coron A, Saegusa-Beecroft E, Hata M, Yanagihara E, Machi J, et al. Backscatter Quantification for the Detection of Metastatic Regions in Human Lymph Nodes. In: Mamou J, Oelze ML, editors. Quantitative Ultrasound in Soft Tissues. Dordrecht: Springer Netherlands; 2013. pp. 147–170. doi:10.1007/978-94-007-6952-6_7

173. Yamaguchi T. The Quantitative Ultrasound Diagnosis of Liver Fibrosis Using Statistical Analysis of the Echo Envelope. In: Mamou J, Oelze ML, editors. Quantitative Ultrasound in Soft Tissues. Dordrecht: Springer Netherlands; 2013. pp. 275–288. doi:10.1007/978-94-007-6952-6_11
174. Kilappa V, Hackenbeck J, Iori G, Du J, Raum K. Assessment of cortical bone pore dimensions by high-frequency backscatter. 2017 IEEE International Ultrasonics Symposium (IUS). Washington, DC, USA: IEEE; 2017. pp. 1–1. doi:10.1109/ULTSYM.2017.8092606
175. Du J, Iori G, Raum K. In-silico validation of microstructure estimation from cortical bone backscatter [Internet]. Conference talk presented at: IUS IEEE; 2018 Oct 25; IEEE International Ultrasonics Symposium, Kobe, Japan. Available: http://sites.ieee.org/ius-2018/
176. Augat P, Schorlemmer S. The role of cortical bone and its microstructure in bone strength. Age Ageing. 2006;35: ii27–ii31. doi:10.1093/ageing/afl081
177. van der Linden JC, Weinans H. Effects of microarchitecture on bone strength. Curr Osteoporos Rep. 2007;5: 56–61.
178. Donnelly E. Methods for Assessing Bone Quality: A Review. Clin Orthop. 2011;469: 2128–2138. doi:10.1007/s11999-010-1702-0
179. Andresen R, Haidekker MA, Radmer S, Banzer D. CT determination of bone mineral density and structural investigations on the axial skeleton for estimating the osteoporosis-related fracture risk by means of a risk score. Br J Radiol. 1999;72: 569–578. doi:10.1259/bjr.72.858.10560339
180. Bjørnerem \AAshild. The clinical contribution of cortical porosity to fragility fractures. BoneKEy Rep. 2016;5.
181. Burr DB. Cortical bone: a target for fracture prevention? The Lancet. 2010;375: 1672–1673. doi:10.1016/S0140-6736(10)60444-8
182. Cheng XG, Lowet G, Boonen S, Nicholson PHF, Perre GVD, Dequeker J. Prediction of Vertebral and Femoral Strength In Vitro by Bone Mineral Density Measured at Different Skeletal Sites. J Bone Miner Res. 1998;13: 1439–1443. doi:10.1359/jbmr.1998.13.9.1439
183. Bouxsein ML, Coan BS, Lee SC. Prediction of the strength of the elderly proximal femur by bone mineral density and quantitative ultrasound measurements of the heel and tibia. Bone. 1999;25: 49–54. doi:10.1016/S8756-3282(99)00093-9
184. Lochmüller E-M, Groll O, Kuhn V, Eckstein F. Mechanical strength of the proximal femur as predicted from geometric and densitometric bone properties at the lower limb versus the distal radius. Bone. 2002;30: 207–216. doi:10.1016/S8756-3282(01)00621-4
185. Kroker A, Plett R, Nishiyama KK, McErlain DD, Sandino C, Boyd SK. Distal skeletal tibia assessed by HR-pQCT is highly correlated with femoral and lumbar vertebra failure loads. J Biomech. 2017;59: 43–49. doi:10.1016/j.jbiomech.2017.05.011
186. Abraham AC, Agarwalla A, Yadavalli A, McAndrew C, Liu JY, Tang SY. Multiscale Predictors of Femoral Neck In Situ Strength in Aging Women: Contributions of BMD, Cortical Porosity, Reference Point Indentation, and Nonenzymatic Glycation. J Bone Miner Res. 2015;30: 2207–2214. doi:10.1002/jbmr.2568
187. Burghardt AJ, Buie HR, Laib A, Majumdar S, Boyd SK. Reproducibility of direct quantitative measures of cortical bone microarchitecture of the distal radius and tibia by HR-pQCT. Bone. 2010;47: 519–528. doi:10.1016/j.bone.2010.05.034
188. Otsu N. A threshold selection method from gray-level histograms. IEEE Trans Syst Man Cybern. 1979;9: 62–66.

189. Ridler T, Calvard S, others. Picture thresholding using an iterative selection method. IEEE Trans Syst Man Cybern. 1978;8: 630–632.
190. Wellner PD. Adaptive thresholding for the DigitalDesk. Xerox EPC1993-110. 1993; 1–19.
191. Dempster DW, Compston JE, Drezner MK, Glorieux FH, Kanis JA, Malluche H, et al. Standardized nomenclature, symbols, and units for bone histomorphometry: A 2012 update of the report of the ASBMR Histomorphometry Nomenclature Committee. J Bone Miner Res. 2013;28: 2–17. doi:10.1002/jbmr.1805
192. Iori G, Heyer F, Kilappa V, Wyers C, Varga P, Schneider J, et al. BMD-based assessment of local porosity in human femoral cortical bone. Bone. 2018;114: 50–61. doi:10.1016/j.bone.2018.05.028
193. Hildebrand T, Rüegsegger P. A new method for the model-independent assessment of thickness in three-dimensional images. J Microsc. 1997;185: 67–75. doi:10.1046/j.1365-2818.1997.1340694.x
194. Briggs A, Briggs GAD, Kolosov O. Acoustic Microscopy: Second Edition. OUP Oxford; 2010.
195. Lemons RA, Quate CF. Acoustic microscope—scanning version. Appl Phys Lett. 1974;24: 163–165. doi:10.1063/1.1655136
196. Lemons RA, Quate CF. Acoustic Microscopy: Biomedical Applications. Science. 1975;188: 905–911.
197. Rohrbach D. Quantitative ultrasound in transverse transmission for bone quality assessment and monitoring fracture healing [Internet]. PhD Thesis, Humboldt-Universität zu Berlin, Mathematisch-Naturwissenschaftliche Fakultät I. 2013. doi:10.18452/16813
198. Schrof S. Multimodal structural, compositional, and mechanical characterization of cortical bone on the micron scale [Internet]. PhD Thesis, Humboldt-Universität zu Berlin, Mathematisch-Naturwissenschaftliche Fakultät. 2017. doi:10.18452/18076
199. Raum K, Reißhauer J, Brandt J. Frequency and resolution dependence of the anisotropic impedance estimation in cortical bone using time-resolved scanning acoustic microscopy. J Biomed Mater Res A. 2004;71A: 430–438. doi:10.1002/jbm.a.30156
200. Raum K, Jenderka KV, Klemenz A, Brandt J. Multilayer analysis: quantitative scanning acoustic microscopy for tissue characterization at a microscopic scale. IEEE Trans Ultrason Ferroelectr Freq Control. 2003;50: 507–516. doi:10.1109/TUFFC.2003.1201463
201. Lakshmanan S, Bodi A, Raum K. Assessment of Anisotropic Tissue Elasticity of Cortical Bone from High-Resolution, Angular Acoustic Measurements. IEEE Trans Ultrason Ferroelectr Freq Control. 2007;54: 1560–1570. doi:10.1109/TUFFC.2007.426
202. Dall'Ara E, Luisier B, Schmidt R, Kainberger F, Zysset P, Pahr D. A nonlinear QCT-based finite element model validation study for the human femur tested in two configurations in vitro. Bone. 2013;52: 27–38. doi:10.1016/j.bone.2012.09.006
203. Benca E, Reisinger A, Patsch JM, Hirtler L, Synek A, Stenicka S, et al. Effect of simulated metastatic lesions on the biomechanical behavior of the proximal femur. J Orthop Res. 2017;35: 2407–2414. doi:10.1002/jor.23550
204. Garcia D, Zysset PK, Charlebois M, Curnier A. A three-dimensional elastic plastic damage constitutive law for bone tissue. Biomech Model Mechanobiol. 2008;8: 149–165. doi:10.1007/s10237-008-0125-2

Chapter 3: Large cortical bone pores in the tibia are associated with proximal femur strength

Gianluca Iori[1], Johannes Schneider[1], Andreas Reisinger[2], Frans Heyer[3,4], Laura Peralta[5,6], Caroline Wyers[3,4], Melanie Gräsel[7], Reinhard Barkmann[7], Claus C. Glüer[7], J. P. van den Bergh[3,4], Dieter Pahr[2,8],and Kay Raum[1*]

[1] Berlin-Brandenburg Center for Regenerative Therapies, Charité – Universitätsmedizin Berlin, corporate member of Freie Universität Berlin, Humboldt-Universität zu Berlin, and Berlin Institute of Health, Berlin, Germany
[2] Division Biomechanics, Karl Landsteiner University of Health Sciences, Krems, Austria
[3] Department of Internal Medicine, NUTRIM School of Nutrition and Translational Research in Metabolism, Maastricht University Medical Center, Maastricht, The Netherlands
[4] Department of Internal Medicine, VieCuri Medical Center, Venlo, The Netherlands
[5] Laboratoire d'Imagerie Biomédicale, Sorbonne Universités, INSERM UMR S 1146, CNRS UMR 7371, Paris, France
[6] Department of Biomedical Engineering, School of Biomedical Engineering & Imaging Sciences, King's College London, London, UK
[7] Sektion Biomedizinische Bildgebung, Klinik für Radiologie und Neuroradiologie, Christian-Albrechts-Universität zu Kiel, Kiel, Germany
[8] Institute for Lightweight Design and Structural Biomechanics, TU Wien, Vienna, Austria

[*] Corresponding author: Kay Raum
E-mail: kay.raum@charite.de

Overview

This chapter targets the identification of relevant cortical bone biomarkers of reduced femur strength. The work was performed *ex vivo* on human cadaveric legs, and investigates the association between the microstructure of cortical bone of the tibia with the mechanics of the proximal femur. Ground truth cortical bone thickness, porosity and size distribution of vascular pores were measured on microCT and high-resolution scanning acoustic microscopy images of 19 cross sections of human tibiae. Finite element simulations validated with mechanical tests provided proximal femur stiffness and strength for the same group of donors. The chapter demonstrates how a reduction in thickness and the accumulation of large pores in the cortical bone of the distal skeleton can indicate an impairment of the hip fracture resistance. The potential of microstructural measurements at the tibia is also compared with a standard hip DXA scan.

My contribution

For this study, I was entirely responsible for sample preparation and circulation, for SAM measurements, mechanical tests, development of FE simulations, data and statistical analysis and for the writing of the original draft. DXA and microCT measurements were performed by MG and RB at the Christian-Albrechts-Universität zu Kiel (Germany). HR-pQCT data collection was initiated by FH and myself and continued by FH and CW at VieCuri Venlo (the Netherlands). I developed the FE analysis based on Medtool scripts that were originally written by Enrico Dall'Ara at the TU Wien (Austria).

Publication notification

(DOI: 10.1371/journal.pone.0215405)

Iori G, Schneider J, Reisinger A, Heyer F, Peralta L, Wyers C, et al. Large cortical bone pores in the tibia are associated with proximal femur strength. PLOS ONE. 2019;14: e0215405.

Data availability

The full anonymized dataset for the reproduction of this study is available on Zenodo.org (DOI: https://doi.org/10.5281/zenodo.2605350). SAM images and the software for reproduction of the image processing described in the article are also available (DOI: https://doi.org/10.5281/zenodo.2593855 and https://doi.org/10.5281/zenodo.2605365).

Abstract

Alterations of structure and density of cortical bone are associated with fragility fractures and can be assessed in vivo in humans at the tibia. Bone remodeling deficits in aging women have been recently linked to an increase in size of cortical pores. In this ex vivo study, we characterized the cortical microarchitecture of 19 tibiae from human donors (aged 69 to 94 years) to address, whether this can reflect impairments of the mechanical competence of the proximal femur, i.e., a major fracture site in osteoporosis. Scanning acoustic microscopy (12 µm pixel size) provided reference microstructural measurements at the left tibia, while the bone vBMD at this site was obtained using microcomputed tomography (microCT). The areal bone mineral density of both left and right femoral necks ($aBMD_{neck}$) was measured by dual-energy X-ray absorptiometry (DXA), while homogenized nonlinear finite element models based on high-resolution peripheral quantitative computed tomography provided hip stiffness and strength for one-legged standing and sideways falling loads. Hip strength was associated with $aBMD_{neck}$ ($r = 0.74$ to 0.78), with tibial cortical thickness ($r = 0.81$) and with measurements of the tibial cross-sectional geometry ($r = 0.48$ to 0.73) of the same leg. Tibial vBMD was associated with hip strength only for standing loads ($r = 0.59$ to 0.65). Cortical porosity (Ct.Po) of the tibia was not associated with any of the femoral parameters. However, the proportion of Ct.Po attributable to large pores (diameter > 100 µm) was associated with hip strength in both standing ($r = -0.61$) and falling ($r = 0.48$) conditions. When added to $aBMD_{neck}$, the prevalence of large pores could explain up to 17% of the femur ultimate force. In conclusion, microstructural characteristics of the tibia reflect hip strength as well as femoral DXA, but it remains to be tested whether such properties can be measured in vivo.

Keywords: Cortical bone; Porosity; Bone strength; Finite Element Analysis; Hip fragility

3.1 Introduction

With >3.5 million fragility fractures annually in Europe only, osteoporosis represents a significant burden on the society [1]. In elderly subjects, the hip is the most frequent and severe osteoporotic fracture site [2]. In a population of increasing age, hip fractures represent a dramatic cause of functional decline, morbidity and mortality [3,4]. Despite these facts, a large number of hip fractures occurs in patients without diagnosed osteoporosis [5]. The failure in detecting alterations of the cortical bone microstructure is considered one of the reasons of the only modest efficacy of the current DXA-based fracture risk assessment [6–8]. In an attempt to fill this diagnostic gap, studies have investigated the association of structural features in cortical bone with fracture risk [9,10]. One motivation for this has been the observation that in long bones, a reduction of the cortical thickness (Ct.Th) and an increase in the cortical porosity (Ct.Po) are responsible for the larger part of the age-related bone loss [11]. Fueled by the advent of new technology such as high-resolution peripheral quantitative computed tomography (HR-pQCT), which allows the imaging of the distal skeleton in vivo with a spatial resolution down to 95 µm, clinical studies have associated Ct.Po and Ct.Th of the tibia and radius of humans with age, disease, fracture history, treatment and training [12–18].

Recent work on morphological alterations of bone multicellular units (BMUs) have extended our understanding of the way in which the microstructure of cortical bone is affected by aging. The age-related uncoupling between bone resorption and formation has been associated with prolonged osteoclastic activity and delayed refilling of resorption cavities in cortical bone [19]. As a consequence, cortical bone pores progressively increase in size and tend to coalesce, as recently observed in iliac crest specimens [20]. Interestingly, similar (large, irregular) cavities have been observed in femoral neck biopsies obtained from patients undergoing joint replacement following hip fracture [21].

Since osteoporosis occurs systemically throughout the skeleton, pore morphological changes are likely to be reflected in peripheral bones, which can be assessed in vivo more easily than the proximal femur. In a clinical study on Type 2 diabetes patients, a larger cortical pore diameter (Po.Dm) and increased diameter heterogeneity were observed at the distal skeleton of fractured subjects when compared to controls [15]. The increased Po.Dm at the distal site of both tibia and radius was accompanied by a significant increase of Ct.Po and by a reduction of the predicted strength of these bones, even though statistical significance was reached only for the distal sites of patients with Diabetes Mellitus. Backed by these findings, we hypothesized that enlarged cortical pores in the peripheral skeleton might reflect an impairment of the mechanical competence of the hip, a site of major relevance for fracture.

Ex vivo studies have investigated the association between the cortical bone of the tibia and the fracture load of human femur samples as early as 1996 [22], but rarely considered features of cortical pore morphology. One recent work has combined mechanical testing with HR-pQCT of tibia samples [23]. The authors reported strong correlations between properties of the distal tibia (total vBMD and simulated strength) and the strength of vertebrae and of proximal femora from the same donor. The microstructure of cortical bone, however, was not considered. Studies that took cortical microarchitecture into account have only included cortical porosity (Ct.Po) as single structural parameter [24].

The aim of this work was to quantify the correlation between the architecture of tibial cortical bone (macro- and microscopic, with an emphasis on variations of pore morphology), with the stiffness and strength of proximal femur samples. The analysis of the cortical bone microstructure was performed on the anteromedial tibia shaft, since this region represents a favorable site for in vivo ultrasound measurements [25]. We also asked whether cortical bone

properties at the tibia are able to explain the mechanical competence of the hip alternatively or in addition to DXA.

3.2 Materials and Methods

3.2.1 Samples

The lower limbs of nineteen human donors were collected at the Anatomy Institute of the Lübeck University. The scientific use of human tissue from body donors is permitted by the German law "Gesetz über das Leichen-, Bestattungsund Friedhofswesen des Landes Schleswig-Holstein - Abschnitt II, §9 (Leichenöffnung, anatomisch)" from 04.02.2005. The donors have agreed to scientific use of their bodies.

Left and right femora were stored, while only the left tibiae were available for the lower leg. All bone specimens were dissected and frozen at −20°C until and between experiments. The average donor age was 84 ± 8 years (69–94 years; 6 male, 13 female). Incomplete or no information was available regarding the medical history of the subjects. Proximal femur samples were prepared by cutting and embedding the diaphysis 80 mm below the lesser trochanter, as described elsewhere [26]. During dissection, the distal portion of the tibia samples had been already removed. The exact proportion of shaft missing was estimated to vary between 25% and 60%.

3.2.2 DXA

DXA measurements of all (left and right) proximal femur samples were performed after dissection and removal of the soft tissues on a Hologic Discovery A scanner (Discovery QDR, Hologic Inc., USA). During the scan, the samples were immersed in 14 cm-deep saline solution in order to simulate soft tissue attenuation. The areal BMD of the femoral neck ($aBMD_{neck}$) was measured from the projection of the bone on the coronal plane.

3.2.3 HR-pQCT

The 38 proximal femora were thawed, fixed in a custom-made plastic chamber [27], submerged in 1% PBS, degassed, and scanned using an XtremeCT II scanner (Scanco Medical AG, Brüttisellen, Switzerland). X-ray tube voltage and current were set to 68 kVp and 1470 µA, respectively. Images were acquired using an integration time of 200 ms and by taking 3000 projections over 180°. The reconstruction led to stacks of 4608 × 4608 images with an isotropic voxel size of 30.3 µm. For the conversion of voxel integers to BMD, the scanner built-in calibration rule was used.

3.2.4 Finite element based mechanical testing

Non-linear homogenized voxel FE models of the proximal femur were developed from the 38 HR-pQCT datasets following an already described procedure [26]. Briefly, the HR-pQCT volume was first coarsened with a factor 10, yielding an isotropic voxel size of 0.303 mm. Voxels of residual air bubbles were set to the gray value of water as obtained from the intensity histogram of the entire scan. Volumes were further coarsened to an isotropic voxel size of 2.7 mm (Fig. 19A), and gray values converted first to vBMD and then to bone volume fraction. For this, a linear calibration rule was derived for the specific set of samples using 3D registered scanning acoustic microscopy (SAM) and HR-pQCT images of the proximal femur shafts [28]. An elastic-yield constitutive law based on the local bone volume fraction was adapted, as described in [26]. This implements a piecewise Hill criterion with different yield stresses for compression and tension [29]. Asymmetric material (elastic and yield) constants for the model

were taken from an experimental study on trabecular bone samples and extrapolated for cortical bone by use of a monotonic scaling function as described elsewhere [26,30]. The failure of each bone was simulated during one-legged standing (STANCE: 20° inclination in the frontal plane; S1 Fig A) as well as during a sideways fall (FALL: 0° internal rotation, 30° adduction angle; S1 Fig B).The models were prepared using medtool 4.1 (Dr. Pahr Ingenieurs e.U, Pfaffstätten, Austria) and solved in Abaqus 6.12 (Simulia, Dassault Systemes, Velizy, France). Stiffness (hvFE_S) and strength (hvFE_Fu) of each proximal femur were calculated for both loading conditions. The proximal femora from 10 out of 19 donors were selected for biomechanical failure tests (S1 Fig). Experiments were performed according to an established protocol [26], and provided validation for the results (hvFE_S and hvFE_Fu) of the FE simulations (S1 Section and S1 Fig).

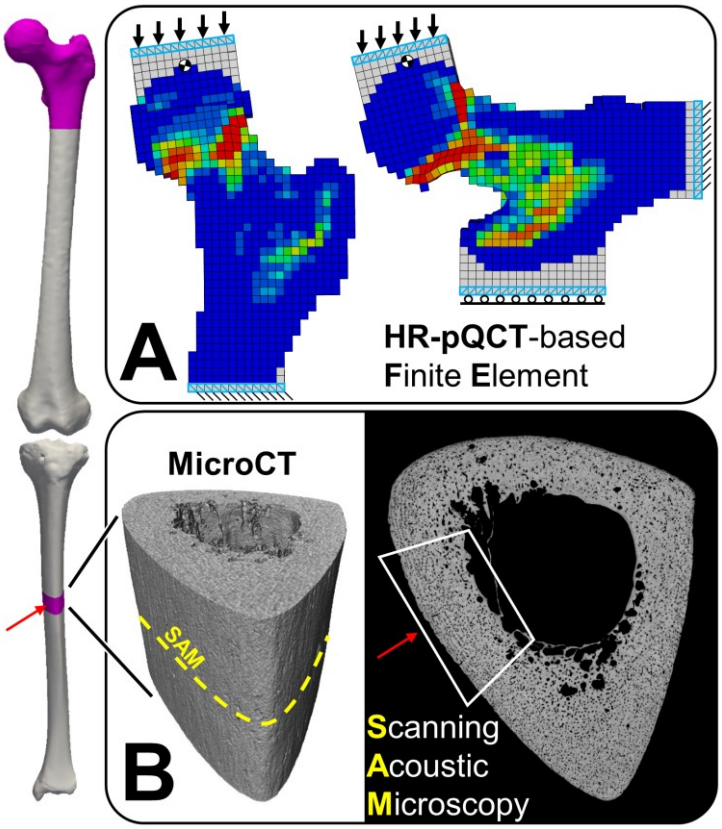

Fig. 19. Summary of materials and methods.

(A) HR-pQCT-based finite element models were developed to compute (left and right) hip stiffness and strength under loading conditions representative of one-legged stance and of a sideways fall.

(B) MicroCT and SAM images from a cross-section of the left tibia midshaft (19.5 ± 3.8 cm away from the knee) of the same donors are used to characterize density and architecture of cortical bone. Microstructural measurements are obtained from a region of the bone that can be reached in vivo by diagnostic ultrasound (red arrow).

3.2.5 Micro CT

The midshaft portion of each left tibia was cut and positioned in the field of view of a small animal microCT system (VivaCT 80; Scanco Medical, Brüttisellen, Switzerland). A custom thermo-isolated plastic cylinder filled with dry ice was used to keep the sample frozen while scanning and the shaft axis was aligned with the rotation axis of the cylinder holder. X-ray tube voltage and current were set to 70 kV and 114 µA, respectively. 500 projections were taken over 360° of rotation and with an exposure time of 200 ms. The field of view had a length of 70 mm and was reconstructed as a stack of 1024 × 1024 voxels images with an isotropic voxel size of 39 µm. The volume data was filtered with a Gaussian smoothing kernel (σ = 1.1 voxels, radius = 2.0 voxels) and Hounsfield units were converted to vBMD based on the calibration procedure provided by the manufacturer.

3.2.6 Scanning acoustic microscopy

Transversal cross sections (21 mm in height) were extracted using a precision band saw (EXACT GmbH, Remscheid, Germany) from the region of the tibia shaft imaged with microCT and at a distance of 19.5 ± 3.8 cm from the proximal end of the bone. After washing, the proximal surface of each cross section was ground and polished on a planar grinder (Phoenix 4000, Buehler Ltd., Illinois) at a constant speed of 50 rpm and with decreasing grain size (ISO/FEPA grit: P80, P600, P1200, P2500 and P4000, Buehler Ltd., Illinois). After polishing, the samples were washed again, submerged in 1% PBS and degassed inside a desiccator for at least 30 min to remove air bubbles from the cortical pores. The scans were performed in 1% degassed PBS solution at a controlled temperature of 25°C, using a custom acoustic microscope described elsewhere [31,32]. The transducer (KSI 100/60°, KSI, Herborn, Germany) had a central frequency of 100 MHz, a −6 dB depth of focus of 139 µm and a diameter of the focused ultrasound beam of 19.8 µm in the focal plane [32]. Signals were processed to obtain calibrated acoustic impedance maps with a pixel size of 12 µm [32] (Fig. 19B and Fig. 20).

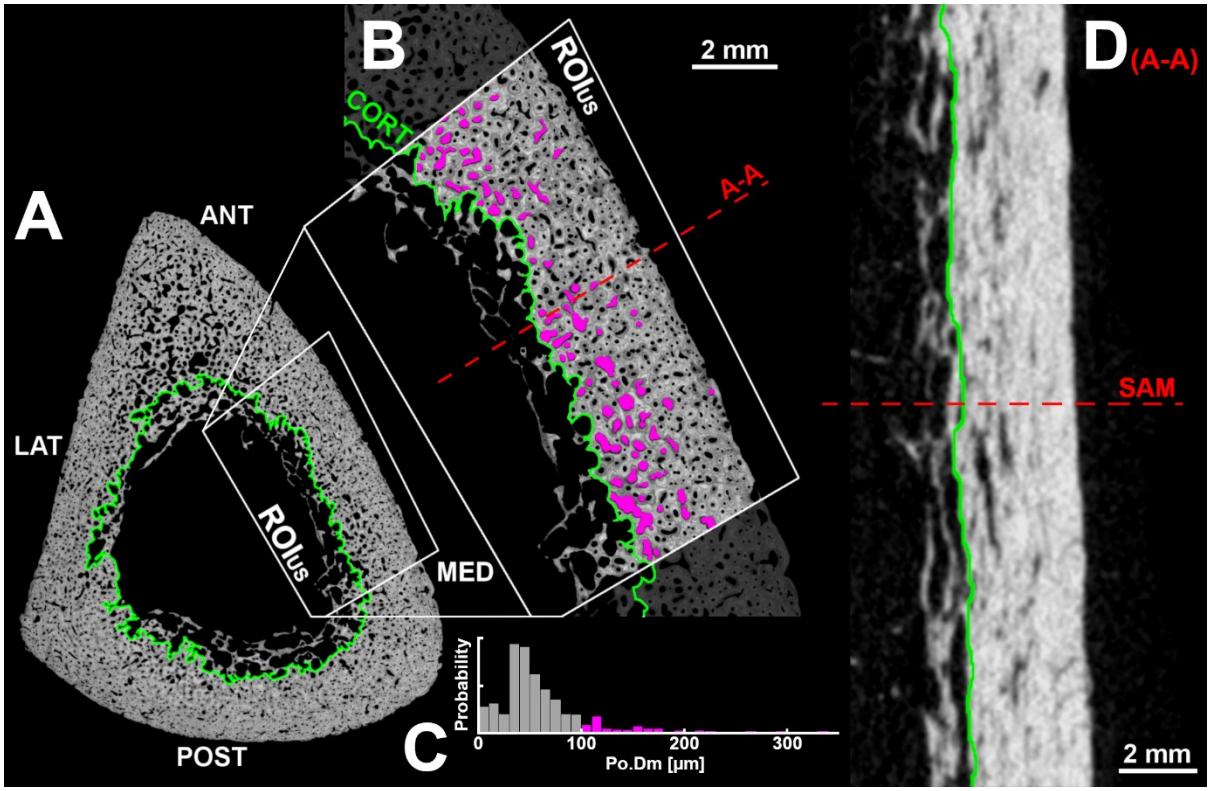

Fig. 20. SAM and microCT image processing. (A) SAM cross section with endosteal boundary marked in green. (B) Anteromedial detail of A, with ROIUS highlighted: this region can be reached in vivo by ultrasound waves. A total number of 11,932 cortical bone pores were analyzed from the ROI_{US} of all samples. Cortical bone pores with diameter (Po.Dm) > 100 µm are colored in magenta. (C) Pore size distribution within the ROI_{US} of B: the tail (Po.Dm > 100 µm) of the histogram represents 53% of the total cortical bone porosity. (D) 20-mm longitudinal microCT section centered through the ROI_{US}.

3.2.7 Image processing

3.2.7.1 MicroCT

A 20 mm-thick portion of the microCT volume centered on the SAM image plane was processed. Voxels belonging to the bone tissue were segmented using Otsu's method [33]. 3D masks of the cortical bone compartment were computed with the algorithm described by

Burghardt et al. [34] For this, the threshold radius for filling of large pores had to be increased to 2.0 mm for the two samples with highest porosity. A binary image of the whole tibia bone was obtained by tracing the external boundary of the cortical bone mask automatically.

3.2.7.2 SAM

An adaptive threshold was applied to separate the bone tissue from the background of the SAM images [35]. Afterwards, the bone tissue mask was cleaned by first removing unconnected objects with area below 0.144 mm², and subsequent filling of all single-pixel pores. The endosteal boundary was drawn manually, following a set of rules described elsewhere [36] (Fig. 20A and B). The periosteal contour was automatically traced on a morphologically closed version of the bone tissue mask (radius of the structuring element = 0.48 mm). Cortical bone porosity (Ct.Po) and the diameter of single Haversian Canals (Po.Dm) were measured on a binary mask of the pores. To investigate the relative contribution of large to giant [37,38] cortical pores on the total pore number and on cortical bone porosity, Po.Dm thresholds of 60, 100, 160, 300 and 385 µm were used (Fig. 20C). The cortical bone microstructure was characterized on SAM images from the anteromedial region of the shaft (ROI_{US}; Fig. 2 and Fig. 20), since this area represents the target of in vivo measurements with ultrasound. The SAM image processing pipeline is available online at: https://doi.org/10.5281/zenodo.2605365 and can be reproduced by downloading the original SAM images from: https://doi.org/10.5281/zenodo.2605350. Table 13 presents abbreviations and a description of all parameters measured from microCT and SAM images.

Table 13. Details of the donors.

	Name	Unit	Description
microCT			
$vBMD_{tot}$ $vBMD_{cort}$	Bone mineral density	[mgHA/cm³]	Of the entire bone Of the cortical bone
SAM			
Tt.Ar	Total area	[mm²]	Area occupied by the bone cross section
Ct.Ar	Cortical area	[mm²]	Area of cortical bone
T.Ar	Tissue area	[mm²]	Area of the bone tissue
Ct.Wba	Areal portion of cortical tissue	[%]	Cortical tissue area / Tt.Ar
Ct.Th	Cortical thickness	[mm]	Most frequent minimum distance between peri- and endosteal surfaces
Ct.Po	Cortical porosity	[%]	100 × (1 – tissue pixels / cortical bone pixels)
Po.D	Pore density	[#/mm²]	Number of pores per square mm
$relPo.n_{60\mu m}$	Prevalence of large pores	[%]	Number of pores with diameter larger than a fixed threshold divided by total number of pores
Po.Dm	Pore diameter	[µm]	Diameter of the largest inscribed circle [20]
$Po.Dm_{10\%}$	Po.Dm quantiles	[µm]	Quantiles of the Po.Dm distribution
$relCt.Po_{60\mu m}$	Relative proportion of porosity	[%]	Proportion of porosity due to pores with diameter above fixed threshold

3.2.8 Statistical analysis

Distributions of single variables were tested for normality using Shapiro-Wilk tests. A paired *t*-test was used to compare left and right $aBMD_{neck}$ from DXA as well as hvFE_S and hvFE_Fu. Associations between $aBMD_{neck}$ or tibial cortical bone and hvFE_S and hvFE_Fu were investigated by linear regression analysis (Pearson's r). Linear regressions were investigated between left tibia properties and separately (i) left and (ii) averaged left and right femoral hvFE_S and hvFE_Fu. Linear partial correlation was used to measure the association between tibial cortical bone and hip stiffness and strength after controlling for $aBMD_{neck}$. The adjusted R^2 of multivariate linear models of hvFE_S and hvFE_Fu was characterized when adding one microstructural covariate to $aBMD_{neck}$. All image and statistical analyses were performed in

Matlab (R2018a, The Mathworks Inc., Natick, MA, USA). Results were considered statistically significant for $p < 0.05$.

3.3 Results

3.3.1 Proximal femur densitometry and mechanics

Proximal femur aBMDneck and mechanical properties (hvFE_S and hvFE_Fu) are summarized in Table 14. The distribution of the differences between left and right $aBMD_{neck}$ values had a mean that did not significantly differ from zero. The same was the case between left and right hvFE_S and hvFE_Fu in STANCE. For FALL simulations, left and right femora showed modest but significant differences in hvFE_S and hvFE_Fu. The results of STANCE FE simulations were in very good agreement with values from biomechanical tests ($R^2 = 0.95$, $p < 0.0001$ and $R^2 = 0.89$, $p < 0.0001$ for hvFE_S and hvFE_Fu, respectively; S1 Fig C and D). FALL simulations showed good agreement with experimental strength ($R^2 = 0.86$, $p < 0.0001$; S1 Fig F) and moderate agreement with experimental stiffness ($R^2 = 0.68$, $p = 0.003$; S1 Fig E).

Table 14. Results from DXA and FE simulations.

	Whole sample (*N* = 38)	left (*N* = 19)	right (*N* = 19)
DXA			
$aBMD_{neck}$ [mgHA/cm²]	532 ± 102 (380−760)	529 ± 96 (404−760)	534 ± 110 (380−755)
FE simulations			
STANCE			
hvFE_S [N/mm]	3394 ± 1400 (1310−6889)	3210 ± 1343 (1310−6664)	3578 ± 1468 (1536−6889)
hvFE_Fu [N]	2582 ± 927 (1243−4926)	2605 ± 903 (1367−4926)	2558 ± 974 (1243−4860)
FALL			
hvFE_S [N/mm]	1221 ± 370 (616−2071)	1314 ± 376 (817−2071)	1127 ± 348 (616−1946)
hvFE_Fu [N]	1372 ± 449 (655−2691)	1456 ± 460 (851−2691)	1289 ± 434 (655−2405)

hvFE_S, homogenized voxel finite element proximal femur stiffness; hvFE_Fu, homogenized voxel finite element proximal femur ultimate force; STANCE, physiological one-legged standing; FALL, sideways fall.

3.3.2 Structure and density of the tibia midshaft

Volumetric BMD and structural properties of the cortical bone of the tibia are summarized in Table 15, together with inter-sample coefficients of variation and correlations with aBMDneck, hvFE_S and hvFE_Fu from the same leg. 95% Confidence Intervals (CIs) of the Pearson r's of Table 15 are collected in S3 Table.

Between the 19 investigated tibiae, cortical bone exhibited large variability in Ct.Th (CV = 40%) and Ct.Po (CV = 32%), modest variations in pore density (Po.D; CV = 11%), and almost invariant vBMD values (CV = 6%). Remarkably, pore density was not associated with Ct.Po (Fig. 21A). On the contrary, the density of pores with a diameter larger than 100 μm showed higher inter-sample variability (CV = 56%) and was strongly correlated with Ct.Po ($r = 0.92$, $p < 0.001$; Fig. 21B). Ct.Po was also correlated with the average Po.Dm ($r = 0.81$, $p < 0.001$; Fig. 21C). Large pores (diameter > 100 μm) were mainly observed at the endosteal side (Fig. 20B) and despite representing only the 7.6% of all the evaluated pores, they contributed, on average, to 40% of the total sample Ct.Po.

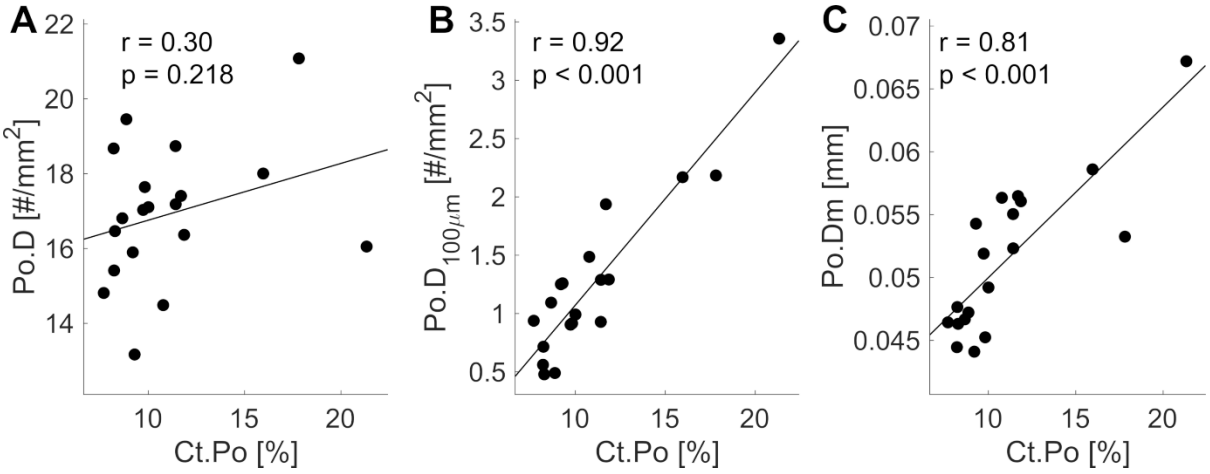

Fig. 21. Cortical bone microstructure of the anteromedial tibia in association with Ct.Po. Ct.Po is independent from the density of canals (A). Its increase is largely explained by an increase of the density of large pores (B) or of the mean pore diameter (C).

3.3.3 Correlation of tibial cortical bone and $aBMD_{neck}$ with femoral stiffness and strength of the same leg

As expected, $aBMD_{neck}$ was associated with both proximal femur hvFE_S ($r = 0.62$ and 0.66 for STANCE and FALL, respectively; both $p < 0.01$) and hvFE_Fu ($r = 0.74$ and 0.78 for STANCE and FALL, respectively; $p < 0.001$, Fig. 22A).

Descriptors of the tibial cross-sectional geometry and total vBMD were only moderately correlated to $aBMD_{neck}$ ($0.46 \leq r \leq 0.51$, $p < 0.05$; Table 15). The correlation between $aBMD_{neck}$ and Ct.Th was strong ($r = 0.75$, $p < 0.001$). No association was found between $aBMD_{neck}$ and the pore microstructure in the tibia.

The mineral density of the tibia was associated with hip stiffness ($r = 0.69$, $p < 0.01$ and $r = 0.72$, $p < 0.001$ for $vBMD_{tot}$ and $vBMD_{cort}$, respectively) and strength ($r = 0.65$ and $r = 0.63$ for $vBMD_{tot}$ and $vBMD_{cort}$, respectively, both $p < 0.01$).

Cortical bone area (Ct.Ar), bone tissue area (T.Ar) and areal portion of cortical bone (Ct.Wba) of the tibia were associated with variations of the hip hvFE_S and hvFE_Fu when measured both in stance and fall conditions (Table 15).

The cortical thickness of the tibia showed strong associations with the stiffness ($r = 0.66$, $p < 0.01$ for STANCE and $r = 0.77$, $p < 0.001$ for FALL) and strength ($r = 0.81$, $p < 0.001$ for both STANCE and FALL; Fig. 22B). Ct.Po did not show significant correlations with the mechanical properties of the hip (Fig. 22C).

There was a clear negative association between parameters describing the density and prevalence of large pores (diameter > 100 µm) with variations of hvFE_S and hvFE_Fu in STANCE (Table 15). The relative contribution of large pores to Ct.Po ($relCt.Po_{100µm}$) was associated with the hip mechanics in both STANCE ($r = -0.61$ and $r = -0.63$ for hvFE_S and hvFE_Fu, respectively; both $p < 0.01$) and FALL ($r = -0.46$ and $r = -0.48$ for hvFE_S and hvFE_Fu, respectively; both $p < 0.05$) loads (regressions with hvFE_Fu are plotted in Fig. 22D). Except for relCt.Po, parameters of the pore microstructure did not show significant associations for FALL loads. Po.Dm thresholds are reported only until 160 µm since larger thresholds did not provide significant associations (data not shown).

Table 15. Hip DXA, macroscopic geometry and vBMD of the tibia midshaft, architecture and composition of tibial cortical bone.

								control for $aBMD_{neck}$			
				STANCE		FALL		STANCE		FALL	
			$aBMD_{neck}$	hvFE_S	hvFE_Fu	hvFE_S	hvFE_Fu	hvFE_S	hvFE_Fu	hvFE_S	hvFE_Fu
	Mean ± SD (min−max)	CV [%]	Pearson r								
Left hip (*N* = 19)											
DXA											
$aBMD_{neck}$ [mgHA /cm²]	529 ± 96 (404−760)	18	/	0.62*	0.74**	0,66*	0,78**	/	/	/	/
Left tibia (*N* = 19)											
MicroCT (whole cross section)											
$vBMD_{tot}$ [mgHA/cm³]	617 ± 133 (261−776)	22	0.46	0.69*	0.65*			0.58	0.52		
$vBMD_{cort}$ [mgHA /cm³]	914 ± 54 (801−988)	6		0.72**	0.63*			0.65*	0.53		
$SD(vBMD_{cort})$ [mgHA /cm³]	185 ± 36 (131−266)	19		−0.66*	−0.59*			−0.62*	−0.54		
SAM (whole cross section)											
Tt.Ar [mm²]	441 ± 110 (326−829)	26									
Ct.Ar [mm²]	238 ± 65 (77−349)	25	0.51	0.59*	0.71**	0,58	0,60*		0.58		
T.Ar [mm²]	235 ± 59 (96−333)	22	0.47	0.52	0.67*	0,57	0,60*		0.55		
Ct.Wba [%]	49.1 ± 14.5 (15.6−69.8)	27	0.51	0.76**	0.73**		0,48	0.65*	0.61*		
SAM (ROI_{US})											
Ct.Th [mm]	2.98 ± 1.19 (0.82−5.35)	40	0.75**	0.66*	0.81**	0,77**	0,81**		0.57	0.56	0.54
Ct.Po [%]	11.1 ± 3.6 (7.7−21.4)	32									
Po.D [1/mm²]	16.9 ± 1.8 (13.2−21.1)	11									
$Po.D_{60\mu m}$ [1/mm²]	4.5 ± 1.1 (2.8−6.2)	25									
$Po.D_{100\mu m}$ [1/mm²]	1.3 ± 0.7 (0.5−3.4)	56		−0.54	−0.56				−0.52		
$Po.D_{160\mu m}$ [1/mm²]	0.3 ± 0.3 (0.1−1.4)	94		−0.52	−0.52			−0.49	−0.54		
$relPo.n_{60\mu m}$ [%]	27.9 ± 6.7 (18.0−38.4)	24									
$relPo.n_{100\mu m}$ [%]	7.6 ± 4.3 (2.5−20.9)	56		−0.53	−0.57			−0.47	−0.56		
$relPo.n_{160\mu m}$ [%]	1.9 ± 1.8 (0.4−8.5)	96		−0.51	−0.52			−0.49	−0.56		
Po.Dm [µm]	51 ± 6 (44−67)	12			−0.47			ns	ns		
SD(Po.Dm) [µm]	34 ± 7 (23−55)	21		−0.55	−0.57			−0.52	−0.60*		
$Po.Dm_{10\%}$ [µm]	19 ± 4 (12−25)	20									
$Po.Dm_{90\%}$ [µm]	91 ± 19 (68−152)	21		−0.49	−0.54				−0.51		
$Ct.Po_{60\mu m}$ [%]	7.9 ± 3.6 (4.5−18.9)	46		−0.46	−0.50				−0.48		
$Ct.Po_{100\mu m}$ [%]	4.8 ± 3.5 (1.5−16.4)	73		−0.50	−0.52				−0.51		
$Ct.Po_{160\mu m}$ [%]	2.4 ± 2.6 (0.4−11.4)	107			−0.47				−0.50		
$relCt.Po_{60\mu m}$ [%]	68.9 ± 8.6 (54.8−88.3)	13		−0.51	−0.60*	−0,49	−0,50		−0.60*		
$relCt.Po_{100\mu m}$ [%]	40.1 ± 13.9 (17.3−77.0)	35		−0.61*	−0.63*	−0,46	−0,48	−0.54	−0.62*		
$relCt.Po_{160\mu m}$ [%]	18.9 ± 12.1 (5.1−53.6)	64		−0.50	−0.53				−0.54		

The last nine columns show the Pearson coefficients of the linear correlation with aBMDneck, hvFE_S and hvFE_Fu and the Pearson r of the linear partial correlation analysis controlling for the effect of $aBMD_{neck}$, for both STANCE and FALL loading conditions. Coefficients are reported only for p-values < 0.05. The 95% Confidence Intervals for the correlation coefficients of this table can be found in S3 Table. * $p < 0.01$; ** $p < 0.001$.

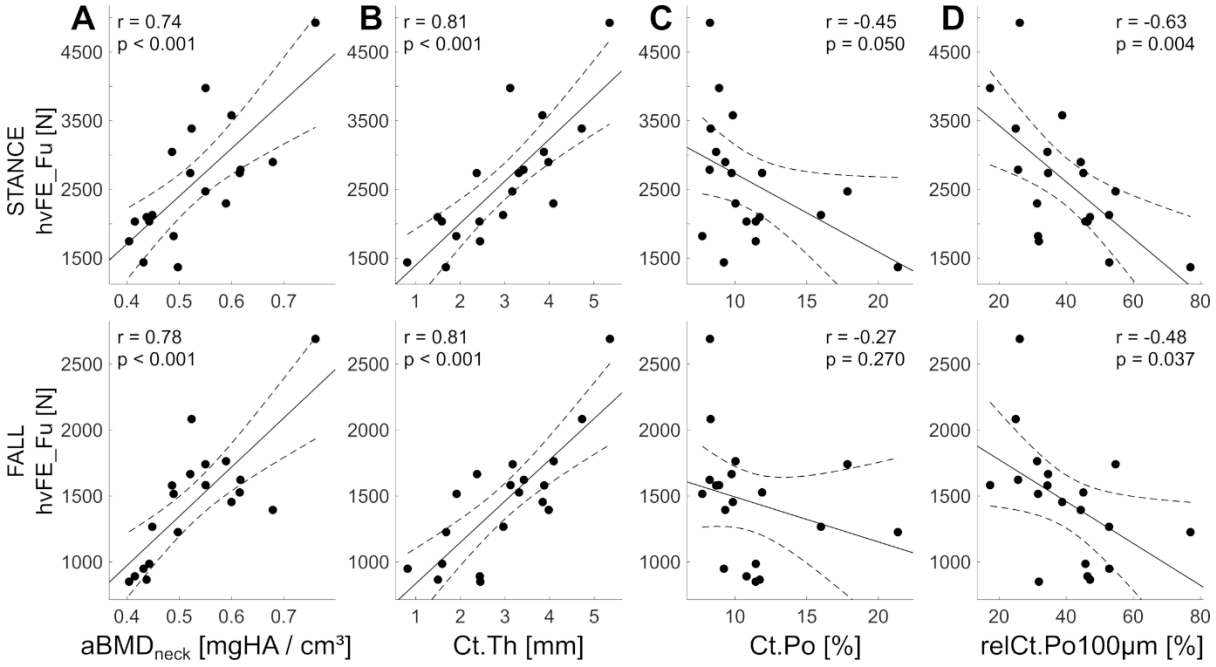

Fig. 22. Associations with proximal femur mechanical competence. Linear regression between DXA aBMD at the femoral neck (A) as well as whole tibia cortical thickness (B), intracortical porosity (C) and relative porosity due to large pores (diameter > 100 µm) in the anteromedial tibia (D) with the FE-based femoral strength under standing and sideways falling loads.

3.3.4 Multivariate models of proximal femur stiffness and strength

After controlling for $aBMD_{neck}$, the degree of association between tibia measurements and the mechanical properties of the proximal femur was generally reduced (last four columns of Table 15). Parameters of the pore morphology maintained a similar degree of association with hvFE_Fu in STANCE even after controlling for the effect of $aBMD_{neck}$.

Linear combinations of $aBMD_{neck}$ and $relCt.Po_{100µm}$ had adjusted R^2 values that were 17% and 16% larger than those of models of $aBMD_{neck}$ alone, for hvFE_S and hvFE_Fu, respectively, but this pattern was limited to standing loads (Table 16). The combination of $aBMD_{neck}$ and Ct.Th did not improve the correlation with hvFE_S and hvFE_Fu, if compared to Ct.Th alone.

Table 16. Multivariate regression models of proximal femur stiffness and strength.

	STANCE						FALL					
	hvFE_S			hvFE_Fu			hvFE_S			hvFE_Fu		
***N* = 19**	**beta**	**p-val**	**R^2**	**beta**	**p-val**	**R^2**	**beta**	**p-val**	**R^2**	**beta**	**p-val**	**R^2**
y = a × **Ct.Th** + b	0.88	2e−3	0.40	0.73	3e−5	0.63	0.29	1e−4	0.57	0.37	3e−5	0.63
y = a × **$aBMD_{neck}$** + b	0.83	5e−3	0.34	0.67	3e−4	0.52	0.25	2e−3	0.41	0.36	9e−5	0.58
y = a × **$aBMD_{neck}$** + …	0.63	0.01	0.51	0.54	6e−4	0.68						
… b × **$relCt.Po_{100µm}$** + c	−0.61	0.02		−0.40	6e−3							

Standardized coefficients (beta), p-values and adjusted R^2 are reported only for multivariate models that showed a significant increase of stiffness or ultimate force prediction if compared to single parameter ones.

3.4 Discussion

In this work, we asked whether the cortical bone of the tibia can reflect changes in the stiffness and fracture resistance of the hip.

3.4.1 vBMD, thickness and presence of large pores in tibial cortical bone are associated with hip stiffness and strength

We found significant associations between the vBMD and structure of the tibia midshaft with the stiffness and ultimate force of the proximal femur as predicted by non-linear, homogenized finite element analysis. The cortical thickness of the tibia showed strong associations with the proximal femur strength, with correlation coefficients comparable to those obtained with a DXA scan.

The heterogeneity and the tail of the Po.Dm distribution were negatively associated with proximal femur stiffness and strength when these were measured by STANCE simulations, pointing out the important role of large cortical pores under physiological loading conditions. Interestingly, the associations between tibial Ct.Po and proximal femur mechanics were significant only when Ct.Po was calculated from the 7.6% of pores with larger diameter, and the same trend was observed for pore density. In a recent report, Ct.Po from the same (anteromedial) region of the tibia diaphysis measured here was associated ($r = -0.50$) with the proximal femur strength by mechanical tests in standing conditions [24]. Even if the correlation was not significant in our study ($p = 0.05$ for tibial Ct.Po and hvFE_S, with n=19, whereas n=28 in Abraham et al.), both works report high variability for the hip strength of legs with low tibial Ct.Po (see the left half (Ct.Po < 15%) of the plots of Fig. 22C). Our data suggest that cases with impaired hip strength could be further distinguished by analyzing the contribution of abnormally large pores on the total Ct.Po of the tibia. This finding is not in contrast with in vivo reports on the association between fracture risk and Ct.Po as measured by HR-pQCT, since the imaging of cortical pores with HR-pQCT is in a way "tuned" towards the detection of large cavities due to the resolution limit of the scanner (i.e. 130 µm and 95 µm for 1st and 2nd generation HR-pQCT, respectively). HR-pQCT can estimate Ct.Po beyond its nominal resolution by using BMD-based approaches [28], meaning that a measurement of relCt.Po is readily available in vivo from HR-pQCT images. Therefore, future HR-pQCT studies should investigate the relation between fracture risk and the prevalence of large pores in the cortical bone of the distal skeleton.

The occurrence of large pores weakens the mechanical resistance of cortical bone. Osteonal diameter has been shown to be negatively associated with cortical bone toughness [39,40], whereas large endosteal pores can increase the strain energy density in the surrounding bone tissue during a compression of the fibula [41]. Local clustering of large and progressively opening cavities have been suggested as a possible causes of regional instability of the femur neck [21,37]. Besides this, the prevalence of pores with abnormal size is a fingerprint of age-induced alterations of bone remodeling, in which Haversian canals drift towards coalescing and partially non-refilled resorption units [19,20]. Our results suggest that the observation of such morphological changes of cortical pores in the tibia of living humans might reveal an impairment of the proximal femur mechanical competence.

3.4.2 Pore size reflects proximal femur strength independently of DXA

Macroscopic changes of vBMD, cortical bone area and thickness at the tibia midshaft had associations with proximal femur mechanics that could in large part be accounted for by a measurement of $aBMD_{neck}$. On the contrary, changes of the pore microstructure were

independent of $aBMD_{neck}$, and adding this information substantially improved the prediction of femur strength obtained by DXA. This suggests that hip strength information provided by measurements of the tibial geometry and vBMD is largely redundant, if acquired in addition to a DXA scan. In contrast, measurements of the pore microarchitecture at the tibia might convey hip strength information which is not captured by aBMD. It should be noted, however, that our results allow this conclusion exclusively for hip strength during one-legged standing, a configuration representing only minor fracture risk [42].

3.4.3 The anteromedial tibia is a favorable site for assessment of the pore microstructure

In a recent report, the hip failure load has been reported to be associated with low vBMD and microstructural alterations of the distal tibia, as assessed (ex vivo) using an HR-pQCT protocol for in vivo scans [23]. In comparison, our results showed significant associations between tibial vBMD and the ultimate force of the proximal femur only for physiological standing loads. Possible reasons for this discrepancy are the different scan regions and the different spatial resolutions. Kroker et al. measured the total vBMD at the distal portion of the tibia, supposedly capturing information from both trabecular and cortical bone density. On the contrary, the midshaft region scanned in our study contains predominantly cortical bone. For comparison, $vBMD_{tot}$ ranges were 261−776 mgHA/cm³ and 52−332 mgHA/cm³ in our and Kroker's study, respectively, confirming the different type of bone tissue considered for the two vBMD measurements. Towards the epiphyses of the tibia, cortical bone becomes thinner and is increasingly replaced by a trabecular core, rising concerns about the precision error of cortical bone structural and density measurements performed at distal and ultradistal sites with HR-pQCT [43,44]. Due to the different measurement site (midshaft, here, instead of distal shaft) we observed a cortical thickness of the tibia that was 2 to 3 times larger than values reported from HR-pQCT studies [15,18,45–47]. In this sense, the tibia midshaft provided a much larger and homogeneous volume of interest for cortical bone microstructural characterization than the distal shaft. Ultrasound waves represent an ionizing radiation free alternative for cortical bone characterization and can non-invasively be transmitted to and along bone at the facies medialis of the tibia midshaft, where the periosteum is covered by a thin layer of soft tissue. At this location, novel quantitative ultrasound techniques can measure thickness, speed of sound and porosity of cortical bone in vivo [25,48,49]. Our findings indicate the relevance of microstructural measurements performed at the facies medialis of the tibia for the prediction of the proximal femur strength. To confirm the advantage of this specific ROI, we repeated all microstructural measurements considering the entire tibia cross section (S1 Table). The degree of association with the hip stiffness and strength was not changed and the same microstructural features (Ct.Th and prevalence of large pores) remained relevant.

Finally, we addressed the clinical scenario in which a subject's hip strength is predicted based on a measurement performed on a single leg by performing regression analyses between properties of the left tibia and the average hvFE_S and hvFE_Fu of left and right femora (S2 Table). This confirmed the relevance of all parameters identified by the left tibia - left hip regressions (i.e. tibia geometry and Ct.Th for both STANCE and FALL loads; tibia vBMD and large pores for STANCE loads). The geometry and Ct.Th of the tibia, however, were less affected by the anatomical side of the correlation, whereas the Pearson r of correlations between pore microstructure and hvFE_S and hvFE_Fu was reduced, on average, by 11.3% and 11.9%, respectively.

3.4.4 Study limitations

The current study presents several limitations. The characterization of the cortical bone microarchitecture was performed on 2D SAM images with a resolution of about 20 µm. Despite this, Ct.Po and Po.Dm values were in very good agreement with 3D gold-standard synchrotron-CT measurements conducted at the diaphysis of the tibia and femur [38,46,50]. Compared to SAM, microCT overestimated Ct.Ar ($p < 0.01$), T.Ar ($p < 0.001$), Ct.Wba ($p < 0.001$) and Ct.Th ($p = 0.04$) (S4 Table). The 3D Ct.Th obtained with microCT from a 20 mm-thick shaft section was 6.7 % to 11.5 % larger than Ct.Th assessed from single 2D cross-sectional SAM images, likely due to the different ways in which the separation between trabecular and cortical bone compartments is obtained for SAM and microCT. Despite this, macroscopic structural properties and Ct.Th obtained from microCT and SAM were in very good agreement ($R^2 = 0.89$ to 0.99; S4 Table).

Considering the ROI for density and microstructural assessments in the tibia, it was not possible to standardize its location along the axis of the diaphysis: the tibiae were measured at a distance from their proximal end that varied between 12.2 cm to 27.2 cm, representing a possible source of error. This was necessary because a portion (between 25% and 60%) of the tibia had been removed during dissection. Despite this kind of variability, our data showed significant relationships with the mechanics of the proximal femur, suggesting that measurements of the tibia remain valuable even under such conditions. In vivo, protocols for the consistent positioning of the measurement ROI should be followed, as is done in pQCT and HR-pQCT procedures [43].

This work used quasi-static homogenized voxel FE models to simulate the mechanical stiffness and strength of 38 human proximal femora. We dedicated a subset of 20 samples to biomechanical testing and replicated the FE validation published in 2013 by Dall'Ara et al., obtaining FE accuracy for strength and for standing stiffness comparable to values from the literature [26,51,52], whereas the lower accuracy for stiffness in FALL could be explained by the poor contact between bone and embedding during the initial loading phase (S1 Section). The displacement rate applied in our experiment was constant and several orders of magnitude smaller than what is expected at the proximal femur or measured at the pelvis during a sideways fall [53,54]. In a recent comparison between fall and fixed displacement rate experiments, Gilchrist et al. reported significant differences between the ultimate force for the two test modalities [55]. Their findings, however, had low statistical power, were dependent on the displacement rate itself and were relevant only for the ultimate force, but not for the proximal femur stiffness. For our purposes, the choice of quasi-static loading was taken in the light of the comparison between biomechanical tests and an already validated FE procedure [26]. Homogenized non-linear quasi-static FE simulations provide accurate predictions of the proximal femur ultimate force, stiffness, fracture energy and location obtained by quasi-static as well as dynamic sideways fall experiments [26,56], supporting the validity of our findings also for higher strain rates.

It should be noted, finally, that microstructural measurements at the tibia of human donors were performed by means of SAM and microCT: two modalities that cannot be used for the examination of tibia properties in living subjects. However, the tibia midshaft can be imaged in vivo both, by 2nd generation HR-pQCT and by US. The ability of these techniques to provide microstructural predictors of hip strength will require further confirmation.

3.5 Conclusion

Recent evidence on intracortical bone remodeling have shown that an age-induced delay in osteoprogenitor recruitment following pore resorption leads to a progressive enlargement and accumulation of cavities in cortical bone [20]. In this ex vivo study, the contribution to cortical porosity of canals with a diameter larger than 100 μm in the tibia of human donors was associated with reduced strength and stiffness of the proximal femur. The cortical bone of the tibia represents a key diagnostic opportunity for the prediction of the bone fracture risk since it is load bearing and can be measured in vivo by HR-pQCT and ultrasound. Our results indicate that cortical bone thickness and the prevalence of large voids in tibial cortical bone should be taken into account as biomarkers of a mechanical impairment of the hip, alternatively or in addition to standard DXA metrics.

Supporting information

S1 Section. FE model validation.

https://doi.org/10.1371/journal.pone.0215405.s001

S1 Fig. Mechanical test setup and FE model validation.

(A) Mechanical test setup for STANCE, showing a detail of the 20° inclination in the frontal plane. (B) FALL mechanical tests (0° internal rotation, 30° adduction angle). The load direction is contained in the plane defined by the femoral neck and shaft axes. (C) Association between finite element predictions and biomechanical measurements of proximal femur stiffness ($R^2 = 0.95$, $p < 0.0001$) and (D) strength ($R^2 = 0.89$, $p < 0.0001$) for STANCE. (E) Association between finite element predictions and biomechanical measurements of proximal femur stiffness ($R^2 = 0.68$, $p < 0.001$) and (D) strength ($R^2 = 0.86$, $p < 0.0001$) for FALL.

https://doi.org/10.1371/journal.pone.0215405.s002

S1 Table. Whole tibia microstructure.

Microstructure of the whole cross-section of the tibia midshaft from SAM, together with Pearson coefficients of the linear correlation with $aBMD_{neck}$, hvFE_S and hvFE_Fu.

https://doi.org/10.1371/journal.pone.0215405.s003

S2 Table. Comparison with the subject's hip stiffness and strength.

Correlation coefficients between LEFT tibia properties and hvFE_S and hvFE_Fu calculated as the average between LEFT and RIGHT femora, together with the relative change with respect to the LEFT-LEFT regression.

https://doi.org/10.1371/journal.pone.0215405.s004

S3 Table. Confidence intervals for Table 14.

Confidence intervals of the coefficients of correlation between tibial cortical bone vBMD and architecture with $aBMD_{neck}$ and proximal femur stiffness and strength.

https://doi.org/10.1371/journal.pone.0215405.s005

S4 Table. Geometry and cortical thickness of the tibia midshaft from microCT.

Mean, Standard Deviation, ranges and coefficient of variation (CV) are reported for each variable together with the R2 and the p-value of the comparison (paired *t*-test or Wilcoxon signed rank test when parameters were not normally distributed) with the corresponding SAM measurement. For Cross-sectional areal properties for microCT are calculated dividing the corresponding volumetric measurement by the height (20 mm) of the analyzed stack.

https://doi.org/10.1371/journal.pone.0215405.s006

Acknowledgments

We acknowledge Dr. Robert Wendlandt for the sample collection, Dr. Juan Du, Dr. Alexander Synek and Dr. Emir Benca for the support during data analysis.

Conflicts of interest

GI and KR have the patent "CortBS: Ultrasonic method for determining pore dimensions in cortical bone" pending. JB reports grants and personal fees from Eli Lilly, Amgen and Will Pharma, outside the submitted work. This does not alter our adherence to PLOS ONE policies on sharing data and materials.

Funding

The work of GI, JS, LP, MG, RB, CCG and KR was supported by the Deutsche Forschungsgemeinschaft (DFG Ra1380/9-1; http://www.dfg.de/en/) and by the Agence Nationale de la Recherche (ANR-14-CE35-0030-01; http://www.agence-nationale-recherche.fr/en/) within the TaCo-Sound project. GI and KR disclose funding also by the Bundesministerium für Bildung und Forschung (BMBF, musculoskeletal research network 01EC1408L, subproject “characterization of cortical and subchondral bone”; https://www.bmbf.de/en/) and by the German Academic Exchange Service (DAAD, grant no. 91578351; https://www.daad.de/en/). FH, CW and JB report funding by the Weijerhorst Foundation (grant no. WH2; http://www.deweijerhorst.nl/). All funders had no role in study design, data collection and analysis, decision to publish, or preparation of the manuscript.

References

1. Hernlund E, Svedbom A, Ivergård M, Compston J, Cooper C, Stenmark J, et al. Osteoporosis in the European Union: medical management, epidemiology and economic burden. A report prepared in collaboration with the International Osteoporosis Foundation (IOF) and the European Federation of Pharmaceutical Industry Associations (EFPIA). Arch Osteoporos. 2013;8: 136. doi:10.1007/s11657-013-0136-1
2. Kanis JA, Johnell O, Oden A, Dawson A, De Laet C, Jonsson B. Ten year probabilities of osteoporotic fractures according to BMD and diagnostic thresholds. Osteoporos Int J Establ Result Coop Eur Found Osteoporos Natl Osteoporos Found USA. 2001;12: 989–995. doi:10.1007/s001980170006
3. Leibson CL, Tosteson ANA, Gabriel SE, Ransom JE, Melton LJ. Mortality, Disability, and Nursing Home Use for Persons with and without Hip Fracture: A Population-Based Study. J Am Geriatr Soc. 2002;50: 1644–1650. doi:10.1046/j.1532-5415.2002.50455.x
4. Boonen S, Autier P, Barette M, Vanderschueren D, Lips P, Haentjens P. Functional outcome and quality of life following hip fracture in elderly women: a prospective controlled study. Osteoporos Int. 2004;15: 87–94. doi:10.1007/s00198-003-1515-z
5. Wainwright SA, Marshall LM, Ensrud KE, Cauley JA, Black DM, Hillier TA, et al. Hip Fracture in Women without Osteoporosis. J Clin Endocrinol Metab. 2005;90: 2787–2793. doi:10.1210/jc.2004-1568
6. Choksi P, Jepsen KJ, Clines GA. The challenges of diagnosing osteoporosis and the limitations of currently available tools. Clin Diabetes Endocrinol. 2018;4: 12. doi:10.1186/s40842-018-0062-7
7. Augat P, Schorlemmer S. The role of cortical bone and its microstructure in bone strength. Age Ageing. 2006;35: ii27–ii31. doi:10.1093/ageing/afl081
8. Ammann P, Rizzoli R. Bone strength and its determinants. Osteoporos Int. 2003;14: 13–18. doi:10.1007/s00198-002-1345-4
9. Bala Y, Zebaze R, Ghasem-Zadeh A, Atkinson EJ, Iuliano S, Peterson JM, et al. Cortical Porosity Identifies Women With Osteopenia at Increased Risk for Forearm Fractures. J Bone Miner Res. 2014;29: 1356–1362. doi:10.1002/jbmr.2167
10. Ahmed LA, Shigdel R, Joakimsen RM, Eldevik OP, Eriksen EF, Ghasem-Zadeh A, et al. Measurement of cortical porosity of the proximal femur improves identification of women with nonvertebral fragility fractures. Osteoporos Int. 2015;26: 2137–2146. doi:10.1007/s00198-015-3118-x
11. Bala Y, Zebaze R, Seeman E. Role of cortical bone in bone fragility: Curr Opin Rheumatol. 2015;27: 406–413. doi:10.1097/BOR.0000000000000183
12. Bala Y, Bui QM, Wang X-F, Iuliano S, Wang Q, Ghasem-Zadeh A, et al. Trabecular and Cortical Microstructure and Fragility of the Distal Radius in Women. J Bone Miner Res. 2015;30: 621–629. doi:10.1002/jbmr.2388
13. Shanbhogue VV, Hansen S, Frost M, Jørgensen NR, Hermann AP, Henriksen JE, et al. Bone Geometry, Volumetric Density, Microarchitecture, and Estimated Bone Strength Assessed by HR-pQCT in Adult Patients With Type 1 Diabetes Mellitus. J Bone Miner Res. 2015;30: 2188–2199. doi:10.1002/jbmr.2573
14. Neto GPC, Pereira RMR, Alvarenga JC, Takayama L, Funari MFA, Martin RM. Evaluation of bone mineral density and microarchitectural parameters by DXA and HR-pQCT in 37 children and adults with X-linked hypophosphatemic rickets. Osteoporos Int. 2017;28: 1685–1692. doi:10.1007/s00198-017-3949-8

15. Patsch JM, Burghardt AJ, Yap SP, Baum T, Schwartz AV, Joseph GB, et al. Increased cortical porosity in type 2 diabetic postmenopausal women with fragility fractures. J Bone Miner Res. 2013;28: 313–324. doi:10.1002/jbmr.1763
16. Chevalley T, Bonjour JP, van Rietbergen B, Ferrari S, Rizzoli R. Fracture history of healthy premenopausal women is associated with a reduction of cortical microstructural components at the distal radius. Bone. 2013;55: 377–383. doi:10.1016/j.bone.2013.04.025
17. Sundh D, Mellström D, Nilsson M, Karlsson M, Ohlsson C, Lorentzon M. Increased Cortical Porosity in Older Men With Fracture. J Bone Miner Res. 2015;30: 1692–1700. doi:10.1002/jbmr.2509
18. Unnikrishnan G, Xu C, Popp KL, Hughes JM, Yuan A, Guerriere KI, et al. Regional variation of bone density, microarchitectural parameters, and elastic moduli in the ultradistal tibia of young black and white men and women. Bone. 2018;112: 194–201. doi:10.1016/j.bone.2018.05.004
19. Lassen NE, Andersen TL, Pløen GG, Søe K, Hauge EM, Harving S, et al. Coupling of Bone Resorption and Formation in Real Time: New Knowledge Gained From Human Haversian BMUs. J Bone Miner Res. 2017; n/a-n/a. doi:10.1002/jbmr.3091
20. Andreasen CM, Delaisse J-M, Eerden BC van der, Leeuwen JP van, Ding M, Andersen TL. Understanding Age-Induced Cortical Porosity in Women: The Accumulation and Coalescence of Eroded Cavities Upon Existing Intracortical Canals Is the Main Contributor. J Bone Miner Res. 2017;33: 606–620. doi:10.1002/jbmr.3354
21. Power J, Loveridge N, Kröger H, Parker M, Reeve J. Femoral neck cortical bone in female and male hip fracture cases: Differential contrasts in cortical width and sub-periosteal porosity in 112 cases and controls. Bone. 2018;0. doi:10.1016/j.bone.2018.05.027
22. Augat P, Reeb H, Claes LE. Prediction of fracture load at different skeletal sites by geometric properties of the cortical shell. J Bone Miner Res. 1996;11: 1356–1363. doi:10.1002/jbmr.5650110921
23. Kroker A, Plett R, Nishiyama KK, McErlain DD, Sandino C, Boyd SK. Distal skeletal tibia assessed by HR-pQCT is highly correlated with femoral and lumbar vertebra failure loads. J Biomech. 2017;59: 43–49. doi:10.1016/j.jbiomech.2017.05.011
24. Abraham AC, Agarwalla A, Yadavalli A, McAndrew C, Liu JY, Tang SY. Multiscale Predictors of Femoral Neck In Situ Strength in Aging Women: Contributions of BMD, Cortical Porosity, Reference Point Indentation, and Nonenzymatic Glycation. J Bone Miner Res. 2015;30: 2207–2214. doi:10.1002/jbmr.2568
25. Renaud G, Kruizinga P, Cassereau D, Laugier P. In vivo ultrasound imaging of the bone cortex. Phys Med Biol. 2018;63: 125010. doi:10.1088/1361-6560/aac784
26. Dall'Ara E, Luisier B, Schmidt R, Kainberger F, Zysset P, Pahr D. A nonlinear QCT-based finite element model validation study for the human femur tested in two configurations in vitro. Bone. 2013;52: 27–38. doi:10.1016/j.bone.2012.09.006
27. Dall'Ara E, Varga P, Pahr D, Zysset P. A calibration methodology of QCT BMD for human vertebral body with registered micro-CT images. Med Phys. 2011;38: 2602. doi:10.1118/1.3582946
28. Iori G, Heyer F, Kilappa V, Wyers C, Varga P, Schneider J, et al. BMD-based assessment of local porosity in human femoral cortical bone. Bone. 2018;114: 50–61. doi:10.1016/j.bone.2018.05.028
29. Garcia D, Zysset PK, Charlebois M, Curnier A. A three-dimensional elastic plastic damage constitutive law for bone tissue. Biomech Model Mechanobiol. 2008;8: 149–165. doi:10.1007/s10237-008-0125-2

30. Rincón-Kohli L, Zysset PK. Multi-axial mechanical properties of human trabecular bone. Biomech Model Mechanobiol. 2008;8: 195–208. doi:10.1007/s10237-008-0128-z
31. Lakshmanan S, Bodi A, Raum K. Assessment of Anisotropic Tissue Elasticity of Cortical Bone from High-Resolution, Angular Acoustic Measurements. IEEE Trans Ultrason Ferroelectr Freq Control. 2007;54: 1560–1570. doi:10.1109/TUFFC.2007.426
32. Raum K, Reißhauer J, Brandt J. Frequency and resolution dependence of the anisotropic impedance estimation in cortical bone using time-resolved scanning acoustic microscopy. J Biomed Mater Res A. 2004;71A: 430–438. doi:10.1002/jbm.a.30156
33. Otsu N. A threshold selection method from gray-level histograms. IEEE Trans Syst Man Cybern. 1979;9: 62–66.
34. Burghardt AJ, Buie HR, Laib A, Majumdar S, Boyd SK. Reproducibility of direct quantitative measures of cortical bone microarchitecture of the distal radius and tibia by HR-pQCT. Bone. 2010;47: 519–528. doi:10.1016/j.bone.2010.05.034
35. Wellner PD. Adaptive thresholding for the DigitalDesk. Xerox EPC1993-110. 1993; 1–19.
36. Malo MKH, Rohrbach D, Isaksson H, Töyräs J, Jurvelin JS, Tamminen IS, et al. Longitudinal elastic properties and porosity of cortical bone tissue vary with age in human proximal femur. Bone. 2013;53: 451–458. doi:10.1016/j.bone.2013.01.015
37. Jordan GR, Loveridge N, Bell KL, Power J, Rushton N, Reeve J. Spatial clustering of remodeling osteons in the femoral neck cortex: a cause of weakness in hip fracture? Bone. 2000;26: 305–313. doi:10.1016/S8756-3282(99)00272-0
38. Chappard C, Bensalah S, Olivier C, Gouttenoire PJ, Marchadier A, Benhamou C, et al. 3D characterization of pores in the cortical bone of human femur in the elderly at different locations as determined by synchrotron micro-computed tomography images. Osteoporos Int. 2013;24: 1023–1033. doi:10.1007/s00198-012-2044-4
39. Granke M, Makowski AJ, Uppuganti S, Nyman JS. Prevalent role of porosity and osteonal area over mineralization heterogeneity in the fracture toughness of human cortical bone. J Biomech. 2016;49: 2748–2755. doi:10.1016/j.jbiomech.2016.06.009
40. Yeni YN, Brown CU, Wang Z, Norman TL. The influence of bone morphology on fracture toughness of the human femur and tibia. Bone. 1997;21: 453–459. doi:10.1016/S8756-3282(97)00173-7
41. Bakalova LP, Andreasen CM, Thomsen JS, Brüel A, Hauge E-M, Kiil BJ, et al. Intracortical Bone Mechanics Are Related to Pore Morphology and Remodeling in Human Bone. J Bone Miner Res. 0. doi:10.1002/jbmr.3561
42. Keyak JH, Skinner HB, Fleming JA. Effect of force direction on femoral fracture load for two types of loading conditions. J Orthop Res. 2001;19: 539–544. doi:10.1016/S0736-0266(00)00046-2
43. Engelke K, Stampa B, Timm W, Dardzinski B, Papp AE de, Genant HK, et al. Short-term in vivo precision of BMD and parameters of trabecular architecture at the distal forearm and tibia. Osteoporos Int. 2012;23: 2151–2158. doi:10.1007/s00198-011-1829-1
44. Boyd SK. Site-Specific Variation of Bone Micro-Architecture in the Distal Radius and Tibia. J Clin Densitom. 2008;11: 424–430. doi:10.1016/j.jocd.2007.12.013
45. Vilayphiou N, Boutroy S, Sornay-Rendu E, Rietbergen BV, Chapurlat R. Age-related changes in bone strength from HR-pQCT derived microarchitectural parameters with an emphasis on the role of cortical porosity. Bone. 2016;83: 233–240. doi:10.1016/j.bone.2015.10.012

46. Ostertag A, Peyrin F, Fernandez S, Laredo JD, de Vernejoul MC, Chappard C. Cortical measurements of the tibia from high resolution peripheral quantitative computed tomography images: A comparison with synchrotron radiation micro-computed tomography. Bone. 2014;63: 7–14. doi:10.1016/j.bone.2014.02.009
47. Waard EAC de, Sarodnik C, Pennings A, Jong JJA de, Savelberg HHCM, Geel TA van, et al. Reliability of HR-pQCT Derived Cortical Bone Structural Parameters When Using Uncorrected Instead of Corrected Automatically Generated Endocortical Contours in a Cross-Sectional Study: The Maastricht Study. Calcif Tissue Int. 2018; 1–14. doi:10.1007/s00223-018-0416-2
48. Sievänen H, Cheng S, Ollikainen S, Uusi-Rasi K. Ultrasound Velocity and Cortical Bone Characteristics In Vivo. Osteoporos Int. 2001;12: 399–405. doi:10.1007/s001980170109
49. Schneider J, Ramiandrisoa D, Armbrecht G, Ritter Z, Felsenberg D, Raum K, et al. In Vivo Measurements of Cortical Thickness and Porosity at the Proximal Third of the Tibia Using Guided Waves: Comparison with Site-Matched Peripheral Quantitative Computed Tomography and Distal High-Resolution Peripheral Quantitative Computed Tomography. Ultrasound Med Biol. 2019;0. doi:10.1016/j.ultrasmedbio.2019.01.008
50. Rohrbach D, Lakshmanan S, Peyrin F, Langer M, Gerisch A, Grimal Q, et al. Spatial distribution of tissue level properties in a human femoral cortical bone. J Biomech. 2012;45: 2264–2270. doi:10.1016/j.jbiomech.2012.06.003
51. Schileo E, Balistreri L, Grassi L, Cristofolini L, Taddei F. To what extent can linear finite element models of human femora predict failure under stance and fall loading configurations? J Biomech. 2014;47: 3531–3538. doi:10.1016/j.jbiomech.2014.08.024
52. Keyak JH. Improved prediction of proximal femoral fracture load using nonlinear finite element models. Med Eng Phys. 2001;23: 165–173. doi:10.1016/S1350-4533(01)00045-5
53. Courtney AC, Wachtel EF, Myers ER, Hayes WC. Effects of loading rate on strength of the proximal femur. Calcif Tissue Int. 1994;55: 53–58. doi:10.1007/BF00310169
54. Feldman F, Robinovitch SN. Reducing hip fracture risk during sideways falls: Evidence in young adults of the protective effects of impact to the hands and stepping. J Biomech. 2007;40: 2612–2618. doi:10.1016/j.jbiomech.2007.01.019
55. Gilchrist S, Nishiyama KK, Bakker P de, Guy P, Boyd SK, Oxland T, et al. Proximal femur elastic behaviour is the same in impact and constant displacement rate fall simulation. J Biomech. 2014;47: 3744–3749. doi:10.1016/j.jbiomech.2014.06.040
56. Varga P, Schwiedrzik J, Zysset PK, Fliri-Hofmann L, Widmer D, Gueorguiev B, et al. Nonlinear quasi-static finite element simulations predict in vitro strength of human proximal femora assessed in a dynamic sideways fall setup. J Mech Behav Biomed Mater. 2016;57: 116–127. doi:10.1016/j.jmbbm.2015.11.026

Chapter 4: Cortical thinning of the tibia reflects structural deterioration of the femoral neck

Gianluca Iori[1], Johannes Schneider[1], Andreas Reisinger[2], Frans Heyer[3,4], Laura Peralta[5,6], Caroline Wyers[3,4], Claus C. Glüer[7], J. P. van den Bergh[3,4], Dieter Pahr[2,8], and Kay Raum[1*]

[1] Berlin-Brandenburg Center for Regenerative Therapies, Charité – Universitätsmedizin Berlin, corporate member of Freie Universität Berlin, Humboldt-Universität zu Berlin, and Berlin Institute of Health, Berlin, Germany
[2] Division Biomechanics, Karl Landsteiner University of Health Sciences, Krems, Austria
[3] Department of Internal Medicine, NUTRIM School of Nutrition and Translational Research in Metabolism, Maastricht University Medical Center, Maastricht, The Netherlands
[4] Department of Internal Medicine, VieCuri Medical Center, Venlo, The Netherlands
[5] Laboratoire d'Imagerie Biomédicale, Sorbonne Universités, INSERM UMR S 1146, CNRS UMR 7371, Paris, France
[6] Department of Biomedical Engineering, School of Biomedical Engineering & Imaging Sciences, King's College London, London, UK
[7] Sektion Biomedizinische Bildgebung, Klinik für Radiologie und Neuroradiologie, Christian-Albrechts-Universität zu Kiel, Kiel, Germany
[8] Institute for Lightweight Design and Structural Biomechanics, TU Wien, Vienna, Austria

[*] Corresponding author: Kay Raum
E-mail: kay.raum@charite.de

Overview

In chapter 3, the thickness of tibial cortical bone and the accumulation of large pores within it were associated with an impairment of the fracture resistance of the proximal femur. The study of this chapter extends the results reported so far by investigating *ex vivo* possible associations between the cortical bone microarchitecture at the tibia and the bone density and structure in the femoral neck. Non-linear hvFE models and mechanical tests are used to estimate femur strength during a sideways fall. The density and microstructure of the femoral neck are analyzed in 3D on HR-pQCT images. These two analyses allow to identify the most important determinants of femur strength in the density and structure of cortical and trabecular bone of the femoral neck. The results of this study show that a reduction in thickness and the accumulation of large pores in the cortical bone of the tibia reflect a structural deterioration of the bone architecture in the femoral neck.

My contribution

I performed sample preparation, SAM measurements, mechanical tests and all FE, image and statistical analysis of this study. The HR-pQCT data was mostly collected by FH and CW at VieCuri Venlo (the Netherlands), after FH and I initiated the procedure.

Publication notification

This work is submitted for publication to the Journal of Bone and Mineral Research (JBMR).

Abstract

Introduction:
Cortical bone thinning and a rarefaction of the trabecular architecture represent possible causes of increased femoral neck (FN) fracture risk. Due to X-ray exposure limits, the bone microstructure is rarely measurable in the FN of subjects but can be assessed at the tibia. Here, we studied whether the tibial cortical microstructure is associated with structural deterioration of the femoral neck and thus increased femur fragility.

Methods:
The cortical and trabecular architectures in the FN of 19 humans were analyzed ex vivo on 3D microcomputed tomography images with 30.3 µm voxel size. Cortical thickness ($Ct.Th_{tibia}$), porosity ($Ct.Po_{tibia}$) and pore size distribution in the tibiae of the same subjects were measured using scanning acoustic microscopy (12 µm pixel size). Femur strength during sideways falls was simulated with homogenized voxel finite element models.

Results:
Femur strength was associated with $Ct.Th_{tibia}$ ($R^2 = 0.62$, $p < 0.001$) and with the prevalence of pores with diameter > 100 µm in tibial cortical bone ($relCt.Po_{100\mu m\text{-}tibia}$; $R^2 = 0.24$, $p < 0.05$). At the same time, femur strength was associated with $vBMD_{tot}$ ($R^2 = 0.23$, $p < 0.01$), $vBMD_{trab}$ ($R^2 = 0.26$, $p < 0.01$), $Ct.Th_{FN}$ ($R^2 = 0.29$, $p < 0.001$), $Tb.BV/TV_{FN}$ ($R^2 = 0.34$, $p < 0.001$), $Tb.Sp_{FN}$ ($R^2 = 0.25$, $p < 0.01$) and $Tb.N_{FN}$ ($R^2 = 0.32$, $p < 0.001$). Smaller $Ct.Th_{tibia}$ was associated with smaller $Ct.Th_{FN}$ ($R^2 = 0.31$, $p < 0.05$), lower $Tb.BV/TV_{FN}$ ($R^2 = 0.29$, $p < 0.05$), higher $Tb.Sp_{FN}$ ($R^2 = 0.33$, $p < 0.05$) and lower $Tb.N_{FN}$ ($R^2 = 0.42$, $p < 0.01$). Higher $relCt.Po_{100\mu m\text{-}tibia}$ indicated higher $Tb.Sp_{FN}$ ($R^2 = 0.36$, $p < 0.01$) and lower $Tb.N_{FN}$ ($R^2 = 0.45$, $p < 0.01$).

Conclusion:
Thickness and the prevalence of large pores in the cortical bone of the tibia might be potential diagnostic biomarkers of femoral neck fragility.

Keywords: Cortical bone; Porosity; Bone strength; Finite Element Analysis; Hip fragility

4.1 Introduction

The hierarchical structure of bone fulfils the mechanical function (i.e. a combined need for rigidity and strength while preserving minimum weight) dictated by efficient locomotion in a gravity environment [1]. In the human femoral neck (FN), the bone architecture is adapted to withstand the stress field generated by physiological motor tasks [2,3]. Despite the heterogeneous strain distribution encountered while performing everyday movements [4], this can be generalized as a compression throughout the inferior aspect of the neck along with tension in the superior arcade [5]. By causing an inversion of the habitual strains in the neck [6,7], sideways falls are associated with the greatest fracture risk for the hip [8]. During this event, FN fractures initiate in the superior aspect of the neck, where bone experiences a peak in compressive strain [7,9].

The cortical bone in the superior, sub-capital region of the neck is thinner in individuals who sustained an osteoporotic hip fracture with respect to healthy controls, likely constituting a reason of neck fragility [10–12]. Structural instability arising from a thin superior cortex might be accompanied by a sparse and rarefied trabecular network [13] providing insufficient structural redundancy [14]. Cumulative deteriorations of both cortical and trabecular compartments have been associated with reduced FN strength [15]. Despite evidence supporting the particular role of the local femoral neck microarchitecture in determining femur strength, current technology does not allow its assessment in subjects in a non-invasive manner.

Microstructural measurements performed with High-Resolution peripheral Quantitative Computed Tomography (HR-pQCT) at the tibia can capture age related bone loss and remodeling [16,17] and might represent an important surrogate of femur strength for the prediction of the individual's fracture risk [18]. Ultrasound (US) waves interacting with the cortical bone of the tibia contain structural information that can be employed for the measurement of cortical bone thickness and porosity *in vivo* and in a non-invasive and ionizing radiation free manner [19–21]. To the best of the authors' knowledge, the association between the bone microstructure in the tibia and in the femoral neck has not been investigated so far. In this work, we characterize *ex vivo* the local microarchitecture of cortical and trabecular bone from the left and right femoral necks of 19 human donors together with the cortical microarchitecture of the left tibiae from the same subjects. The question we pose is whether local microstructural changes in the femoral neck that are determinant for hip fragility are also associated with microstructural changes of tibial cortical bone.

4.2 Materials and Methods

4.2.1 Samples

The left and right femora and the left tibiae of nineteen human donors (6 male, 13 female, age: 69–94 years, mean: 84 ± 8 years) were obtained in accordance with the German law "Gesetz über das Leichen-, Bestattungs- und Friedhofswesen des Landes Schleswig-Holstein - Abschnitt II, §9 (Leichenöffnung, anatomisch)" from 04.02.2005.

4.2.2 High resolution peripheral quantitative computed tomography

Proximal femur samples were dissected and prepared for imaging in a second generation HR-pQCT scanner (XtremeCT II, Scanco Medical AG, Brüttisellen, Switzerland) as described previously [22]. The bones were thawed, submerged in 1% PBS, degassed and scanned inside a custom sealed Plexiglas chamber [23] using X-ray tube voltage of 68 kVp, current of 1470 μA and 200 ms integration time. The projections (3000, taken over 180°) were reconstructed as

stacks of 4608 × 4608 images with isotropic voxel size of 30.3 µm. Voxel Hounsfield Units (HU) were converted to bone mineral density (BMD) using the scanner built-in calibration rule.

4.2.3 Simulations of proximal femur strength

The failure of the proximal femora under quasi-static sideways fall load conditions (0° internal rotation, 30° adduction angle) was simulated using non-linear homogenized voxel finite element (hvFE) models that were developed from the HR-pQCT images following a validated protocol [24]. The HR-pQCT datasets were coarsened to 2.7 mm isotropic voxels and converted first to vBMD (using the HR-pQCT scanner built-in calibration rule) and then to bone volume fraction [22]. Elastic and yield properties depended on local damage [25] and were initially mapped on the model using an empirical function of the bone volume fraction of single voxels [24,26]. The FE models were generated with medtool 4.1 (Dr. Pahr Ingenieurs e.U, Pfaffstätten, Austria) and solved in Abaqus 6.12 (Simulia, Dassault Systemes, Velizy, France). The maximum force recorded during the simulation was taken as the femoral strength.

For the purpose of validation, one femur (random left or right) from each of 10 out of 19 donors were mechanically tested until failure following a procedure described elsewhere [24]. The test was quasi-static, with displacements applied on the femoral head at a rate of 5 mm/min. The maximum force recorded during the experiment was taken as the experimental femoral strength.

4.2.4 Scanning acoustic microscopy

A cross-section from the midshaft region of each tibia (Fig. 23B) was extracted for microstructural characterization using Scanning Acoustic Microscopy (SAM). The sections were washed and prepared by removing soft tissues and by grinding and polishing one surface on a planar grinder (Phoenix 4000, Buehler Ltd., Illinois) using grain sizes of P80, P600, P1200, P2500 and P4000 (ISO/FEPA grit; Buehler Ltd., Illinois). Debris and air bubbles were finally removed by washing and degassing the samples in a desiccator for 30 min while submerged in 1% PBS. Scanning was performed with a custom-built acoustic microscope [27,28], maintaining the sample at a fixed temperature of 25°C in 1% degassed PBS solution. The microscope was equipped with a KSI transducer (KSI 100/60°, KSI, Herborn, Germany) with a central frequency of 100 MHz, and a lateral resolution (diameter of the focused ultrasound beam in the focal plane) of 19.8 µm [28]. RF signals were processed and converted to acoustic impedance maps with a pixel size of 12 µm (Fig. 23A) as described in previous works [28,29]. SAM images can be downloaded from: https://doi.org/10.5281/zenodo.2605350.

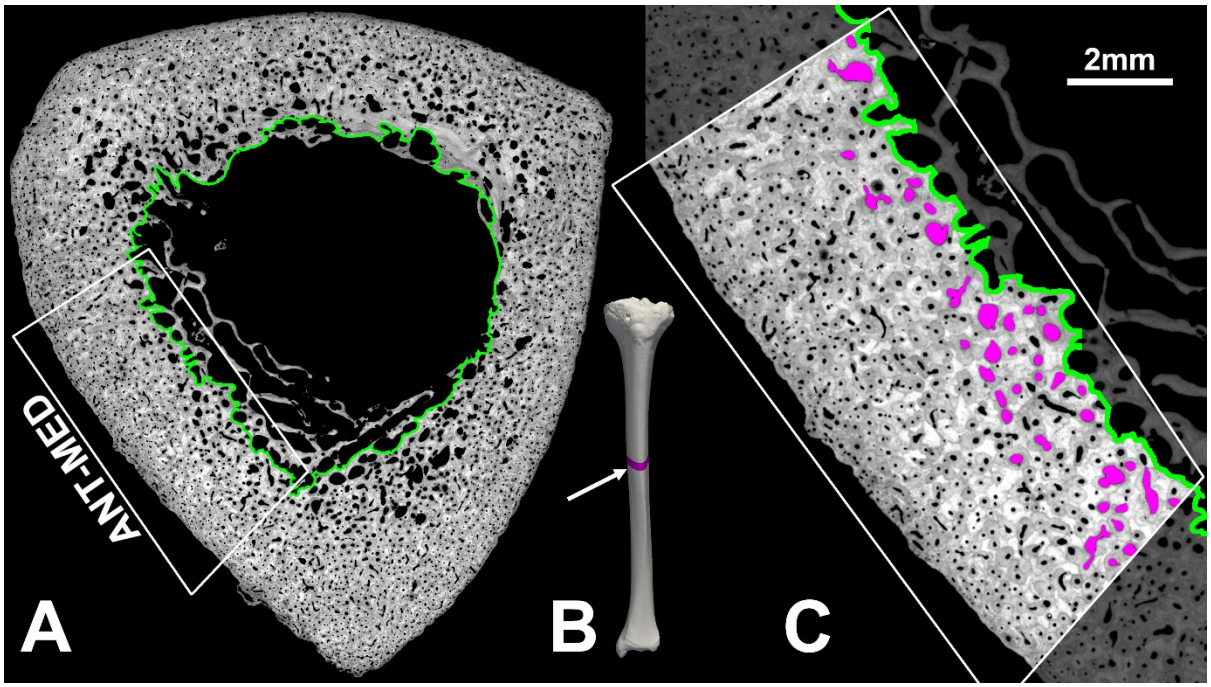

Fig. 23. 2D histomorphometric analysis of the tibia midshaft by SAM. A cross section of the tibia midshaft is scanned with SAM (A). Cortical and trabecular bone compartments are separated (green) and cortical thickness, porosity and pore size measurements are performed on the anterior-medial portion of cortical bone below the *facies medialis* of the tibia (A and arrow in B). Pores with a diameter larger than 100 µm are highlighted in magenta in (C), where a detail of the anteromedial region of (A) is shown.

4.2.5 Histomorphometry

4.2.5.1 Femoral neck

A 7-mm thick cross section of each FN was extracted for microstructural characterization from the HR-pQCT datasets perpendicular to the neck anatomical axis [30] (Fig. 24B). Since the neck strength strongly depends on location along its axis [31], the sections were centered around the cross-section with minimum area [32]. The volume was filtered with a Gaussian kernel (sigma = 1.06 voxels) to remove high frequency noise, coarsened with factor 2 (yielding 60.6 µm voxel size) and rotated to align the image Z-axis with the neck anatomical axis and the inferior aspect of the neck towards the bottom of the image (Fig. 24A). A binary mask of the cortical bone (green in Fig. 24A and C) was obtained applying the automatic procedure proposed for tibia images by Burghardt et al. [33], followed by a manual correction step which was required by the much thinner cortical bone in the neck. Trabecularized regions of the neck, where it was not possible to identify compact cortical bone tissue (*NOcort*) were manually marked on each slice of the stack (Fig. 24C) using Amira (Zuse Institute Berlin, Germany). The neck was then divided in twelve 30°-wide circumferential sectors (Fig. 24A) to analyze local bone structure and vBMD. Binary masks of trabecular and cortical tissue were segmented independently by computing thresholds from the intensity histogram of the two bone regions separately [34]. Local trabecular number ($Tb.N_{FN}$), thickness ($Tb.Th_{FN}$) and separation ($Tb.Sp_{FN}$) were measured in medtool 4.1 (Dr. Pahr Ingenieurs e.U, Pfaffstätten, Austria). The cortical bone thickness ($Ct.Th_{FN}$) was measured as the mean of the distance distribution between periosteum and endosteum contours [35], while cortical bone porosity (Ct.Po) and trabecular bone volume fraction (Tb.BV/TV) were measured from the binary images of the bone tissue and of the cortical and trabecular bone compartments, respectively. For each

circumferential sector, the percentage of trabecularized (*NOcort*) and of ultra-thin (Ct.Th < 0.1 mm) cortical bone were also quantified. To obtain a value for each one of the quadrants (inferior, anterior, superior and posterior), measurements from 3 adjacent sectors (90° in total) were smoothed with a Gaussian kernel ($\sigma = 1.2$). Measurements were also performed on the whole FN. Apart from the exceptions reported in the text, image processing was conducted in Matlab (R2018a, The Mathworks Inc., Natick, MA, USA).

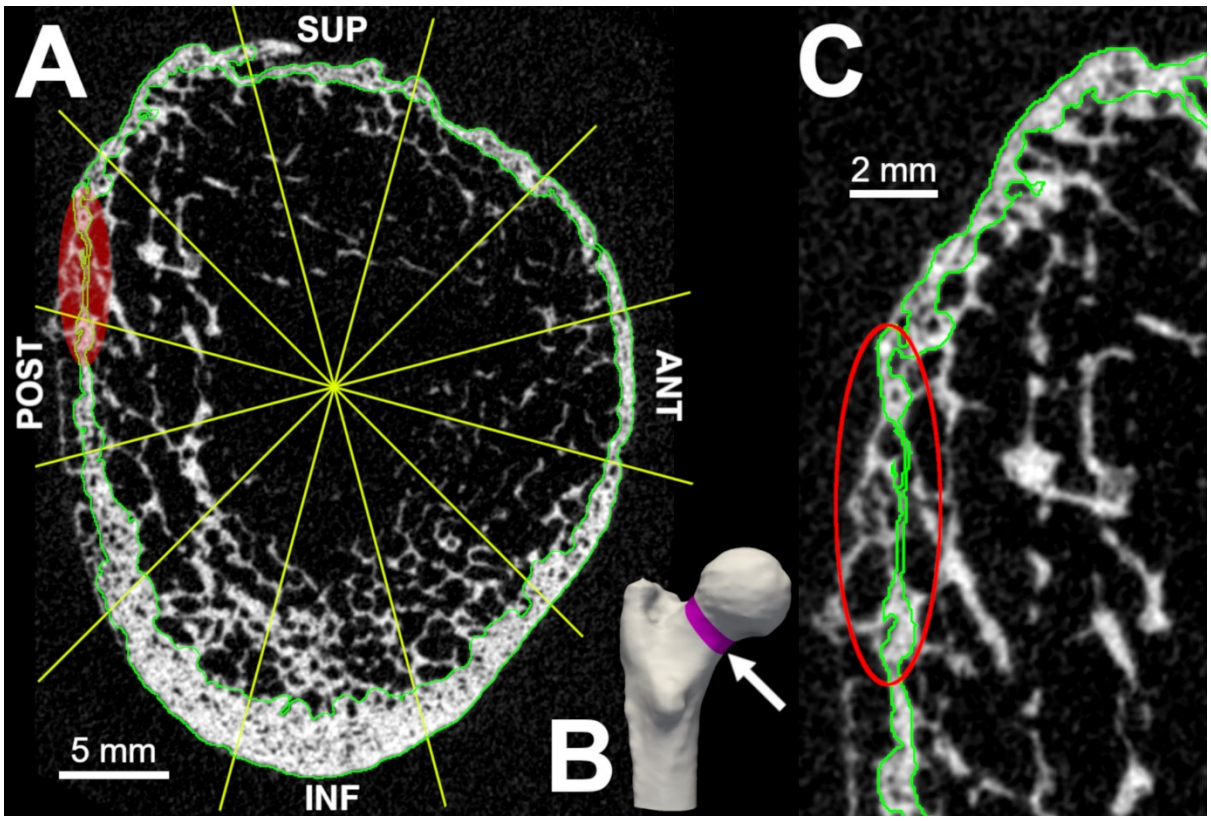

Fig. 24. 3D histomorphometric analysis of the femoral neck. (A) 7 mm of the neck (magenta in B) were extracted perpendicular to the neck axis for histomorphometric and density measurements. The section was rotated in a standard anatomical reference plane (inferior-medial region pointing towards the bottom of the image) and divided into 12 circumferential sectors with 30° width. (C) Detail of a trabecularized region (superior-posterior) of the cortex.

4.2.5.2 Tibia

SAM images of the tibia (Fig. 23) were binarized applying a global adaptive threshold [36]. Structures with an area > 0.144 mm² and not connected to the main bone tissue were removed and all single-pixel voids were filled. The cortical bone was manually separated from the trabecularized regions according to a set of rules described for SAM images with the same resolution [37]. $Ct.Th_{tibia}$, $Ct.Po_{tibia}$ and single pore diameters ($Po.Dm_{tibia}$) were computed on the anteromedial portion of the shaft (Fig. 23C; arrow in Fig. 23B) since this region represents the target of *in vivo* measurements of cortical bone with quantitative ultrasound. The contribution to the total $Ct.Po_{tibia}$ of only pores with diameter larger than 100 µm (magenta in Fig. 23C) was also quantified ($relCt.Po_{100\mu m\text{-}tibia}$). The software for reproduction of the analysis is available at: https://doi.org/10.5281/zenodo.2605365.

4.2.6 Statistical analysis

Parameters were tested for normality using the Shapiro–Wilk test. For each microstructural or vBMD measurement in the FN, the difference between inferior, anterior, superior and posterior quadrants was tested by one-way ANOVA or Kruskal-Wallis test, depending on the normality of the parameter distribution. If the test indicated significant differences, pairs of quadrants were compared with a paired Student's t-test or with a Wilcoxon signed-rank test, for normally or non-normally distributed parameters, respectively. The R^2 of the linear regression was used to assess the degree of association between i) femur strength and microstructural properties of the cortical bone of the tibia, ii) femur strength and FN microstructure or vBMD, and iii) cortical microstructure of the tibia and microstructure or vBMD of the FN. When comparing single quadrants within the FN, a Bonferroni correction was applied with $m = 4$ and overall significance level $\alpha = 0.05$. The significance level of single linear regressions was therefore set at $p = 0.05/4 = 0.0125$. Measurements of the cortical bone microstructure of the left tibia were compared to the simulated strength of only left, only right or to the average strength of left and right proximal femora. In addition, the associations between tibial microstructural parameters and experimental proximal femur strength from mechanical tests were investigated for a subset of 10 (left and right) donors. The comparison between tibial and FN microstructures was also repeated considering only left, only right or the average between left and right FN properties. All analyses were repeated excluding circumferential sectors of the FN in which trabecularized areas exceeded 50% of the external neck surface. This was done to verify that trabecularized regions did not affect the calculation of femoral neck cortical bone parameters.

4.3 Results

4.3.1 Tibial cortical thickness reflects proximal femur strength

Properties of the cortical bone microstructure of the left anteromedial tibia shaft are reported in Table 17. The average strength of the left and right proximal femora was strongly associated with $Ct.Th_{tibia}$ ($R^2 = 0.62$, $p < 0.001$; Table 17) and inversely associated with $relCt.Po_{100\mu m\text{-}tibia}$ ($R^2 = 0.24$, $p < 0.05$; Table 17). No association was found between $Ct.Po_{tibia}$ or $Po.Dm_{tibia}$ and the strength of the proximal femur (Table 17). The results of Table 17 were confirmed also when separately considering the simulated strength of left and right femora, or the experimental strength from mechanical tests on a subset of $N = 10$ (left or right) bones (Supplemental Table 1).

Table 17. Cortical bone microstructure of the tibia and significant associations with proximal femur strength (mean of left and right femora) from hvFE simulations ($N = 19$).

			Femur strength (hvFE simulated)
	Mean ± SD (min-max)	CV [%]	R^2
Ct.Th [mm]	2.98 ± 1.19 (0.82-5.35)	40	0.62**
Ct.Po [%]	11.1 ± 3.5 (7.7-21.4)	32	
Po.Dm [µm]	51.5 ± 5.8 (44.1-67.2)	11	
relCt.Po$_{100\mu m}$ [%]	40.1 ± 13.9 (17.3-77.0)	35	0.24

SD = standard deviation; CV = coefficient of variation; hvFE = homogenized voxel finite element. Coefficients are reported only for p-values < 0.05. * $p \leq 0.01$; ** $p \leq 0.001$.

4.3.2 Associations between femoral neck microstructure or vBMD and femur strength

The strength of the proximal femur was positively associated with the total and trabecular femoral neck vBMD ($R^2 = 0.23$ and $R^2 = 0.26$ respectively, both $p < 0.01$; Table 18), with $Ct.Th_{FN}$ ($R^2 = 0.29$, $p < 0.001$; Table 18) as well as with $Tb.BV/TV_{FN}$, $Tb.Sp_{FN}$ and $Tb.N_{FN}$ ($R^2 = 0.34$, $R^2 = 0.25$ and $R^2 = 0.32$ respectively, all $p < 0.001$; Table 18). The proportion of ultra-thin (Ct.Th < 0.1 mm) cortex in the FN was also associated with femur strength ($R^2 = 0.18$, $p < 0.01$; Table 18). $Ct.Po_{FN}$, $vBMD_{cort}$ and $Tb.Th_{FN}$ were not associated with femur strength (Table 18).

Table 18. Femoral neck volumetric BMD, microstructure and their associations with hvFE simulated proximal femur strength ($N = 38$) and tibial cortical bone microstructure ($N = 19$).

			Femur	**Tibia**			
			Strength	**Ct.Th**	**Ct.Po**	**Po.Dm**	**relCt.Po$_{100\mu m}$**
	Mean ± SD (min-max)	CV [%]			R^2		
vBMD$_{tot}$ [mgHA/cm³]	214 ± 49 (126-314)	23	**0.23***				
vBMD$_{cort}$ [mgHA/cm³]	801 ± 44 (688-885)	6			**0.58****	**0.48****	0.31
vBMD$_{trab}$ [mgHA/cm³]	85 ± 38 (23-189)	45	**0.26****				
Ct.Th [mm]	0.95 ± 0.19 (0.60-1.37)	20	**0.29****	0.31			
Ct.Po [%]	3.4 ± 1.5 (1.2-7.0)	44					
Tb.BV/TV [%]	15.8 ± 3.7 (10.7-24.2)	24	**0.34****	0.29			
Tb.Th [mm]	0.28 ± 0.02 (0.24-0.34)	9					
Tb.Sp [mm]	1.46 ± 0.58 (0.92-3.37)	40	**0.25****	**0.33***			**0.36***
Tb.N [mm]	0.65 ± 0.13 (0.39-0.87)	20	**0.32****	**0.42***			**0.45***
NOcort [%]	6.8 ± 7.6 (0.0-27.8)	112					
Ct.Th < 0.1 mm [%]	13.8 ± 8.5 (2.1-36.7)	62	**0.18***				

SD = standard deviation; CV = coefficient of variation; hvFE = homogenized voxel finite element.
Coefficients are reported only for p-values < 0.05. * $p \leq 0.01$; ** $p \leq 0.001$.

4.3.3 Analyses of single femoral neck quadrants

The distributions of vBMD and microstructural properties in the FN (Fig. 25) showed a clear regional pattern. The inferior FN had a thicker (Fig. 25D) and denser (Fig. 25B) cortical bone, as well as higher Tb.BV/TV (Fig. 25H) and Tb.Th (Fig. 25I). On average, 6.8% (min: 0%, max: 27.8%) and 13.8% (min: 2.1%, max: 36.7%) of the outer femoral neck perimeter was heavily trabecularized (*NOcort*) or extremely thin (Ct.Th < 0.1 mm), respectively (Table 18). These features were mostly observed in the posterior aspect of the FN (Fig. 25G and F, respectively).

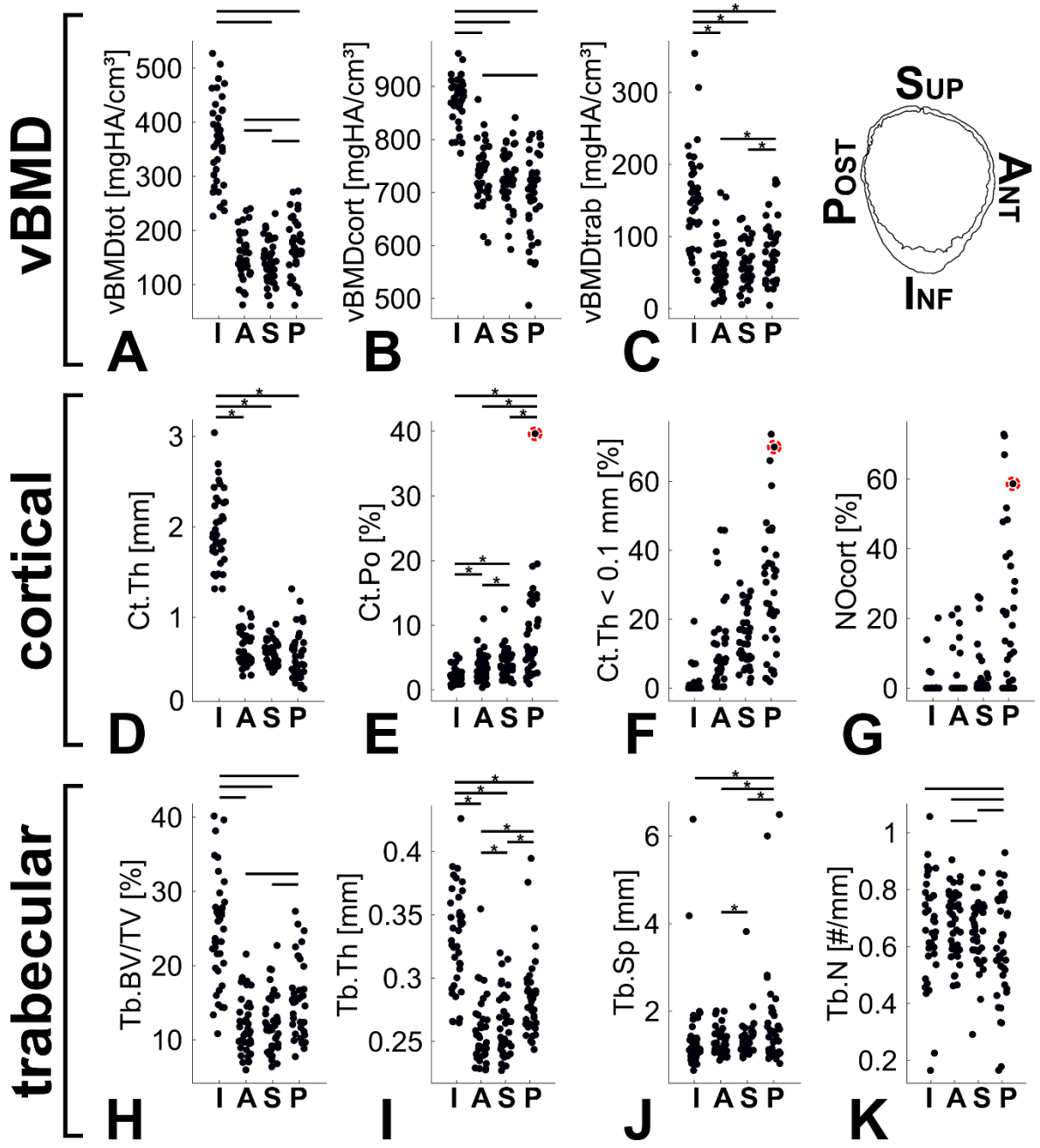

Fig. 25. Local vBMD and microstructure in the quadrants of the femoral neck. Higher $vBMD_{tot}$ (A), $vBMD_{cort}$ (B) and $vBMD_{trab}$ (C), larger $Ct.Th_{FN}$ (D), $Tb.BV/TV_{FN}$ (H) and $Tb.Th_{FN}$ (I) were found in the inferior femoral neck. $Ct.Po_{FN}$ (E) was lower in the inferior and larger in the posterior neck. One sample had $Ct.Po_{FN}$ = 39.5% in the posterior femoral neck quadrant (dashed circle in E). For this sample, 59% of the cortical shell in the posterior neck was marked as trabecularized (G) and 66% of the same quadrant had $Ct.Th_{FN}$ < 0.1 mm (F). The posterior neck was the quadrant where the majority of ultra-thin (F) and trabecularized (G) regions of the cortex were observed. Posteriorly, trabeculae had larger separation (J) and lower number (K).

The letters I, A, S and P on the horizontal axes indicate inferior, anterior, superior and posterior quadrants, respectively.

* indicates a Wilcoxon signed-rank test.

Left and right measurements are pooled. (N = 38).

Fig. 26 illustrates the associations between proximal femur strength and local vBMD and microarchitecture within the FN. The associations between strength and $vBMD_{tot}$ ($R^2 = 0.33$, $p < 0.001$; Fig. 26A), and $Ct.Th_{FN}$ ($R^2 = 0.43$, $p < 0.001$; Fig. 26D) were particularly strong when these properties were assessed in the superior quadrant of the FN (+10% and +14% with respect to the R^2 of whole FN properties, respectively). There was no association between femur strength and the local $vBMD_{cort}$ (Fig. 26D) and $Ct.Po_{FN}$ (not shown) of the femoral neck. After excluding trabecularized regions of the cortical bone, femur strength remained strongly associated with $Ct.Th_{FN}$ in the superior neck quadrant ($R^2 = 0.30$, $p < 0.001$; Supplemental Fig. 1). Properties of the trabecular architecture showed similar or stronger associations with femur strength when assessed over the entire FN (Fig. 26E to G).

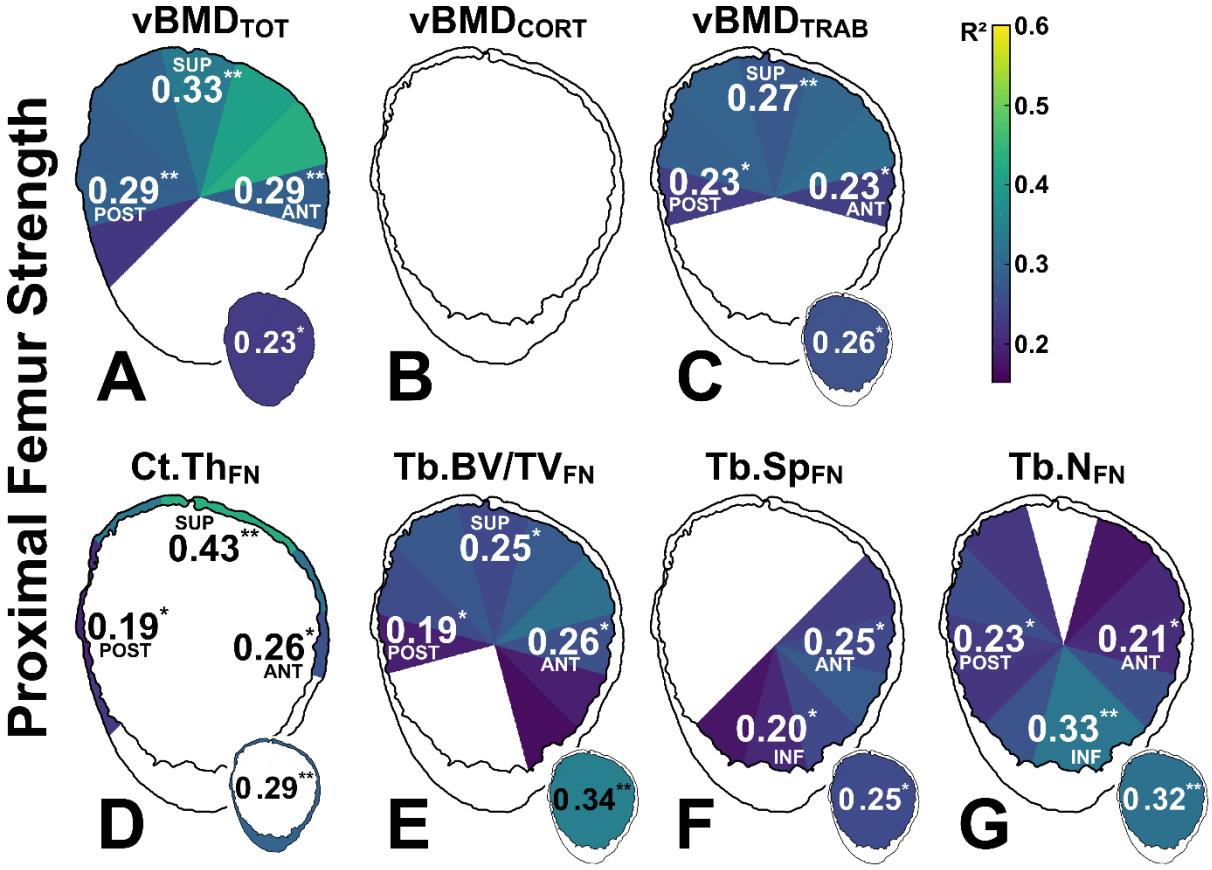

Fig. 26. Structural determinants of femur strength. The ultimate force registered during a simulated sideways fall was associated with $vBMD_{tot}$ (A), $vBMD_{trab}$ (C), $Ct.Th_{FN}$ (D), $Tb.BV/TV_{FN}$ (E), $Tb.Sp_{FN}$ (F) and $Tb.N_{FN}$ (G) of the femoral neck. Colored areas have $p < 0.05$.

*$p < 0.01$. **$p < 0.001$. $N = 38$.

4.3.4 Tibial cortical bone microstructure reflects bone architecture in the femoral neck

The coefficients of determination reported in this paragraph refer to the linear regression between left tibia properties and average quantities from the left and right femoral necks. Significant associations were confirmed by comparing the left tibia separately with the left or with the right vBMD and microstructure of the FN (Supplemental Table 2).

$Ct.Th_{tibia}$ was associated with $Ct.Th_{FN}$ ($R^2 = 0.31$, $p < 0.05$; Table 18 and Fig. 27A), $Tb.BV/TV_{FN}$, ($R^2 = 0.29$, $p < 0.05$; Table 18 and Fig. 27B), $Tb.Sp_{FN}$ ($R^2 = 0.33$, $p = 0.01$; Table 18 and Fig. 27C) and $Tb.N_{FN}$ ($R^2 = 0.42$, all $p < 0.01$; Table 18 and Fig. 27D) of the whole FN.

$Ct.Th_{tibia}$ was strongly associated with $Ct.Th_{FN}$ in the superior-anterior aspect of the FN ($R^2 > 0.33$, $p < 0.01$; Fig. 27A) and with $Tb.BV/TV_{FN}$ ($R^2 = 0.32$, $p < 0.01$; Fig. 27B), $Tb.Sp_{FN}$ ($R^2 = 0.39$, $p < 0.01$; Fig. 27C) and $Tb.N_{FN}$ ($R^2 = 0.59$, all $p < 0.001$; Fig. 27D) in the inferior FN. The association between $Ct.Th_{tibia}$ and $Ct.Th_{FN}$ was limited to the anterior FN after excluding trabecularized regions of the cortex (panel B in Supplemental Fig. 2).

$Ct.Po_{tibia}$ and $Po.Dm_{tibia}$ were both strongly associated with $vBMD_{cort}$ of the whole FN ($R^2 = 0.58$ and $R^2 = 0.48$, respectively; $p \leq 0.001$; Table 18 and Fig. 28), even after excluding trabecularized cortical bone regions (panels D and F in Supplemental Fig. 2, respectively). A greater prevalence of large pores in the cortical bone of the tibia ($relCt.Po_{100\mu m\text{-}tibia}$) reflected a lower FN $vBMD_{cort}$ ($R^2 = 0.31$, $p = 0.014$; Table 18) as well as larger $Tb.Sp_{FN}$ ($R^2 = 0.36$ $p < 0.01$; Table 18 and Fig. 29A) and lower $Tb.N_{FN}$ ($R^2 = 0.45$, $p < 0.01$; Table 18 and Fig. 29B).

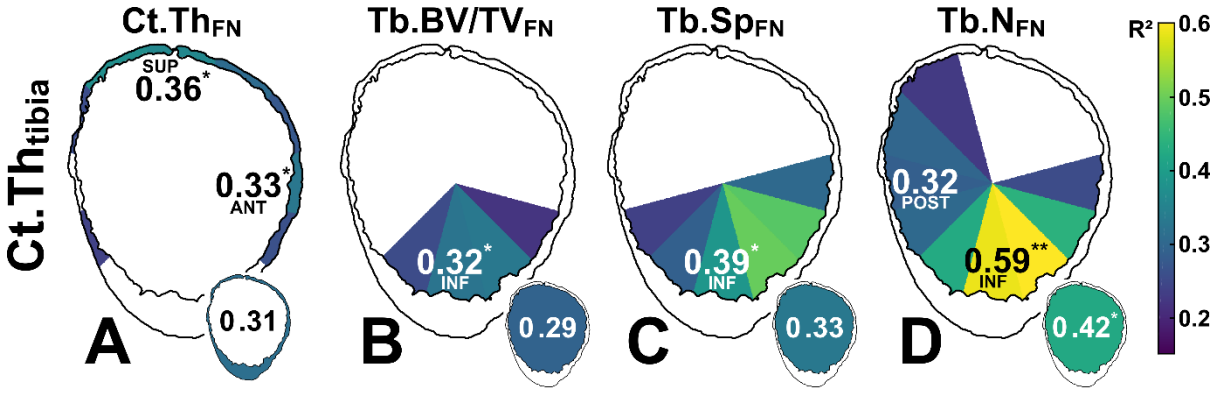

Fig. 27. Correlation between $Ct.Th_{tibia}$ and the microstructure of the femoral neck. A thinner cortical bone in the anteromedial tibia as measured *ex vivo* on SAM images was associated with a thinner cortex of the femoral neck (A) as well as with lower $Tb.BV/TV_{FN}$ (B) and $Tb.N_{FN}$ (D) and with higher $Tb.Sp_{FN}$ (C). Colored areas have $p < 0.05$. *$p < 0.01$. **$p < 0.001$. $N = 19$.

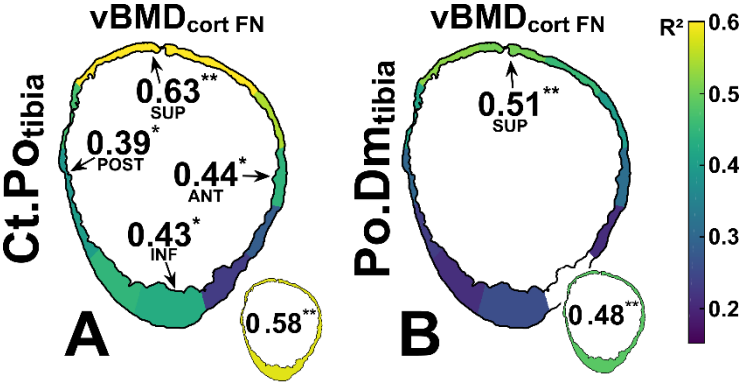

Fig. 28. Cortical porosity (A) and pore size (B) in the tibia are associated with $vBMD_{cort}$ of the femoral neck.

Colored areas have $p < 0.05$.

*$p < 0.01$. **$p < 0.001$. $N = 19$.

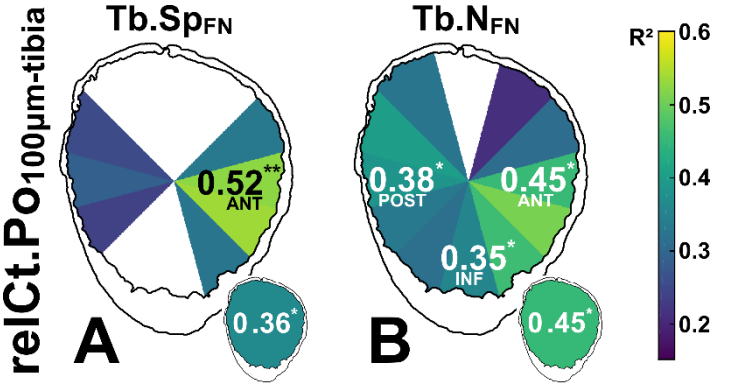

Fig. 29. Large pores in the tibia reflect a sparser trabecular architecture of the femoral neck.

A higher prevalence of large (diameter > 100 µm) pores in the tibia ($relCt.Po_{100\mu m\text{-}tibia}$) was associated with higher $Tb.Sp_{FN}$ (A) and lower $Tb.N_{FN}$ (B). Colored areas have $p < 0.05$.

*$p < 0.01$. **$p < 0.001$. $N = 19$.

4.4 Discussion

Variations in the proximal femur strength predicted by non-linear homogenized FE models were associated with changes in the cortical bone microstructure of the tibia. We have recently demonstrated how a thinner cortex and the prevalence of large pores in the cortical bone of the tibia correlate with reduced femur strength from hvFE simulations in both standing and falling conditions [38]. Here, we showed that the cortical microstructure of the tibia is associated with a structural deterioration of the femoral neck causing impaired femur strength. A thinner cortical bone in the midshaft of the tibia was associated with a thinner cortex and a less dense, sparser trabecular architecture in the femoral neck. Moreover, a higher proportion of abnormally large cavities in the tibia indicated sparser trabecular structures in the femoral neck.

During a fall to the side, femoral neck fractures originate in the superior neck [9] as a result of peak compressive strains that can outweigh tensile ones by a factor of two [7]. Such compression leads to the collapse of a bone region which is subject to tension during physiological tasks [6]. The fractured femoral necks of subjects with osteoporosis have been consistently reported to present thinner cortical bone in the superior sub-capital aspect [10,11,13,39]. Reduced Ct.Th in this region is a probable cause of structural instability of the femoral neck during a fall to the side, as captured by our simulations of proximal femur failure (Fig. 26A and D). The role of Ct.Po in the femoral neck for femur strength is less clear. Bell et al. found higher porosity in the superior neck of controls compared to osteoporotic hip fracture patients and a distinct regional pattern of porosity (inferior $Ct.Po_{FN}$ was lower and superior $Ct.Po_{FN}$ higher in controls, whereas anteriorly $Ct.Po_{FN}$ was 40% higher in OP fracture cases) [40]. Similarly, Blain et al. observed altered patterns of local $Ct.Po_{FN}$ in femoral neck biopsies of OP fracture patients, even though in this study porosity was higher in the anterior neck of controls, possibly due to the use of osteoarthritis patients as controls [13]. In our dataset of 19 elderly subjects, we did not find associations between femoral neck Ct.Po or $vBMD_{cort}$ and the simulated strength of the proximal femur.

Considering trabecular bone, our study shows significant associations of trabecular density, separation and number with an impairment of the femur strength (Fig. 26B-D). Understanding the relative role of trabecular bone in femoral neck fragility is complicated by the fact that the proportion of trabecular tissue in the femoral neck varies with femur strength [14] and subject age [41] as a result of adaptation to loading [2]. Less dense and sparser trabeculae were observed in fractured femoral necks of OP patients with respect to osteoarthritic controls [13]. For elderly subjects, mechanical tests have suggested a marginal role of the spongiosa for femur strength [42], but have considered only standing loads. When sideways fall loads were implemented in numerical simulations (also on an elderly cohort), the contribution to femur strength of the trabecular compartment was similar [6] or even prominent [14] with respect to that of cortical bone. Our results supports a combined role of trabecular and cortical bone in determining the stability of the femoral neck in the elderly.

The process underlying cortical bone loss is understood as the uncoupling between resorption and formation phases within remodeling bone multicellular units (BMUs) [11,43]. This leads to the progressive enlargement and clustering of non-refilled pores [40,44,45], and gradually reduces the thickness of a trabecularized cortical bone wall. Interestingly, the same cellular mechanism (i.e. reversal phase arrest between resorption and formation in the bone remodeling unit) is responsible for trabecular bone loss in post-menopausal osteoporosis [46,47], and has been observed at different skeletal sites such as iliac crest [44,46], proximal femur [43], fibula [43,48] and femoral head [46]. The concept of a common microstructural pattern of bone loss throughout the skeleton, with shared cellular mechanism between cortical and trabecular bone, supports the importance of resorption in both tissue types

for bone fragility [15]. This is corroborated by HR-pQCT studies, where the microarchitecture of the distal skeleton was associated with fracture risk at both peripheral and central sites [18,49–52].

As opposed to investigations on humans by HR-pQCT, we have performed cortical bone measurements *ex vivo* and over a portion of the tibia which is different (midshaft instead of distal or ultra-distal shaft) than the one typically measured *in vivo*. Compared to the distal shaft, the mid-diaphysis of the tibia experiences high bending moments during gait [53,54], has a cortical bone that is thicker and is mainly composed of cortical tissue (Fig. 23), making it less affected by axial ROI positioning [55]. The anteromedial portion was selected for analysis since this site is easily reachable by ultrasound waves that can travel with little attenuation through the thin layer of soft tissue covering the *facies medialis* [20,21]. We confirmed the advantage of this measurement site by repeating the analysis on whole tibia cross-sections: despite being generally weaker, associations with local microstructural features of the femoral neck were confirmed also when taking properties from whole tibial cross sections (Supplemental Table 3). Finally, we asked whether microstructural measurements from the left tibia can reflect changes of femur strength and of femoral neck architecture independent of side. Lower Ct.Th and higher relCt.P0$_{100\mu m}$ in the left tibia were associated with lower strength of both the left and right proximal femora (Supplemental Table 1). The association between structural changes in the tibia and those in the neck were confirmed independently for left and right femoral necks (Supplemental Table 2).

The current study presents several limitations. First, it does not explain why cortical thinning and accumulation of large pores in the midshaft of the tibia might reflect a thinning of the superior neck, where gait generates tension strains. At the same time, a cortical thinning of the tibia was not associated with a thinner cortex in the inferior neck (the aspect subject to compression during gait) [5]. In analogy with the superior femoral neck, the anterior aspect of the tibial diaphysis is adapted to resist the tensile stress generated by bending moments in the sagittal plane [3,54]. Apart from this, adaptation to physiological loads during growth is achieved at the femoral neck by an elliptical shape with varying thickness (Fig. 24), in which a wider cortex accommodates larger stresses inferiorly. This pattern of bone tissue distribution around the neck's axis however, is subject to variability among individuals [2], representing a plausible explanation for the lack of association with the inferior Ct.Th$_{FN}$ in our results.

A second limitation of this work consists in the use of structural information from the cortical bone of the tibia obtained *ex vivo* by SAM with 19.8 μm resolution. In the tibia of living humans, such detail of microstructural characterization is unfeasible with current technology. Second generation HR-pQCT imaging is not limited to distal ROIs as for the parent, first generation scanner, and can assess the tibial midshaft with resolution down to 95.2 μm [56]. This makes such modality particularly interesting, since large resorption units can be directly imaged, while assessing Ct.Po based on vBMD beyond the scanner resolution limit [57].

Even though the shape of the tibia diaphysis can vary along the bone axis [54], the cross-sections analyzed in this study were extracted at varying distance from the upper extremity, thus representing a possible cause of error. Finally, by pooling male and female data together, our work might overlook sex differences in microarchitecture and bone loss at the tibia [58].

Despite these limitations, our work identifies associations between architectural causes of femoral neck fragility and structural features that can be observed in the cortical bone of the tibia. Our findings support the use of microstructural measurements performed in the cortical bone of the tibia for the prediction of hip fracture risk. Research on living humans should target the assessment of the cortical thickness and of large resorption units in the midshaft of the tibia as potential biomarkers of a structural deterioration of the femoral neck.

Acknowledgments
This work was supported by grants from the Deutsche Forschungsgemeinschaft (DFG Ra1380/9-1, Gl 289/8-1), by the Agence Nationale de la Recherche (ANR-14-CE35-0030-01), by the Bundesministerium für Bildung und Forschung (BMBF, musculoskeletal research network 01EC1408L) within the subproject "characterization of cortical and subchondral bone", by the German Academic Exchange Service (DAAD, grant no. 91578351) and by the Weijerhorst Foundation (grant no. WH2). We thank Dr. Robert Wendlandt for the sample collection and Dr. Juan Du for the support during data analysis.

Authors' roles: Study design and conduct: GI and KR. Data collection: GI, JS, AR, FH, LP, CW and JB. Data analysis: GI, JS, AR, FH and DP. Data interpretation: GI, DP, CCG and KR. Drafting manuscript: GI. Revising manuscript content: GI, LP, AR, DP, JB, CCG and KR. Approving final version of manuscript: all authors. GI and KR take responsibility for the integrity of the data analysis.

Supplemental Table 1. Cortical bone microstructure of the tibia: associations with proximal femur strength from hvFE simulations ($N = 19$) and from quasi-static mechanical tests ($N = 10$).

	hvFE simulations						**Mechanical tests**	
	LEFT ($N = 19$)		**RIGHT ($N = 19$)**		**mean(L, R) ($N = 19$)**		**($N = 10$)**	
	R^2	*p*-val	R^2	*p*-val	R^2	*p*-val	R^2	*p*-val
***Ct.Th*$_{tibia}$ [mm]**	0.65	3×10^{-5}	0.51	6×10^{-4}	0.62	6×10^{-5}	0.80	4×10^{-4}
***Ct.Po*$_{tibia}$ [%]**		0.270		0.340		0.286		0.138
***Po.Dm*$_{tibia}$ [µm]**		0.088		0.175		0.112		0.187
***relCt.Po*$_{100µm\text{-}tibia}$ [%]**	0.23	0.037	0.22	0.043	0.24	0.033	0.44	0.036

Supplemental Table 2. Associations between microstructure of tibial cortical bone and the microstructure or vBMD of the LEFT, RIGHT or of the average LEFT and RIGHT femoral neck. R^2 of the linear regression, together with the corresponding p-value and its position within the femoral neck. (N = 19).

	LEFT FN			**RIGHT FN**			**Mean(LEFT, RIGHT) FN**		
	R^2	*p*-val	sector	R^2	*p*-val	sector	R^2	*p*-val	Sector
	Ct.Th$_{tibia}$								
***Ct.Th*$_{FN}$**	0.31	0.0132	SUP	0.42	0.0025	WHOLE	0.36	0.0068	SUP
***Tb.BVTV*$_{FN}$**	0.36	0.0068	WHOLE	0.22	0.0290	WHOLE	0.32	0.0110	INF
***Tb.Sp*$_{FN}$**	0.39	0.0046	WHOLE	0.38	0.0053	INF	0.33	0.0100	WHOLE
***Tb.N*$_{FN}$**	0.52	0.0005	INF	0.55	0.0003	INF	0.59	0.0001	INF
	Ct.Po$_{tibia}$								
***vBMD*$_{cort\ FN}$**	0.48	0.0011	WHOLE	0.59	0.0001	SUP	0.58	0.0002	WHOLE
***Tb.Sp*$_{FN}$**	0.22	0.0428	ANT	0.24	0.0342	ANT	0.25	0.0309	ANT
***Tb.N*$_{FN}$**									
	Po.Dm$_{tibia}$								
***vBMD*$_{cort\ FN}$**	0.48	0.0010	WHOLE	0.37	0.0054	SUP	0.48	0.0009	WHOLE
***Tb.Sp*$_{FN}$**	0.32	0.0117	ANT	0.39	0.0042	ANT	0.38	0.0049	ANT
***Tb.N*$_{FN}$**				0.30	0.0161	ANT	0.26	0.0255	ANT
	relCt.Po$_{100µm\text{-}tibia}$								
***vBMD*$_{cort\ FN}$**	0.31	0.0140	WHOLE				0.36	0.0068	SUP
***Tb.Sp*$_{FN}$**	0.44	0.0019	ANT	0.54	0.0004	ANT	0.52	0.0005	ANT
***Tb.N*$_{FN}$**	0.39	0.0042	WHOLE	0.44	0.0018	WHOLE	0.45	0.0016	WHOLE

Supplemental Table 3. Associations between the local microstructure of the femoral neck and the microstructure of tibial cortical bone as assessed over the anteromedial tibia or over the entire midshaft cross-section (WHOLE). Coefficient of determination (R^2) of the linear regression, together with the corresponding p-value and its position within the femoral neck. (N = 19).

	tibia					
	ANTEROMEDIAL			**WHOLE**		
	R^2	*p*-val	sector	R^2	*p*-val	sector
	$Ct.Th_{tibia}$					
***vBMD*$_{tot\ FN}$**		0.074			0.060	
***vBMD*$_{cort\ FN}$**		0.659			0.611	
***vBMD*$_{trab\ FN}$**		0.068		0.26	0.024	WHOLE
***Ct.Th*$_{FN}$**	0.36	0.007	SUP		0.069	
***Ct.Po*$_{FN}$**		0.986			0.294	
***Tb.BV/TV*$_{FN}$**	0.29	0.017	WHOLE	0.30	0.016	WHOLE
***Tb.Sp*$_{FN}$**	0.39	0.004	INF	0.37	0.006	ANT
***Tb.N*$_{FN}$**	0.59	1×10^{-4}	INF	0.42	0.003	INF
	$Ct.Po_{tibia}$					
***vBMD*$_{cort\ FN}$**	0.58	2×10−4	WHOLE	0.57	3×10^{-4}	WHOLE
	$Po.Dm_{tibia}$					
***vBMD*$_{cort\ FN}$**	0.58	2×10^{-4}	WHOLE	0.57	3×10^{-4}	WHOLE
	$relCt.Po_{100\mu m}$					
***vBMD*$_{cort\ FN}$**	0.31	0.014	WHOLE	0.29	0.019	WHOLE
***Tb.Sp*$_{FN}$**	0.52	4×10^{-4}	ANT	0.45	0.002	ANT
***Tb.N*$_{FN}$**	0.45	0.002	WHOLE	0.39	0.004	ANT

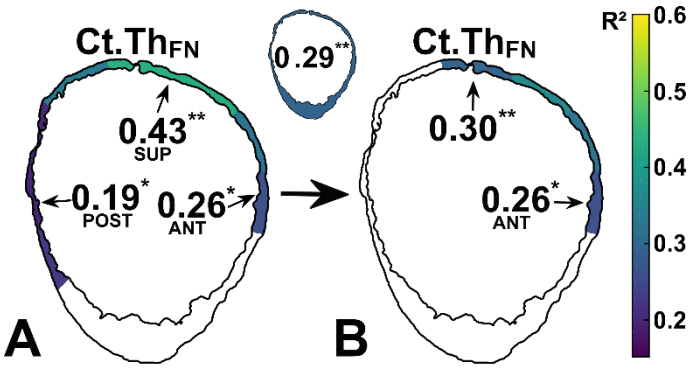

Supplemental Fig. 1. Association between proximal femur strength from hvFE simulations and local femoral neck cortical bone thickness.

After excluding trabecularized regions of the neck for calculation (B), $Ct.Th_{FN}$ of the superior quadrant remained strongly associated with proximal femur strength. Colored areas have $p < 0.05$. $*p < 0.01$. $**p < 0.001$. $N = 19$.

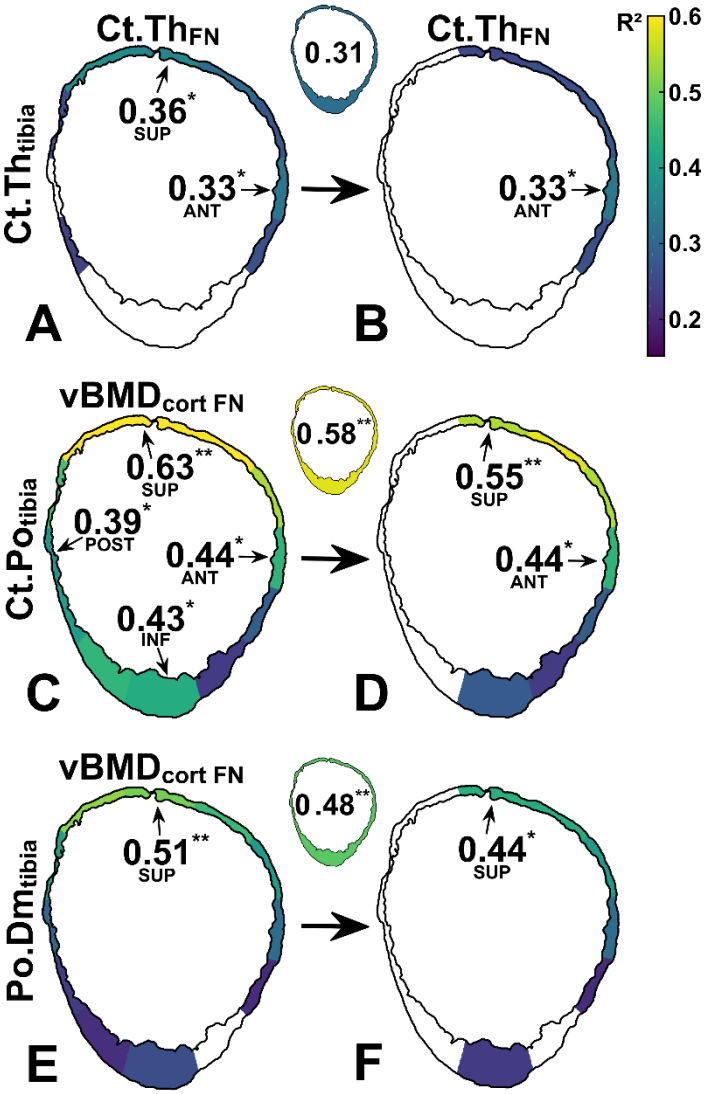

Supplemental Fig. 2. Association between tibial microstructure and local femoral neck cortical bone properties.

Effect of the exclusion of trabecularized cortical bone regions on the associations with $Ct.Th_{FN}$ (B) and $vBMD_{cort}$ (D and F) of the femoral neck. Colored areas have $p < 0.05$. $*p < 0.01$. $**p < 0.001$. $N = 19$.

References

1. Fratzl P, Weinkamer R. Nature's hierarchical materials. Prog Mater Sci. 2007;52: 1263–1334. doi:10.1016/j.pmatsci.2007.06.001
2. Zebaze RMD, Jones A, Knackstedt M, Maalouf G, Seeman E. Construction of the Femoral Neck During Growth Determines Its Strength in Old Age. J Bone Miner Res. 2007;22: 1055–1061. doi:10.1359/jbmr.070329
3. Cristofolini L. In vitro evidence of the structural optimization of the human skeletal bones. J Biomech. 2015;48: 787–796. doi:10.1016/j.jbiomech.2014.12.010
4. Kersh ME, Martelli S, Zebaze R, Seeman E, Pandy MG. Mechanical Loading of the Femoral Neck in Human Locomotion. J Bone Miner Res. 0. doi:10.1002/jbmr.3529
5. Rietbergen BV, Huiskes R, Eckstein F, Rüegsegger P. Trabecular Bone Tissue Strains in the Healthy and Osteoporotic Human Femur. J Bone Miner Res. 2003;18: 1781–1788. doi:10.1359/jbmr.2003.18.10.1781
6. Verhulp E, van Rietbergen B, Huiskes R. Load distribution in the healthy and osteoporotic human proximal femur during a fall to the side. Bone. 2008;42: 30–35. doi:10.1016/j.bone.2007.08.039
7. Zani L, Erani P, Grassi L, Taddei F, Cristofolini L. Strain distribution in the proximal Human femur during in vitro simulated sideways fall. J Biomech. doi:10.1016/j.jbiomech.2015.02.022
8. Keyak JH, Skinner HB, Fleming JA. Effect of force direction on femoral fracture load for two types of loading conditions. J Orthop Res. 2001;19: 539–544. doi:10.1016/S0736-0266(00)00046-2
9. de Bakker PM, Manske SL, Ebacher V, Oxland TR, Cripton PA, Guy P. During sideways falls proximal femur fractures initiate in the superolateral cortex: Evidence from high-speed video of simulated fractures. J Biomech. 2009;42: 1917–1925. doi:10.1016/j.jbiomech.2009.05.001
10. Poole KES, Treece GM, Mayhew PM, Vaculík J, Dungl P, Horák M, et al. Cortical Thickness Mapping to Identify Focal Osteoporosis in Patients with Hip Fracture. PLOS ONE. 2012;7: e38466. doi:10.1371/journal.pone.0038466
11. Power J, Loveridge N, Kröger H, Parker M, Reeve J. Femoral neck cortical bone in female and male hip fracture cases: Differential contrasts in cortical width and sub-periosteal porosity in 112 cases and controls. Bone. 2018;114: 81–89. doi:10.1016/j.bone.2018.05.027
12. Johannesdottir F, Poole KES, Reeve J, Siggeirsdottir K, Aspelund T, Mogensen B, et al. Distribution of cortical bone in the femoral neck and hip fracture: A prospective case-control analysis of 143 incident hip fractures; the AGES-REYKJAVIK Study. Bone. 2011;48: 1268–1276. doi:10.1016/j.bone.2011.03.776
13. Blain H, Chavassieux P, Portero-Muzy N, Bonnel F, Canovas F, Chammas M, et al. Cortical and trabecular bone distribution in the femoral neck in osteoporosis and osteoarthritis. Bone. 2008;43: 862–868. doi:10.1016/j.bone.2008.07.236
14. Nawathe S, Akhlaghpour H, Bouxsein ML, Keaveny TM. Microstructural Failure Mechanisms in the Human Proximal Femur for Sideways Fall Loading: FEMORAL STRENGTH MICROMECHANICS. J Bone Miner Res. 2014;29: 507–515. doi:10.1002/jbmr.2033
15. Seeman E. Pathogenesis of bone fragility in women and men. The Lancet. 2002;359: 1841–1850. doi:10.1016/S0140-6736(02)08706-8

16. Nishiyama KK, Macdonald HM, Buie HR, Hanley DA, Boyd SK. Postmenopausal women with osteopenia have higher cortical porosity and thinner cortices at the distal radius and tibia than women with normal aBMD: an in vivo HR-pQCT study. J Bone Miner Res Off J Am Soc Bone Miner Res. 2010;25: 882–890. doi:10.1359/jbmr.091020
17. Christen P, Boutroy S, Ellouz R, Chapurlat R, Rietbergen B van. Least-detectable and age-related local in vivo bone remodelling assessed by time-lapse HR-pQCT. PLOS ONE. 2018;13: e0191369. doi:10.1371/journal.pone.0191369
18. Ohlsson C, Sundh D, Wallerek A, Nilsson M, Karlsson M, Johansson H, et al. Cortical Bone Area Predicts Incident Fractures Independently of Areal Bone Mineral Density in Older Men. J Clin Endocrinol Metab. 2017;102: 516–524. doi:10.1210/jc.2016-3177
19. Laugier P. Instrumentation for in vivo ultrasonic characterization of bone strength. IEEE Trans Ultrason Ferroelectr Freq Control. 2008;55: 1179–1196. doi:10.1109/TUFFC.2008.782
20. Renaud G, Kruizinga P, Cassereau D, Laugier P. In vivo ultrasound imaging of the bone cortex. Phys Med Biol. 2018;63: 125010. doi:10.1088/1361-6560/aac784
21. Schneider J, Ramiandriosa D, Armbrecht G, Ritter Z, Felsenberg D, Raum K, et al. In vivo measurements of cortical thickness and porosity at the proximal third of the tibia using guided waves: comparison with site-matched pQCT and distal HR-pQCT. Ultrasound Med Biol. 2018;
22. Iori G, Heyer F, Kilappa V, Wyers C, Varga P, Schneider J, et al. BMD-based assessment of local porosity in human femoral cortical bone. Bone. 2018;114: 50–61. doi:10.1016/j.bone.2018.05.028
23. Dall'Ara E, Varga P, Pahr D, Zysset P. A calibration methodology of QCT BMD for human vertebral body with registered micro-CT images. Med Phys. 2011;38: 2602. doi:10.1118/1.3582946
24. Dall'Ara E, Luisier B, Schmidt R, Kainberger F, Zysset P, Pahr D. A nonlinear QCT-based finite element model validation study for the human femur tested in two configurations in vitro. Bone. 2013;52: 27–38. doi:10.1016/j.bone.2012.09.006
25. Garcia D, Zysset PK, Charlebois M, Curnier A. A three-dimensional elastic plastic damage constitutive law for bone tissue. Biomech Model Mechanobiol. 2008;8: 149–165. doi:10.1007/s10237-008-0125-2
26. Rincón-Kohli L, Zysset PK. Multi-axial mechanical properties of human trabecular bone. Biomech Model Mechanobiol. 2008;8: 195–208. doi:10.1007/s10237-008-0128-z
27. Lakshmanan S, Bodi A, Raum K. Assessment of Anisotropic Tissue Elasticity of Cortical Bone from High-Resolution, Angular Acoustic Measurements. IEEE Trans Ultrason Ferroelectr Freq Control. 2007;54: 1560–1570. doi:10.1109/TUFFC.2007.426
28. Raum K, Reißhauer J, Brandt J. Frequency and resolution dependence of the anisotropic impedance estimation in cortical bone using time-resolved scanning acoustic microscopy. J Biomed Mater Res A. 2004;71A: 430–438. doi:10.1002/jbm.a.30156
29. Hube R, Mayr H, Hein W, Raum K. Prediction of biomechanical stability after callus distraction by high resolution scanning acoustic microscopy. Ultrasound Med Biol. 2006;32: 1913–1921. doi:10.1016/j.ultrasmedbio.2006.06.010
30. Hartel MJ, Petersik A, Schmidt A, Kendoff D, Nüchtern J, Rueger JM, et al. Determination of Femoral Neck Angle and Torsion Angle Utilizing a Novel Three-Dimensional Modeling and Analytical Technology Based on CT Datasets. PLOS ONE. 2016;11: e0149480. doi:10.1371/journal.pone.0149480
31. Carpenter R Dana, Beaupré Gary S, Lang Thomas F, Orwoll Eric S, Carter Dennis R. New QCT Analysis Approach Shows the Importance of Fall Orientation on Femoral Neck Strength. J Bone Miner Res. 2009;20: 1533–1542. doi:10.1359/JBMR.050510

32. Lang T, Keyak J, Heitz M, Augat P, Lu Y, Mathur A, et al. Volumetric quantitative computed tomography of the proximal femur: precision and relation to bone strength. Bone. 1997;21: 101–108.
33. Burghardt AJ, Buie HR, Laib A, Majumdar S, Boyd SK. Reproducibility of direct quantitative measures of cortical bone microarchitecture of the distal radius and tibia by HR-pQCT. Bone. 2010;47: 519–528. doi:10.1016/j.bone.2010.05.034
34. Ridler T, Calvard S, others. Picture thresholding using an iterative selection method. IEEE Trans Syst Man Cybern. 1978;8: 630–632.
35. Hildebrand T, Rüegsegger P. A new method for the model-independent assessment of thickness in three-dimensional images. J Microsc. 1997;185: 67–75. doi:10.1046/j.1365-2818.1997.1340694.x
36. Wellner PD. Adaptive thresholding for the DigitalDesk. Xerox EPC1993-110. 1993; 1–19.
37. Malo MKH, Rohrbach D, Isaksson H, Töyräs J, Jurvelin JS, Tamminen IS, et al. Longitudinal elastic properties and porosity of cortical bone tissue vary with age in human proximal femur. Bone. 2013;53: 451–458. doi:10.1016/j.bone.2013.01.015
38. Iori G, Schneider J, Reisinger A, Heyer F, Peralta L, Wyers C, et al. Large cortical bone pores in the tibia are associated with proximal femur strength. PLOS ONE. 2019;14: e0215405. doi:10.1371/journal.pone.0215405
39. Bell KL, Loveridge N, Power J, Garrahan N, Stanton M, Lunt M, et al. Structure of the femoral neck in hip fracture: cortical bone loss in the inferoanterior to superoposterior axis. J Bone Miner Res Off J Am Soc Bone Miner Res. 1999;14: 111–119. doi:10.1359/jbmr.1999.14.1.111
40. Bell KL, Loveridge N, Power J, Garrahan N, Meggitt BF, Reeve J. Regional differences in cortical porosity in the fractured femoral neck. Bone. 1999;24: 57–64. doi:10.1016/S8756-3282(98)00143-4
41. Chen H, Zhou X, Shoumura S, Emura S, Bunai Y. Age- and gender-dependent changes in three-dimensional microstructure of cortical and trabecular bone at the human femoral neck. Osteoporos Int. 2010;21: 627–636. doi:10.1007/s00198-009-0993-z
42. Holzer G, von Skrbensky G, Holzer LA, Pichl W. Hip Fractures and the Contribution of Cortical Versus Trabecular Bone to Femoral Neck Strength. J Bone Miner Res. 2009;24: 468–474. doi:10.1359/jbmr.081108
43. Lassen NE, Andersen TL, Pløen GG, Søe K, Hauge EM, Harving S, et al. Coupling of Bone Resorption and Formation in Real Time: New Knowledge Gained From Human Haversian BMUs. J Bone Miner Res. 2017;32: 1395–1405. doi:10.1002/jbmr.3091
44. Andreasen CM, Delaisse J-M, Eerden BC van der, Leeuwen JP van, Ding M, Andersen TL. Understanding Age-Induced Cortical Porosity in Women: The Accumulation and Coalescence of Eroded Cavities Upon Existing Intracortical Canals Is the Main Contributor. J Bone Miner Res. 2017;33: 606–620. doi:10.1002/jbmr.3354
45. Jordan GR, Loveridge N, Bell KL, Power J, Rushton N, Reeve J. Spatial clustering of remodeling osteons in the femoral neck cortex: a cause of weakness in hip fracture? Bone. 2000;26: 305–313. doi:10.1016/S8756-3282(99)00272-0
46. Andersen TL, Hauge EM, Rolighed L, Bollerslev J, Kjærsgaard-Andersen P, Delaisse J-M. Correlation between Absence of Bone Remodeling Compartment Canopies, Reversal Phase Arrest, and Deficient Bone Formation in Post-Menopausal Osteoporosis. Am J Pathol. 2014;184: 1142–1151. doi:10.1016/j.ajpath.2013.12.005

47. Andreasen CM, Ding M, Overgaard S, Bollen P, Andersen TL. A reversal phase arrest uncoupling the bone formation and resorption contributes to the bone loss in glucocorticoid treated ovariectomised aged sheep. Bone. 2015;75: 32–39. doi:10.1016/j.bone.2015.02.014
48. Bakalova LP, Andreasen CM, Thomsen JS, Brüel A, Hauge E-M, Kiil BJ, et al. Intracortical Bone Mechanics Are Related to Pore Morphology and Remodeling in Human Bone. J Bone Miner Res. 0. doi:10.1002/jbmr.3561
49. Patsch JM, Burghardt AJ, Yap SP, Baum T, Schwartz AV, Joseph GB, et al. Increased cortical porosity in type 2 diabetic postmenopausal women with fragility fractures. J Bone Miner Res. 2013;28: 313–324. doi:10.1002/jbmr.1763
50. Chevalley T, Bonjour JP, van Rietbergen B, Ferrari S, Rizzoli R. Fracture history of healthy premenopausal women is associated with a reduction of cortical microstructural components at the distal radius. Bone. 2013;55: 377–383. doi:10.1016/j.bone.2013.04.025
51. Bala Y, Bui QM, Wang X-F, Iuliano S, Wang Q, Ghasem-Zadeh A, et al. Trabecular and Cortical Microstructure and Fragility of the Distal Radius in Women. J Bone Miner Res. 2015;30: 621–629. doi:10.1002/jbmr.2388
52. Sundh D, Nilsson AG, Nilsson M, Johansson L, Mellström D, Lorentzon M. Increased cortical porosity in women with hip fracture. J Intern Med. 2017;281: 496–506. doi:10.1111/joim.12587
53. Wehner T, Claes L, Simon U. Internal loads in the human tibia during gait. Clin Biomech. 2009;24: 299–302. doi:10.1016/j.clinbiomech.2008.12.007
54. Cristofolini L, Angeli E, Juszczyk JM, Juszczyk MM. Shape and function of the diaphysis of the human tibia. J Biomech. 2013;46: 1882–1892. doi:10.1016/j.jbiomech.2013.04.026
55. Boyd SK. Site-Specific Variation of Bone Micro-Architecture in the Distal Radius and Tibia. J Clin Densitom. 2008;11: 424–430. doi:10.1016/j.jocd.2007.12.013
56. Manske SL, Zhu Y, Sandino C, Boyd SK. Human trabecular bone microarchitecture can be assessed independently of density with second generation HR-pQCT. Bone. 2015;79: 213–221. doi:10.1016/j.bone.2015.06.006
57. Zebaze R, Ghasem-Zadeh A, Mbala A, Seeman E. A new method of segmentation of compact-appearing, transitional and trabecular compartments and quantification of cortical porosity from high resolution peripheral quantitative computed tomographic images. Bone. 2013;54: 8–20. doi:10.1016/j.bone.2013.01.007
58. Dalzell N, Kaptoge S, Morris N, Berthier A, Koller B, Braak L, et al. Bone micro-architecture and determinants of strength in the radius and tibia: age-related changes in a population-based study of normal adults measured with high-resolution pQCT. Osteoporos Int. 2009;20: 1683–1694. doi:10.1007/s00198-008-0833-6

Chapter 5: BMD-based assessment of local porosity in human femoral cortical bone

Gianluca Iori[1], Frans Heyer[2,3], Vantte Kilappa[4], Caroline Wyers[2,3], Peter Varga[5], Johannes Schneider[1], Melanie Gräsel[6], Robert Wendlandt[7], Reinhard Barkmann[6], J. P. van den Bergh[2,3] and Kay Raum[1*]

[1] Berlin-Brandenburg Center for Regenerative Therapies, Charité – Universitätsmedizin Berlin, corporate member of Freie Universität Berlin, Humboldt-Universität zu Berlin, and Berlin Institute of Health, Berlin, Germany
[2] Department of Internal Medicine, NUTRIM School of Nutrition and Translational Research in Metabolism, Maastricht University Medical Center, Maastricht, The Netherlands
[3] Department of Internal Medicine, VieCuri Medical Center, Venlo, The Netherlands
[4] Mango Solutions, Jyväskylä, Finland
[5] AO Research Institute Davos, Davos, Switzerland
[6] Sektion Biomedizinische Bildgebung, Klinik für Radiologie und Neuroradiologie, Christian-Albrechts-Universität zu Kiel, Kiel, Germany
[7] Universitätsklinikum Schleswig-Holstein, Lübeck, Germany

[*] Corresponding author: Kay Raum
E-mail: kay.raum@charite.de

Overview

In chapter 3 and 4 of the thesis, it was shown that microstructural measurements in cortical bone can identify a condition of impaired resistance to fracture of the human proximal femur. In particular, the studies presented so far indicate that an impairment of the proximal femur strength and a deterioration of the microarchitecture of the femoral neck are both associated with reduced cortical bone thickness and increased prevalence of abnormally large pores in the cortical bone of the tibia.

In chapter 3 and 4, micro-scale cavities in cortical bone were imaged using high-resolution scanning acoustic microscopy, a technique not available *in vivo*. This chapter explores the assessment of unresolved local cortical bone porosity using second-generation HR-pQCT, a modality that can be applied to living subjects. The work is performed *ex vivo* on human cadaveric proximal femur samples. Ground truth cortical bone porosity is obtained from scanning acoustic microscopy images, which are spatially registered to the HR-pQCT data. A novel approach for the measurement of cortical porosity is developed, which incorporates the BMD heterogeneity in addition to the average BMD, and reduces the prediction error compared to methods from the literature. The reasons for the improvement in the prediction of cortical porosity are discussed in appendix C of the thesis.

My contribution

I performed sample preparation, SAM measurements and all image and data analysis steps for this work. HR-pQCT measurements were initiated by FH and myself and continued by FH and CW at VieCuri Venlo (the Netherlands).

Publication notification

This is the accepted manuscript of a work published in the journal Bone, and available under:

https://www.sciencedirect.com/science/article/pii/S8756328218302187

(DOI: 10.1016/j.bone.2018.05.028)

Iori G, Heyer F, Kilappa V, Wyers C, Varga P, Schneider J, et al. BMD-based assessment of local porosity in human femoral cortical bone. Bone. 2018;114: 50–61.

Abstract

Cortical pores are determinants of the elastic properties and of the ultimate strength of bone tissue. An increase of the overall cortical porosity (Ct.Po) as well as the local coalescence of large pores cause an impairment of the mechanical competence of bone. Therefore, Ct.Po represents a relevant target for identifying patients with high fracture risk. However, given their small size, the in vivo imaging of cortical pores remains challenging. The advent of modern high-resolution peripheral quantitative computed tomography (HR-pQCT) triggered new methods for the clinical assessment of Ct.Po at the peripheral skeleton, either by pore segmentation or by exploiting local bone mineral density (BMD). In this work, we compared BMD-based Ct.Po estimates with high-resolution reference values measured by scanning acoustic microscopy. A calibration rule to estimate local Ct.Po from BMD as assessed by HR-pQCT was derived experimentally. Within areas of interest smaller than 0.5 mm^2, our model was able to estimate the local Ct.Po with an error of 3.4%. The incorporation of the BMD inhomogeneity and of one parameter from the BMD distribution of the entire scan volume led to a relative reduction of the estimate error of 30%, if compared to an estimate based on the average BMD. When applied to the assessment of Ct.Po within entire cortical bone cross-sections, the proposed BMD-based method had better accuracy than measurements performed with a conventional threshold-based approach.

Keywords:

Cortical bone; Scanning acoustic microscopy; HR-pQCT; Porosity; Image registration

5.1 Introduction

Cortical porosity (Ct.Po) is referred to cavities that permeate the extracellular mineralized matrix of cortical bone at several length scales, from millimeter-sized artery channels, to micro-scale (Haversian canals and resorption lacunae) and nano-scale (lacuno-canalicular network) pores. Throughout life, cortical bone is continuously remodeled, i.e., extracellular mineralized bone matrix is resorbed leaving remodeling cavities (also called basic multicellular units [BMUs]), which are subsequently refilled by new osteons including a central Haversian canal. These cylindrically shaped pores have a typical diameter between 25 and 200 µm [1–3], contain blood vessels and are responsible for the major part of intracortical porosity [4]. The balance

between bone tissue resorption and synthesis, which determines the porosity level, is affected by multiple factors, including age, sex, body size [5] and bone pathologies [6]. An alteration of this balance in adulthood (i.e., bone resorption rate exceeding bone formation rate) may lead to higher Ct.Po levels as a result of an increase in the number or size of pore, or a combination thereof.

Recent clinical studies using high-resolution peripheral quantitative computed tomography (HR-pQCT) associated cortical bone porosity increase with a higher incidence of fragility fractures of the distal radius [7,8]. These observations are in agreement with elastic and plastic theories of bone tissue, i.e., an increased porosity leads to decreased elastic properties [9–11] and fracture resistance [12]. In particular, researchers suggested that pores affect the fracture toughness of cortical bone by acting as stress concentrators [12,13]. With respect to this, not only the average porosity level but also the local distribution of pores plays an important role. Indeed, the occurrence of local regions of high porosity caused by the accumulation of resorption cavities within the cortical shell reduces the strength of the femoral neck [14,15]. Due to the small size of Haversian canals, a direct in vivo assessment of Ct.Po with current medical imaging devices remains impossible.

Since its introduction, high-resolution peripheral quantitative computed tomography (HR-pQCT) is increasingly applied for the characterization of cortical porosity in vivo at peripheral sites of the skeleton (i.e., distal radius and tibia) [16,17]. The potential of HR-pQCT-based Ct.Po measurements for fracture risk discrimination has been suggested recently [18]. These methods rely on the possibility to segment the spatially resolved cortical pore structure. However, such approaches are able to detect only pores that are larger than the spatial resolution limit, leading to a systematic underestimation of Ct.Po [19]. More recently, another strategy has been proposed, which utilizes bone mineral density (BMD) of HR-pQCT voxels as a surrogate measure of porosity [20]. This method is based on a two-phase composite material idealization of cortical bone, i.e., cortical bone is assumed to consist of a homogeneous extracellular bone matrix with a constant degree of mineralization and water-filled cavities. However, at the length scale of HR-pQCT voxels (i.e., 82 µm and 61 µm for first and second-generation systems, respectively), BMD is determined by the relative proportion of the void phase (i.e. pores) and by the mineral content of the extracellular bone matrix. Because of the low variability of the mineral content within mineralized bone tissue [21,22], Ct.Po has been suggested to be the major determinant of BMD. BMD voxels from HR-pQCT images convey information, which could be exploited for the direct assessment of cortical bone porosity. Recently, Jorgenson et al. [23] compared threshold and BMD-based approaches for the measurement of Ct.Po on (5 x 5 x 5) mm^3 samples obtained from human tibiae, confirming a good agreement of both strategies by comparison with (gold standard) synchrotron radiation micro-computed tomography (SRµCT).

In this context, we aimed at extending the BMD-based assessment of Ct.Po from an estimation of the sample average porosity to its local description (Study 1). To this end, we used registered second-generation HR-pQCT and 100-MHz scanning acoustic microscopy (SAM) images, which were obtained from femoral shaft samples of 20 human donors in vitro, to access local site matched BMD and Ct.Po. The characteristic error of the BMD-based measurement of Ct.Po was characterized for length scales from a few tens of microns up to the millimeter scale. We hypothesized that complementary information obtained from HR-pQCT scans could be used to further improve the Ct.Po estimation. We propose a multi-parameter model that utilizes local BMD combined with characteristics of the sample BMD histogram. Ct.Po estimates obtained with this method were compared with reference values from SAM as well as with conventional threshold-based Ct.Po estimates. Study 2 simulates the application of

the proposed model to HR-pQCT images with lower resolution (mimicking typical in vivo scan protocols) whereas in Study 3 we demonstrate its validity for the analysis of 3D volumes.

5.2 Materials and Methods

5.2.1 Sample Preparation

Twenty pairs of proximal femur samples from human cadavers (7 male, 13 female, age: 69-94 years, mean: 83.6 ± 8.0 years) were obtained from the Anatomy Institute of the Lübeck University in accordance with the German law "Gesetz über das Leichen-, Bestattungs- und Friedhofswesen des Landes Schleswig-Holstein - Abschnitt II, §9 (Leichenöffnung, anatomisch)" from 04.02.2005. The bones were frozen at -20°C immediately after dissection and were prepared for CT scanning and mechanical testing following an established protocol [24]. The proximal portion of each femur was extracted by cutting the bone at a distance of 80 mm distal from the middle point of the lesser trochanter and perpendicular to the functional axis of the femur shaft [25]. Soft tissue was removed from the femoral shaft, lesser trochanter and greater trochanter. The distal end (approx. 30 mm) of the proximal shaft was embedded in polyurethane (SG 140 / PUR 12, ebalta, Arundel, UK) (Fig. 30A).

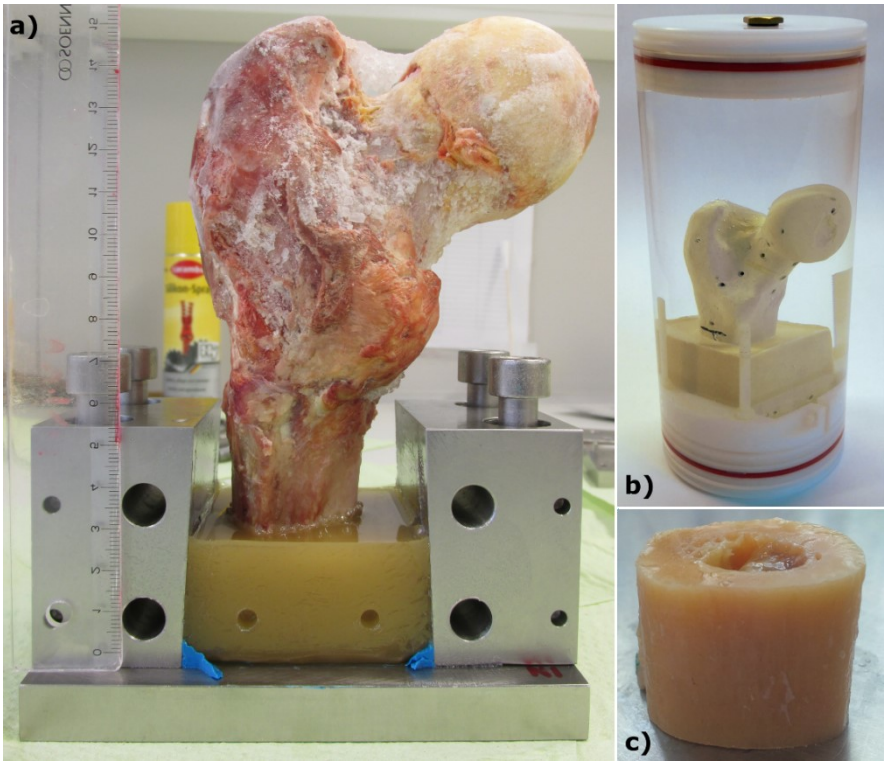

Fig. 30. (A) Preparation of a (left) proximal femur sample for HR-pQCT and SAM. The anatomical axis is drawn on the femoral shaft and a cut is realized perpendicular to this using a hand saw. A polyurethane embedding provided a holder for the HR-pQCT chamber (B). During preparation, the proximal side of the sample is wrapped with plastic bags containing dry ice (not shown here) in order to prevent the thawing of the hip.

(C) 21 mm of the proximal shaft are extracted for SAM analysis.

5.2.2 HR-pQCT scanning

The samples were placed inside a desiccator, submerged in 1% PBS solution, and exposed to partial vacuum (approx. 4 kPa) for 10 minutes right before scanning in order to remove air bubbles. The bones were then positioned inside a custom-made plastic chamber [26] (Fig. 30B) filled with 1% PBS, penicillin (50 U/ml) and streptomycin (50 µg/ml), and scanned with a second-generation HR-pQCT scanner (XtremeCT II; Scanco Medical AG, Brüttisellen, Switzerland) orienting the femur axis parallel to the z-axis of the scanner. Scanning settings were: 68 kVp X-ray tube potential, 1470 µA X-ray tube current, 200 ms integration time for 3000 projections over 180°. The acquisition required up to 18 stacks; adjusting the field of view

according to individual specimen length (min: 146 mm; max: 182 mm). Images were reconstructed as a 4608 × 4608 image matrix, yielding a 30.3 μm isotropic voxel size. A 3D Gaussian filter (σ = 1.1 voxels, radius = 2.0 voxels) was applied to the HR-pQCT image volume in order to remove high-frequency noise. Voxels integer values were converted to bone mineral density (BMD) with the scanner built-in calibration rule. According to the manufacturer's instructions, the validity of this rule was verified daily by scanning a calibration phantom with known densities (Scanco Medical AG, Brüttisellen, Switzerland). After scanning, the samples were frozen again at −20°C.

5.2.3 Scanning Acoustic Microscopy (SAM)

One 21-mm thick section (Fig. 30C) of the proximal shaft was extracted from each femur sample for a microelastic measurement by means of quantitative time-resolved SAM. Transversal cuts were performed with a band saw (EXACT GmbH, Remscheid, Germany) perpendicular to the shaft axis, 18 mm and 39 mm below the middle point of the lesser trochanter. Distances between cut planes and bottom of the sample were measured to determine the approximate position of the cross section within the HR-pQCT volume. The cross sections were washed 3 to 5 times in 1% PBS solution and approximately 5 mm of the distal side of each sample was embedded in acrylic resin (VariKleer®, Buehler Ltd., Lake Bluff, IL). Proximal surfaces were then polished on a planar grinder (Phoenix 4000, Buehler Ltd., Illinois) at a constant speed of 50 rpm and with decreasing grain size (ISO/FEPA grit: P80, P600, P1200, P2500 and P4000, Buehler Ltd., Illinois). Samples were maintained wet during surface preparation. After polishing, samples were washed and then submerged in 1% PBS for vacuum degas inside a desiccator for at least 30 min to remove air bubbles from the cortical pores. Before scanning, surfaces were cleaned with a soft paintbrush.

The acoustic measurements were performed using a custom-built quantitative scanning acoustic microscope. Device and scanning procedure have been described in detail elsewhere [27,28]. A 100-MHz spherically focused transducer (KSI 100/60°, KSI, Herborn, Germany) was used. The −6 dB bandwidth of the confocal pulse echo was 84.4–100.7 MHz, and the −6 dB depth of focus and lateral beam diameter in the focal plane were 139 μm and 19.8 μm, respectively [29]. During measurements, samples were immersed in a temperature-controlled tank containing 25 °C degassed 1% PBS. Images were acquired by moving the transducer along the x-y-plane with a scan increment of 12 μm. The scan time was up to 5 h. The recorded signals were filtered using a Chebyshev filter with cutoff frequencies of 5 and 200 MHz and the amplitude of the reflected signal was determined as the maximum of the (Hilbert-transformed) envelope signal. A previously described procedure [30] for defocus correction and conversion to acoustic impedance values was applied. For this, a reference phantom consisting of titanium and polymethylmethacrylate (PMMA), i.e. two homogenous materials with known impedances was scanned before and after each bone sample measurement.

5.2.4 Image analysis

The image processing and data workflow to the individual sub-studies of this work are shown in Fig. 31. All analyses were performed in Matlab (R2017a, The Mathworks Inc., Natick, MA, USA).

5.2.4.1 3D registration

The 3D registration of the HR-pQCT data with the SAM cross-section was accomplished using a semi-automatic procedure described in the supplementary materials in the online version of this article. Briefly, the technique was based on an initial 2D registration step, performed in xy-planes of the HR-pQCT volume to find the approximate longitudinal (z) position of the

corresponding cross-section, followed by a second step, in which the 3D misalignment between the HR-pQCT and the SAM images was corrected. After 3D registration, HR-pQCT slices were resized by bicubic interpolation to match the pixel size of the SAM image. Plots of the 2D-correlation coefficient between the SAM image and single slices of the HR-pQCT stack were compared before and after 3D registration.

5.2.4.2 Segmentation

Segmentation of the SAM images was obtained by applying a previously described adaptive threshold [28]. For the HR-pQCT images, binary masks of the bone tissue were obtained using the Otsu's method [31]. Masks of the cortical bone compartment were automatically generated for HR-pQCT data using the algorithm proposed by Burghardt et al. [16]. This step was performed on both 2D slices registered to the SAM images and 3-mm thick (~100 slices) stacks extracted around the SAM plane. The masks were then morphologically eroded using a disk-shaped structuring element with a radius of 0.06 mm to compensate for the morphological closing applied by the cortical mask algorithm, which would lead to a slight overestimation of the periosteal surface. It should be noted that no manual correction of the endosteal boundary was applied. Posterior sites of muscle insertion corresponding to the linea aspera were manually cropped and excluded from the characterization of local properties, since it was not possible to separate the cortical bone compartment from the trabecular one for this site.

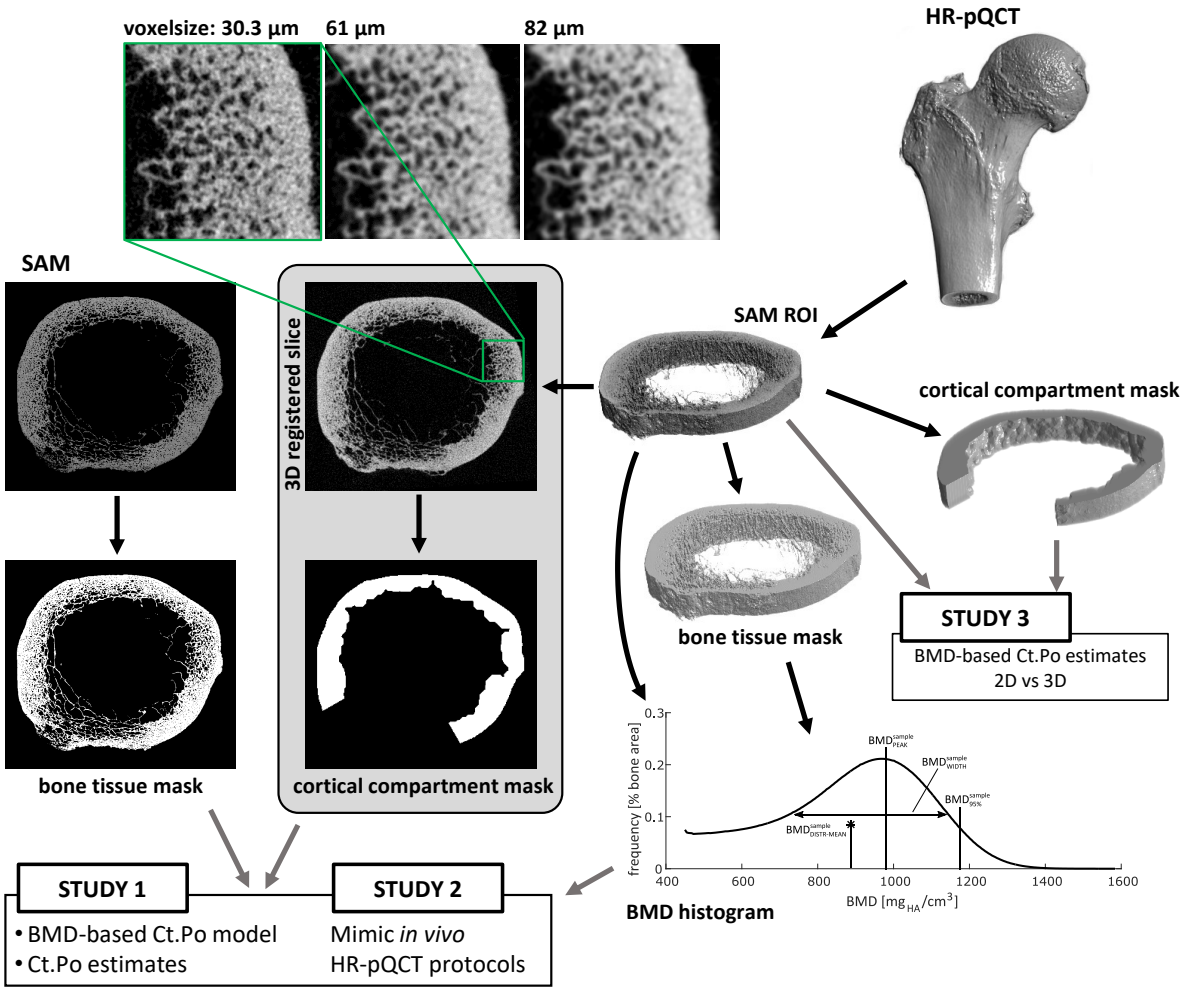

Fig. 31. Image processing steps for SAM (LEFT) and HR-pQCT (RIGHT) indicating the inputs of the different sub-studies.

5.2.5 STUDY 1: Modelling cortical bone porosity based on BMD

Hereinafter, we use the superscripts local and sample to distinguish variables assessed over local ROIs from those measured over entire samples.

5.2.5.1 Model parameters and representative volume element (RVE) size

An isotropic grid with increasing size (0.060, 0.084, 0.132, 0.204, 0.324, 0.444, 0.540, 0.660, 0.756, 0.90, 1.044, and 1.212 mm) was overlaid to the registered SAM and HR-pQCT images (Fig. 32) and only those ROIs falling entirely within the cortical bone compartment were further analyzed. The lower grid size limit was chosen, as it represents the voxel size of 2nd generation HR-pQCT scanners for in vivo scans. For each grid ROI, the local average BMD (BMD_{MEAN}^{local}) as well as the BMD inhomogeneity (expressed by means of the local BMD standard deviation BMD_{STD}^{local}) were calculated from the HR-pQCT image, whereas $Ct.Po^{local}$ was extracted from the corresponding ROI of the SAM image. $Ct.Po^{local}$ was measured from the segmented images as the number of void pixels divided by the total number of ROI pixels. Correlations between BMD_{MEAN}^{local}, BMD_{STD}^{local} and $Ct.Po^{local}$ were evaluated after pooling together the data for all samples.

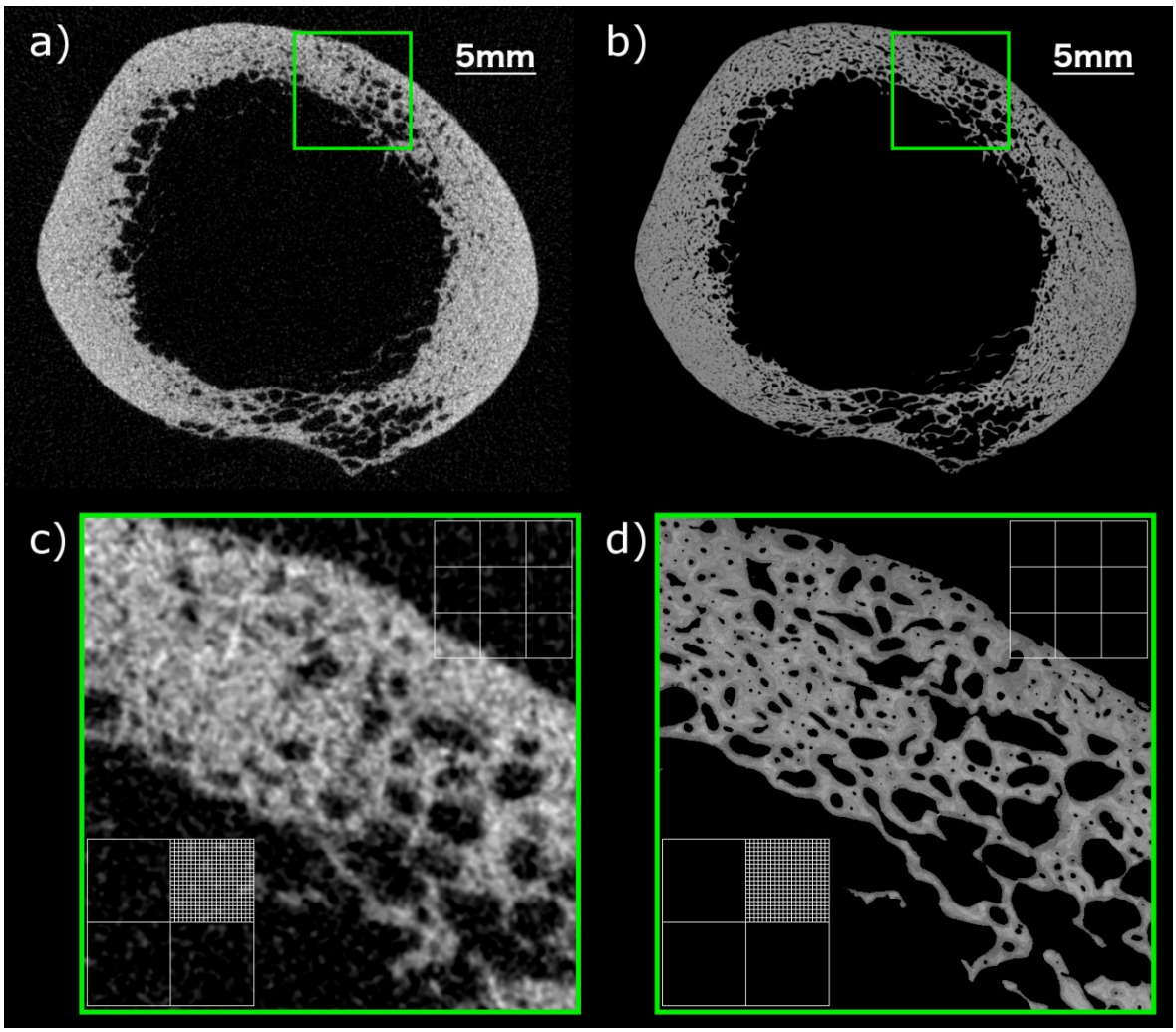

Fig. 32. Assessment of local Ct.Po, BMD and acoustic impedance from 3D-registered HR-pQCT (A) and SAM (B) images. A detail of the cortex is shown in (C) (HR-pQCT) and (D) (SAM) together with the largest and finest ROI sizes for the assessment of local properties (bottom left corner of the detail images; large ROI size: 1.212 mm, fine ROI size: 0.060 mm). The RVE size selected for the analysis of correlation between local properties (0.660 mm) is shown on the top right corner of the detail images.

In addition to the ROI-based BMD evaluation, histograms of the BMD distribution were derived, for each sample, within a sub-volume consisting of 100 slices (~3 mm) centered at the SAM cross-section. The following parameters were extracted for each sample: $BMD_{95\%}^{sample}$ (the BMD value corresponding to the 95th percentile of the BMD distribution), BMD_{PEAK}^{sample} (the distribution peak frequency), $BMD_{DISTR-MEAN}^{sample}$ and BMD_{WIDTH}^{sample} (BMD distribution weighted mean and full width at half maximum, respectively) (Fig. 33).

A linear stepwise regression of all HR-pQCT parameters (BMD_{MEAN}^{local}, BMD_{STD}^{local}, $BMD_{DISTR-MEAN}^{sample}$, BMD_{PEAK}^{sample}, BMD_{WIDTH}^{sample}, $BMD_{95\%}^{sample}$) was used to model $Ct.Po^{local}$ at each ROI size. Only ROIs with $Ct.Po^{local}$ between 0 and 40% were considered to exclude from the analysis any region belonging to potentially trabecularized sites. After adding each significant parameter to the stepwise regression, porosity estimates were characterized in terms of their Root Mean Squared Error (RMSE), allowing the selection of the minimum number of explanatory variables for a Ct.Po model. A representative volume element (RVE) size was selected as the smallest ROI size providing an RMSE of the $Ct.Po^{local}$ estimate below 3%. This size was adopted for all further analyses.

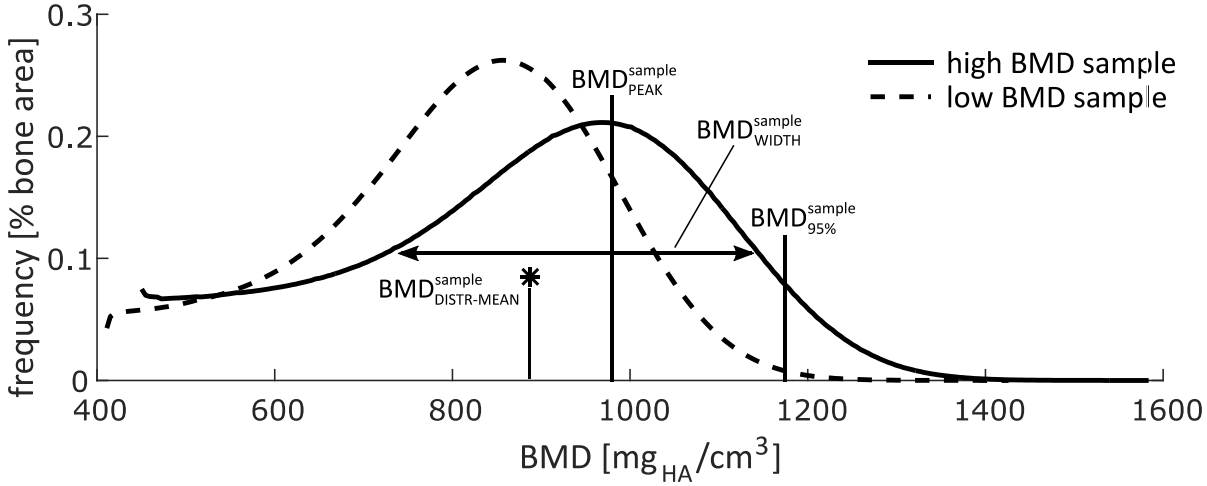

Fig. 33. Histograms of the BMD distribution for a high BMD donor and a low BMD one. The 95th percentile level of the BMD histogram ($BMD_{95\%}^{sample}$) as well as the histogram weighted mean ($BMD_{DISTR-MEAN}^{sample}$), peak value ($BMD_{PEAK}^{sample}$) and full width at half maximum of the distribution (BMD_{WIDTH}^{sample}) are shown for the high BMD sample curve.

5.2.5.2 Ct.Po predictions

After model derivation, $Ct.Po^{local}$ predictions obtained using the RVE size were compared with the $Ct.Po^{local}$ measured from SAM images. Ct.Po was also predicted for entire femoral cross-sections ($Ct.Po^{sample}$). In order to do this, BMD_{MEAN}^{sample} and BMD_{STD}^{sample} were calculated over the cortical compartment. For comparison, threshold-based measurements of $Ct.Po^{sample}$ were obtained for the same cortical bone region by means of a previously described approach [16]. Both, BMD-model based and threshold-based $Ct.Po^{sample}$ values were compared with values measured with SAM.

5.2.6 STUDY 2: conventional HR-pQCT resolutions

In vivo HR-pQCT images were simulated from the original 3D registered volumes. First, a Gaussian filter was applied to mimic the point-spread function (PSF) of in vivo scan protocols of 1st and 2nd generation HR-pQCT scanners (i.e. 130 and 95 µm, respectively [32]). The volumes were then downsampled to the voxel size of the corresponding in vivo scan protocols

(i.e., 82 and 61 µm) and BMD_{MEAN}^{local}, BMD_{STD}^{local} (at the RVE size) as well as BMD distribution parameters were recalculated. The same procedure for the derivation of a porosity model and for the prediction of $Ct.Po^{local}$ and $Ct.Po^{sample}$ described in section 1.1.1 was applied to the lower resolution data.

5.2.7 STUDY 3: 3D Ct.Po estimates

We investigated the agreement of 2D slice based $Ct.Po^{sample}$ predictions with those obtained from a 3-mm thick 3D cross-section extracted around the SAM cut plane. For predicting $Ct.Po^{sample}$ over a 3D volume, BMD_{MEAN}^{sample} and BMD_{STD}^{sample} were extracted from the entire cortical bone volume.

5.2.8 Statistical analysis

Normality of the parameter distributions was tested using the Shapiro-Wilk test. Spearman's rank correlation coefficients ρ were calculated to assess the relationship between BMD parameters and Ct.Po. Linear stepwise regressions were used for the model development. The following post-hoc leave-n-out test was performed for Ct.Po model cross-validation: 12 randomly selected samples (approx. 30% of the data) were excluded for model derivation and the RMSE of the $Ct.Po^{local}$ estimate of the left out samples was characterized; 1000 repetitions of the test were performed. Pearson linear regression analysis and Bland-Altmann plots [33] were used to compare the model predictions with the SAM-based values. Differences between properties measured on the left and right samples were tested using a Wilcoxon rank-sum test. A paired *t*-test (or Wilcoxon signed-rank test for all variables that did not follow a normal distribution) was used to assess sample "left versus right" differences as well as the agreement between $Ct.Po^{sample}$ estimates and reference $Ct.Po^{sample}$ from SAM. The significance level was set to $p = 0.05$.

5.3 Results

5.3.1 3D registration

For 39 of the 40 evaluated samples, the 3D registration procedure was able to identify on the HR-pQCT volume a best fitting sectioning plane corresponding to the SAM image. The fitting algorithm converged, on average, after 114 trials. No convergence after a maximum number of 1000 trials was reached in one case. The exception could be explained by a severe misalignment (inclination) between the HR-pQCT slices plane and the cross-sectional plane scanned with SAM, invalidating the first 2D rigid registration step. This sample was excluded from further calculations. For the remaining 39 samples, the average maximum 2D correlation coefficients were 0.83 and 0.86 before and after 3D registration, respectively. An improvement of the correlation coefficient was observed for all samples after the 3D registration step (Fig. 34).

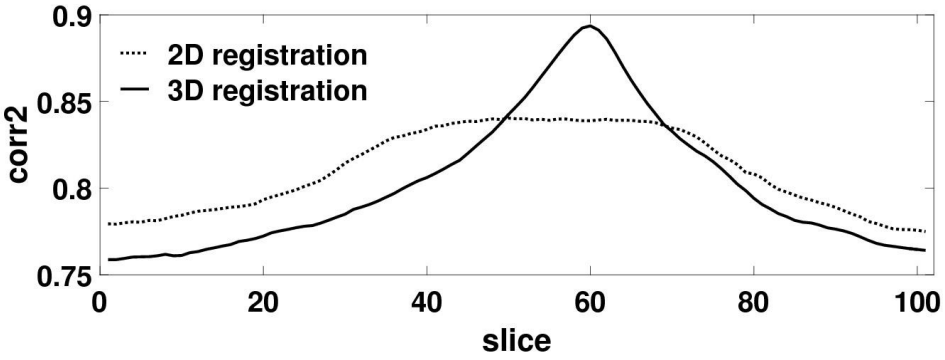

Fig. 34. Representative plot of the 2D correlation coefficient (corr2) between single slices of the HR-pQCT dataset and the SAM image before and after 3D registration of the HR-pQCT data. Data is showed for 100 slices in proximity of the cut plane for SAM cross section extraction. The HR-pQCT slice corresponding to the SAM plane can be identified as the slice with maximum corr2 after 3D registration.

5.3.2 STUDY 1

5.3.2.1 Ct.Po model

Both BMD_{MEAN}^{local} and BMD_{STD}^{local} were correlated with $Ct.Po^{local}$ at all evaluated ROI sizes, with Spearman's ρ ranging from 0.38 to 0.94 and from 0.21 to 0.91 for BMD_{MEAN}^{local} and BMD_{STD}^{local}, respectively (ROI size: 60 µm, 2.1 million evaluated ROIs to ROI size: 1.212 mm, 3294 evaluated ROIs). Stepwise linear regression always included BMD_{MEAN}^{local} as the first parameter, followed by BMD_{STD}^{local} and BMD_{WIDTH}^{sample}. Given the large number of observations, all variables had p-value smaller than 0.001. However, no further improvement of the model RMSE was observed after including more than 3 HR-pQCT variables (Fig. 35). We therefore restricted the number of model parameters to 3, yielding RMSE values of 8.89% and 2.57% for ROI sizes of $(60\ \mu m)^2$ (not shown) and $(1.212\ mm)^2$, respectively (Fig. 35). The smallest ROI size reaching the criterion of RMSE ≤ 3% was $(660\ \mu m)^2$, which was used for all further analyses. Under these conditions, the RMSE of $Ct.Po^{local}$ dropped from 4.3% to 3.0% (30% relative reduction) and 594 estimates were obtained, on average, per sample cross section (max: 825; min: 256 for the sample with the smallest cortical thickness). The following model equation for $Ct.Po^{local}$ was obtained:

$$Ct.Po^{local} = 36.79\% - \left(0.0539\ BMD_{MEAN}^{local} - 0.0439\ BMD_{STD}^{local} - 0.0527\ BMD_{WIDTH}^{sample}\right)\frac{\%}{mg_{HA}/cm^3} \quad (13)$$

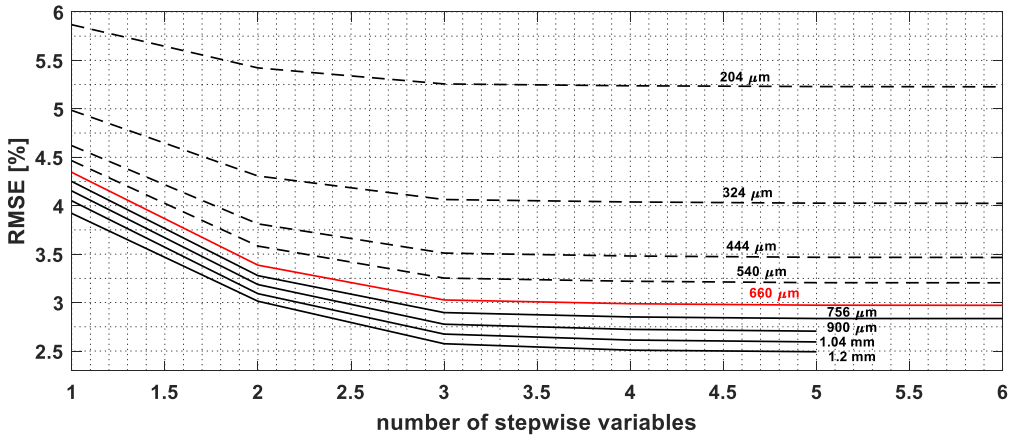

Fig. 35. Root Mean Squared Error of the $Ct.Po^{local}$ prediction for increasing ROI size and number of explanatory HR-pQCT variables included in the stepwise $Ct.Po^{local}$ model. Results obtained with ROI sizes of 0.060 mm, 0.084 mm, and 0.132 mm are omitted for clarity.

5.3.2.2 Correlation of local and sample properties

Local variables measured within 660 x 660 µm² RVEs were pooled for all 39 samples: $Ct.Po^{local}$, BMD_{MEAN}^{local} and BMD_{STD}^{local} were in the range between 1.8–76.4 % (CV: 68%), 346–1121 mg_{HA}/cm^3 (CV: 13%) and 63–545 mg_{HA}/cm^3 (CV: 53%), respectively, for a total number of 23,149 evaluated RVEs (Table 19). Approximately 5% of all RVEs had Ct.Po > 40% and were discarded from the regression analyses. Both, BMD_{MEAN}^{local} and BMD_{STD}^{local} were strongly correlated with Ct.Po ($\rho = -0.87$; $p < 0.001$ and $\rho = 0.89$; $p < 0.001$). When measured over entire sample cross-sections, the BMD inhomogeneity (BMD_{STD}^{sample}) was a better predictor for $Ct.Po^{sample}$ than BMD_{MEAN}^{local} (Spearman's $\rho = 0.80$; $p < 0.001$ and $\rho = -0.57$; $p < 0.001$, respectively). No difference between left and right populations was observed for all sample variables. Only BMD_{STD}^{local} was different between left and right.

Table 19. Local and sample intracortical porosity and BMD parameters.

Local properties (*N* = 23,149)		**Mean ± SD**	**Range**	**rho**	**p**
$Ct.Po^{local}$	[%]	16.7 ± 11.3	1.8 ÷ 76.4		ns[a]
BMD_{MEAN}^{local}	[mg_{HA}/cm^3]	855.3 ± 113.0	346.1 ÷ 1121.0	-0.87	ns[a]
BMD_{STD}^{local}	[mg_{HA}/cm^3]	181.9 ± 96.7	63.1 ÷ 545.4	0.89	0.02[a]
Sample properties (N = 39)					
$Ct.Po^{sample}$	[%]	12.0 ± 3.6	6.8 ÷ 21.0		ns[b]
BMD_{MEAN}^{sample}	[mg_{HA}/cm^3]	898.8 ± 36.6	820.4 ÷ 973.6	-0.57	ns
BMD_{STD}^{sample}	[mg_{HA}/cm^3]	152.1 ± 16.5	125.0 ÷ 190.2	0.80	ns[b]
BMD_{WIDTH}^{sample}	[mg_{HA}/cm^3]	335.5 ± 29.9	298.6 ÷ 422.7	0.70	ns[b]
$BMD_{DISTR-MEAN}^{sample}$	[mg_{HA}/cm^3]	867.4 ± 39.8	789.8 ÷ 949.4	-0.71	ns
BMD_{PEAK}^{sample}	[mg_{HA}/cm^3]	927.7 ± 33.0	857.0 ÷ 990.5	-0.39	ns
$BMD_{95\%}^{sample}$	[mg_{HA}/cm^3]	1132.5 ± 40.5	1054.4 ÷ 1224.7	-0.48	ns

Mean value, standard deviation (SD); minimum and maximum values; correlation with Ct.Po (Spearman's rho); significance of the paired sample *t*-test (p) for the comparison "left versus right".
[a] Wilcoxon rank-sum test
[b] Wilcoxon signed rank test

5.3.2.3 Ct.Po estimates

$Ct.Po^{local}$ estimates (RVE size: (660 µm)², 23,149 ROIs evaluated) obtained with Eq. (13) showed excellent agreement with the local $Ct.Po^{local}$ measured by SAM, providing a correlation coefficient of $R^2 = 0.91$ ($p < 0.001$) and root mean squared error of the estimate RMSE = 3.4% (Fig. 36).

Similarly, $Ct.Po^{sample}$ estimates for 2D HR-pQCT slices were in very good agreement with $Ct.Po^{sample}$ obtained from the corresponding registered SAM images ($N = 39$, $p < 0.001$, $R^2 = 0.80$, Fig. 37A). In contrast, the threshold-based approach had a lower correlation coefficient ($R^2 = 0.77$, $p < 0.001$) and was affected by a measurement bias that was highly dependent on the $Ct.Po^{sample}$ level (Fig. 37C). Both methods significantly underestimated $Ct.Po^{sample}$ ($p < 0.001$) but the deviation of the threshold-based approach remained much larger (mean difference: −10.44% versus −0.91% for the BMD-based method, Fig. 37B and C).

5.3.2.4 Model cross-validation

Twelve out of 39 samples were left out for $Ct.Po^{local}$ model cross-validation. $Ct.Po^{local}$ estimates obtained for the left out data points had an RMSE of 3.51 ± 0.22% (min: 2.88%; max: 4.32%), which was only slightly larger than the 3.4% error obtained with the entire sample set (Fig. 36A).

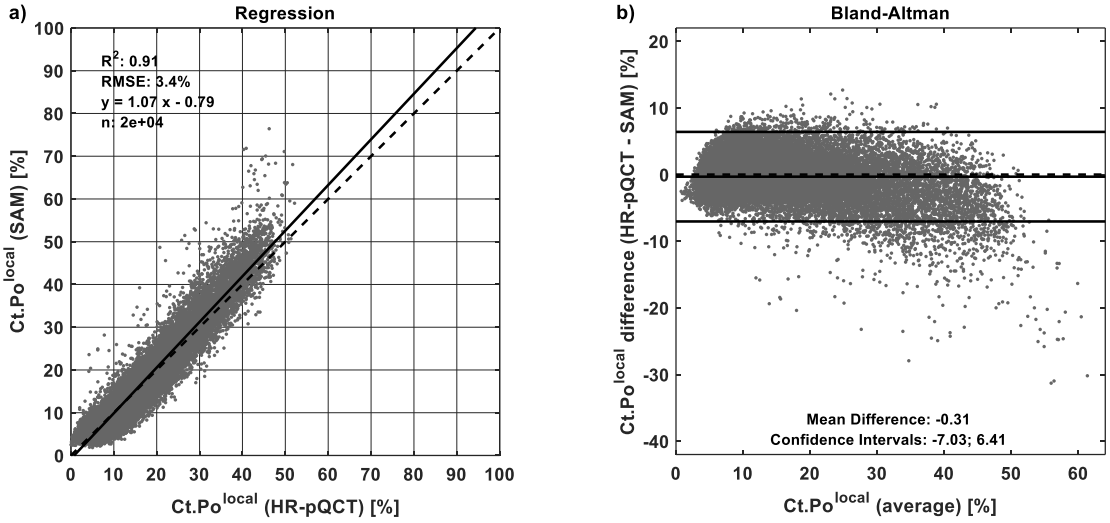

Fig. 36. BMD-based $Ct.Po^{local}$ estimates obtained with Eq. (13) over (660 µm)^2 RVEs from (N = 39) samples. Regression (A) and corresponding Bland-Altman plot (B).

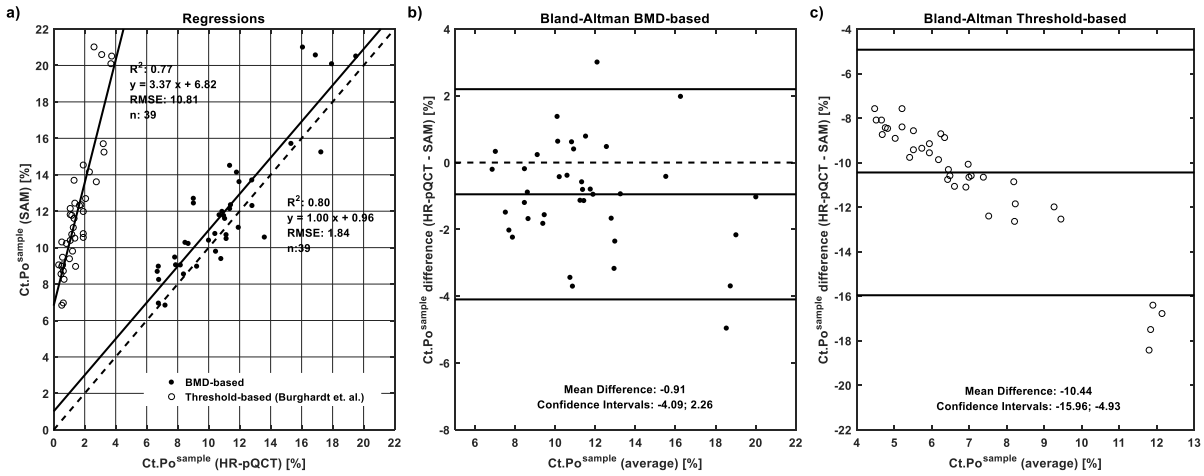

Fig. 37. Comparison of BMD-based $Ct.Po^{sample}$ estimates obtained for entire proximal femur cross-sections by means of the proposed model with $Ct.Po^{sample}$ measurements realized on the same HR-pQCT cross section using a threshold-based approach. Linear regression analysis (A) and Bland-Altman plots (B and C) of the comparison of both HR-pQCT techniques with the reference (12-µm pixel size SAM). Mean measurement difference and its confidence intervals are shown with horizontal lines in (B) and (C). (N = 39 cadaveric proximal femur samples from human donors).

5.3.3 STUDY 2: simulated in vivo resolution HR-pQCT

A simulated degradation of the image resolution affected the calculation of the BMD (local as well as sample) inhomogeneity as well as all BMD distribution parameters (Table 20). Nevertheless, the correlation between BMD parameters and porosity remained essentially unchanged.

Table 20. Local and sample BMD parameters obtained from datasets with native resolution and from (simulated) in vivo resolution HR-pQCT (mean value, standard deviation (SD) and Spearman's rho of the correlation with Ct.Po).

		2nd generation; *in vitro*		2nd generation; *in vivo*		1st generation; *in vivo*	
Local properties (*N* = 23,149)		**Mean ± SD**	**rho**	**Mean ± SD**	**rho**	**Mean ± SD**	**rho**
BMD_{MEAN}^{local}	[mg_{HA}/cm^3]	855.3 ± 113.0	−0.87	854.8 ± 113.0	−0.88	854.4 ± 113.0	−0.88
BMD_{STD}^{local}	[mg_{HA}/cm^3]	181.9 ± 96.7	0.89	149.8 ± 104.5	0.89	137.6 ± 106.4	0.88
Sample properties (*N* = 39)							
BMD_{MEAN}^{sample}	[mg_{HA}/cm^3]	898.8 ± 36.6	−0.57	896.5 ± 36.7	−0.58	894.9 ± 36.7	−0.58
BMD_{STD}^{sample}	[mg_{HA}/cm^3]	152.1 ± 16.5	0.80	123.6 ± 16.7	0.83	114.6 ± 16.0	0.83
BMD_{WIDTH}^{sample}	[mg_{HA}/cm^3]	335.5 ± 29.9	0.70	233.3 ± 35.1	0.64	213.6 ± 38.8	0.65
$BMD_{DISTR-MEAN}^{sample}$	[mg_{HA}/cm^3]	867.4 ± 39.8	−0.71	858.0 ± 40.9	−0.73	851.7 ± 42.1	−0.76
BMD_{PEAK}^{sample}	[mg_{HA}/cm^3]	927.7 ± 33.0	−0.39	934.2 ± 35.4	−0.33	934.6 ± 35.3	ns
$BMD_{95\%}^{sample}$	[mg_{HA}/cm^3]	1132.5 ± 40.5	−0.48	1059.1 ± 35.8	−0.41	1040.6 ± 34.4	−0.37

The error of the $Ct.Po^{local}$ estimate obtained from simulated in vivo images was only 0.1% and 0.2% larger (3% and 6% relative increase), respectively for 2nd and 1st generation HR-pQCT, if compared to native resolution (Table 21). The effect on $Ct.Po^{sample}$ estimates was stronger: 9% and 18% relative increase of the RMSE compared to results obtained with 30.3 µm voxels.

Table 21. Local and sample porosity estimates obtained from datasets with native resolution and from (simulated) in vivo resolution HR-pQCT (R^2, RMSE and mean difference (MD) of the comparison with reference SAM Ct.Po).

$Ct.Po^{local}$	Resolution [µm]	Voxel size [µm]	R^2	RMSE [%]	MD [%]
2nd generation; *in vitro*	55.9	30.3	0.91	3.4	-0.3
2nd generation; *in vivo*	95.0	61.0	0.91	3.5	-0.3
1st generation; *in vivo*	130.0	82.0	0.90	3.6	-0.3
$Ct.Po^{sample}$					
2nd generation; *in vitro*	55.9	30.3	0.80	1.8	0.8
2nd generation; *in vivo*	95.0	61.0	0.77	2.0	1.1
1st generation; *in vivo*	130.0	82.0	0.74	2.2	1.3
model coefficients					
2nd generation; *in vitro*	$Ct.Po^{local} = 36.79\% - (0.0539\ BMD_{MEAN}^{local} - 0.0439\ BMD_{STD}^{local} - 0.0527\ BMD_{WIDTH}^{sample}) \frac{\%}{mg_{HA}/cm^3}$				
2nd generation; *in vivo*	$Ct.Po^{local} = 45.24\% - (0.0525\ BMD_{MEAN}^{local} - 0.0421\ BMD_{STD}^{local} - 0.0416\ BMD_{WIDTH}^{sample}) \frac{\%}{mg_{HA}/cm^3}$				
1st generation; *in vivo*	$Ct.Po^{local} = 49.48\% - (0.0542\ BMD_{MEAN}^{local} - 0.0397\ BMD_{STD}^{local} - 0.0359\ BMD_{WIDTH}^{sample}) \frac{\%}{mg_{HA}/cm^3}$				

5.3.4 STUDY 3: $Ct.Po^{sample}$ prediction from 3D volumes

BMD-based $Ct.Po^{sample}$ predictions obtained from 2D cross-sections were not significantly different from predictions obtained from 3-mm thick regions extracted around the SAM cross-section (p = 0.60, Fig. 38).

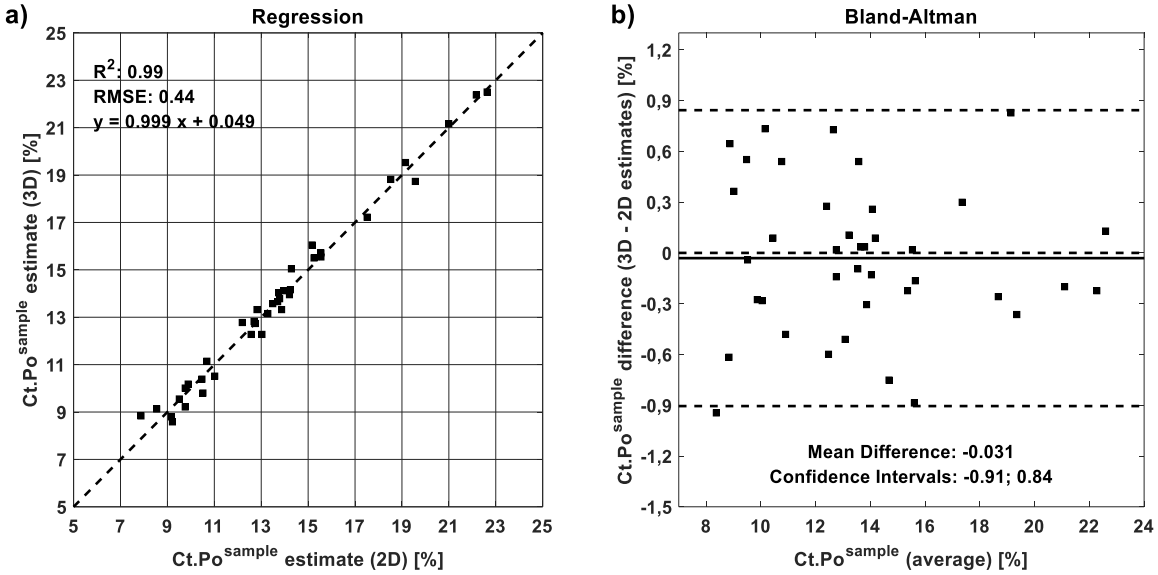

Fig. 38. 2D vs 3D $Ct.Po^{sample}$ estimates; regression (A) and Bland-Altman plot (B). 2D $Ct.Po^{sample}$ estimates were obtained from single HR-pQCT slices (N = 39) extracted at the location of SAM. 3D estimates were calculated over a 3-mm thick cross-section centered on the slice considered for the 2D estimation.

5.4 Discussion

Within this ex vivo study on human proximal femur samples, we used registered HR-pQCT and SAM images to investigate the local association between volumetric BMD and porosity in cortical bone. At a spatial length scale of (660 μm)², both the BMD inhomogeneity (assessed as the standard deviation of BMD within the investigated region) as well as the average BMD were strongly correlated with the local Ct.Po (Spearman's ρ = 0.89 and -0.87, respectively) throughout the cortex of 20 human donors. When sample properties were calculated considering entire cortical sections, the inhomogeneity of BMD alone became the better predictor of (Spearman's ρ = 0.80). The strong correlation between BMD as assessed by QCT and bone porosity was already reported for trabecular [26,34] as well as for cortical bone [17,34,35]. These studies have investigated bone regions with dimensions of a few millimeter or more. Our study on HR-pQCT images confirms the BMD-Ct.Po correlation also for sub-millimeter length scales, suggesting that the information contained within the HR-pQCT voxels may be exploited for an accurate estimate of the local porosity.

5.4.1 STUDY 1: BMD-based Ct.Po assessment

We propose the assessment of based on the local BMD as well as on the distribution of BMD throughout the entire examined cortical bone tissue.

When added to the porosity model, the BMD inhomogeneity (BMD_{STD}^{local}) together with BMD_{WIDTH}^{sample}, a parameter derived from the sample BMD distribution histogram, provided a relative reduction of the $Ct.Po^{local}$ estimate RMSE of 30% compared with a model based on BMD_{MEAN}^{local} alone. It should be noted that the model of Eq. (13) was obtained experimentally

with no a priori assumption regarding the attenuation or BMD level of fully mineralized bone and provided $Ct.Po^{local}$ estimates with an RMSE of 3.4% for sub-millimeter regions of compact cortical bone ($Ct.Po^{local} < 40\%$).

A variety of texture indexes was proposed for the structural characterization of bone from CT images, which were not investigated here. The potential of fractal measurements such as lacunarity and fractal signature [36] or variogram approaches like the Trabecular Bone Score (TBS) [37] was demonstrated for trabecular bone. Recently, Lowitz et al. applied BMD inhomogeneity measurements (together with four other texture parameters) to HR-pQCT images of (trabecular and) cortical bone ROIs of human knee joints [38]. Our study makes use of very limited texture information but shows how this can be utilized for the measurement of porosity also in cortical bone.

We applied the derived model to obtain $Ct.Po^{sample}$ estimates for entire cortical bone cross-sections and compared these results with threshold-based $Ct.Po^{sample}$ estimates. In agreement with the results of other studies [17,20,23], a threshold-based approach underestimates $Ct.Po^{sample}$ due to its intrinsic inability to detect pores with characteristic sizes below the scanner resolution. Our data confirms this finding also for second generation HR-pQCT images obtained at 30.3 µm voxel size.

As already reported by Zebaze et al. [20], the bias of the threshold-based measurement was dependent on the $Ct.Po^{sample}$ level (see Bland-Altman plot of Fig. 37C). In the study of Jorgenson et al. [23], a similar trend is visible for Ct.Po up to 20%. For larger values (up to 50%), the bias became independent of Ct.Po.

5.4.2 STUDY 2: towards in vivo HR-pQCT

Our HR-pQCT images were acquired using a voxel size (30.3 µm) which is only available ex vivo. This poses a question concerning the translation of our findings for in vivo HR-pQCT applications (for comparison, the voxel size for in vivo measurements are 82 and 61 µm for first and second-generation HR-pQCT systems, respectively). Primarily, the level of porosity information conveyed by BMD voxels needs to be confirmed also for lower resolution HR-pQCT protocols. For this study, we simulated second (61 µm) to first (82 µm) generation HR-pQCT in vivo voxels by low-pass filtering and downsampling the 30.3 µm voxels obtained with the ex vivo scanning protocol of a second-generation HR-pQCT. BMD distribution histograms are flattened and constantly shifted towards lower BMD levels as the voxel size increases. Nevertheless, BMD inhomogeneity and BMD distribution information remained available also for the simulated in vivo images. Particularly, the correlation coefficient between porosity and the BMD inhomogeneity remained as high as 0.88 and 0.83 for local and sample measurements, respectively, suggesting that this method may also be applicable for in vivo measurements in patients. The coefficients of the porosity model were different for the three investigated image resolutions (Table 21), confirming that specific calibration rules should be established with respects to scanner, measurement site, and system settings.

Besides image quality, the effect of artifacts such as image noise and beam hardening changes with scan resolution and source voltage as well as within different families of devices. The signal-to-noise ratio is also affected by the presence of soft tissues, which could be disregarded in our experiment. In a recent multi-site investigation, Burghardt et al. [39] concluded on the good agreement of bone density measurements performed with different HR-pQCT scanners. BMD assessments were less affected by intra-site variability compared to structural (i.e., Ct.Po) parameters obtained by conventional segmentation. In agreement with this finding, our results further support the reliability of a porosity calibration rule for HR-pQCT scanners based on BMD distribution parameters.

5.4.3 STUDY 3: validity of a 3D $Ct.Po^{sample}$ estimation

Previous comparative studies made use of 3D synchrotron radiation µCT (SRµCT) as reference for porosity [17,23]. SRµCT provides 3D images at the necessary resolution. However, the field of view is limited, which restricts the analysis to small tissue regions. In our study, we obtained $Ct.Po^{local}$ by means of SAM, which allowed us to measure porosity over entire femoral shaft cross-sections, but on 2D planes.

100-MHz SAM provides a spatial resolution similar to that obtained by SRµCT at 10-µm voxel size [29,40]. In diaphyseal cortical bones, the Haversian canals are predominantly orientated parallel to the long bone axis and their average length is 4 mm [41]. Due to this translational symmetry, the porosity values derived from a single cross-section can be assumed representative also for adjacent cross-sectional stacks. To verify that our procedure for the BMD-based $Ct.Po^{sample}$ estimate is also valid for 3D HR-pQCT cross-sections (for which reference data was not available) we compared single 2D cross-sections with those assessed in an adjacent 3-mm thick volume. The results support the generic applicability of the proposed model.

5.4.4 Perspective

A BMD-based measurement of $Ct.Po^{local}$ offers several advantages. First, the scanner ability to resolve and threshold single cortical pores do not limit the $Ct.Po^{local}$ estimation. This allows to minimize partial volume effects and to take into account the contribution of pores with characteristic diameters below the resolution limit. It should be noted, however, that the reported model does not consider pores smaller than the resolution limit of the SAM image, e.g. osteocytes and their canaliculi. The local character of the proposed porosity model allows not only the estimation of a patient-specific mean cortical bone porosity, but also the 3D mapping of local cortical porosity within the scanned bone region. This can be used for the detection of local regions with altered pore morphology, e.g., regions affected by a higher bone resorption rate and subsequent bone loss, impaired by decreased elastic properties [11] and bone fracture resistance [14,15,42].

Techniques based on the 3D mapping of the bone tissue mechanical properties from BMD voxels have been proposed and validated for Finite Element analyses of the mechanical competence of long bones [43,44]. Particularly, the relationship of bone tissue porosity with both elastic and failure properties have been elucidated [9–12,45]. While the macroscopic mechanical behavior of cortical and trabecular tissue has been suggested to depend similarly on the bone volume fraction [44], calibration rules for the local mapping of the volume fraction from BMD have been established only for trabecular tissue [26]. Our work extends this approach also to human cortical bone tissue.

Another field of application of the $Ct.Po^{local}$ mapping is the combination with in vivo bone quantitative ultrasound (QUS). The transmission of acoustic waves through and along the cortical bone shell can be used to infer structural (e.g., Ct.Po, Ct.Th) and material (e.g., extracellular matrix mineralization and stiffness) properties of cortical bone [46,47]. However, the relative contributions of structural and material properties to the measured sound propagation characteristics remain challenging to discern [46]. QUS devices are portable, use non-ionizing radiation, and are increasingly applied in clinical studies [48,49] at distal sites of the skeleton (e.g., radius and tibia), which represent the same imaging target of HR-pQCT. With this respect, 3D descriptions of the local cortical porosity obtained from HR-pQCT could be combined with site-matched experimental measurements and numerical simulations of ultrasound propagation in long bones, to help elucidating the interplay between ultrasound and the cortical microstructure.

5.5 Conclusion

BMD measurements obtained by HR-pQCT can be used for the in vivo assessment of Ct.Po. We confirm the use of BMD also for the local mapping of porosity on regions of cortical bone below 0.5 mm in size. In addition, we propose a rule for the cortical porosity estimation based on multiple parameters that are derived from HR-pQCT data. Applied to ex vivo samples, this method is more accurate than established BMD and threshold-based approaches.

Conflicts of interest

None.

Acknowledgments

This work was supported by the Deutsche Forschungsgemeinschaft (DFG Ra1380/9-1), by the Bundesministerium für Bildung und Forschung (BMBF, musculoskeletal research network subproject "characterization of cortical and subchondral bone"), by the German Academic Exchange Service (DAAD), and by the Weijerhors Foundation (grant no. WH2). We acknowledge Mario Thiele for the data archiving, Dr. Daniel Rohrbach for the scripts for BMD histogram analysis and Dr. Ahmed BenSaïda for the Matlab implementation of the Shapiro-Wilk test.

References

1. Carter Y, Thomas CDL, Clement JG, Peele AG, Hannah K, Cooper DML. Variation in osteocyte lacunar morphology and density in the human femur — a synchrotron radiation micro-CT study. Bone. 2013;52: 126–132. doi:10.1016/j.bone.2012.09.010
2. Wachter NJ, Augat P, Krischak GD, Mentzel M, Kinzl L, Claes L. Prediction of cortical bone porosityIn Vitro by microcomputed tomography. Calcif Tissue Int. 2001;68: 38–42. doi:10.1007/BF02685001
3. Currey JD, Shahar R. Cavities in the compact bone in tetrapods and fish and their effect on mechanical properties. J Struct Biol. 2013;183: 107–122. doi:10.1016/j.jsb.2013.04.012
4. Cooper DML, Kawalilak CE, Harrison K, Johnston BD, Johnston JD. Cortical Bone Porosity: What Is It, Why Is It Important, and How Can We Detect It? Curr Osteoporos Rep. 2016;14: 187–198. doi:10.1007/s11914-016-0319-y
5. Cooper DML, Thomas CDL, Clement JG, Turinsky AL, Sensen CW, Hallgrímsson B. Age-dependent change in the 3D structure of cortical porosity at the human femoral midshaft. Bone. 2007;40: 957–965. doi:10.1016/j.bone.2006.11.011
6. Seeman E. Pathogenesis of bone fragility in women and men. The Lancet. 2002;359: 1841–1850. doi:10.1016/S0140-6736(02)08706-8
7. Bala Y, Zebaze R, Ghasem-Zadeh A, Atkinson EJ, Iuliano S, Peterson JM, et al. Cortical Porosity Identifies Women With Osteopenia at Increased Risk for Forearm Fractures. J Bone Miner Res. 2014;29: 1356–1362. doi:10.1002/jbmr.2167
8. Bala Y, Bui QM, Wang X-F, Iuliano S, Wang Q, Ghasem-Zadeh A, et al. Trabecular and Cortical Microstructure and Fragility of the Distal Radius in Women. J Bone Miner Res. 2015;30: 621–629. doi:10.1002/jbmr.2388
9. Currey JD. The effect of porosity and mineral content on the Young's modulus of elasticity of compact bone. J Biomech. 1988;21: 131–139. doi:10.1016/0021-9290(88)90006-1

10. Schaffler MB, Burr DB. Stiffness of compact bone: Effects of porosity and density. J Biomech. 1988;21: 13–16. doi:10.1016/0021-9290(88)90186-8
11. Granke M, Grimal Q, Saïed A, Nauleau P, Peyrin F, Laugier P. Change in porosity is the major determinant of the variation of cortical bone elasticity at the millimeter scale in aged women. Bone. 2011;49: 1020–1026. doi:10.1016/j.bone.2011.08.002
12. Yeni YN, Brown CU, Wang Z, Norman TL. The influence of bone morphology on fracture toughness of the human femur and tibia. Bone. 1997;21: 453–459. doi:10.1016/S8756-3282(97)00173-7
13. Currey JD. Stress Concentrations in Bone. J Cell Sci. 1962;s3-103: 111–133.
14. Bell KL, Loveridge N, Power J, Garrahan N, Meggitt BF, Reeve J. Regional differences in cortical porosity in the fractured femoral neck. Bone. 1999;24: 57–64. doi:10.1016/S8756-3282(98)00143-4
15. Jordan GR, Loveridge N, Bell KL, Power J, Rushton N, Reeve J. Spatial clustering of remodeling osteons in the femoral neck cortex: a cause of weakness in hip fracture? Bone. 2000;26: 305–313. doi:10.1016/S8756-3282(99)00272-0
16. Burghardt AJ, Buie HR, Laib A, Majumdar S, Boyd SK. Reproducibility of direct quantitative measures of cortical bone microarchitecture of the distal radius and tibia by HR-pQCT. Bone. 2010;47: 519–528. doi:10.1016/j.bone.2010.05.034
17. Ostertag A, Peyrin F, Fernandez S, Laredo JD, de Vernejoul MC, Chappard C. Cortical measurements of the tibia from high resolution peripheral quantitative computed tomography images: A comparison with synchrotron radiation micro-computed tomography. Bone. 2014;63: 7–14. doi:10.1016/j.bone.2014.02.009
18. Burghardt AJ, Kazakia GJ, Ramachandran S, Link TM, Majumdar S. Age- and gender-related differences in the geometric properties and biomechanical significance of intracortical porosity in the distal radius and tibia. J Bone Miner Res Off J Am Soc Bone Miner Res. 2010;25: 983–993. doi:10.1359/jbmr.091104
19. Zebaze R, Seeman E. Cortical Bone: A Challenging Geography. J Bone Miner Res. 2015;30: 24–29. doi:10.1002/jbmr.2419
20. Zebaze R, Ghasem-Zadeh A, Mbala A, Seeman E. A new method of segmentation of compact-appearing, transitional and trabecular compartments and quantification of cortical porosity from high resolution peripheral quantitative computed tomographic images. Bone. 2013;54: 8–20. doi:10.1016/j.bone.2013.01.007
21. Follet H, Boivin G, Rumelhart C, Meunier PJ. The degree of mineralization is a determinant of bone strength: a study on human calcanei. Bone. 2004;34: 783–789. doi:10.1016/j.bone.2003.12.012
22. Bergot C, Wu Y, Jolivet E, Zhou LQ, Laredo JD, Bousson V. The degree and distribution of cortical bone mineralization in the human femoral shaft change with age and sex in a microradiographic study. Bone. 2009;45: 435–442. doi:10.1016/j.bone.2009.05.025
23. Jorgenson BL, Buie HR, McErlain DD, Sandino C, Boyd SK. A comparison of methods for in vivo assessment of cortical porosity in the human appendicular skeleton. Bone. 2015;73: 167–175. doi:10.1016/j.bone.2014.11.023
24. Dall'Ara E, Luisier B, Schmidt R, Pretterklieber M, Kainberger F, Zysset P, et al. DXA predictions of human femoral mechanical properties depend on the load configuration. Med Eng Phys. 2013;35: 1564–1572. doi:10.1016/j.medengphy.2013.04.008
25. Fessy MH, Seutin B, Béjui J. Anatomical basis for the choice of the femoral implant in the total hip arthroplasty. Surg Radiol Anat SRA. 1997;19: 283–286.

26. Dall'Ara E, Varga P, Pahr D, Zysset P. A calibration methodology of QCT BMD for human vertebral body with registered micro-CT images. Med Phys. 2011;38: 2602. doi:10.1118/1.3582946
27. Raum K, Jenderka KV, Klemenz A, Brandt J. Multilayer analysis: quantitative scanning acoustic microscopy for tissue characterization at a microscopic scale. IEEE Trans Ultrason Ferroelectr Freq Control. 2003;50: 507–516. doi:10.1109/TUFFC.2003.1201463
28. Lakshmanan S, Bodi A, Raum K. Assessment of Anisotropic Tissue Elasticity of Cortical Bone from High-Resolution, Angular Acoustic Measurements. IEEE Trans Ultrason Ferroelectr Freq Control. 2007;54: 1560–1570. doi:10.1109/TUFFC.2007.426
29. Raum K, Reißhauer J, Brandt J. Frequency and resolution dependence of the anisotropic impedance estimation in cortical bone using time-resolved scanning acoustic microscopy. J Biomed Mater Res A. 2004;71A: 430–438. doi:10.1002/jbm.a.30156
30. Hube R, Mayr H, Hein W, Raum K. Prediction of biomechanical stability after callus distraction by high resolution scanning acoustic microscopy. Ultrasound Med Biol. 2006;32: 1913–1921. doi:10.1016/j.ultrasmedbio.2006.06.010
31. Otsu N. A threshold selection method from gray-level histograms. IEEE Trans Syst Man Cybern. 1979;9: 62–66.
32. Metcalf LM, Dall'Ara E, Paggiosi MA, Rochester JR, Vilayphiou N, Kemp GJ, et al. Validation of calcaneus trabecular microstructure measurements by HR-pQCT. Bone. 2018;106: 69–77. doi:10.1016/j.bone.2017.09.013
33. Altman DG, Bland JM. Measurement in Medicine: The Analysis of Method Comparison Studies. J R Stat Soc Ser Stat. 1983;32: 307–317. doi:10.2307/2987937
34. Schileo E, Dall'Ara E, Taddei F, Malandrino A, Schotkamp T, Baleani M, et al. An accurate estimation of bone density improves the accuracy of subject-specific finite element models. J Biomech. 2008;41: 2483–2491. doi:10.1016/j.jbiomech.2008.05.017
35. Bousson V, Bergot C, Meunier A, Barbot F, Parlier-Cuau C, Laval-Jeantet A-M, et al. CT of the Middiaphyseal Femur: Cortical Bone Mineral Density and Relation to Porosity. Radiology. 2000;217: 179–187. doi:10.1148/radiology.217.1.r00se11179
36. Dougherty G. A comparison of the texture of computed tomography and projection radiography images of vertebral trabecular bone using fractal signature and lacunarity. Med Eng Phys. 2001;23: 313–321. doi:10.1016/S1350-4533(01)00048-0
37. Pothuaud L, Carceller P, Hans D. Correlations between grey-level variations in 2D projection images (TBS) and 3D microarchitecture: applications in the study of human trabecular bone microarchitecture. Bone. 2008;42: 775–787. doi:10.1016/j.bone.2007.11.018
38. Lowitz T, Museyko O, Bousson V, Chappard C, Laouisset L, Laredo J-D, et al. Advanced Knee Structure Analysis (AKSA): a comparison of bone mineral density and trabecular texture measurements using computed tomography and high-resolution peripheral quantitative computed tomography of human knee cadavers. Arthritis Res Ther. 2017;19: 1. doi:10.1186/s13075-016-1210-z
39. Burghardt AJ, Pialat J-B, Kazakia GJ, Boutroy S, Engelke K, Patsch JM, et al. Multicenter precision of cortical and trabecular bone quality measures assessed by high-resolution peripheral quantitative computed tomography. J Bone Miner Res. 2013;28: 524–536. doi:10.1002/jbmr.1795
40. Raum K, Leguerney I, Chandelier F, Talmant M, Saïed A, Peyrin F, et al. Site-matched assessment of structural and tissue properties of cortical bone using scanning acoustic microscopy and synchrotron radiation μCT. Phys Med Biol. 2006;51: 733–746. doi:10.1088/0031-9155/51/3/017

41. Cooper DML, Thomas CDL, Clement JG, Hallgrímsson B. Three-dimensional microcomputed tomography imaging of basic multicellular unit-related resorption spaces in human cortical bone. Anat Rec A Discov Mol Cell Evol Biol. 2006;288A: 806–816. doi:10.1002/ar.a.20344
42. Zebaze RM, Ghasem-Zadeh A, Bohte A, Iuliano-Burns S, Mirams M, Price RI, et al. Intracortical remodelling and porosity in the distal radius and post-mortem femurs of women: a cross-sectional study. The Lancet. 2010;375: 1729–1736. doi:10.1016/S0140-6736(10)60320-0
43. Taddei F, Schileo E, Helgason B, Cristofolini L, Viceconti M. The material mapping strategy influences the accuracy of CT-based finite element models of bones: an evaluation against experimental measurements. Med Eng Phys. 2007;29: 973–979. doi:10.1016/j.medengphy.2006.10.014
44. Garcia D, Zysset PK, Charlebois M, Curnier A. A three-dimensional elastic plastic damage constitutive law for bone tissue. Biomech Model Mechanobiol. 2008;8: 149–165. doi:10.1007/s10237-008-0125-2
45. Granke M, Makowski AJ, Uppuganti S, Does MD, Nyman JS. Identifying Novel Clinical Surrogates to Assess Human Bone Fracture Toughness. J Bone Miner Res. 2015;30: 1290–1300. doi:10.1002/jbmr.2452
46. Bossy E, Talmant M, Peyrin F, Akrout L, Cloetens P, Laugier P. An In Vitro Study of the Ultrasonic Axial Transmission Technique at the Radius: 1-MHz Velocity Measurements Are Sensitive to Both Mineralization and Intracortical Porosity. J Bone Miner Res. 2004;19: 1548–1556. doi:10.1359/JBMR.040513
47. Ashman RB, Cowin SC, Van Buskirk WC, Rice JC. A continuous wave technique for the measurement of the elastic properties of cortical bone. J Biomech. 1984;17: 349–361. doi:10.1016/0021-9290(84)90029-0
48. Nguyen TV, Center JR, Eisman JA. Bone mineral density-independent association of quantitative ultrasound measurements and fracture risk in women. Osteoporos Int. 2004;15: 942–947. doi:10.1007/s00198-004-1717-z
49. Olszynski WP, Adachi JD, Hanley DA, Davison KS, Brown JP. Comparison of Speed of Sound Measures Assessed by Multisite Quantitative Ultrasound to Bone Mineral Density Measures Assessed by Dual-Energy X-Ray Absorptiometry in a Large Canadian Cohort: the Canadian Multicentre Osteoporosis Study (CaMos). J Clin Densitom Off J Int Soc Clin Densitom. 2015; doi:10.1016/j.jocd.2015.04.004

Chapter 6: Measurement of the prevalence of large pores with HR-pQCT

6.1 Overview and Motivation

In chapters 3 and 4, two distinct diagnostic biomarkers of reduced femur strength were proposed, that can be assessed from the microstructure of cortical bone in the human tibia. These are: i) the thickness of cortical bone and ii) the prevalence of large pores within it.

While cortical bone thickness in the tibia has been quantified in different ways in living subjects (sections 1.3.2 and 1.3.3 for examples), there is to date no report of a measurement of the prevalence of large pores in cortical bone *in vivo*. The method that can more likely provide such information is HR-pQCT, since it can resolve cavities in cortical bone with a size of 100 μm and above [1]. Measurement of pore diameter and topology (e.g. orientation and connectivity) from HR-pQCT images have been explored already [2]. In subjects with type-II diabetes, HR-pQCT was used to demonstrate a significant increase of the mean cortical pore diameter [3]. Spatially registered HR-pQCT and MRI images allow to distinguish fat-filled from vessel-filled cortical bone pores, which is expected to provide insights on the origin of large cavities in type-II diabetic cortical bone [4]. Despite such positive examples, most analyses of the cortical bone architecture have concentrated until now on the parameters cortical thickness (Ct.Th) and cortical porosity (Ct.Po).

The direct measurement of the prevalence of large pores performed in chapter 3 and 4 required the characterization of the size of single cortical bone cavities. 60% to 90% of the pores in cortical bone, however, have a diameter below 100 μm [1] (see Fig. 20C) and remain therefore invisible to HR-pQCT.

In 2013, the first method for the BMD-based assessment of Ct.Po was proposed [5], which accounts for cavities that remain beyond the resolution of HR-pQCT. In chapter 5, it was shown how the accuracy of BMD-based Ct.Po can be improved considering a non-linear relationship between vBMD and Ct.Po. I explain a possible reasons for such improvement in appendix C of the thesis.

Once an accurate estimate of Ct.Po from pores smaller than the scanner resolution can be measured with HR-pQCT, it is straightforward to ask if the same approach can also provide information on the prevalence of large pores. The **aim** of this chapter was therefore to demonstrate a measurement of relCt.Po using HR-pQCT data.

6.2 Methods

6.2.1 Human samples and imaging

For this chapter, I used the set of 3D registered SAM and HR-pQCT images of the human proximal femur shaft utilized in chapter 5. From the original dataset (N = 39), 5 pairs of SAM and HR-pQCT images had to be excluded due to an error in data archiving that corrupted part of the files.

6.2.2 Image processing

The image processing for this chapter was performed with algorithms presented in previous sections of the thesis. Registration of HR-pQCT and SAM images as well as segmentation of binary masks of the bone tissue (for both HR-pQCT and SAM) and of the cortical bone compartment are described in chapter 5. Reference values of Ct.Po and relCt.Po$_{100\mu m}$ were computed from SAM images using the procedure presented in section 3.2.7.2 of chapter 3.

6.2.3 Prevalence of large pores from HR-pQCT images

Let us recall what "prevalence of large pores" (relCt.Po) indicates. In chapters 3 and 4, I have called *large* all voids contained in cortical bone with a diameter at least one SD above the typical Haversian canal diameter (i.e. 60 to 70 µm). Based on the pore size distributions observed in the left tibiae of a cohort of elderly human donors (see chapter 3), all pores with diameter > 100 µm were considered abnormally large. The contribution of such cavities to the total cortical bone porosity was called relCt.Po$_{100\mu m}$.

In practice, relCt.Po$_{100\mu m}$ is calculated as:

$$relCt.Po_{100\mu m} = 100 \times \frac{Ct.Po_{(\emptyset > 100\mu m)}}{Ct.Po} \quad (14)$$

In HR-pQCT terms, the denominator of Eq. (14) is given by a Ct.Po estimate that includes also cavities with a size below the scanner resolution, such as the BMD-based one of chapter 5. The upper term of Eq. (14) becomes the standard, threshold-based, measure of Ct.Po. This because the physical resolution of *in vivo* HR-pQCT images is very close to 100 µm (~95 µm for second generation HR-pQCT) and one can assume pores with a diameter below this limit to remain invisible. The latter assumption is reasonable since protocols for Ct.Po assessment from HR-pQCT attribute pores smaller than 5 voxels to noise and discard them for the calculation of Ct.Po$_{threshold\text{-}based}$ [6]. Therefore, the prevalence of large pores can be estimated from HR-pQCT images as:

$$relCt.Po_{HR-pQCT} = 100 \times \frac{Ct.Po_{threshold-based}}{Ct.Po_{BMD-based}} \quad (15)$$

In this chapter, I compare relCt.Po$_{HR\text{-}pQCT}$ calculated using Eq. (15) with reference relCt.Po$_{100\mu m}$ measured on registered 12 µm pixelsize SAM images and considering the same portion of cortical bone.

6.3 Results

The agreement between relCt.Po$_{HR\text{-}pQCT}$ and relCt.Po$_{100\mu m}$ was strong (R^2 = 0.83, RMSE: 6.03, Fig. 39A), although Eq. (15) largely underestimated relCt.Po$_{100\mu m}$. Alone, Ct.Po$_{threshold\text{-}based}$ was strongly predictive of relCt.Po$_{100\mu m}$ (R^2 = 0.79, RMSE: 6.80, Fig. 39B). The relation between Ct.Po$_{threshold\text{-}based}$ and relCt.Po$_{100\mu m}$ was non-linear and best approximated by a 3rd order polynomial (Fig. 39B).

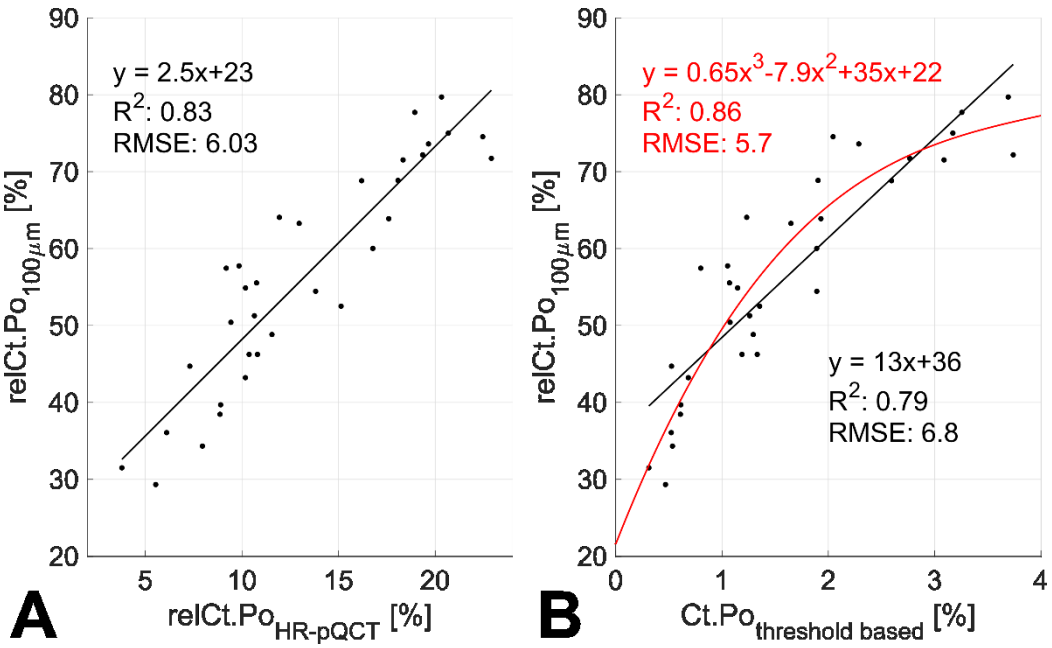

Fig. 39. (A) Linear regression between prevalence of large pores estimated from HR-pQCT with Eq. (15) and reference relCt.Po$_{100µm}$ from 12-µm pixel size SAM. (B) Comparison between threshold-based Ct.Po assessed from HR-pQCT and reference relCt.Po$_{100µm}$ from SAM. N = 34 proximal femur shaft samples.

6.4 Discussion

relCt.Po$_{HR-pQCT}$ obtained with Eq. (15) largely underestimated the reference relCt.Po$_{100µm}$ from SAM, suggesting that a considerable number of cavities with diameter > 100 µm was excluded for the calculation of the upper term of Eq. (15) (Ct.Po$_{threshold-based}$). In the box plot of Fig. 40, Ct.Po$_{threshold-based}$ (red arrow) is compared with reference Ct.Po measured from registered SAM images considering only pores above fixed diameter thresholds. Fig. 40 suggests that threshold-based Ct.Po measurements from HR-pQCT images are comparable with Ct.Po from pores above 300 µm in diameter. The reasons for such underestimate of Ct.Po are:

- Limited image quality (lower contrast and higher noise) of HR-pQCT compared to SAM. This limits the size of the smallest detectable pore.
- Larger voxel size (30.3 µm) of HR-pQCT in comparison with SAM (pixel size 12.0 µm). This is associated with higher partial volume effect at the surface of cavities, and causes an underestimate of the void area independently of pore size.

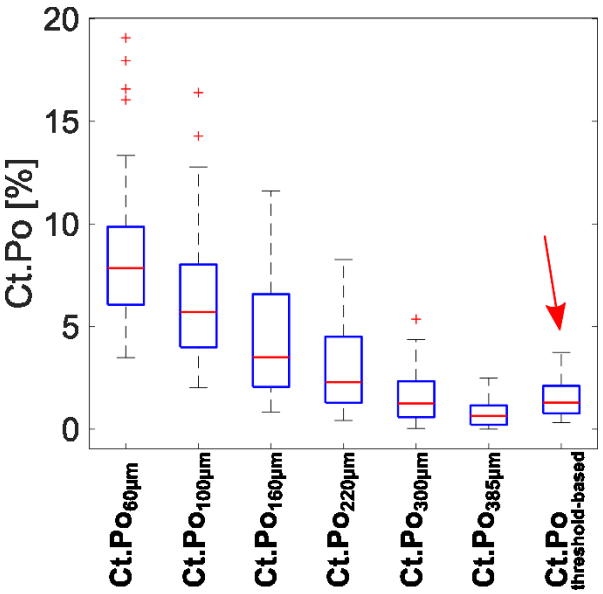

Fig. 40. Threshold-based Ct.Po from HR-pQCT (last column) in comparison with reference Ct.Po calculated from SAM selecting only pores with diameter above increasing thresholds (60 to 385 µm). Ct.Po$_{threshold-based}$ by HR-pQCT is comparable to a Ct.Po measurement performed considering only cavities with diameter above 300 µm. N = 34 proximal femur shaft samples.

Besides this, HR-pQCT was able to capture 83% of the variance of relCt.$Po_{100\mu m}$. The evidence provided in this chapter suggests that it is possible to measure the prevalence of large pores in cortical bone using HR-pQCT.

If the measurement of relCt.$Po_{HR\text{-}pQCT}$ is performed with Eq. (15) on different data sets, the following considerations should be kept in mind:

- The BMD-based measurement of Ct.Po utilized here differs from the one provided by StrAx1.0 and makes use of information derived from the BMD distribution histogram. In chapter 5, it was shown that this approach improves the accuracy of the Ct.$Po_{BMD\text{-}based}$ measurement. The coefficients of Eq. (13), however, differ (and should therefore be recalculated) for different scanners and/or sets of acquisitions [7].
- The prediction of relCt.Po from Eq. (15) was only moderately better (+4% R^2) than the information provided alone by a standard measurement of Ct.$Po_{threshold\text{-}based}$ (Fig. 39B). This would support the calculaiton of Ct.$Po_{threshold\text{-}based}$ (which is more direct) over relCt.$Po_{HR\text{-}pQCT}$. Nevertheless, if one aims at tracking relative changes in the prevalence of large pores, the non-linear dependency of relCt.Po from Ct.$Po_{threshold\text{-}based}$ might represent a drawback.
- The accuracy of the Ct.$Po_{BMD\text{-}based}$ measurement depends on image resolution. In section 5.3.3, the error of Ct.$Po_{BMD\text{-}based}$ estimates was characterized simulating the image resolution provided *in vivo* by 1st and 2nd generation HR-pQCT. In addition to image resolution, increased noise due to the presence of soft tissue surrounding the bone might affect the Ct.$Po_{BMD\text{-}based}$ prediction. Noise and image resolution are both sources of error that should be considered when relCt.$Po_{HR\text{-}pQCT}$ is measured *in vivo*.
- Finally, not only Ct.$Po_{BMD\text{-}based}$ but also Ct.$Po_{threshold\text{-}based}$ is affected by image resolution. Here, Ct.$Po_{threshold\text{-}based}$ was obtained from segmented images with a physical resolution of 55.9 µm not achievable *in vivo*. The accuracy of both, Ct.$Po_{threshold\text{-}based}$ and relCt.$Po_{HR\text{-}pQCT}$ for the prediction of the prevalence of large pores should be quantified using the same scanner settings of *in vivo* protocols and accounting for the additional effect of soft tissues.

References

1. Bjørnerem \AAshild. The clinical contribution of cortical porosity to fragility fractures. BoneKEy Rep. 2016;5.
2. Tjong W, Nirody J, Burghardt AJ, Carballido-Gamio J, Kazakia GJ. Structural analysis of cortical porosity applied to HR-pQCT data. Med Phys. 2014;41. doi:10.1118/1.4851575
3. Patsch JM, Burghardt AJ, Yap SP, Baum T, Schwartz AV, Joseph GB, et al. Increased cortical porosity in type 2 diabetic postmenopausal women with fragility fractures. J Bone Miner Res. 2013;28: 313–324. doi:10.1002/jbmr.1763
4. Wu P, Gibbons M, Foreman S, Carballido-Gamio J, Krug R, Liu J, et al. Multi-modality in vivo detection of cortical bone vasculature: comparison of diabetes patients to healthy controls [Internet]. Conference talk presented at: QMSKI; 2019 Jan 3; Lake Louise, Alberta (AB), Canada. Available: https://qmski.org/
5. Zebaze R, Ghasem-Zadeh A, Mbala A, Seeman E. A new method of segmentation of compact-appearing, transitional and trabecular compartments and quantification of cortical porosity from high resolution peripheral quantitative computed tomographic images. Bone. 2013;54: 8–20. doi:10.1016/j.bone.2013.01.007
6. Burghardt AJ, Buie HR, Laib A, Majumdar S, Boyd SK. Reproducibility of direct quantitative measures of cortical bone microarchitecture of the distal radius and tibia by HR-pQCT. Bone. 2010;47: 519–528. doi:10.1016/j.bone.2010.05.034

7. Soltan N, Kawalilak CE, Cooper DM, Kontulainen SA, Johnston JD. Cortical porosity assessment in the distal radius: A comparison of HR-pQCT measures with Synchrotron-Radiation micro-CT-based measures. Bone. 2019;120: 439–445. doi:10.1016/j.bone.2018.12.008

Chapter 7: Summary and conclusions

This thesis examined the connection between the microstructure of cortical bone and femur strength. The scope of the investigation was to understand if and how a modification in the microstructure of cortical bone can reveal a condition of increased hip fragility. What motivates these questions is that novel technologies such as HR-pQCT and ultrasound can measure the human cortical bone microstructure non-invasively. Particularly, HR-pQCT would allow the validation of the findings of this thesis *in vivo*. At the same time, the possibility to perform the measurement with widely available clinical ultrasound devices might provide a unique opportunity for a cheap and non-invasive estimate of fracture risk.

Key results

In chapter 3, it was demonstrated how the prevalence of large pores and the thickness of cortical bone in the tibia of humans are associated with the strength of the proximal femur under both, standing and falling loads. In this thesis, femur strength was estimated using hvFE simulations, which certainly represents an approximation. Furthermore, strength alone cannot capture entirely a femur's propensity to fracture [1].

The femora of hip fracture patients have less dense trabeculae and a thinner wall of cortical bone in the neck, where fractures often start. This is what motivated the characterization of the femoral neck bone microarchitecture presented in chapter 4. In this chapter, the relationship between the thickness and prevalence of large pores in the cortical bone of the tibia with a deterioration of the trabecular and cortical architecture in specific regions of the femoral neck was demonstrated.

The same analysis was also used to show that strength predictions by hvFE models are able to capture the relative role of cortical and trabecular bone for femoral neck fragility and the dependence of this role on the loading conditions (appendix D). This despite the strong approximation of the bone architecture introduced by the hvFE procedure.

Together, the results of chapters 3 and 4 suggest that measurements of the cortical bone microstructure in the tibia might expose a condition of femur fragility, since they reflect reduced cortical thickness and less dense, thinner trabeculae in the femoral neck. The thickness of cortical bone and the prevalence of large cortical pores in the tibia are here proposed as structural biomarkers of reduced femur strength.

HR-pQCT offers an immediate opportunity to test the validity of the findings of this work. Databases of HR-pQCT images are already available that allow to study both retrospectively and prospectively the association between bone microstructure and fracture [2,3]. Since bone strength examined in a laboratory setting like the current one doesn't directly translate to fracture risk, the two structural biomarkers proposed in this work should be ultimately tested against the probability of fracture.

If cortical thickness is routinely considered for the analysis of cortical bone by HR-pQCT, the prevalence of large pores is not. HR-pQCT moreover, can only effectively visualize pores with a diameter above few hundreds of microns, which represents a small fraction of the entire cortical bone porosity.

In chapter 5, a method was developed that provides precise estimates of porosity from HR-pQCT images including the contribution of cavities at the micrometer level. It was demonstrated that if porosity is measured based on the BMD instead of segmenting single pores on the images, cavities that are smaller than the scanner resolution can be taken into account. The same approach was extended in chapter 6 for the measurement of the prevalence of large

pores in cortical bone. Here, I demonstrated how HR-pQCT images can be used to characterize the contribution of large resorption cavities to the cortical bone porosity. This suggests that the prevalence of large pores in cortical bone (the second biomarker of femur strength proposed by this thesis) could be readily validated in terms of fracture discrimination using HR-pQCT datasets that are already available.

Why cortical bone?

The current thesis focused uniquely on cortical bone tissue for the development of structural markers of reduced femur strength. There were several reasons for this. First of all, cortical bone has long been overlooked in the discussion of bone fragility [4,5]. As an example, in a review from 2001, Harold M. Frost postulated that cortical bone loss would occur mainly at the endosteum and not by resorption on the cortical bone pores [6]. Frost and others were drawing on the observation that cortical porosity increases with age at a pace slower than total bone loss. As soon as HR-pQCT images of the cortical microstructure became available, researchers started associating cortical porosity, not only thickness, with fracture. It is now well accepted that cortical bone is lost as a reduction of cortical thickness due to endosteal resorption as well as via an increase in porosity due to resorption within the pores, with both processes contributing to bone fragility [7]. In recent years, the mechanism leading to the increase of intracortical porosity has been unraveled [8]. Due to the uncoupling between bone resorption and formation, pores increase in size and coalesce in large, non-refilled cavities with heterogeneous shape. Since this is more likely to happen near the endosteum, the distribution of pore size in human cortical bone is non-homogeneous (i.e. has a gradient towards the endosteum). In addition, the resorption cavities growing to an extraordinary large diameter might remain limited in number. Hence, the common way of describing the microarchitecture of cortical pores (i.e. by a single porosity measure), captures the progression of resorption only partially. As a confirmation, porosity was not associated with femur strength in our data. On the contrary, chapters 3 and 4 suggest that cortical bone measurements should assess porosity in combination with pore size.

The second reason why this work considered exclusively cortical bone has to do with available technology. Although HR-pQCT represents the easiest way to quantify the bone microstructure *in vivo*, its application is limited by the scarce availability of the scanner. Due to high cost and low versatility, the use of HR-pQCT is not reimbursed by national health agencies. In addition and similarly to DXA, a dose of ionizing radiation is associated with each HR-pQCT scan. The research of this thesis was performed jointly with measurements using quantitative ultrasound methods that might become a valid alternative for the characterization of the cortical bone structure *in vivo*. Ultrasound axial transmission was applied *ex vivo* on the same bones and at the same measurement site (anteromedial midshaft) of the 19 human tibiae used for this thesis, which led to the validation of BDAT for the estimation of cortical bone thickness and porosity [9]. *In vivo*, the same approach has also provided promising results [10]. Apart from BDAT, which utilizes a dedicated system, clinical ultrasound devices can image *in vivo* the cortex of the tibia [11], and might provide estimates of the cortical pore size [12]. Due to attenuation, the high frequencies utilized by novel ultrasound approaches cannot travel to deep tissue layers and require the measurement to be performed close to the surface of the body. Therefore, quantitative ultrasound for the monitoring of bone strength has cortical bone as its preferential measurement target.

Future perspective

The current standard for the diagnosis of osteoporosis is DXA. Due to ionizing radiation and to the limited availability of devices, common guidelines for the management of osteoporosis recommend a BMD measurement by DXA only when other clinical factors point towards high fracture risk [13]. Early ultrasound densitometers were ionizing-radiation free, cheap and portable. Measurements of the broadband ultrasound attenuation (BUA) and speed of sound (SOS) at the calcaneus demonstrated fracture risk prediction ability similar to that of DXA [14,15]. Despite this, BUA and SOS measurements never obtained the same recognition as X-ray-based densitometry. The limited success of ultrasound densitometers in the field of osteoporosis assessment can be explained by the lower precision and accuracy of ultrasound in comparison to BMD by DXA [16]. Apart from this, QUS still suffers from the lack of standardization (e.g. of devices, parameters..) and from the lack of reference data [16–18].

If a measurement of the bone structure can be performed with an ultrasound device which is available in the clinics, the constrains imposing a risk threshold for the bone examination could be overcome. Thanks to the vast presence of the scanners, to their relatively low cost and complete non-invasiveness, an ultrasound screening of bone strength could be extended to low risk groups (e.g. younger subjects), in which still a large number of fractures occurs, and for which current osteoporosis diagnosis is deficient.

Nevertheless, the standardization of ultrasound measurements must be addressed before this can happen. The lack of standardization regarding (i) modality, (ii) output and (iii) interpretation of the measurements limits the acceptance of ultrasound for the management of osteoporosis [18]. In other words, we should soon agree on where (i.e. at which site) measurements should be performed, and what parameters of the bone structure they should assess. The output of the current work with respect to such questions is presented in Table 22 and Table 23. In summary, ultrasound measurements should be performed at the anteromedial midshaft of the tibia for the reasons listed in Table 22. The exact height of the measurement position (e.g. distance from the knee) was not controlled here and should be considered by future works.

Table 22. Thesis output in the context of ultrasound for hip strength prediction: measurement site.

Where to measure?			
		Advantages	Explanation
Bone:	**Tibia**	- Mechanical loading:	Tibia and femur share the loads caused by gait. Therefore, adaptation and disuse affecting the bone structure of the femoral neck should be reflected also in the structure of the tibia.
Site:	**Anteromedial midshaft**	- Reference values:	pQCT data on the microarchitecture of cortical bone is available for the tibia, although mainly for the distal shaft instead of midshaft.
		- Thin soft tissue:	A large portion of the anteromedial tibia is free from muscles attachment and covered by a thin layer of soft tissue. High frequency ultrasound can travel here with minimum attenuation.

Considering possible measurement parameters (Table 23), the direct measurement of the prevalence of large pores in cortical bone would require the quantification of the size of single cavities and is therefore likely to remain unfeasible with ultrasound *in vivo*. However, its value might be retrieved from surrogate measurements of the pore size distribution. For example, for the 19 human tibiae considered in this work, the variance in the prevalence of large pores in cortical bone was almost entirely ($R^2 = 0.96$, $p = 1\times10^{-12}$) explained by the heterogeneity of the pore size (Fig. 41). This might represent an advantage for methods that are able to model the size distribution of the pores (e.g. quantitative analysis of the ultrasound backscatter). On the other hand, large pores are encountered almost uniquely in the proximity of the endosteum. If a technique can distinguish between depths in cortical bone, porosity and pore size should be assessed in layers of tissue close to the endosteum.

Table 23. Thesis output in the context of ultrasound for hip strength prediction: measurement parameters.

What to measure?	Ultrasound available	Strength associated	Notes
Cortical thickness	✓	✓	
Prevalence of large pores	×	✓	
Cortical porosity	✓	×[a]	- Techniques able to perform layer analysis should target cortical porosity and pore size in deep layers of cortical bone (close to the endosteum).
Pore size	?	✓[b]	
Pore size distribution	?	✓[b]	- **Heterogeneity** and **kurtosis** of the distribution. - Potential for cortical backscatter: theory already available for soft tissue characterization [19].

[a] Other works have shown associations between porosity and femur strength [20] or fracture [21].
[b] Descriptors of the pore size and of the pore size distribution were associated with strength for standing loads but not for sideways fall (see chapter 3).

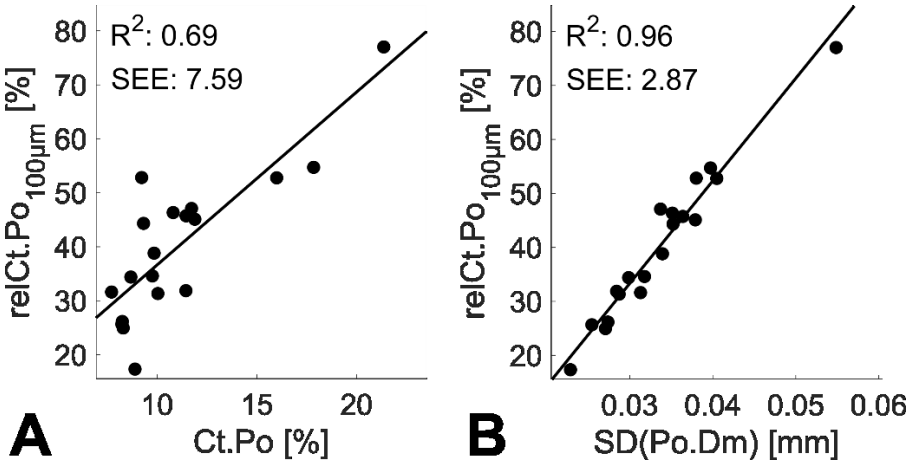

Fig. 41. The prevalence of large pores in cortical bone is poorly captured by cortical porosity (A) but highly dependent on the heterogeneity of the pore size (B). Data from the anteromedial tibia. $N = 19$.

Limitations

There are two limitations worth mentioning regarding the content of this section. The first one concerns the use of cortical bone thickness as biomarker for strength. Contrary to BMD and to measurements of the pore size, cortical thickness is influenced by bone (and body) size. In particular, cortical bone becomes thicker with increasing weight and BMI [22] independently of osteoporosis. At the same time, the larger bones of a taller skeleton tend to have a wider medullar cavity and lower cortical thickness [23]. In general, the bones of a larger body have a higher ultimate strength, since they have to resist higher (weight-related) mechanical loads during everyday tasks. This, however, without necessary meaning that they can better resist fracture during an extraordinary event such as a fall. If bone size is merely determined by the size of the organism[*], it is the bone architecture that holds the footprint of resorption and of osteoporosis. When one compares cortical thickness with bone strength, the effect of bone size might be amplified. Therefore, the associations between cortical thickness and femur strength reported here are likely to be affected by a "double" bias and do not translate in a true potential of cortical thickness for fracture risk prediction. Indeed, pQCT and HR-pQCT have demonstrated already that the cortical thickness of the tibia can discriminate fracture, but is not a better predictor than BMD by DXA or other BMD and structural parameters of tibial trabecular and cortical bone [2,24,25].

The second limitation is multifaceted and is given by the use of femur strength as benchmark. Several uncertainties affect the way in which femur failure was simulated with laboratory experiments and numerical models. Appendix A shows that the boundary conditions (i.e. the mechanical loads) applied during the mechanical tests utilized for this work might have differed from what was expected. In particular, an undesired bending moment might have acted on the femur head during the experiment. In addition, the test was quasi-static and did not consider the effects of inertia and viscosity. FE simulations of femur failure, on the other hand, were based on a rather simplistic approximation of the bone microarchitecture. First, trabecular and cortical bone were assumed to be isotropic, which we know is not the case. Second, the constitutive law used for the elasticity and yield of cortical bone was far from optimal, since it was empirically extrapolated from elastic and yield constants of trabecular tissue.

Even if one could remove these uncertainties, ultimate femur strength would still capture only one of the aspects of the hip fracture risk. This because aging does not only affect the microstructure of bone, but also the mechanical properties of the collagen matrix. In particular, bone tissue loses its material toughness with age due to the accumulation of cross-links between collagen fibrils [26]. An accurate characterization of femur fragility *in vitro* should therefore consider ultimate bone strength as well as fracture toughness and fatigue strength [1]. At the same time, structural biomarkers of bone resorption like the ones proposed in this thesis should be evaluated in combination with markers of collagen cross-linking such as serum-based assessments of glycation end-products.

In conclusion, the scope of this work was to identify biomarkers of reduced femur strength in the microstructure of cortical bone. Two parameters of cortical bone were proposed, that can be measured at the midshaft of the tibia and are associated with both, reduced femur strength and a phenotype of structural fragility in the femoral neck. These are the thickness of cortical bone and the prevalence of extraordinarily large pores in the cortex. This thesis also shows that measurements of the cortical bone architecture should be performed at the anteromedial shaft of the tibia, since this region is accessible by several techniques including ultrasound. A

[*] This is not the case if a person suffered from immobilization or from nutrition and hormonal deficiencies during growth.

quantification of the prevalence of large pores can and should be evaluated in living subjects considering the incidence of fracture as benchmark.

References

1. Hernandez CJ, van der Meulen MC. Understanding Bone Strength Is Not Enough. J Bone Miner Res. 2017;32: 1157–1162. doi:10.1002/jbmr.3078
2. Fink HA, Langsetmo L, Vo TN, Orwoll ES, Schousboe JT, Ensrud KE. Association of High-resolution Peripheral Quantitative Computed Tomography (HR-pQCT) bone microarchitectural parameters with previous clinical fracture in older men: The Osteoporotic Fractures in Men (MrOS) study. Bone. 2018;113: 49–56. doi:10.1016/j.bone.2018.05.005
3. Shanbhogue VV, Brixen K, Hansen S. Age- and Sex-Related Changes in Bone Microarchitecture and Estimated Strength: A Three-Year Prospective Study Using HRpQCT. J Bone Miner Res. 2016;31: 1541–1549. doi:10.1002/jbmr.2817
4. Zebaze RM, Ghasem-Zadeh A, Bohte A, Iuliano-Burns S, Mirams M, Price RI, et al. Intracortical remodelling and porosity in the distal radius and post-mortem femurs of women: a cross-sectional study. The Lancet. 2010;375: 1729–1736. doi:10.1016/S0140-6736(10)60320-0
5. Burr DB. Cortical bone: a target for fracture prevention? The Lancet. 2010;375: 1672–1673. doi:10.1016/S0140-6736(10)60444-8
6. Frost HM. From Wolff's law to the Utah paradigm: Insights about bone physiology and its clinical applications. Anat Rec. 2001;262: 398–419. doi:10.1002/ar.1049
7. Bala Y, Zebaze R, Seeman E. Role of cortical bone in bone fragility: Curr Opin Rheumatol. 2015;27: 406–413. doi:10.1097/BOR.0000000000000183
8. Andreasen CM, Delaisse J-M, Eerden BC van der, Leeuwen JP van, Ding M, Andersen TL. Understanding Age-Induced Cortical Porosity in Women: The Accumulation and Coalescence of Eroded Cavities Upon Existing Intracortical Canals Is the Main Contributor. J Bone Miner Res. 2017;33: 606–620. doi:10.1002/jbmr.3354
9. Schneider J, Iori G, Ramiandrisoa D, Hammami M, Gräsel M, Chappard C, et al. Ex vivo cortical porosity and thickness predictions at the tibia using full spectrum ultrasonic guided wave analysis. Arch Osteoporos. 2018; (submitted).
10. Schneider J, Ramiandrisoa D, Armbrecht G, Ritter Z, Felsenberg D, Raum K, et al. In Vivo Measurements of Cortical Thickness and Porosity at the Proximal Third of the Tibia Using Guided Waves: Comparison with Site-Matched Peripheral Quantitative Computed Tomography and Distal High-Resolution Peripheral Quantitative Computed Tomography. Ultrasound Med Biol. 2019;0. doi:10.1016/j.ultrasmedbio.2019.01.008
11. Renaud G, Kruizinga P, Cassereau D, Laugier P. In vivo ultrasound imaging of the bone cortex. Phys Med Biol. 2018;63: 125010. doi:10.1088/1361-6560/aac784
12. Du J, Iori G, Raum K. In-silico validation of microstructure estimation from cortical bone backscatter [Internet]. Conference talk presented at: IUS IEEE; 2018 Oct 25; IEEE International Ultrasonics Symposium, Kobe, Japan. Available: http://sites.ieee.org/ius-2018/
13. Kanis JA, Cooper C, Rizzoli R, Reginster J-Y, Foundation (IOF) on behalf of the SAB of the ES for C and EA of O (ESCEO) and the C of SA and NS of the IO. European guidance for the diagnosis and management of osteoporosis in postmenopausal women. Osteoporos Int. 2018; 1–42. doi:10.1007/s00198-018-4704-5

14. Bauer DC, Glüer CC, Cauley JA, Vogt TM, Ensrud KE, Genant HK, et al. Broadband Ultrasound Attenuation Predicts Fractures Strongly and Independently of Densitometry in Older Women: A Prospective Study. Arch Intern Med. 1997;157: 629–634. doi:10.1001/archinte.1997.00440270067006
15. Hans D, Dargent-Molina P, Schott A, Sebert J, Cormier C, Kotzki P, et al. Ultrasonographic heel measurements to predict hip fracture in elderly women: the EPIDOS prospective study. The Lancet. 1996;348: 511–514. doi:10.1016/S0140-6736(95)11456-4
16. Glüer C-C. Quantitative Ultrasound Techniques for the Assessment of Osteoporosis: Expert Agreement on Current Status. J Bone Miner Res. 1997;12: 1280–1288. doi:10.1359/jbmr.1997.12.8.1280
17. Hans D, Baim S. Quantitative Ultrasound (QUS) in the Management of Osteoporosis and Assessment of Fracture Risk. J Clin Densitom. 2017;20: 322–333. doi:10.1016/j.jocd.2017.06.018
18. Laugier P. Instrumentation for in vivo ultrasonic characterization of bone strength. IEEE Trans Ultrason Ferroelectr Freq Control. 2008;55: 1179–1196. doi:10.1109/TUFFC.2008.782
19. Ghoshal G, Mamou J, Oelze ML. State of the Art Methods for Estimating Backscatter Coefficients. In: Mamou J, Oelze ML, editors. Quantitative Ultrasound in Soft Tissues. Dordrecht: Springer Netherlands; 2013. pp. 3–19. doi:10.1007/978-94-007-6952-6_1
20. Abraham AC, Agarwalla A, Yadavalli A, McAndrew C, Liu JY, Tang SY. Multiscale Predictors of Femoral Neck In Situ Strength in Aging Women: Contributions of BMD, Cortical Porosity, Reference Point Indentation, and Nonenzymatic Glycation. J Bone Miner Res. 2015;30: 2207–2214. doi:10.1002/jbmr.2568
21. Bala Y, Zebaze R, Ghasem-Zadeh A, Atkinson EJ, Iuliano S, Peterson JM, et al. Cortical Porosity Identifies Women With Osteopenia at Increased Risk for Forearm Fractures. J Bone Miner Res. 2014;29: 1356–1362. doi:10.1002/jbmr.2167
22. Sornay-Rendu E, Boutroy S, Vilayphiou N, Claustrat B, Chapurlat RD. In Obese Postmenopausal Women, Bone Microarchitecture and Strength Are Not Commensurate to Greater Body Weight: The Os des Femmes de Lyon (OFELY) Study. J Bone Miner Res. 2013;28: 1679–1687. doi:10.1002/jbmr.1880
23. Bjørnerem \AAshild. The clinical contribution of cortical porosity to fragility fractures. BoneKEy Rep. 2016;5.
24. Chevalley T, Bonjour JP, van Rietbergen B, Ferrari S, Rizzoli R. Fracture history of healthy premenopausal women is associated with a reduction of cortical microstructural components at the distal radius. Bone. 2013;55: 377–383. doi:10.1016/j.bone.2013.04.025
25. Sheu Y, Zmuda JM, Boudreau RM, Petit MA, Ensrud KE, Bauer DC, et al. Bone strength measured by peripheral quantitative computed tomography and the risk of nonvertebral fractures: The osteoporotic fractures in men (MrOS) study. J Bone Miner Res. 2011;26: 63–71. doi:10.1002/jbmr.172
26. Vashishth D. The role of the collagen matrix in skeletal fragility. Curr Osteoporos Rep. 2009;5: 62–66. doi:10.1007/s11914-007-0004-2

List of Figures

List of Tables

Acknowledgments

I will start by expressing my gratitude to the Berlin-Brandenburg School for Regenerative Therapies of the Charité Universitätsmedizin Berlin, where I conducted my PhD research. My work was supported by the Deutsche Forschungsgemeinschaft (DFG Ra1380/9-1) and by the Agence Nationale de la Recherche (ANR-14-CE35-0030-01) within the TaCo-Sound project, by the German Academic Exchange Service (DAAD, grant no. 91578351), by the Bundesministerium für Bildung und Forschung (BMBF, musculoskeletal research network 01EC1408L) within the subproject "characterization of cortical and subchondral bone" and by the Nachwuchskommission of the Charité.

I want to thank my PhD supervisor Kay Raum for the constant support and for giving me the opportunity and the tools to perform this research. I also would like to acknowledge Dieter Pahr for hosting me at the Institute for Lightweight Design and Structural Biomechanics (ILSB) of the TU Vienna and supervising an important part of my work. Many thanks to Claudia Fleck who welcomed and supported my doctorate at the Faculty III of the TU Berlin and to her, Kay Raum and Richard Weinkamer for accepting to review my thesis.

Special thanks to my colleagues and friends Regina, Susanne and Johannes for all the time spent together and the encouragement during these years. Also thanks to the colleagues and friends of AG Raum and in particular to Anke, Huong, Jana, Janos, Jiahan, Martin, Mohammad, Omar, Nirina, Timm and Urszula.

Many thanks to Frans Heyer and Laura Peralta for the big effort they put in this work, to my former mentors Vantte Kilappa and Juan Du, to Peter Varga for sharing his ideas with me when I was starting my PhD and to Daniel Rohrbach, Andreas Reisinger, Alexander Synek, Emir Benca, Paul Walter, Nicolas Vilayphiou, Joop van den Bergh, Claus Glüer and Paul Zaslansky for their important feedback and suggestions.

Thank you Susanne, Regina, Daniel, Urszula, Johannes, Nicholas and Genevieve for proof reading this thesis.

I would like to thank my mother Emanuela and my brother Lorenzo for their unconditional help.

Finally, I want to thank HIER & JETZT: Connections and B.L.O. Ateliers for hosting me during the weeks of thesis writing, and the people of HeartChor and DIE KOMPANIE for loving and inspiring me.

Appendix A: Stiffness coefficients of compressive and bending nature of the proximal femur

Background and scope

One of the assumptions of the mechanical tests setup used for this PhD (Fig. A42) and of the FE procedure for which the mechanical test served as validation is that the sample is loaded with a pure vertical force. In other words, it is assumed that the embedding of the femoral head allows the frictionless rotation of the bone. The objective of the study described in this section was to measure the moment M_2 introduced on the femoral head by the coupling with the testing machine.

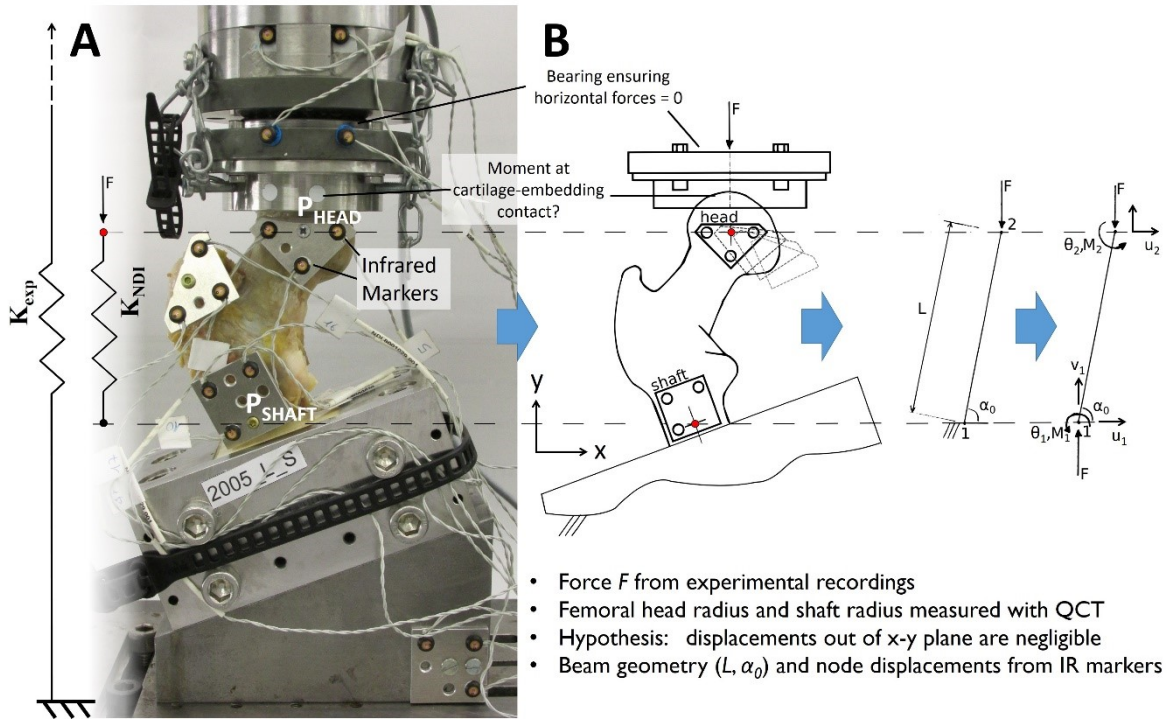

Fig. A42. (A) Setup of a TacoSound STANCE mechanical test. The femur apparent stiffness can be calculated from the vertical displacement of the machine actuator (K_{exp}) or by the vertical component of displacement (difference between P_{HEAD} and P_{SHAFT}) recorded by the infrared markers at the femoral head and shaft (K_{NDI}) [1]. (B) Approximation of the mechanical test with a 2D beam finite element. In the drawing on the right, the displacement vectors at the head (u_2, v_2, θ_2) and shaft (u_1, v_1, θ_1) of the femur as well as the beam geometry (L and α_0) can be derived from the infrared markers readings. The force F is recorded by the load cell during the experiment.

2D Finite Element beam theory

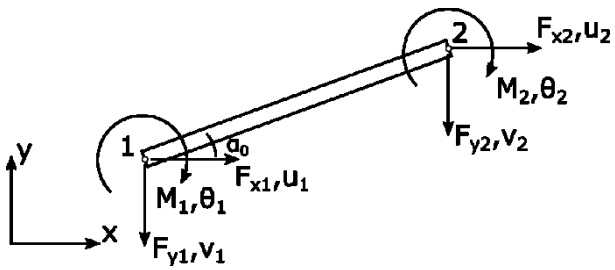

Fig. A43. Euler-Bernoulli FE beam element in 2D.

For the Finite Element (FE) of Fig. A43, for which shear deformations are assumed to be negligible (Euler-Bernoulli approximation), nodal displacements and rotations in the local reference system (in the x-y plane) are related to the external loads through the system of equations:

$$\begin{bmatrix} \gamma & 0 & 0 & -\gamma & 0 & 0 \\ 0 & 12\beta & 6L\beta & 0 & -12\beta & 6L\beta \\ 0 & 6L\beta & 4L^2\beta & 0 & -6L\beta & 2L^2\beta \\ -\gamma & 0 & 0 & \gamma & 0 & 0 \\ 0 & -12\beta & -6L\beta & 0 & 12\beta & -6L\beta \\ 0 & 6L\beta & 2L^2\beta & 0 & -6L\beta & 4L^2\beta \end{bmatrix} \begin{bmatrix} u_1 \\ v_1 \\ \theta_1 \\ u_2 \\ v_2 \\ \theta_2 \end{bmatrix} = \begin{bmatrix} Fx_1 \\ Fy_1 \\ M_1 \\ Fx_2 \\ Fy_2 \\ M_2 \end{bmatrix} \tag{A16}$$

In which:

$$\gamma = \frac{EA}{L} \qquad \text{and} \qquad \beta = \frac{EJ}{L^3} \tag{A17}$$

Represent the stiffness coefficients of compressive and bending nature of the element of Fig. A43, respectively. Eq. (A16) can be generalized for a global reference system (u', v', θ') by:

$$\begin{bmatrix} u' \\ v' \\ \theta' \end{bmatrix} = \begin{bmatrix} c_0 & s_0 & 0 \\ s_0 & -c_0 & 0 \\ 0 & 0 & 1 \end{bmatrix} \begin{bmatrix} u \\ v \\ \theta \end{bmatrix} = T_0 \begin{bmatrix} u \\ v \\ \theta \end{bmatrix} \tag{A18}$$

Where:

$$c_0 = \cos\alpha_0 \qquad \text{and} \qquad s_0 = \sin\alpha_0 \tag{A19}$$

Imposing the equivalence of the strain energy in the local and global systems, it can be demonstrated that:

$$K = T^T \overline{K} T = T^T \begin{bmatrix} \overline{K}_1 & \overline{K}_2 \\ \overline{K}_2^T & \overline{K}_3 \end{bmatrix} T \tag{A20}$$

Where:

$$T = \begin{bmatrix} T_0 & 0 \\ 0 & T_0 \end{bmatrix} \tag{A21}$$

And:

$$\begin{aligned} \overline{K}_1 &= \begin{bmatrix} \gamma c_0^2 + 12\beta s_0^2 & c_0 s_0(\gamma - 12\beta) & 6L\beta s_0 \\ c_0 s_0(\gamma - 12\beta) & \gamma s_0^2 + 12\beta c_0^2 & -6L\beta c_0 \\ 6L\beta s_0 & -6L\beta c_0 & 4L^2\beta \end{bmatrix} \\ \overline{K}_2 &= \begin{bmatrix} -\gamma c_0^2 - 12\beta s_0^2 & c_0 s_0(-\gamma + 12\beta) & 6L\beta s_0 \\ c_0 s_0(-\gamma + 12\beta) & -\gamma s_0^2 - 12\beta c_0^2 & -6L\beta c_0 \\ -6L\beta s_0 & 6L\beta c_0 & 2L^2\beta \end{bmatrix} \\ \overline{K}_3 &= \begin{bmatrix} \gamma c_0^2 + 12\beta s_0^2 & c_0 s_0(\gamma - 12\beta) & -6L\beta s_0 \\ c_0 s_0(\gamma - 12\beta) & \gamma s_0^2 + 12\beta c_0^2 & 6L\beta c_0 \\ -6L\beta s_0 & 6L\beta c_0 & 4L^2\beta \end{bmatrix} \end{aligned} \tag{A22}$$

Which, substituting in Eq. (A16) gives:

$$\begin{bmatrix} \gamma c_0^2 + 12\beta s_0^2 & c_0 s_0(\gamma - 12\beta) & 6L\beta s_0 & -\gamma c_0^2 - 12\beta s_0^2 & c_0 s_0(-\gamma + 12\beta) & 6L\beta s_0 \\ c_0 s_0(\gamma - 12\beta) & \gamma s_0^2 + 12\beta c_0^2 & -6L\beta c_0 & c_0 s_0(-\gamma + 12\beta) & -\gamma s_0^2 - 12\beta c_0^2 & -6L\beta c_0 \\ 6L\beta s_0 & -6L\beta c_0 & 4L^2\beta & -6L\beta s_0 & 6L\beta c_0 & 2L^2\beta \\ -\gamma c_0^2 - 12\beta s_0^2 & c_0 s_0(-\gamma + 12\beta) & -6L\beta s_0 & \gamma c_0^2 + 12\beta s_0^2 & c_0 s_0(\gamma - 12\beta) & -6L\beta s_0 \\ c_0 s_0(-\gamma + 12\beta) & -\gamma s_0^2 - 12\beta c_0^2 & 6L\beta c_0 & c_0 s_0(\gamma - 12\beta) & \gamma s_0^2 + 12\beta c_0^2 & 6L\beta c_0 \\ 6L\beta s_0 & -6L\beta c_0 & 2L^2\beta & -6L\beta s_0 & 6L\beta c_0 & 4L^2\beta \end{bmatrix} \begin{bmatrix} u_1 \\ v_1 \\ \theta_1 \\ u_2 \\ v_2 \\ \theta_2 \end{bmatrix} = \begin{bmatrix} Fx_1 \\ Fy_1 \\ M_1 \\ Fx_2 \\ Fy_2 \\ M_2 \end{bmatrix} \tag{A23}$$

Modelling of a STANCE mechanical test using the 2D FE theory

Applying the formulation of (A23) to the beam of Fig. A43, we know that:

$$\begin{aligned} Fx_1 &= Fx_2 = 0 \\ Fy_1 &= -Fy_2 = F \end{aligned} \tag{A24}$$

And the displacements (u_2, v_2, θ_2) and shaft (u_1, v_1, θ_1) are known from the markers recordings. We can than solve the system of (A23) for M_1, M_2, γ and β.

Results

The correlation between K_{exp} and K_{NDI} for the 10 TacoSound proximal femur samples measured in STANCE was very poor ($R^2 = 0.29$, Fig. A44), suggesting that the loading conditions might change between samples.

The moment M_2 acting on the femoral head was 34.4 ± 20.8 Nm (min: 3.0 Nm; max = 83.0 Nm).

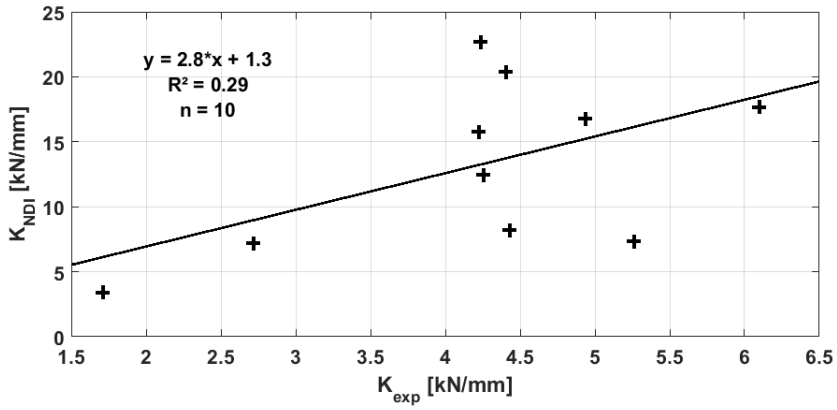

Fig. A44. Regression between apparent stiffness from the machine recording and from the axial displacement between femur head and shaft.

Discussion and criticism

The results reported in this section suggest that a non-zero moment acting at the cartilage-embedding contact on top of the femoral head might represent a confounding factor for the interpretation of results from this mechanical testing setup. Additionally, this would substantially affect the comparison with FE models since the boundary conditions implemented in our numerical simulations are of pure vertical load and free rotation of the femoral head.

The results reported here might be affected by the following factors:

1. The approximation of the test to a 2D FE beam element hypotheses negligible displacements out of the x-y plane of Fig. A42B. Displacements and rotation components of the femur head perpendicular to this plane as measured by the infrared markers system were indeed smaller compared to the components (u_2, v_2, θ_2) (data not shown). We do not possess enough data, however, to conclude that the former are negligible.

2. Most importantly, the Euler-Bernoulli formulation utilized here assumes negligible shear deformations. During physiological tasks, the proximal femur is mainly loaded in bending and compression in the frontal plane, giving rise to strong shear stress on the bone axis [2,3]. Due to this fact, the assumption of negligible shear deformations in the femoral neck seems unjustified.

In conclusion, this sections shows that the setup utilized for our mechanical tests of proximal femur strength might introduce a bending moment on the femoral head. Future experiments should consider the improvement of the experimental setup. Finite element simulations, on the other hand, could be used to verify this finding by modifying in silico the boundary conditions of the test to account for bending moments as well as axial loading.

Acknowledgments

I would like to thank Prof. Francesco Cesari and Prof. Philippe Zysset for the feedback and support on the content of this appendix.

References

1. Dall'Ara E, Luisier B, Schmidt R, Kainberger F, Zysset P, Pahr D. A nonlinear QCT-based finite element model validation study for the human femur tested in two configurations in vitro. Bone. 2013;52: 27–38. doi:10.1016/j.bone.2012.09.006
2. Cristofolini L. In vitro evidence of the structural optimization of the human skeletal bones. J Biomech. 2015;48: 787–796. doi:10.1016/j.jbiomech.2014.12.010
3. Cristofolini L, Juszczyk M, Taddei F, Viceconti M. Strain distribution in the proximal human femoral metaphysis. Proc Inst Mech Eng [H]. 2009;223: 273–288. doi:10.1243/09544119JEIM497

Appendix B: Sensitivity study on the hvFE element size

Background and scope

The use of nonlinear homogenized voxel FE (hvFE) simulations with approximately 3 mm voxel size was motivated by the following aspects:

1. ~3 mm hvFE models were validated by Dall'Ara et al. using quasi-static mechanical tests of femoral failure [1]. In this appendix, I reproduced the procedure of these authors, as well as the validation with mechanical tests. For a fair comparison with Dall'Ara et al. it was therefore desirable to maintain the same element size that they have used.
2. A ~3 mm hvFE can be processed within limited computation time on a desktop computer, making it feasible for clinical translation.

The homogenization to ~3 mm voxels, however, involves a poor description of the bone morphology. It does not allow a smooth rendering of the outer bone contour and, most importantly, to depict the smooth transition from compact to trabecular bone. Partial volume effects are therefore expected to strongly affect the average density (and therefore the material properties) of the model elements.

The objective of this sensitivity study is to investigate if a reduction of the voxel element size (and therefore higher accuracy in the description of the local bone architecture and material properties), although maintaining an identical FE procedure based on homogenized hexahedra, could improve the FE prediction of femur strength and stiffness.

Methods

I developed 0.909 mm voxel size hvFE models (both STANCE and FALL) of the 40 proximal femora of Table 4. The FE procedure remained identical to the one adopted for the 2.7 mm hvFE described in Table 11 in section 2.3.2. The second coarsening step (step 5 in Table 11) was adapted (factor 3 instead that 9) to provide 0.909^3 mm^3 hexahedra.

Results

As expected, 0.909 and 2.727 mm hvFE predictions of femur strength and stiffness are in strong agreement ($R^2 > 0.91$, Panel A in Fig. A45 and $R^2 > 0.93$, Panel C in Fig. A45 for strength and stiffness, respectively). Nevertheless, the difference in stiffness and strength predictions between 2.727 and 0.909 hvFE models seems to depend on the average stiffness or strength level (Bland-Altman plots in Panels B and D of Fig. A45). 3 mm hvFE models seem to underestimate the stiffness in STANCE in particular (Panel D in Fig. A45).

Compared with the results from mechanical testing, both the 0.909 and the 2.727 mm hvFE models underestimate femur strength (regression plots in Panels A and C of Fig. A46 for STANCE and FALL loading conditions, respectively). This result is in agreement with the study of Dall'Ara et al. (red dashed lines in Fig. A46) [1]. For stiffness, smaller voxels seem to provide a better estimate in STANCE (see smaller SEE in Panel B of Fig. A46). The R^2 with the results from mechanical testing, however, was always smaller for 3 mm voxels (Fig. A46).

Discussion

The results of this section do not allow to conclude on the higher performance of a smaller model voxel size for the prediction of the mechanical properties of the femur. If smaller voxels seem to capture slightly better the bone stiffness, this cannot be said for femur strength.

Conclusion

In a recent work, Panyasantisuk et al. have reported very similar observations and concluded by discouraging the reduction of the voxel size for an hvFE procedure [2]. Confirming their findings, this appendix does not recommend a reduction of the voxel size of the homogenized FE procedure from 3 to 1 mm. As shown, this is not motivated by an improvement of the femur strength prediction and involves a large increase in computation time.

Given the uncertainties intrinsic in the use of ultimate strength and stiffness as endpoints for the comparison with mechanical tests, future studies should investigate the effect of a reduction in the element size by taking fracture location as well as stress and strain fields into account.

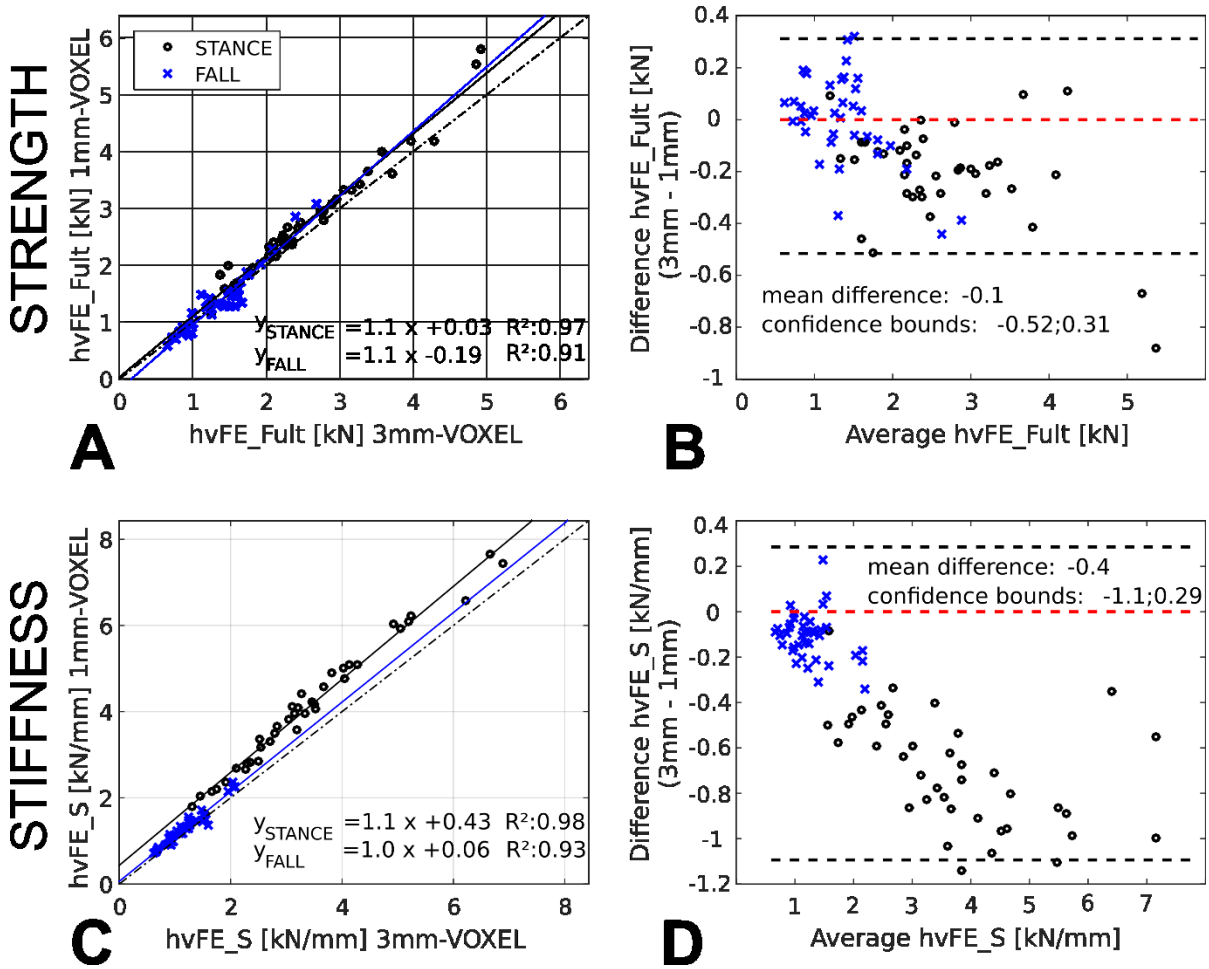

Fig. A45. Comparison between 0.909 and 2.727 mm hvFE voxel size. (A) Regression for predicted femur strength. (B) Bland-Altman plot for strength. (C) Regression for predicted femur stiffness. (D) Bland-Altman plot for stiffness.

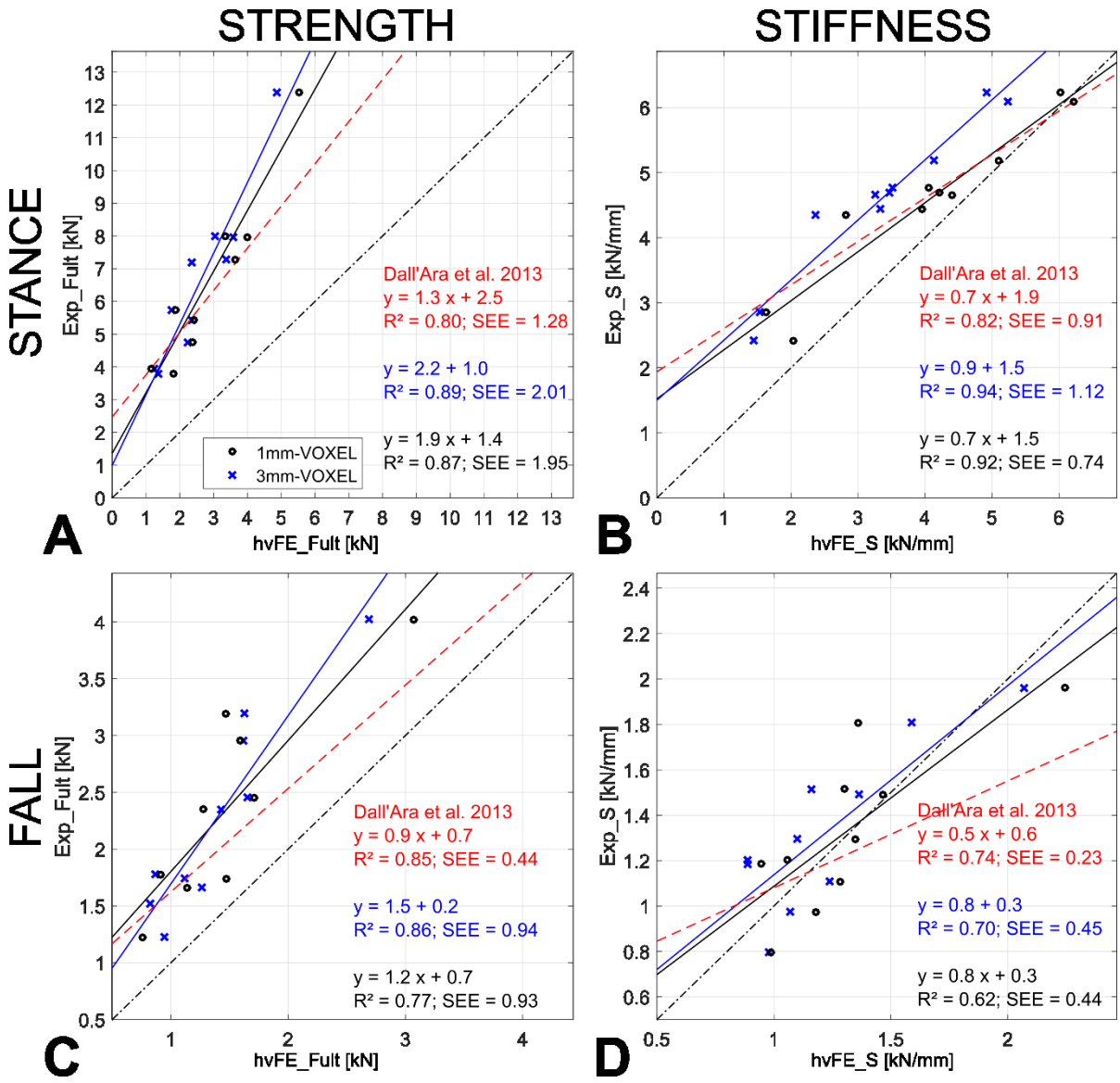

Fig. A46. Comparison with experimental strength and stiffness from mechanical tests. (A) STANCE strength. (B) STANCE stiffness. (C) FALL strength. (D) FALL stiffness

References

1. Dall'Ara E, Luisier B, Schmidt R, Kainberger F, Zysset P, Pahr D. A nonlinear QCT-based finite element model validation study for the human femur tested in two configurations in vitro. Bone. 2013;52: 27–38. doi:10.1016/j.bone.2012.09.006
2. Panyasantisuk J, Dall'Ara E, Pretterklieber M, Pahr DH, Zysset PK. Mapping anisotropy improves QCT-based finite element estimation of hip strength in pooled stance and side-fall load configurations. Med Eng Phys. 2018;0. doi:10.1016/j.medengphy.2018.06.004

Appendix C: vBMD−BV/TV relationship: simulations based on information theory

Background

The idea of the first non-threshold-based approach [1] (StrAx1.0, StraxCorp Pty Ltd, Melbourne, VIC, Australia) for the measurement of Ct.Po from HR-pQCT images can be summarized as follows.

If one considers cortical bone as a two-phase composite of mineralized tissue and water-filled cavities, the mineral phase will have X-ray absorption coefficients around 10 times higher than the second (water) [2]. Under this assumption, the X-Ray attenuation of a unit volume of cortical bone will be equal to:

$$\begin{aligned}\mu_{cort} &= \mu_{bone\ tissue} \times \mathrm{BV} + \mu_{H_2O} \times (TV - BV) \\ &= \mu_{bone\ tissue} \times \frac{BV}{TV} + \mu_{H_2O} \times \left(1 - \frac{BV}{TV}\right) \\ &= \left(\mu_{bone\ tissue} - \mu_{H_2O}\right) \times \frac{BV}{TV} + \mu_{H_2O}\end{aligned}$$

Where $\mu_{bone\ tissue}$ and μ_{H_2O} are the X-Ray attenuation coefficients of mineralized bone tissue and water, respectively, and BV and TV are bone and total volume, respectively.

Since $\mu_{H_2O} \ll \mu_{bone\ tissue}$ this gives:

$$\mu_{cort} \approx \mu_{bone\ tissue} \times \frac{BV}{TV}$$

Accordingly, a linear relationship should exist between the local bone volume fraction (and therefore Ct.Po) and the intensity (or the BMD) of cortical bone voxels from HR-pQCT images.

In chapter 5, it was demonstrated that BMD-based Ct.Po estimates are improved if the BMD-BV/TV relationship becomes non-linear. Particularly, Ct.Po predictions became better after the inclusion of the BMD heterogeneity (standard deviation) in the model. In this section, I present a possible explanation based on considerations from information theory for why BMD_{STD} might improve the prediction of local Ct.Po in cortical bone.

Methods

I developed in silico, 3D binary images of cortical bone like those illustrated in Fig. A47:

- Each volume was composed of 82 × 82 × 82 voxels which, for a simulated HR-pQCT voxelsize of 30.3 µm, gives a volume of approx. 2.5^3 mm³.
- Cylinder-shaped voids were added to the volumes with
  A. Typical diameter of Haversian Canals in human femoral cortical bone (0.05 mm [3,4]; bottom row in Fig. A47)
  B. Diameter = 0.20 mm (large pores; top row in Fig. A47)
- Volumes were generated with BV/TV varying in the 0.60-0.99 range.
- Images were converted to double-precision in the 0-1 range (0 = void; 1 = bone).
- The physical resolution of a hypothetical 2nd generation HR-pQCT was simulated by applying a Gaussian blur with:

$$\sigma = \frac{PSF}{voxel\ size}$$

With a point spread function (PSF) of 55.9 µm [5] and voxel size 30.3 µm.

- Gaussian white noise with noise mean = 0 and σ = 0.1 was added to the images. The resulting SNR was approximately 6.5 and 10 for small and large pores, respectively.
- All voxels were multiplied for 1200, representing a typical value of BMD for fully mineralized bone tissue, in mgHA/cm³.
- BMD_{mean} and BMD_{STD} were finally calculated as the average and the standard deviation of the intensity within each volume, respectively.

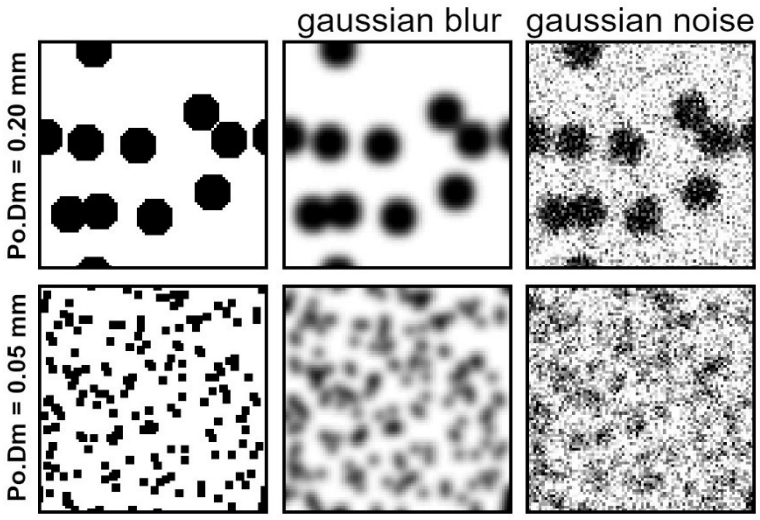

Fig. A47. In silico academic models of cortical bone tissue with pore size of 0.20 mm (top row) and 0.05 mm (bottom row). The finite resolution of the imaging modality is simulated applying a Gaussian blur with σ computed from the HR-pQCT point spread function (second column). Gaussian white noise is than added to the images (third column).

Results

Fig. A48A and B show the relationship between BV/TV and BMD_{mean} and BMD_{STD}, respectively. The ideal (linear) relationship between BMD and BV/TV (black squares and triangles in Fig. A48) becomes less-than-linear in the presence of image blur and noise (yellow symbols in Fig. A48A). In addition the BMD-BV/TV relationship for volumes containing small and large pores is different, with BMD_{mean} being slightly overestimated for small pores (yellow triangles) in comparison to large pores (yellow squares).

The finite resolution of the scanner (image blur) affects the local distribution of BMD, making the BMD_{STD} of volumes containing only small or only large pores vary greatly for the same BV/TV value (orange symbols in Fig. A48B). This effect is diminished by image noise. At SNR = 6-10 dB, large and small pores volumes can still be distinguished based on their BMD_{STD} (yellow symbols in Fig. A48B).

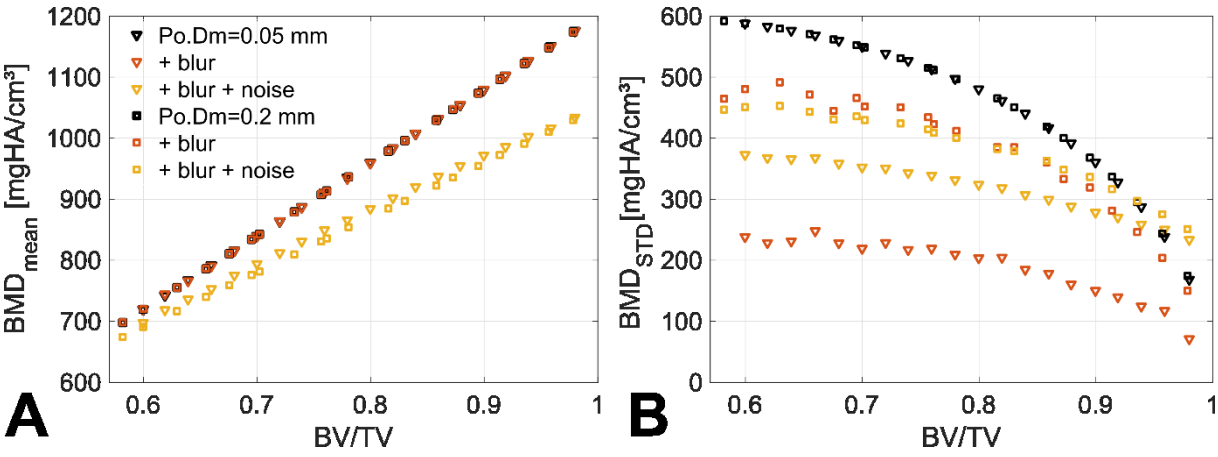

Fig. A48. (A) BMD_{mean}-BV/TV relationship for in silico images of cortical bone with different pore size and in the presence of image blur (orange symbols) and combination of image blur and noise (yellow symbols). (B) BMD_{STD}-BV/TV relationship.

Discussion

Due to image noise and to the finite resolution of HR-pQCT images, two volumes of cortical bone tissue with identical BV/TV but different pore size result in different local BMD. The local BMD heterogeneity can distinguish between these two cases. Therefore, the combination of BMD_{mean} and BMD_{STD} might improve the estimate of local BV/TV from HR-pQCT images. Higher noise levels and beam hardening of polychromatic X-rays might further complicate this picture.

Acknowledgments

I would like to thank Dr. Felix Thomsen for the conversations about the topics of this appendix.

References

1. Zebaze R, Ghasem-Zadeh A, Mbala A, Seeman E. A new method of segmentation of compact-appearing, transitional and trabecular compartments and quantification of cortical porosity from high resolution peripheral quantitative computed tomographic images. Bone. 2013;54: 8–20. doi:10.1016/j.bone.2013.01.007
2. Suplee C. X-Ray Mass Attenuation Coefficients. In: NIST [Internet]. 17 Sep 2009 [cited 13 Sep 2019]. Available: https://www.nist.gov/pml/x-ray-mass-attenuation-coefficients
3. Chappard C, Bensalah S, Olivier C, Gouttenoire PJ, Marchadier A, Benhamou C, et al. 3D characterization of pores in the cortical bone of human femur in the elderly at different locations as determined by synchrotron micro-computed tomography images. Osteoporos Int. 2013;24: 1023–1033. doi:10.1007/s00198-012-2044-4
4. Perilli E, Bala Y, Zebaze R, Reynolds KJ, Seeman E. Regional Heterogeneity in the Configuration of the Intracortical Canals of the Femoral Shaft. Calcif Tissue Int. 2015;97: 327–335. doi:10.1007/s00223-015-0014-5
5. Metcalf LM, Dall'Ara E, Paggiosi MA, Rochester JR, Vilayphiou N, Kemp GJ, et al. Validation of calcaneus trabecular microstructure measurements by HR-pQCT. Bone. 2018;106: 69–77. doi:10.1016/j.bone.2017.09.013

Appendix D: Nonlinear homogenized voxel finite element models reflect the distinct role of the cortical and trabecular femoral neck architecture for femur strength

Gianluca Iori,[1] Laura Peralta,[2,3]† Andreas Reisinger,[4]† Frans Heyer,[5,6]† Caroline Wyers,[5,6] Joop van den Bergh,[5,6] Dieter Pahr[4,7], and Kay Raum[1*]

[1] Berlin-Brandenburg Center for Regenerative Therapies, Charité – Universitätsmedizin Berlin, corporate member of Freie Universität Berlin, Humboldt-Universität zu Berlin, and Berlin Institute of Health, Berlin, Germany
[2] Laboratoire d'Imagerie Biomédicale, Sorbonne Universités, INSERM UMR S 1146, CNRS UMR 7371, Paris, France
[3] Department of Biomedical Engineering, School of Biomedical Engineering & Imaging Sciences, King's College London, London, UK
[4] Division Biomechanics, Karl Landsteiner University of Health Sciences, Krems, Austria
[5] Department of Internal Medicine, NUTRIM School of Nutrition and Translational Research in Metabolism, Maastricht University Medical Center, Maastricht, The Netherlands
[6] Department of Internal Medicine, VieCuri Medical Center, Venlo, The Netherlands
[7] Institute for Lightweight Design and Structural Biomechanics, TU Wien, Vienna, Austria

† These authors contributed equally to the current work.
* Corresponding author: Kay Raum
E-mail: kay.raum@charite.de

My contribution

I performed sample preparation, mechanical tests, FE analyses, image and statistical processing for this study. The HR-pQCT data was mostly collected by FH and CW at VieCuri Venlo (the Netherlands), after FH and I initiated the procedure.

Publication notification

This chapter contains extracts of a work under preparation for submission to the journal Medical Engineering and Physics.

Abstract

Introduction:
In the human femoral neck, the cortical and trabecular architectures play a mechanical role that changes with the load direction. Subject specific homogenized voxel finite element (hvFE) models can be implemented from quantitative computed tomography (QCT) scans to simulate femur strength under multiple configurations of load. In these models, however, the bone microstructure is homogenized to a continuum. The aim of this work was to understand if hvFE models correctly capture the distinct role of the cortical and trabecular femoral neck architecture for femur strength.

Methods:
The strength of 10 pairs of human femora was measured *ex vivo* using quasi-static mechanical tests and nonlinear QCT-derived hvFE models. One-legged standing and sideways falling loads were applied. Associations between femur strength and the volumetric bone mineral density (vBMD) or microstructure of femoral neck cortical and trabecular bone were compared for mechanical tests and hvFE simulations as well as for standing and falling loads.

Results:
While standing, femur strength was strongly associated with the total vBMD ($R^2 = 0.83$, $p < 0.001$) and cortical bone thickness ($R^2 = 0.75$, $p < 0.01$) of the femoral neck. For falling loads, the strongest determinant of femur strength was the trabecular bone volume fraction in the femoral neck ($R^2 = 0.87$, $p < 0.001$). For both load directions, associations computed taking femur strength from hvFE models were in excellent agreement with those by mechanical experiments.

Conclusion:
Despite approximating the bone microarchitecture to a continuum, hvFE models capture the distinct role of the femoral neck cortical and trabecular structures for femur strength.

Keywords:
Osteoporosis; Femoral neck; Bone strength; Finite Element Analysis; Hip fragility

Introduction

Subject specific homogenized finite element (FE) models of the hip can be developed automatically from quantitative computed tomography (QCT) datasets that are available in the clinics [1] and provide femur strength predictions that are superior to those by dual-energy X-ray absorptiometry (DXA, the current standard in the assessment of osteoporosis) or QCT [2]. The possibility to test the proximal femur *in silico* under multiple loading conditions improves the potential of FE for hip fracture prediction [3] and represents one of the key advantages of the FE approach. Simulating the mechanical solicitations of both ordinary gait and extraordinary events might identify, for example, over-adapted femora that have become particularly fragile under non-habitual loading [4,5].

The fragility of the human femoral neck is determined by the amount and organization (architecture) of the bone tissue that composes it. Cortical bone thinning in the femoral neck was associated with increased incidence of fractures [6–8]. The trabecular bone of the femoral neck, at the same time, contributes to femoral stability [9] and its architecture is altered structure in osteoporosis [10]. Furthermore, the relative importance of the cortical and trabecular structures in the femoral neck varies depending on the load case. During one-legged standing, hip strength is mainly determined by the cortical compartment, while trabecular bone might contribute only marginally [11]. The density and connectivity of trabecular tissue, on the other hand, seem to reinforce the femoral neck particularly during a fall on the side [9].

In hvFE models of the proximal femur, cortical and trabecular tissues are homogenized to a continuum within voxels of several millimeters. Due to the homogenization procedure, the geometrical detail of the bone microarchitecture is lost. This raises the question if hvFE models neglect, totally or in part, the role of the bone microstructure for hip fragility.

In this study on cadaveric specimens, we assessed the contribution of the density and microstructure of femoral neck cortical and trabecular bone to the ultimate load of the proximal femur under standing and falling loads. The architecture and vBMD of the femoral necks from 20 human donors were quantified on high-resolution peripheral QCT (HR-pQCT) images, whereas femur strength was measured, for the same bones, using mechanical tests and HR-pQCT-based nonlinear hvFE models.

The goal was to elucidate if femur strength predictions by nonlinear hvFE models capture the different role of the cortical and trabecular architectures in the femoral neck as well as the correct dependence of this role on the load direction.

Materials and Methods

Samples and imaging

Left and right femora from ten human donors (Table A24) were used for this study. The subjects had given consent for scientific use of their bodies. Samples were collected at the anatomy institute of the Lübeck University in accordance with the German law.

High resolution microCT scans with isotropic voxel size of 30.3 µm of the proximal femora were acquired using a second generation HR-pQCT (XtremeCT II, Scanco Medical AG, Brüttisellen, Switzerland). The scanning procedure was already described [12]. Briefly: scanner settings were: X-ray tube voltage = 68 kVp, current = 1470 µA, integration time = 200 ms, number of projections = 3000, total rotation = 180°, image matrix = 4608 × 4608.

Table A24. Details of the donor's age, sex and T-Score. The latter was calculated comparing the areal BMD of the femoral neck with sex- and ethnicity adjusted reference values [13]. For this, DXA scans of the proximal femora were performed on a Hologic Discovery A scanner (Discovery QDR, Hologic Inc., USA) after immerging the bones in 14 mm-deep saline solution.

ID	Sex	Age	Condition / Medication	T-Score
#1	m	88	Pancreatic cancer	−3.00
#2	w	80	Lung cancer (Pancoast)	−3.63
#3	w	94	(Diagnosed) osteoporosis	−4.00
#4	m	80		−3.19
#5	w	92		−3.64
#6	m	70		−1.31
#7	w	85		−2.32
#8	w	82		−3.30
#9	w	69	Non-Hodgkin lymphoma (B-cell)	−2.44
#10	m	94		−4.04
Median		83.5		−3.24
SD		9.0		0.86
Range		69-94		−4.04 −1.31

Mechanical testing

The femora were experimentally tested to failure following an established protocol [14]. From each pair of legs, one side was selected randomly and tested mechanically in a configuration representative of one-legged standing (STANCE: 20° inclination in the frontal plane, load direction in the plane defined by the femoral neck and shaft axes). The contralateral leg was tested simulating a side-backwards fall (FALL: 0° internal rotation, 30° adduction angle). Before each test, a preconditioning cycle of 10 compressions was applied on the femoral head. After this, the femoral head was displaced at a rate of 5 mm/min until failure, while measuring the axial force with a 100 kN load cell (U3 force transducer, HBM, Germany). The experimental bone strength (Exp_Fu) was defined as the ultimate force recorded during the experiment.

Finite element modelling

Nonlinear homogenized voxel Finite Element (hvFE) models were obtained from microCT images to simulate proximal femur failure under both STANCE and FALL loads. The procedure had been previously validated [14]. Air voxels trapped inside the bone were set to the HU of water and the datasets coarsened to 2.7 mm voxel size. The resulting voxel intensity was converted to bone volume fraction (BV/TV) using a linear calibration rule that was obtained for the specific set of scans [12]. The constitutive law applied to the model voxels implements BV/TV-dependent elastic and damage properties and a piecewise Hill yield criterion based on stress [15]. Elasticity and yield constants for the material model were scaled according to an empirical function of the local BV/TV [14,16]. The models were generated with medtool 4.1 (Dr. Pahr Ingenieurs e.U, Pfaffstätten, Austria) and solved in Abaqus 6.12 (Simulia, Dassault Systemes, Velizy, France). The hvFE-based proximal femur strength (hvFE_Fu) in STANCE and FALL conditions was calculated as the maximum reaction force recorded during the simulations.

Image processing of the femoral neck

A 7 mm-thick cross section was extracted from the microCT images around the femoral neck section with minimum area (Panel A in Fig. A49). High frequency noise was removed applying a 3D Gaussian filter (sigma = 1.06 voxels). The volume was downsampled to 60.6 μm voxel size and rotated aligning the z-axis with the femoral neck axis (Panel B in Fig. A49). Binary

masks of cortical and trabecular tissues were obtained by two separate steps of adaptive thresholding [17]. The two thresholds were computed independently from the intensity histograms of only cortical and only trabecular bone, respectively. For the segmentation of the cortical compartment, an already described semi-automatic procedure [18] was adapted to the higher resolution of our microCT data. Particularly, the endosteum boundary was manually corrected in Amira (Zuse Institute Berlin, Germany) and combined with a mask of the bone tissue.

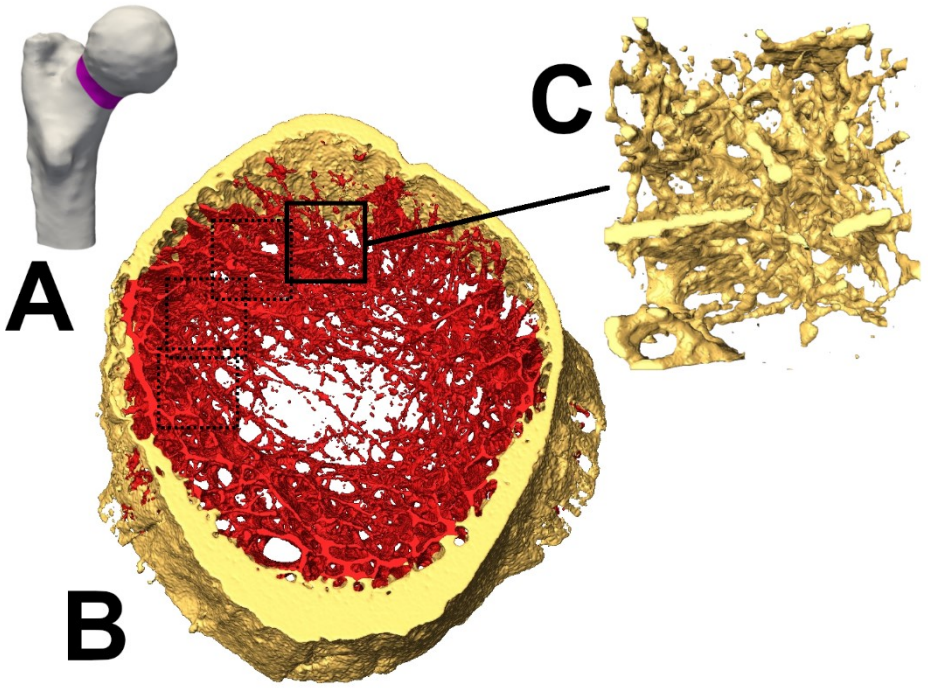

Fig. A49. 3D histomorphometry of the femoral neck. (A) Measurements were performed on a 7 mm-thick cross section of the femoral neck centered on the plane where the neck section has minimum area. (B) All images were rotated perpendicular to the neck axis before separating the trabecular core (red) by a semi-automatic procedure. (C) Tb.Th, Tb.Sp and Tb.N were measured on 12 parallelepiped regions of the neck and then averaged.

Density and histomorphometry calculations

Volumetric BMD (total: $vBMD_{tot}$, cortical: $vBMD_{cort}$, and trabecular: $vBMD_{trab}$), cortical bone porosity (Ct.Po), cortical thickness (Ct.Th) and trabecular bone volume fraction (Tb.BV/TV) of the femoral neck were measured. The percentage of cortical bone surface with Ct.Th < 0.10 mm (ultrathin) [7] and the volume ratio between trabecular and cortical bone tissue in the femoral neck [9] were also measured. Trabecular number (Tb.N), thickness (Tb.Th) and separation (Tb.Sp) were measured in medtool 4.1 (Dr. Pahr Ingenieurs e.U, Pfaffstätten, Austria) on 12 parallelepiped sub-volumes of the spongiosa distributed circumferentially around the femoral neck (Panels B and C in Fig. A49) and then averaged.

Statistics

The ultimate strength of a bone depends on its size. In order to compensate for anatomical differences within the samples, femur strength was normalized dividing it for the minimum cross-sectional area of the femoral neck (*Tt.Ar*). Tt.Ar was calculated considering both bone tissue and marrow space.

$$Exp\_Fu_{norm} = \frac{Exp\_Fu}{Tt.Ar} \qquad hvFE\_Fu_{norm} = \frac{hvFE\_Fu}{Tt.Ar} \tag{A25}$$

Associations between the normalized ultimate load of the femoral neck (both Exp_Fu_{norm} and hvFE_Fu_{norm}) and the vBMD and microarchitecture of the femoral neck were investigated by linear regression analysis. For each parameter showing significant associations with strength, the R^2 with Exp_Fu_{norm} and hvFE_Fu_{norm} were compared. The significance level was set at $p < 0.05$. All analyses were performed in Matlab (R2018a, The Mathworks Inc., Natick, MA, USA), unless stated otherwise.

Results

Proximal femur strength

Numerical simulations with the hvFE method underestimated femur strength in comparison with mechanical tests (Table A25) but the two measurement were strongly correlated ($R^2 = 0.89$, SEE = 800 N and $R^2 = 0.86$, SEE = 309 N for STANCE and FALL, respectively). The results of the hvFE validation have been published already [19].

Table A25. Ultimate force of the proximal femur from mechanical tests and hvFE simulations.

	STANCE Mean ± SD (min-max)	FALL Mean ± SD (min-max)
***Exp_Fu* [N]**	6646 ± 2555 (3780-12396)	2292 ± 881 (1230-4026)
***hvFE_Fu* [N]**	2616 ± 1117 (1243-4860)	1403 ± 553 (821-2691)

Determinants of femur strength in the femoral neck

Table A26 collects the results of vBMD and structural measurements performed at the femoral neck. The last four columns show the coefficient of determination of the linear regression of each vBMD and architectural variable with the ultimate load of the proximal femur after normalizing this for the whole FN cross-sectional area.

Table A26. Density and architecture of the femoral neck and R^2 of their association with femur strength normalized for femoral neck cross-sectional area. Associations with strength are shown for both STANCE and sideways FALL loading conditions and for mechanical tests (Exp) and nonlinear homogenized voxel FE simulations (hvFE) of proximal femur failure. ($N = 10$).

			Fu_{norm}			
			STANCE		FALL	
			Exp	hvFE	Exp	hvFE
	Mean ± SD (min-max)	CV [%]	Coefficient of determination (R^2)			
***$vBMD_{tot}$* [mgHA/cm³]**	209 ± 52 (107-314)	25	**0.83****	**0.84****	**0.66***	**0.82****
***$vBMD_{cort}$* [mgHA/cm³]**	799 ± 45 (688-885)	6				
***$vBMD_{trab}$* [mgHA/cm³]**	82 ± 39 (18-189)	47	**0.64***	**0.59***	**0.70***	**0.82****
***Tt.Ar* [mm²]**	7.08 ± 1.60 (4.99-11.10)	23				
***Ct.Th* [mm]**	0.94 ± 0.19 (0.60-1.37)	21	**0.75***	**0.82****	**0.63***	0.54
***Ultrathin* [%]**	14.7 ± 9.1 (2.1-36.7)	62	0.53	0.57	0.41	
***Ct.Po* [%]**	3.4 ± 1.5 (1.2-7.0)	43				
***Tb.BV/TV* [%]**	15.6 ± 3.7 (10.7-24.2)	24	0.41		**0.87****	**0.82****
***Tb.Th* [mm]**	0.28 ± 0.02 (0.24-0.34)	9				
***Tb.Sp* [mm]**	1.50 ± 0.60 (0.92-3.37)	40				
***Tb.N* [mm]**	0.64 ± 0.13 (0.39-0.87)	20				
FN trabecular/cortical volume ratio	0.80 ± 0.23 (0.35-1.44)	28				

SD = standard deviation; CV = coefficient of variation; *p < 0.01; **p < 0.001.

Bone mineral density

In STANCE, both Exp_Fu_{norm} and $hvFE\_Fu_{norm}$ were strongly associated with $vBMD_{tot}$ ($R^2 \geq 0.83$; both $p < 0.001$; Table A26) and moderately associated with $vBMD_{trab}$ ($R^2 \geq 0.59$; both $p < 0.01$; Table A26). In FALL conditions hvFE simulations overestimated the role of $vBMD_{tot}$ ($R^2 = 0.82$, $p < 0.001$; Table A26) and $vBMD_{trab}$ ($R^2 = 0.82$, $p < 0.001$; Table A26) for proximal femur strength. There was no association between $vBMD_{cort}$ and femur strength (Table A26).

Bone architecture

Ct.Th in the femoral neck was associated with the normalized ultimate load of the proximal femur for both standing and sideways fall loads (Table A26). Associations were particularly strong in STANCE ($R^2 = 0.75$, $p < 0.01$ for Exp_Fu_{norm} and $R^2 = 0.82$, $p < 0.001$ for $hvFE\_Fu_{norm}$; Table A26) and analogous between hvFE simulations and mechanical tests of proximal femur failure. Always for STANCE, the percentage of ultrathin cortical bone showed mild, negative associations with both Exp_Fu_{norm} and $hvFE\_Fu_{norm}$ ($R^2 = 0.53$ and 0.57, respectively; both $p < 0.05$; Table A26).

Tb.BV/TV of the femoral neck was strongly associated with proximal femur strength only for FALL loads. This result was captured by both mechanical tests ($R^2 = 0.87$, $p < 0.001$; Table A26) and hvFE ($R^2 = 0.82$, $p < 0.001$; Table A26) simulations of proximal femur failure. Association between Exp_Fu_{norm} or $hvFE\_Fu_{norm}$ and Tb.Th, Tb.Sp, Tb.N or trabecular/cortical volume ratio in the femoral neck were non-significant (Table A26).

Discussion

In this study, we asked if nonlinear hvFE models of hip failure capture the relative contribution of femoral neck cortical and trabecular bone tissue to the ultimate femur strength. Since such contribution is expected to vary depending on the load direction, we developed hvFE simulations and applied mechanical tests in two different conditions of load: physiological one-legged STANCE and sideways FALL. The density and microstructure of the femoral neck was analyzed on the same HR-pQCT images utilized for hvFE model generation.

Compared with histology, HR-pQCT allowed the 3D histomorphometric characterization and precise control on the position of the femoral neck cross section selected for the analysis [20]. The measured Ct.Th was close to values found for analogous age groups [7,10]. Ct.Po was lower than already reported [10], since only large pores can be segmented on HR-pQCT images [21]. Tb.Th and Tb.BV/TV were overestimated [10,22] also due to the physical resolution (55.9 µm [23]) of 2nd generation HR-pQCT. In view of the uncertain representation of thinnest trabeculae, we decided not to quantify trabecular connectivity.

The ultimate strength of the proximal femur was strongly associated with the total and trabecular vBMD as well as with the cortical thickness and trabecular bone volume fraction in the femoral neck of 10 elderly donors. Associations with femur strength were non-significant for cortical bone vBMD, cortical porosity or morphological properties (thickness, separation and number) of the trabecular microstructure in the femoral neck. Importantly, strength predictions by hvFE models identified the same density and structural determinants of proximal femur strength in the femoral neck as the ultimate strength from mechanical tests.

The direction of mechanical loading had a marked influence on the relative contribution of femoral neck cortical and trabecular tissues to the ultimate femur strength. During physiological standing, the thickness of the cortical bone shell in the femoral neck played the principal role in determining the experimental ultimate load of the femur. In comparison with

cortical thickness, trabecular bone density and volume fraction had modest or non-significant associations with femur strength. This is in very good agreement with a previous experimental investigation by mechanical testing conducted *ex vivo* on a similar cohort of samples [11]. The prominent role of cortical thickness in determining the standing strength of the femur was properly captured by nonlinear hvFE simulations of femur failure. On the other hand, it suggests that as long as resistance to standing loads is concerned, a measurement of the cortical thickness in the femoral neck might represent a more direct assessment of strength-relevant information than hvFE. In this sense, the direct mapping of cortical bone thickness on CT images of the proximal femur [24] was already demonstrated, and femoral neck Ct.Th was proposed as a predictor of osteoporotic hip fractures [6,8].

When the proximal femur was subjected to the transversal forces of a fall on the greater trochanter, fracture resistance was the combined product of the cortical and trabecular architectures. In this load scenario (which is associated to the highest risk of fracture [25]), the vBMD and particularly the BV/TV of trabecular bone in the femoral neck showed the strongest correlations with the experimental femur strength. This observation can be explained by the strengthening function accomplished by trabecular bone during a sideways fall [9], which becomes even more important for osteoporotic femora like the ones used in our study [9]. For FALL conditions too, our hvFE simulations were in agreement with mechanical tests, and were able to point out the prevalent role of the femoral neck trabecular bone for femur strength.

Taken together, the findings of this work suggest that it is reliable to attribute low femur strength predictions by nonlinear hvFE to the weakening of the bone microarchitecture. The agreement of simulations and experiments for both STANCE and FALL is important since *in silico* tests of multiple loading conditions can enhance the strength [26] and fracture risk information attainable by homogenized FE models [3].

Three limitations of the current research are worth mentioning. The first of these is represented by the low number of samples ($N = 10$) originating from a cohort of elderly and osteoporotic (median femoral neck T-Score: −3.24) donors.

Second, the mechanical testing and hvFE analyses considered only two between the many directions of load experienced by the proximal femur during routine tasks [27] and caused by a fall to the ground [25].

Third, experiments and hvFE simulations were based on strain rates far from those experienced by the hip during gait or falls. The reason for measuring femur strength under quasi-static loads was to rely on a procedure already validated in terms of femur strength predictions [14]. One should remind, however, that the ultimate strength of proximal femur differs under impact and fixed displacement rate [28]. In addition, due to the viscous flow of the marrow, the strength of bulk cortical and trabecular bone tissues varies depending on the applied strain rate [29].

Conclusion

Until now, the validation of nonlinear homogenized voxel FE models of the proximal femur has considered whole bone strength [14,30,31], stiffness [14,31] or fracture location [14] as output parameters for the comparison with mechanical tests. In this work, we showed that mechanical tests and nonlinear hvFE capture equally well the relative contribution of femoral neck cortical and trabecular bone to the ultimate femur strength. Our results support the use of hvFE to simulate varying conditions of load of the human hip. Further studies should address the confirmation of our findings using clinical QCT data.

References

1. Qasim M, Farinella G, Zhang J, Li X, Yang L, Eastell R, et al. Patient-specific finite element estimated femur strength as a predictor of the risk of hip fracture: the effect of methodological determinants. Osteoporos Int. 2016;27: 2815–2822. doi:10.1007/s00198-016-3597-4
2. Engelke K, Rietbergen B van, Zysset P. FEA to Measure Bone Strength: A Review. Clin Rev Bone Miner Metab. 2016;14: 26–37. doi:10.1007/s12018-015-9201-1
3. Falcinelli C, Schileo E, Balistreri L, Baruffaldi F, Bordini B, Viceconti M, et al. Multiple loading conditions analysis can improve the association between finite element bone strength estimates and proximal femur fractures: A preliminary study in elderly women. Bone. 2014;67: 71–80. doi:10.1016/j.bone.2014.06.038
4. Weinans H. Is osteoporosis a matter of over-adaptation? Technol Health Care. 1998;6: 299–306.
5. Verhulp E. Analyses of trabecular bone failure. 2006; doi:10.6100/IR608109
6. Poole KES, Treece GM, Mayhew PM, Vaculík J, Dungl P, Horák M, et al. Cortical Thickness Mapping to Identify Focal Osteoporosis in Patients with Hip Fracture. PLOS ONE. 2012;7: e38466. doi:10.1371/journal.pone.0038466
7. Power J, Loveridge N, Kröger H, Parker M, Reeve J. Femoral neck cortical bone in female and male hip fracture cases: Differential contrasts in cortical width and sub-periosteal porosity in 112 cases and controls. Bone. 2018;114: 81–89. doi:10.1016/j.bone.2018.05.027
8. Johannesdottir F, Poole KES, Reeve J, Siggeirsdottir K, Aspelund T, Mogensen B, et al. Distribution of cortical bone in the femoral neck and hip fracture: A prospective case-control analysis of 143 incident hip fractures; the AGES-REYKJAVIK Study. Bone. 2011;48: 1268–1276. doi:10.1016/j.bone.2011.03.776
9. Nawathe S, Akhlaghpour H, Bouxsein ML, Keaveny TM. Microstructural Failure Mechanisms in the Human Proximal Femur for Sideways Fall Loading: FEMORAL STRENGTH MICROMECHANICS. J Bone Miner Res. 2014;29: 507–515. doi:10.1002/jbmr.2033
10. Blain H, Chavassieux P, Portero-Muzy N, Bonnel F, Canovas F, Chammas M, et al. Cortical and trabecular bone distribution in the femoral neck in osteoporosis and osteoarthritis. Bone. 2008;43: 862–868. doi:10.1016/j.bone.2008.07.236
11. Holzer G, von Skrbensky G, Holzer LA, Pichl W. Hip Fractures and the Contribution of Cortical Versus Trabecular Bone to Femoral Neck Strength. J Bone Miner Res. 2009;24: 468–474. doi:10.1359/jbmr.081108
12. Iori G, Heyer F, Kilappa V, Wyers C, Varga P, Schneider J, et al. BMD-based assessment of local porosity in human femoral cortical bone. Bone. 2018;114: 50–61. doi:10.1016/j.bone.2018.05.028
13. Looker AC, Wahner HW, Dunn WL, Calvo MS, Harris TB, Heyse SP, et al. Updated Data on Proximal Femur Bone Mineral Levels of US Adults. Osteoporos Int. 1998;8: 468–490. doi:10.1007/s001980050093
14. Dall'Ara E, Luisier B, Schmidt R, Kainberger F, Zysset P, Pahr D. A nonlinear QCT-based finite element model validation study for the human femur tested in two configurations in vitro. Bone. 2013;52: 27–38. doi:10.1016/j.bone.2012.09.006
15. Garcia D, Zysset PK, Charlebois M, Curnier A. A three-dimensional elastic plastic damage constitutive law for bone tissue. Biomech Model Mechanobiol. 2008;8: 149–165. doi:10.1007/s10237-008-0125-2

16. Rincón-Kohli L, Zysset PK. Multi-axial mechanical properties of human trabecular bone. Biomech Model Mechanobiol. 2008;8: 195–208. doi:10.1007/s10237-008-0128-z
17. Ridler T, Calvard S, others. Picture thresholding using an iterative selection method. IEEE Trans Syst Man Cybern. 1978;8: 630–632.
18. Burghardt AJ, Buie HR, Laib A, Majumdar S, Boyd SK. Reproducibility of direct quantitative measures of cortical bone microarchitecture of the distal radius and tibia by HR-pQCT. Bone. 2010;47: 519–528. doi:10.1016/j.bone.2010.05.034
19. Iori G, Schneider J, Reisinger A, Heyer F, Peralta L, Wyers C, et al. Large cortical bone pores in the tibia are associated with proximal femur strength. PLOS ONE. 2019;14: e0215405. doi:10.1371/journal.pone.0215405
20. Lang T, Keyak J, Heitz M, Augat P, Lu Y, Mathur A, et al. Volumetric quantitative computed tomography of the proximal femur: precision and relation to bone strength. Bone. 1997;21: 101–108.
21. Jorgenson BL, Buie HR, McErlain DD, Sandino C, Boyd SK. A comparison of methods for in vivo assessment of cortical porosity in the human appendicular skeleton. Bone. 2015;73: 167–175. doi:10.1016/j.bone.2014.11.023
22. Bell KL, Loveridge N, Power J, Garrahan N, Stanton M, Lunt M, et al. Structure of the femoral neck in hip fracture: cortical bone loss in the inferoanterior to superoposterior axis. J Bone Miner Res Off J Am Soc Bone Miner Res. 1999;14: 111–119. doi:10.1359/jbmr.1999.14.1.111
23. Metcalf LM, Dall'Ara E, Paggiosi MA, Rochester JR, Vilayphiou N, Kemp GJ, et al. Validation of calcaneus trabecular microstructure measurements by HR-pQCT. Bone. 2018;106: 69–77. doi:10.1016/j.bone.2017.09.013
24. Treece GM, Gee AH, Mayhew PM, Poole KES. High resolution cortical bone thickness measurement from clinical CT data. Med Image Anal. 2010;14: 276–290. doi:10.1016/j.media.2010.01.003
25. Keyak JH, Skinner HB, Fleming JA. Effect of force direction on femoral fracture load for two types of loading conditions. J Orthop Res. 2001;19: 539–544. doi:10.1016/S0736-0266(00)00046-2
26. Keyak JH. Relationships between femoral fracture loads for two load configurations. J Biomech. 2000;33: 499–502. doi:10.1016/S0021-9290(99)00202-X
27. Bergmann G, Deuretzbacher G, Heller M, Graichen F, Rohlmann A, Strauss J, et al. Hip contact forces and gait patterns from routine activities. J Biomech. 2001;34: 859–871. doi:10.1016/S0021-9290(01)00040-9
28. Gilchrist S, Nishiyama KK, Bakker P de, Guy P, Boyd SK, Oxland T, et al. Proximal femur elastic behaviour is the same in impact and constant displacement rate fall simulation. J Biomech. 2014;47: 3744–3749. doi:10.1016/j.jbiomech.2014.06.040
29. Carter DR, Hayes WC. Bone compressive strength: the influence of density and strain rate. Science. 1976;194: 1174–1176. doi:10.1126/science.996549
30. Keyak JH, Rossi SA, Jones KA, Skinner HB. Prediction of femoral fracture load using automated finite element modeling. J Biomech. 1997;31: 125–133.
31. Nishiyama KK, Gilchrist S, Guy P, Cripton P, Boyd SK. Proximal femur bone strength estimated by a computationally fast finite element analysis in a sideways fall configuration. J Biomech. 2013;46: 1231–1236. doi:10.1016/j.jbiomech.2013.02.025

Publication list:

Included in the thesis:

Iori G, Heyer F, Kilappa V, Wyers C, Varga P, Schneider J, et al. BMD-based assessment of local porosity in human femoral cortical bone. Bone. 2018;114: 50–61. doi:10.1016/j.bone.2018.05.028

Iori G, Schneider J, Reisinger A, Heyer F, Peralta L, Wyers C, et al. Large cortical bone pores in the tibia are associated with proximal femur strength. PLOS ONE. 2019;14: e0215405. doi:10.1371/journal.pone.0215405

Iori G, Schneider J, Reisinger A, Heyer F, Peralta L, Wyers C, et al. Cortical thinning reflects structural deterioration of the femoral neck. 2019. Submitted to the Journal of Bone and Mineral Research (JBMR).

Iori G, Peralta L, Reisinger A, Heyer F, Wyers C, van den Bergh JP, et al. Femur strength predictions by non-linear homogenized voxel finite element models are affected by femoral neck architecture. In preparation for Medical Engineering & Physics.

Other publications:

T. Potsika V, N. Grivas K, Gortsas T, **Iori G**, C. Protopappas V, Raum K, et al. Computational Study of the Effect of Cortical Porosity on Ultrasound Wave Propagation in Healthy and Osteoporotic Long Bones. Materials. 2016;9: 205. doi:10.3390/ma9030205

Schneider J, **Iori G**, Ramiandrisoa D, Hammami M, Gräsel M, Chappard C, et al. Ex vivo cortical porosity and thickness predictions at the tibia using full-spectrum ultrasonic guided-wave analysis. Arch Osteoporos. 2019;14: 21. doi:10.1007/s11657-019-0578-1

Karbalaeisadegh Y, Yousefian O, **Iori G**, Raum K, Muller M. Acoustic diffusion constant of cortical bone: Numerical simulation study of the effect of pore size and pore density on multiple scattering. The Journal of the Acoustical Society of America. 2019;146: 1015–1023. doi:10.1121/1.5121010

Du J, **Iori G**, Raum K. Imaging of cortical pores using ultrasound contrast agents: Phantom and ex vivo studies. 2017 IEEE International Ultrasonics Symposium (IUS). Washington, DC, USA: IEEE; 2017. pp. 1–4. doi:10.1109/ULTSYM.2017.8091590

Potsika VT, Fotiadis DI, Gortsas T, **Iori G**, Raum K. High-frequency cortical backscatter reveals cortical microstructure - A simulation study. 2015 6th European Symposium on Ultrasonic Characterization of Bone. Corfu, Greece: IEEE; 2015. pp. 1–4. doi:10.1109/ESUCB.2015.7169890

Mardones J, **Iori G**, Becerra A, Diaz M, Zagal JC. Using digital fabrication on small satellite projects. Proceedings of the International Symposium on Small Satellites Systems and Services-4S Symposium-, Portorož, Slovenia. 2012.

Patents:

Raum K, Du J, Iori G. System, method, and computer program product for determining cortical bone characteristics [Internet]. 27 Dec 2018. Available: https://patentscope2.wipo.int/search/en/detail.jsf;jsessionid=B29E2BDF91FC64A4FB235FB21380FA2E?docId=WO2018234472&tab=PCTBIBLIO